CONTROL OF ION+PHOTOELECTRON ENTANGLEMENT IN ATTOSECOND PUMP-PROBE EXPERIMENTS

Dissertation
zur Erlangung des Grades eines
Doktors der Naturwissenschaften
(*Dr. rer. nat.*)

am Fachbereich Physik
der Freien Universität Berlin

vorgelegt von
Lisa-Marie Koll

Berlin 2024

Erstgutachter:	Prof. Dr. Tobias Kampfrath
Zweitgutachter :	Prof. Dr. Guiseppe Sansone

Tag der Disputation: 21.01.2025

ABSTRACT

Entanglement is a fundamental principle in quantum mechanics, and is known for its crucial part in quantum information science and quantum communication, among others. In attosecond science, the possible effects of entanglement in light-matter interaction are receiving more and more attention. In this research field, typically radiation in the extreme ultraviolet (XUV) or x-ray regime is used to study time-dependent dynamics in time-resolved spectroscopy experiments. The high photon energy of this radiation leads to ionization of any sample placed in the way, thus creating multicomponent quantum systems with possible entangled subsystems, e.g. ion and photoelectron. Entanglement between the subsystems can have measurable effects on the outcome of an experiment, and can even prevent the observation of time-dependent observables. This notion is most prominent if the experiment includes only measurements in one of the subsystems, which means for example in the case of molecular photoionization, that only the ion or photoelectron is measured.
This setting leads to interesting questions about the role of entanglement in attosecond photoionization processes. In particular, what is the role of entanglement between the ion and departing photoelectron regarding the observability of coherence-based dynamics in the ion? Furthermore, is it possible to control the degree of coherence in the ion and the degree of ion+photoelectron entanglement, respectively, by alternating the pulse properties of the ionizing pulses?
To answer these questions, an experimental protocol is described in this thesis, which utilizes two phase-locked XUV pulses together with a near-infrared pulse (NIR) to dissociatively ionize hydrogen molecules. The main experiments presented here investigate the impact of entanglement between the cation and photoelectron, first on vibrational coherence, and subsequently on electronic coherence created in H_2^+. In the first experiment, a pair of phase-locked XUV pulses creates a vibrational wave packet in the $1s\sigma_g$ state of H_2^+, which is subsequently probed by the NIR pulse dissociating the ion. The spectral properties of the ionizing pulses are tailored by alternating the delay between the two XUV pulses, thus controlling the degree of vibrational coherence and the degree of ion+photoelectron entanglement, respectively. In the second experiment, the two XUV pulses create an entangled ion+photoelectron system during the dissociative ionization of H_2. The NIR probe pulse can subsequently project the initially entangled system into a coherent superposition of the first *gerade* ($1s\sigma_g$) and *ungerade* ($2p\sigma_u$) electronic states of the H_2^+ cation. The ability of the NIR pulse to convert the initially entangled system into a coherent superposition of electronic states is controlled by changing the time delay between the ionizing XUV pulses. These studies show the crucial role of ion+photoelectron entanglement in attosecond science, especially in attosecond pump-probe experiments, and they present a first attempt to link ultrafast science with quantum information theory.

ZUSAMMENFASSUNG

Quantenmechanische Verschränkung ist ein grundlegendes Prinzip der Quantenmechanik, bedeutend unter anderem in der Quanteninformatik und -kommunikation. In der Attosekundenphysik wird den möglichen Auswirkungen von Verschränkung in der Licht-Materie-Wechselwirkung immer mehr Aufmerksamkeit geschenkt. In diesem Forschungsbereich wird üblicherweise Strahlung im extrem ultravioletten (XUV) oder Röntgenbereich verwendet, um zeitabhängige Dynamiken in zeitaufgelösten Spektroskopieexperimenten zu untersuchen. Die hohe Photonenenergie führt zur Ionisierung jeglicher Probe, die sich im Weg der Strahlung befindet, wodurch multikomponentige Quantensysteme mit möglicherweise verschränkten Teilsystemen entstehen, z. B. Ion und Photoelektron. Die Verschränkung zwischen den Teilsystemen kann messbare Auswirkungen auf das Ergebnis eines Experiments haben und sogar die Beobachtung zeitabhängiger Messgrößen verhindern. Dies ist vor allem dann der Fall, wenn das Experiment nur Messungen in einem der Teilsysteme vorsieht, d. h. wenn beispielsweise nur das Ion oder das Photoelektron gemessen wird.
Dies führt zu interessanten Fragen über die Rolle der Verschränkung in Attosekunden-Ionisationsprozessen. Insbesondere welche Rolle spielt die Verschränkung zwischen dem Ion und dem emittierenden Elektron in Bezug auf die Beobachtbarkeit von kohärenzbasierten Dynamiken im Ion? Ist es darüber hinaus möglich, den Grad der Verschränkung zwischen dem Ion und Elektron und den Grad der Kohärenz im Ion zu kontrollieren, indem die Eigenschaften der ionisierenden Pulse geändert werden? Zu deren Beantwortung wird in dieser Arbeit ein experimentelles Protokoll präsentiert, bei dem zwei phasenverschränkte XUV-Pulse zusammen mit einem nahinfraroten (NIR) Puls zur dissoziativen Ionisierung von H_2 verwendet werden. Die hier vorgestellten Experimente untersuchen die Auswirkung der Verschränkung zwischen dem Kation und dem Photoelektron, zunächst auf die Schwingungskohärenz, und anschließend auf die elektronische Kohärenz in H_2^+. Im ersten Experiment erzeugen die XUV-Pulse ein Schwingungswellenpaket im $1s\sigma_g$-Zustand von H_2^+, das anschließend durch den NIR-Puls, der das Ion dissoziiert, untersucht wird. Die spektralen Eigenschaften der XUV-Pulse werden durch die zeitliche Verschiebung zwischen den beiden variiert, wodurch der Grad der Schwingungskohärenz bzw. der Grad der Ionen- und Photoelektronenverschränkung kontrolliert wird. Im zweiten Experiment erzeugen die XUV-Pulse während der dissoziativen Ionisierung von H_2 ein verschränktes Ionen-Photoelektronen-System. Der NIR-Puls kann anschließend das verschränkte System in eine kohärente Überlagerung des ersten *geraden* ($1s\sigma_g$) und *ungeraden* ($2p\sigma_u$) elektronischen Zustandes des H_2^+-Kations projizieren. Die Fähigkeit des NIR-Pulses, das ursprünglich verschränkte System in eine kohärente Überlagerung elektronischer Zustände umzuwandeln, wird durch die Änderung des Zeitabstandes zwischen den XUV-Pulsen kontrolliert. Diese Studien zeigen die entscheidende Rolle der Ionen-Photoelektronen Verschränkung in der Attosekundenphysik und stellen einen ersten Versuch dar, die Physik der ultraschnellen Prozesse mit der Quanteninformationstheorie zu verbinden.

Thesis in a nutshell

In the last three and a half years I conducted experiments in the scope of my PhD thesis in the attosecond lab at the Max-Born-Institute in Berlin. My focus was to rebuild and optimize the attosecond pump-probe setup, and perform experiments to study the role of entanglement in attosecond science. These experiments and their interpretation led to several publications [1–3].

The setup consists of a Ti:Sapphire laser system, a hollow-core fiber pulse compression [4] (HCF) part, a pump and probe arm, where the pump arm is used for high harmonic generation [5] (HHG), a velocity map imaging spectrometer [6] (VMI) and an extreme-ultraviolet (XUV) spectrometer [7]. One of the special features of this setup is a self-built passively and actively stabilized Mach-Zehnder interferometer (MZI) in the pump arm for the generation of two phase-locked XUV pulses.

In the first steps of my PhD work, I guided the Master thesis [8] of Laura Maikowski, where we built, optimized and characterized the MZI. The initial development of the MZI had already been done by Laura Maikowski and Tobias Witting. We implemented the MZI in the setup, and performed autocorrelation experiments to characterize the spectra of the two interfering XUV pulses. Afterwards, I performed a Fourier transform spectroscopy experiment to determine the absolute accuracy and long term stability of the MZI by retrieving the well known Rydberg energies of helium. I prepared the experiments, and conducted and analyzed the data under the supervision of Tobias Witting. This led to a publication in Optics Express [1]. I wrote the manuscript together with Tobias Witting, and Marc J. J. Vrakking internally reviewed the manuscript.

In the next experiment during the first year, the setup was used to investigate the role of entanglement in attosecond pump-probe experiments, where hydrogen molecules were ionized by the two phase-locked XUV pulses, and the vibrational wave packet dynamics in the H_2^+ were observed as a function of the delays between both XUV pulses as well as an near-infrared (NIR) probe pulse. I preparation and conducted the experiments, as well as analyzed the data under the supervision of Tobias Witting. The experimental results in conjunction with the theoretical work done by Marc J. J. Vrakking [9] led to a publication in Physical Review Letters [2], as well as in the Proceedings of the ATTO 8 conference [3]. In the

former I generated the main figures and internally reviewed the manuscript, and in the latter I wrote the manuscript about the experimental results. Further, in the second half of my PhD work, I presented these results at several conferences as an invited (ATTO 9, DAMOP) as well as a contributed speaker (DPG, ATTO 8).

In the second year, I prepared a new experiment, which investigated ultrafast electronic dynamics in H_2^+ under the scope of ion+photoelectron entanglement created during the ionization of the molecule by two phase-locked XUV and an NIR pulse. This experiment was extremely challenging and required a lot of optimizations of the setup. For example, a carrier-envelope phase (CEP) stability, attosecond phase-locking between all three pulses and isolated attosecond pulses (IAPs) were required. Firstly, I helped our laser technician Ahmet Akin Uenal to reinstall the CEP stabilization in the oscillator [10]. I built a spectrometer for the f-to-2f interferometer [11, 12] to ensure CEP stability after the hollow-core fiber. I adjusted the dispersion in the setup to create close to single-cycle NIR pulses, and consequently to generate two phase-locked isolated attosecond pulses. In addition, I rebuilt the NIR probe arm to ensure a higher intensity in the pump arm for optimal HHG, as well as to correct the probe pulse compression. After rebuilding the setup as described, I performed the experiments, and analyzed the data. A manuscript about the experimental results in collaboration with the theoretical work (TDSE calculations) performed by A. Rubio, A. Palacios, R. Bello, and F. Martin is in preparation. I presented the experimental results at several conferences as an invited speaker (ATTO 9, DAMOP), as well as contributed speaker (DPG).

All the laboratory work and analysis during my PhD was supervised by Tobias Witting, who also implemented the initial setup and the used lab and analysis software. The project supervision and the theoretical work for the interpretation of the conducted experiments were provided by Marc J. J. Vrakking.

During the whole time of my PhD, my laboratory work consisted among other things of the following:
optimizing the laser output pulses and the HCF pulse compression; performing SPIDER measurements [13]; aligning the laser beam; handling the CEP stabilization and the HHG; finding the temporal and spacial overlap of all pulses; handling the VMI and XUV spectrometer. In addition, throughout the years I replaced broken MCPs and HCFs, and repaired the VMI and the XUV spectrometer.
I performed the data analysis using Python scrips. The main analysis methods were Abel inversions [14], Fourier analysis, data fitting and filtering. All the experimental data shown in this thesis was taken by me.

Besides the experiments described in this thesis, I participated in several collaborations. My role was to prepare the setup to meet the requirements of newly proposed experiments by the collaborators. Additionally I carried out the experiments, acquired the data, and analyzed the data together with the collaboration partners.
The first collaboration is with Peter Jürgens (MBI) et al., who proposed to generate high harmonics in different solids with two phase-locked collinear NIR pulses

to investigate the samples dipole phase. The second collaboration is with Omer Kneller, Nirit Dudovich, et al. (Weizmann Institute), where we performed transient absorption measurements with two phase-locked IAPs and an NIR pulse. In the third collaboration we carried out RABBITT measurements in NH_3 together with Ignacio M. Casasús, Luis Bañares (Complutense University of Madrid) et al.
In all the collaboration experiments publications are in preparation.

List of publications

Associated with this thesis

- L.-M. Koll, L. Maikowski, L. Drescher, M. J. J. Vrakking, and T. Witting, *Phase-locking of time-delayed attosecond XUV pulse pairs*, Optics Express, vol. 30, no. 5, pp. 7082–7095 (2022) [1]. DOI: `https://doi.org/10.1364/OE.452018`

  Author contributions: The Mach-Zehnder interferometer (MZI) was developed by L. Maikowski and T. Witting. The experiments were conceived by L.-M. Koll, T. Witting and M. J. J. Vrakking. The MZI was characterized by L.-M. Koll and L. Maikowski. The further experiments were performed and the data was analyzed by L.-M. Koll under the supervision of T. Witting. The manuscript was written by L.-M. Koll and T. Witting with the help and discussion of the other co-authors.

- L.-M. Koll, L. Maikowski, L. Drescher, T. Witting, and M. J. J. Vrakking, *Experimental control of quantum-mechanical entanglement in an attosecond pump-probe experiment*, Physical Review Letters, vol. 128, no. 4, p. 043201 (2022) [2]. DOI: `https://doi.org/10.1103/PhysRevLett.128.043201`

  Author contributions: The experiments were performed and the data was analyzed by L.-M. Koll under the supervision of T. Witting. The conceptual idea and the theoretical work were developed by M. J. J. Vrakking. The main figures of the manuscript were produced by L.-M. Koll, and the manuscript was written by M. J. J. Vrakking with the help and discussion of the other co-authors.

- L.-M. Koll, T. Witting, and M. J. J. Vrakking, *Control of photoelectron-ion entanglement in attosecond laser-induced photoionization of H_2*, Proceedings of the 8th International Conference on Attosecond Science and Technology (ATTO 8). Springer Proceedings in Physics, vol 300. Springer, pp. 155-165 (2024) [3]. DOI: `https://doi.org/10.1007/978-3-031-47938-0_15`

  Author contributions: The experiments were performed and the data was analyzed by L.-M. Koll under the supervision of T. Witting. The conceptual idea, the theoretical work and calculations were developed by M. J. J.

Vrakking. The manuscript was written by L.-M. Koll and M. J. J. Vrakking, where the part about the experimental results was mainly written by L.-M. Koll, and the part about the theoretical calculations was mainly written by M. J. J. Vrakking.

- L.-M. Koll†, A. Rubio†, T. Witting, R. Bello, A. Palacios, F. Martin, and M. J. J. Vrakking, *Quantum entanglement and electronic coherence in attosecond molecular photoionization*, in preparation

  Author contributions: The experiments were performed and the data was analyzed by L.-M. Koll under the supervision of T. Witting. The conceptual idea and the theoretical work were developed by M. J. J. Vrakking. The accompanying TDSE calculations were performed by A. Rubio under the supervision of A. Palacios and F. Martin.

Other

- O. Kneller, L.-M. Koll, T. Witting, N. Yaffe, C. Mor, M. J. J. Vrakking, and N. Dudovich, *Two attosecond pulse interferometrically resolved spectroscopy*, in preparation

- L.-M. Koll†, S. V. B. Jensen†, P. van Essen, E. Olsson, T. Witting, A. Husakou, M. J. J. Vrakking, L. B. Madsen, P. M. Kraus and P. Jürgens, *Extreme ultraviolet spectral interferometry of strong-field-induced dipole phase dynamics in solids*, in preparation

- I. M. Casasús, L.-M. Koll, C. M. González-Collado, K. K. Shaw, D. Sorribes, L. Drescher, T. Witting, O. Kornilov, M. J. J. Vrakking, A. Palacios, F. Martín, and L. Bañares, *RABBITT experiments in a vibrational active ammonia molecule*, in preparation

† co-first authorship

Conference contributions

Invited talks

- 54th Annual Meeting of the APS Division of Atomic, Molecular and Optical Physics (DAMOP), Volume 68, Number 7, June 5-9, 2023 in Spokane, WA USA
  Control of ion+photoelectron entanglement in attosecond experiments, L.-M. Koll, L. Maikowski, L. Drescher, T. Witting, M. J. J. Vrakking

- 9th International Conference on Attosecond Science and Technology (ATTO 9), July 9 – 14, 2023 Jeju, South Korea
  Control of ion+photoelectron entanglement in attosecond experiments, L.-M. Koll, L. Maikowski, L. Drescher, T. Witting, M. J. J. Vrakking

Contributed talks

- DPG Spring Meeting "Erlangen 2022", 14.03. - 18.03.2022
  Experimental control of quantum-mechanical entanglement in an attosecond pump-probe experiment, L.-M. Koll, L. Maikowski, L. Drescher, T. Witting, and M. J. J. Vrakking

- 8th International Conference on Attosecond Science and Technology in Physics (ATTO VIII), July 11 -15 2022, University of Central Florida (UCF) in Orlando, USA
  Experimental control of quantum-mechanical entanglement in an attosecond pump-probe experiment, L.- M. Koll, L. Maikowski, L. Drescher, T. Witting, and M. J. J. Vrakking

- DPG Spring Meeting of the Atomic, Molecular, Quantum Optics and Photonics Section (SAMOP) 2023, Hannover, 05.03. - 10.03.2023
  1.) *Control of ion+photoelectron entanglement in an attosecond pump-probe experiment*, L.-M. Koll, T. Witting, M. J. J. Vrakking

  2.) *RABBITT experiments in a vibrationally active ammonia molecule*, L.-M. Koll, I. Martínez Casasús, D. Sorribes Ortiz, T. Witting, L. Drescher, O. Kornilov, M. J. J. Vrakking, F. Martin, and L. Bañares

Structure of thesis

This thesis begins with a detailed introduction, cf. chapt. 1, starting with a brief overview of the history of quantum mechanics, a description of the most important concepts as for example *quantum superposition* and *entanglement*, followed by the invention of the laser, the beginning of ultrafast laser spectroscopy, as well as attosecond science, and ends with the new research field of entanglement in attosecond science. In the last part, the scope of this thesis and the open questions, which are addressed in this work are presented.

Subsequently, in the first part of this thesis the theoretical background (cf. chapt. 2) needed to understand the here presented experiments are explained, summarizing the history, the most important theories, and tools of entanglement (cf. sect. 2.1). After explaining the basic concepts of high harmonic generation and pump-probe spectroscopy in sect. 2.2.2, and 2.2.3, respectively, the role of entanglement in attosecond pump-probe experiments is emphasized.

An overview of the experimental setup is given in chapt. 3, and a detailed description on isolated attosecond pulse generation in chapt. 4.

Chapter 5 is dedicated to different Fourier transform spectroscopy experiments to demonstrate the important features of the ultra-stable Mach-Zehnder interferometer (MZI), which was specially developed to create two phase-locked XUV pulses. In the first section 5.1.2, the spectrum of the two phase-locked XUV pulses is analyzed in detail, as well as the implications due to high harmonic

generation by two collinear phase-locked NIR pulses. In the final section 5.2 the stability, and the accuracy of the MZI is validated by retrieving the well known Rydberg states of helium [1].

The main work of this thesis is presented in chapter 6 and 7. Here two experiments are performed to investigate the coherence properties between different intermediate states in H_2^+ created during the photoionization of neutral H_2 by two phase-locked XUV pulses and an NIR pulse, and how ion+photoelectron entanglement is affecting the observability of these coherence-based dynamics.
In the first experiment [2, 3], the coherence properties between different vibrational states in H_2^+ is explored, and in the second experiment electronic coherence created during the XUV+NIR dissociative ionization of H_2 is studied under the scope of ion+photoelectron entanglement. The former experimental results are validated by deriving the reduced ionic density matrix, and comparing the results to theory [9].

Contents

chapter 1

Introduction

"God runs electromagnetics on Monday, Wednesday, and Friday by the wave theory, and the devil runs it by quantum theory on Tuesday, Thursday, and Saturday." - Lawrence Bragg

Light is all around us, light is the reason we exist, and live. Light is the fastest entity in the universe, and light allows us to look into the past of the universe. Understanding the properties, the essence of light is a desire older than Galileo.

Historical background of quantum mechanics Until the 1900s light was thought of as a wave, whereas electrons and atoms were understood as particles. Even though Isaac Newton advocated in the 17th century that light consists of *corpuscles* [15], i.e. particles, Christian Huygens's wave theory of light [16] was mainly believed, and appeared to be fully validated in 1801 by Thomas Young's double-slit experiment [17]. In 1845, an experiment done by Michael Faraday first linked light with electromagnetism [18], which inspired James Clerk Maxwell, who claimed in 1862, that light is a form of electromagnetic radiation, and phrased in 1873 the famous *Maxwell equations* [19].

In 1901, Max Planck, who tried to explain black-body radiation, suggested that even though light was a wave, it can only lose or gain energy in finite amounts, in so called energy *quanta* [20]. In 1905, Albert Einstein elaborated the idea of light quanta to describe the photoelectric effect [21]. He derived the formula of the energy of a single quantum of light with the frequency f:

$$E = hf, \tag{1.1}$$

where h is the Planck constant. Max Planck as well as Albert Einstein were once again attributing particle properties to light.

In 1924, Louis de Broglie formulated a groundbreaking hypothesis, namely that matter has wave properties [22]. Elaborating de Broglie's idea, in 1925 Werner Heisenberg, Pascual Jordan, and Max Born developed matrix mechanics [23–25], followed by the introduction of wave mechanics by Erwin Schrödinger, and the derivation of the non-relativistic Schrödinger equation [26].

The new area of quantum mechanics was born, attributing to light, and particles, such as electrons and atoms, both wave-like and particle-like properties (*wave-particle duality*). This phenomenon can be observed in double-slit experiments [17], which shows the wave (interference signal after slit) and particle (measurement of single particles) character of light, electron, atoms, and molecules [27–29].
Another milestone in this era was the phrasing of the *uncertainty principle* in 1927 by Heisenberg [30], stating that for a quantum particle either the position, or the momentum can be known for certain, but never both at the same time.

One of the main quantum-mechanical foundations born during this time is known today as *quantum superposition*, which describes that a quantum-mechanical microscopic system, for example an atom, molecule or condensed matter, can exist in many possible states simultaneously. The total state of the whole system is thus described by a linear combination of all possible states, and only after a measurement is performed the system is found to be in a defined state. Werner Heisenberg explained this in terms of a collapse of the wave function upon measurement [30].

In the following years many famous scientists tried to interpret the mathematical concepts of quantum mechanics, which led to for example the *Copenhagen interpretation* founded on the thoughts of Niels Bohr, Max Born, and Werner Heisenberg, among others [31]. The Copenhagen interpretation is based on the *correspondence rule* [32] (quantum-mechanical systems behave in the limit of large quantum numbers classically), *complementarity* [33] (quantum-mechanical objects have pairs of properties, which can not be observed/measured simultaneously, as for example the position and momentum, and in Bohr's view also the wave and particle character), the *Born rule* [25] (the probability of a measurement outcome is contained in the wave function of the system), and *indeterminacy* [34] (an experimental observable is given by a probability distribution leading to fundamental uncertainty of measurements, as well as the uncertainty principle).

Schrödinger's cat In an attempt to show the paradoxicality of the Copenhagen interpretation in relation to reality, Erwin Schrödinger extended the concept of superposition to a macroscopic system, which is today known as *Schrödinger's cat* [35]. In this thought experiment from 1935 an imaginary cat is trapped inside a closed box. The box is opaque, and an outside observer can only see the cat if the box is open. Inside the box together with the cat a small amount of radioactive material is placed. The decay of one atom triggers the release of a toxic chemical via a Geiger counter, leading to the death of the cat. The amount of the radioactive material inside the box is so small that every hour only one atom decays with a probability of 50 percent. The wave function of the

atom can thus be described by a superposition of both possible states, i.e.

$$|\text{atom}\rangle = a_1\,|\text{decayed}\rangle + a_2\,|\text{not decayed}\rangle\,, \tag{1.2}$$

where a_i is the amplitude of each state i with $a_1 = a_2 = 1/\sqrt{2}$. An observer can now come to the conclusion that after one hour the cat is either alive, if no atom has decayed so far, or is dead if an atom has decayed. However, the observer can only be certain about the state ($|\text{alive}\rangle$ or $|\text{dead}\rangle$) of the cat if they open the box and look inside.

In an attempt to apply the superposition principle to the cat's state as it is done in the case of the atom, before the box is opened the state of the cat could be written as (a more accurate expression follows, see Eq. 1.7)

$$|\text{cat}\rangle = 1/\sqrt{2}\big(\,|\text{alive}\rangle + |\text{dead}\rangle\,\big), \tag{1.3}$$

which results in the probability of $|1/\sqrt{2}|^2 = 50\%$ that the cat is alive or dead. Accordingly, in line with the Copenhagen interpretation the cat is in a superimposed state of being alive and dead at the same time. After the box is opened and an observation about the state of the cat is made, Eq. 1.3 becomes

$$|\text{cat}\rangle = |\text{alive}\rangle\,, \tag{1.4}$$

or

$$|\text{cat}\rangle = |\text{dead}\rangle\,, \tag{1.5}$$

and the cat is either dead or alive with a probability of 100%. Thus the former quantum superposition is turned into reality after performing a measurement/observation. But how can the cat be both dead and alive at the same time? This seems contradictory, since if the cat survives, it basically was alive the whole time.

In reality, the quantum superposition of macroscopic systems rapidly decoheres into statistic mixtures[1], due to the strong interaction with the environment [36–39]. As described in detail in [40], the decoherence time of a coherent superposition state of a particle is given by

$$\tau_D \cong \tau_R \left(\frac{\lambda_{dB}}{\Delta x}\right)^2, \tag{1.6}$$

where λ_{dB} is the thermal de Broglie wavelength, $\tau_R = \gamma^{-1}$ is the relaxation time[2] (i.e. the time a particle needs to return back to its original state) inversely proportional to the relaxation rate γ, x is the position, and $\Delta x \sim x - x'$ is the spatial separation of pieces in the wave packet. The decoherence time for macroscopic systems is quite short, e.g $\tau_D \sim 10^{-23}\,\text{s}$ [40], whereas for microscopic system the decoherence time is substantially longer, e.g. in the case of a rubidium atom $\tau_D \sim 10^{-5}\,\text{s}$ [41] or for an electron spin $\tau_D \sim 10^{-3}\,\text{s}$ [42]. Accordingly, any superposition character of the cat's state would have been destroyed immediately.

[1] A statistic mixture is an ensemble of states described by a probability distribution function

[2] For example for radioactive materials the half-life, i.e. the time for one-half of the isotope to decay is related to the relaxation time by $t_{1/2} = \ln(2) \cdot \tau_R$

Quantum-mechanical entanglement Around the same time, Albert Einstein, Boris Podolsky and Nathan Rosen introduced another thought experiment known today as the EPR paradox [43], which became the foundation of a further quantum-mechanical principle, namely *quantum-mechanical entanglement*. The basic concept of entanglement can be explained with Schrödinger's cat by regarding the whole system, i.e. the cat and the atom. The state of the total system is given by

$$|\text{cat+atom}\rangle = 1/\sqrt{2}\big(\,|\text{alive}\rangle\,|\text{not decayed}\rangle + |\text{dead}\rangle\,|\text{decayed}\rangle\,\big). \tag{1.7}$$

The state of the cat is entangled with the state of the environment, since the cat is only dead if the atom has decayed and vice versa. Thus, by measuring or making an observation of the one system, knowledge about the other system is gained. Entanglement adapted to reality seems quite logical, however entanglement of quantum-mechanical particles can become quite unintuitive.

The original EPR thought experiment [44] postulated the paradox that if two particles, which are entangled in position and momentum, are measured (e.g. the position of particle one and the momentum of particle two), both observables would be known for both particles simultaneously. This would seemingly contradict the uncertainty principle. Accordingly, entanglement violates *local realism*, i.e. the theory that a physical object is completely characterized by individual properties, which determine the outcome of a measurement (*realism*), and that the result is not influenced by another measurement performed in a space separated system (*locality*) [45]. That is why entanglement was first considered as an indicator that quantum mechanics is incomplete [44, 46].

Only thirty years after the phrasing of the EPR paradox, a protocol was proposed, which could show experimentally the violation of *local realism* by the so called *Bell inequality* [47, 48]. In 1972, Stuart Freedman and John Clauser first showed the violation of the *Bell inequality* in an experiment using entangled photons [49]. After a decade Alain Aspect [50–52], and later Anton Zeilinger et al. [53] improved the previous experimental design, which now avoided so called 'locality loopholes' [45]. However, only in 2015 the first completely loophole free Bell experiments [54–56] were performed. These experiments proved the existence of stronger quantum correlations than those allowed by *local realism* [57–59]. The violation of the *Bell inequality* led to a high interest in quantum correlations [45], and their possible technological applications, which are nowadays investigated in quantum information science [60–62], quantum imaging [63, 64], cryptography [65, 66] or teleportation [67–69].

Giving quantum-mechanical mathematical concepts an interpretation not only gave Albert Einstein, Werner Heisenberg, Erwin Schrödinger or Max Born a headache, still today the principle of wave-particle duality or entanglement, among others, seem hard to grasp.

Ultrafast laser spectroscopy Quantum mechanics not only aims at understanding the fundamental properties of light, and matter, but it also describes their interaction. The interaction of light and matter can be encountered in every

day life processes such as photosynthesis [70], visual perception [71] or radiation therapy for cancer cells [72, 73]. The characteristic timescales of the motion of atoms and molecules in such processes are in the femtosecond region [74] (1 fs $= 10^{-15}$ s), and of the motion of electrons in the attosecond region [5] (1 as $= 10^{-18}$ s).

Only after the laser was invented in 1960 by Theodore Maiman [75], it became possible to observe dynamics on these fast timescales. The development of continuous wave (CW) lasers [76,77], and thus laser with an extreme narrow bandwidth, allowed to characterize the properties of atoms and molecules with a high spectral resolution [78–80]. Pulsed lasers [81–86] on the other side, enabled to disentangle atomic and molecular temporal dynamics initiated upon the interaction with the laser field [87–90]. In these experiments, induced effects are typically resolved by a combination of a pump pulse, which initiates a certain process, and a second pulse, which subsequently probes the evolved dynamics [91, 92]. As the pulse duration of laser systems became shorter and shorter, in the 80s the development of femtosecond lasers [93–96] created its own research field, namely the field of *femtochemistry* [74]. Radiation in the extreme ultraviolet (XUV) regime, with a pulse duration of a few hundred attoseconds, became accessible due to the discovery of high harmonic generation [97, 98], which then allowed to study photoelectron dynamics. The field of attosecond physics [5] started in 2002 with Drescher et al. [99] directly measuring Auger decay times in krypton in a first attosecond pump-probe experiment, and until today the research field of attosecond science mainly studies the dynamics of valence or outer-shell electrons in atoms and molecules [5, 100, 101]. However recently Einstein's "*spooky action at a distance*" gained interest, and the awareness about quantum-mechanical entanglement in the field of attosecond physics has been renewed, sensitizing for possible experimental implications as well as applications [102].

Entanglement in attosecond photoionization In general, quantum entanglement plays a crucial role in any experiment involving ionization. Due to the high photon energy of the radiation typically used in attosecond science, any studied sample is ionized, thus creating a multicomponent quantum system, where the subsystems can be entangled. In the case of molecular photoionization, for example the ion and photoelectron can be entangled. Thus the total wave function of the bipartite system is given as a sum of direct products [103]

$$|\Psi_{\text{total}}\rangle \sim \sum_{i,j} |\phi_{\text{ion},i}\rangle \otimes |\chi_{\text{photoelectron},j}\rangle \,, \tag{1.8}$$

with i, j as a full set of quantum numbers, and can not be simplified as a single direct product of individual parts

$$|\Psi_{\text{total}}\rangle \neq |\phi_{\text{ion}}\rangle \otimes |\chi_{\text{photoelectron}}\rangle \,, \tag{1.9}$$

where $|\phi_{\text{ion}}\rangle$ is the ionic, and $|\chi_{\text{photoelectron}}\rangle$ is the photoelectronic wave function. It should be noted that the same type of quantum entanglement arises in any photoionization experiment, not only in ionization by attosecond pulses.

Entanglement between the ion and photoelectron means that a measurement (or just the possibility of a measurement) in one of the subsystems, i.e. measuring the properties of the ion or photoelectron leads automatically to knowledge about the properties of the other part, similarly to the cat and the atom. In attosecond pump-probe experiments it is really common to only measure the dynamics of the ion or the photoelectron, and thus integrating over the properties of the part, which is not measured. These measurements strongly depend on the coherence properties of the subsystem under investigation. In other words, a well-defined phase relationship between the ionic wave functions $\sum_i |\phi_{\text{ion},i}\rangle$ and between the photoelectronic wave functions $\sum_j |\chi_{\text{photoelectron},j}\rangle$, respectively, is required.
An example of coherence-based experiments are charge migrations [104–107], where the electronic motion in the ion is observed after photoionization of the molecule, and the electronic motion strongly depends on the electronic coherence properties of the system. However, entanglement between different subsystems (e.g. ion+photoelectron entanglement) can limit the coherence properties of the investigated system (e.g. when measuring the properties of the ion), and thus can even prevent the observation of specific time-dependent effects (e.g. charge migration in the ion).

Thus, first questions arise, namely what is the role of entanglement in attosecond experiments, specifically in atomic and molecular photoionization processes, and how can one characterize and control entanglement in these processes?

The first papers [108, 109], which alerted to a possible role of entanglement in attosecond science, pointed out that in the experimental work of Goulielmakis et al. [110], which investigated coherent hole dynamics in Kr^+, in fact entanglement between the ion and photoelectron limits the electronic coherence in the cation. This argument was extended to polyatomic molecules by Ruberti [111], who introduced the limitation imposed on the observability of charge migration dynamics due to ion+photoelectron entanglement.

Based on these early works, in the last years multiple research groups started to investigate the importance of entanglement between different subsystems in attosecond science. For example Nishi et al. [112] explored the role of entanglement between the photoelectron kinetic energy and the vibrational dynamics in H_2^+, and Shobeiry et al. [113] demonstrated the control of electronic entangled states in a single hydrogen molecule. He et al. [114] recently showed that in the dissociative ionization of hydrogen molecules ion+photoelectron entanglement can lead to double-slit interference in the momentum distribution of the ion. Laurell et al. [115,116] implemented a quantum state tomography scheme to characterize ion+photoelectron entanglement in the vicinity of a Fano resonance in helium and argon. Morrigan et al. [117] designed a molecular frame quantum tomography protocol for polyatomic systems, which was experimentally tested in the case of electronic dynamics in ammonia, and can be useful as a measure of electronic and nuclear entanglement. Busto et al. [118] studied entanglement between the photoelectron's radial and angular degree of freedom, emerging during the photoionization of an atom. In molecular photoexcitation entanglement between nuclear and electronic motion can occur, which was recently investigated by

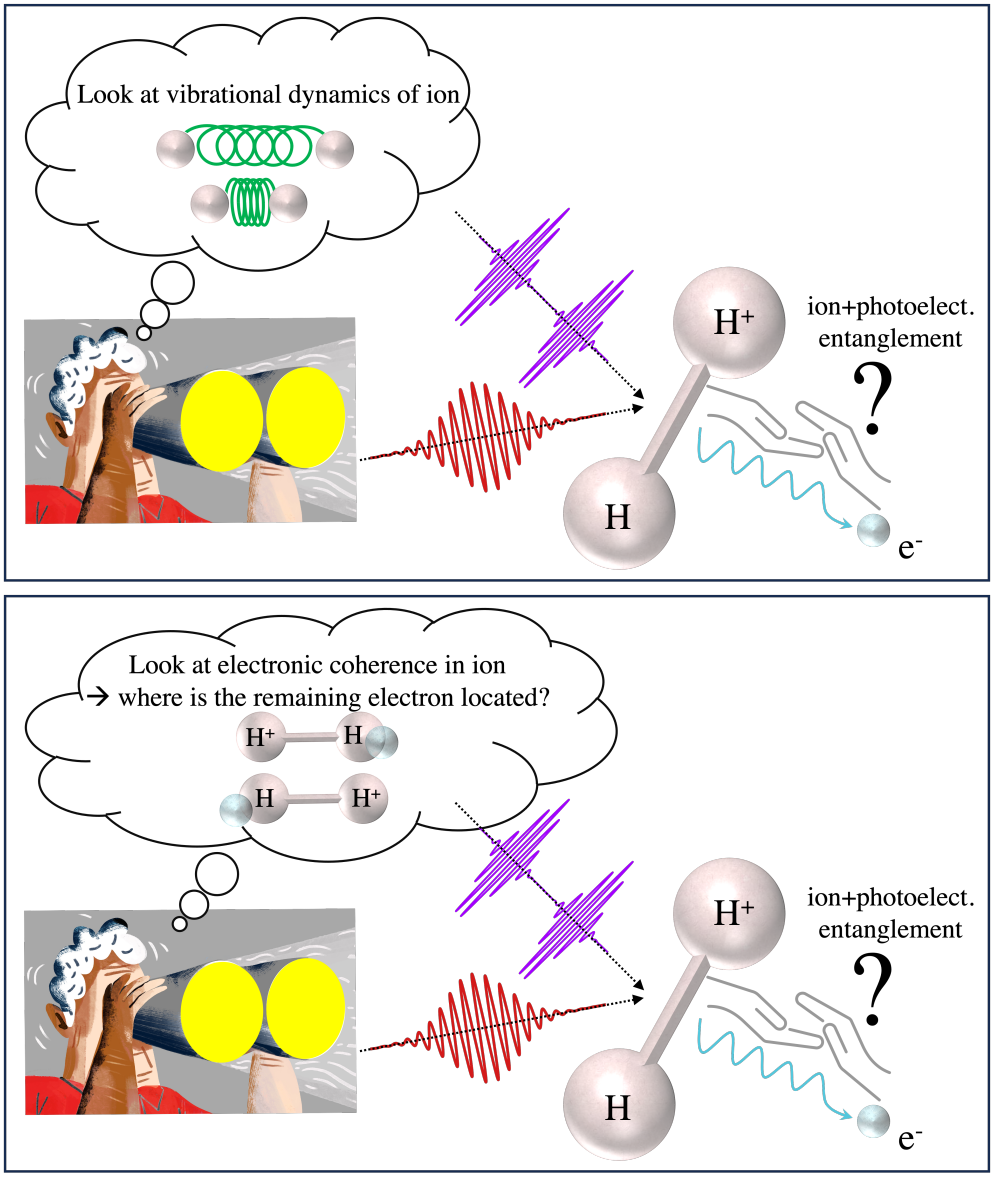

Figure 1.1: Schematic illustration of the two main experiments presented in this thesis. In the first experiment (upper figure, cf. chapter 6) neutral hydrogen molecules are ionized by two phase-locked XUV pulses, creating a photoelectron and a vibrational wave packet in the cation. The dynamics of the vibrational wave packet, and thus the coherence properties between the vibrational states are subsequently probed by a NIR probe pulse. In the second experiment (lower figure, chapter 7) neutral hydrogen molecules are dissociatively ionized by two phase-locked XUV pulses and a NIR probe pulse, creating a photoelectron and a coherent superposition of electronic states in the cation. Electronic coherence leads to the observation of electron localization, i.e. the remaining electron in the cation is localized at one of the protons. In both experiments, it is investigated how entanglement between the ion and photoelectron influences the experimental outcome, in particular the observability of the coherence-based dynamics in the ion. It should be noted that in the actual experiments all three pulses are collinear.

Blavier et al. [119, 120]. Furthermore, Maxwell et al. [121] investigated entangled orbital angular momenta of photoelectrons in non-sequential double ionization processes to improve attosecond imaging, and Eckart et al. [122] generated, and studied two Bell's state like neutral oxygen atoms with their valence electrons entangled in magnetic quantum number. And recently Ruberti et al. [123] designed a Bell test to directly probe entanglement in attosecond photoionization.

Scope of this thesis The main goal of this thesis is to highlight the important role of entanglement in coherence dependent experiments, and to investigate its limiting properties in detail. In particular, the following questions are addressed:

- What is the role of entanglement between the ion and photoelectron regarding the observability of coherence-based dynamics in the ion?
- Is it possible to control the degree of ion+photoelectron entanglement and the degree of coherence in the ion, respectively, by alternating the pulse properties of the ionizing pulses?
- How can the degree of entanglement, which arises in the ionization process, be quantified?

In this thesis two pump-probe experiments are presented, which investigate the role of ion+photoelectron entanglement towards the observability of vibrational coherence [2] and electronic coherence, respectively, during the photoionization of H_2 by two phase-locked XUV pulses serving as a pump, and an NIR probe pulse (cf. Fig. 1.1). It is further analyzed how the degree of ion+photoelectron entanglement and the degree of vibrational, and electronic coherence, respectively, depend on the delay between the two XUV pulses, and the delay between those pulses and the NIR pulse. The former experiment is based on the theoretical work of M. J. J. Vrakking [9].

In conclusion, all the here presented, and aforementioned scientific studies are working towards a link between attosecond science and quantum information theory, which imparts a new approach of describing and understanding ultrafast processes, and in addition can even provide new tools for quantum technologies [124–126].

In the next chapter, the theoretical background of quantum-mechanical entanglement, photoionization dynamics and attosecond spectroscopy, which is needed to better understand the following experimental results, is described in detail.

chapter 2

Theoretical background

2.1 Quantum-mechanical entanglement

For a better understanding of the later on presented experimental results, a brief overview of the history and the basic concepts of quantum-mechanical entanglement are presented in this chapter. In addition, the basic notions and different methods of how entanglement within a system is quantified, are introduced. More detailed descriptions of the measures, concepts and implications of entanglement in different systems can be found in [103, 127–130].

In general entanglement in atomic and molecular physics can deal with many-body systems with rather large Hilbert spaces, facing the difficulty to actually identify the subsystems, which are entangled [103]. The quantum-mechanical systems handled in this thesis are few-body systems consisting of an ion and a photoelectron created upon photoionization of a molecule. To simplify the rather complex structure of the two subsystems, in the following chapters it is assumed that the ion and photoelectron are fully described by one degree of freedom, which can be for example the vibrational or electronic states in the ion or the kinetic energy in the case of the photoelectron.

2.1.1 Historical background - EPR paradox

The beginning of quantum-mechanical entanglement is rooted in the thought experiment [43] of Albert Einstein, Boris Podolsky and Nathan Rosen in 1935 as described in detail in the introduction of this thesis. A more detailed overview of the historical background of entanglement can be found in [131].

In this first thought experiment two moving entangled particles are measured using non-commuting operators[1]. Consequently, for each pair of observables with non-commuting operators, the observables are *incompatible*, i.e. there exists an uncertainty relation between them. So for example if one of the observable is the position of a particle $\hat{A} = \hat{x}$, and the other observable is the momentum of the particle $\hat{B} = (\hbar/i)d/d\hat{x}$, the two particles have to satisfy $[\hat{x}, \hat{p}] = i\hbar$, which is nothing else than the Heisenberg uncertainty principle [30][2] (cf. appendix A.1 for the derivation of the general uncertainty principle with non-commuting operators). Either the momentum or the position of the particle can be known, but never both simultaneously.

In 1951 David Bohm proposed another experiment with two entangled spin-1/2 particles [46] (the total spin is zero). The spin operators $\hat{S}_i$ and $\hat{S}_j$ of the same particle are non-commuting, and thus satisfy $\left[\hat{S}_i, \hat{S}_j\right] = i\hbar\epsilon^{ijk}\hat{S}_k$, where ϵ^{ijk} is the Levi-Civita epsilon, which states total antisymmetry in the indices.

The spin wave function of the two spin-1/2 particles is maximally entangled in the so called *Bell's state* [133] given by

$$|\psi_{\pm}\rangle = 1/\sqrt{2}\,(|\uparrow\rangle \otimes |\downarrow\rangle \pm |\downarrow\rangle \otimes |\uparrow\rangle)\,. \tag{2.1}$$

The two entangled spin-1/2 particles are send into opposite directions from the source towards two independent detectors (Alice + Bob), and the spin component of each particle is measured in a specific direction $\vec{a}$ (Alice), and $\vec{b}$ (Bob). Thus, Alice measures $\hat{\vec{S}} \cdot \vec{a}$ and Bob is measuring $\hat{\vec{S}} \cdot \vec{b}$, respectively.

In the first example Alice and Bob are measuring the particles spin in the z-direction, i.e. $\vec{a} = \vec{b} = \vec{z}$. Alice now finds the spin to be either up or down. Bob however, finds his particle to have spin up, whenever Alice measured spin down, or vice versa, since the orientation of the pair's spin is perfectly anti-correlated. This means, that Alice's measurement leads to a result for both particles, independent if Bob is actually measuring his particle or not. If Bob now chooses to measure the spin in the x-direction instead, i.e. $\vec{a} \neq \vec{b}$ with $\vec{a} = \vec{z}$ and $\vec{b} = \vec{x}$ the combined measurement of Alice and Bob would lead to distinct spin values in perpendicular directions, which paradoxically would be more precise than allowed by the uncertainty principle [30].

This contradiction led to the believe that either the particles do not share the same reality, or the theory that quantum mechanics is incomplete. A possible solution to the latter could be given by so called *local hidden variables* [134,135], which are predefined properties of a particle predetermining the result of a measurement.

This theory gave the cause for John Bell to formulate the first *Bell inequality*, which showed mathematically that no *hidden variable* model would derive to the same prediction as quantum mechanics [47]. This first inequality was only

[1] A commutator of two operators $\hat{A}$ and $\hat{B}$ is a measure of how non-commutative they are, i.e. $[\hat{A}, \hat{B}] = \hat{A}\hat{B} - \hat{B}\hat{A}$ [132]

[2] *Compatible* observables are for example the momentum and the kinetic energy of the particle.

applicable to a thought experiment, and thus was reformulated by Clauser, Horne, Shimony and Holt [48], which then allowed to demonstrate the violation of the inequality by an experiment with entangled photons [49].

2.1.2 Separable and entangled states

The Hilbert space of a two-body system is given by $\mathscr{H} = \mathscr{H}_1 \otimes \mathscr{H}_2$, where $\mathscr{H}_1$ and $\mathscr{H}_2$ are the Hilbert spaces of two well-separated subsystems with dimension d_1 and d_2, respectively. The two subsystems could represent for example an ion and a photoelectron created upon photoionzation of an atom or molecule. Now it is assumed that the two-body system is a pure state, and thus any interaction with the environment is neglected.

It then follows for the wave function of the bipartite quantum state

$$|\Psi\rangle \in \mathscr{H}_1 \otimes \mathscr{H}_2, \tag{2.2}$$

with

$$|\Psi\rangle = \sum_{j,k=1}^{d_1,d_2} c_{j,k} \, |\phi_j\rangle \otimes |\chi_k\rangle \,, \tag{2.3}$$

where $c_{j,k}$ is the coefficient matrix with $\sum_{j,k=1}^{d_1,d_2} |c_{j,k}|^2 = 1$, and $|\phi_j\rangle$ and $|\chi_k\rangle$ are orthonormal single-particle states, according to $\langle\phi_j|\phi_k\rangle = \delta_{jk} = \langle\chi_j|\chi_k\rangle$.

Separable states If there exist single-particle states $|\psi_i\rangle \in \mathscr{H}_i$, leading to

$$|\Psi\rangle = |\psi_1\rangle \otimes |\psi_2\rangle \,, \tag{2.4}$$

the total wave function of the bipartite system is described by a product state, and thus is *separable*. Consequently, the coefficient matrix $c_{j,k}$ in Eq. 2.3 can be written as a product, i.e. $c_{j,k} = c_j \cdot c_k$, and each subsystem contains all information about the possible states of the single-particle. Thus, a measurement of one of the subsystems has no measurable effect on the other subsystem. [103]

Entangled states If the bipartite system is not separable, i.e.

$$|\Psi\rangle \neq |\psi_1\rangle \otimes |\psi_2\rangle \,, \tag{2.5}$$

there is no further simplification of the total wave function (Eq. 2.3) possible since $c_{j,k} \neq c_j \cdot c_k$. This means that the total state $|\Psi\rangle$ is *entangled*. Accordingly, the result of a measurement performed in one of the subsystems predicts the state of the other subsystem. [103]

For example for maximally entangled bipartite qubit states (i.e. *Bell's states* [133], where j and k can have the values 0 or 1, and $d = 2$), the wave function is given by

$$\begin{aligned} |\Psi^{\pm}\rangle_{\text{Bell}} &= \frac{1}{\sqrt{2}} \left(|0\rangle_1 \otimes |0\rangle_2 \pm |1\rangle_1 \otimes |1\rangle_2 \right) \\ |\Phi^{\pm}\rangle_{\text{Bell}} &= \frac{1}{\sqrt{2}} \left(|0\rangle_1 \otimes |1\rangle_2 \pm |1\rangle_1 \otimes |0\rangle_2 \right) . \end{aligned} \tag{2.6}$$

The state of the single qubit is in general undetermined. However, if one performs a measurement for example in subsystem 1, the result determines the outcome of a possible measurement in subsystem 2, which guarantees to yield the same value for a $|\Psi^{\pm}\rangle_{\text{Bell}}$ state and the opposite value for a $|\Phi^{\pm}\rangle_{\text{Bell}}$ state.

Mixed states So far the two-body system was assumed to be a pure state. However in reality it is quite likely to encounter a mixed state, since quantum systems are difficult to completely isolate from their environment.

A mixed quantum system is a statistical ensemble, which is given by the probability p_i to find the system in the pure state $|\Psi_i\rangle$. This is described by the system's density matrix [103, 130], according to

$$\rho_{\text{mixed}} = \sum_{i}^{d} p_i \left|\Psi_i\right\rangle \left\langle\Psi_i\right| , \tag{2.7}$$

with $\sum_i^d p_i = 1$, which is a fully mixed state that has no off-diagonal elements, i.e. no coherence at all between different states $|\Psi_i\rangle$. It is important to note that the mixedness of the density matrix does not necessarily mean that the system is entangled. In fact separable mixed states exhibit no entanglement, but rather strong classical correlations. Thus differentiating between entangled and separable mixed states is a non-trivial challenge, and much more complex than in the case of pure systems. [103]

In the following the two-body system is considered to be a pure total state.

2.1.3 Schmidt decomposition and reduced density matrix

Retrieving the full representation of the total wave function of a given system and thereby determining if the states of the system are entangled, poses an important and complex problem.

Schmidt decomposition One possibility is to perform a Schmidt decomposition [119, 130]. In this case the total wave function, i.e. Eq. 2.3, which is a tensor product of two basis, is projected onto a single basis. Thus, the total wave function can be written as a single sum

$$|\Psi\rangle = \sum_{n=1}^{N} c_n \left|\phi_n\right\rangle \otimes \left|\chi_n\right\rangle , \tag{2.8}$$

where c_n are the *Schmidt weights* (also known as *Schmidt coefficients*), with $\sum_{n=1}^{N} |c_n|^2 = 1$, and $|\phi_n\rangle$ and $|\chi_n\rangle$ are the *Schmidt vectors*, which depend on the given Ψ. The number of products N corresponds to the *Schmidt rank*.

In this wave function representation it can be easily recognized if the wave function is separable or entangled. Namely, if the Schmidt rank is 1, i.e.

$$|\Psi\rangle = \left|\phi_1\right\rangle \otimes \left|\chi_1\right\rangle , \tag{2.9}$$

the wave function is separable.

If the Schmidt rank is 2 or higher, i.e.

$$|\Psi\rangle = c_1 |\phi_1\rangle \otimes |\chi_1\rangle + c_2 |\phi_2\rangle \otimes |\chi_2\rangle + ..., \tag{2.10}$$

the states $|\phi_n\rangle$ and $|\chi_n\rangle$ are mixed, and the total wave function is entangled. The Schmidt weights c_n are a measure of the degree of entanglement between the states (cf. sect. 2.1.4).

The Schmidt vectors can be found via a singular-value decomposition [136] (SVD), which allows to factorize a $m \times n$ matrix according to

$$\mathbf{M} = \mathbf{u}\sigma\mathbf{v}^\dagger, \tag{2.11}$$

where σ is a $m \times n$ rectangular diagonal matrix, and σ_{ii} are non-negative real numbers, which correspond to the singular values of $\mathbf{M}$. The factor $\mathbf{u}$ is a $m \times m$ matrix, and $\mathbf{v}$ is a $n \times n$ complex unitary matrix with its conjugated transposed $\mathbf{v}^\dagger$. This representation is useful since the matrices $\mathbf{u}$ and $\mathbf{v}$ correspond directly to the Schmidt-vector bases, i.e.

$$\begin{aligned} \mathbf{u} &= (\phi_1\, \phi_2\, \phi_3 ...) \\ \mathbf{v} &= (\chi_1\, \chi_2\, \chi_3 ...), \end{aligned} \tag{2.12}$$

where ϕ_n and χ_n are column vectors. The singular-value matrix encodes the Schmidt weights, according to $\sigma_{ii} = c_n$ (with $i = n$).

Thus, it follows

$$\mathbf{u}\sigma\mathbf{v}^\dagger = (\phi_1\, \phi_2\, \phi_3 ...) \begin{pmatrix} c_1 & 0 & 0 & ... \\ 0 & c_2 & 0 & ... \\ 0 & 0 & c_3 & ... \\ ... & ... & ... & ... \end{pmatrix} \begin{pmatrix} \chi_1^\dagger \\ \chi_2^\dagger \\ \chi_3^\dagger \\ ... \end{pmatrix} = \sum_{n=1}^{N} c_n \phi_n \chi_n^\dagger. \tag{2.13}$$

Reduced density matrix More generally, the quantum state of the given system can be described via the density matrix [103, 130], i.e.

$$\rho = |\Psi\rangle \langle\Psi| = \sum_{n=1}^{N} \sum_{n'=1}^{N} c_n c_{n'}^* |\phi_n\rangle \langle\phi_{n'}| \otimes |\chi_n\rangle \langle\chi_{n'}| . \tag{2.14}$$

The reduced density matrix of the system is then given by taking the partial trace over the degree of freedom of $|\phi\rangle$, i.e.

$$\rho_\chi = \mathrm{Tr}_\phi(\rho) = \sum_{n=1}^{N} |c_n|^2 |\chi_n\rangle \langle\chi_n| , \tag{2.15}$$

since $\mathrm{Tr}(|\phi_n\rangle \langle\phi_{n'}|) = \delta_{nn'}$. Accordingly, $|\chi_n\rangle$ are the eigenvectors, and $|c_n|^2$ are the eigenvalues of the reduced density matrix ρ_χ, with $\langle\chi_n|\chi_{n'}\rangle = \delta_{nn'}$.

The same conclusion is retrieved by taking the partial trace over the other subsystems degree of freedom, i.e.

$$\rho_\phi = \mathrm{Tr}_\chi(\rho) = \sum_{n=1}^{N} |c_n|^2 \, |\phi_n\rangle \, \langle\phi_n| \,, \tag{2.16}$$

where now $|\phi_n\rangle$ are the eigenvectors, and $|c_n|^2$ are the eigenvalues of the reduced density matrix ρ_ϕ.

2.1.4 Quantification of entanglement

After deriving a convenient representation of the total wave function, the next important question arises, namely how to quantify entanglement?

In general there exist different methods. Firstly, the amount of entanglement within a system, and especially its dimensionality, is encoded in the entanglement spectrum, which is given by the Schmidt weights. Furthermore, the Schmidt weights can be used to calculate the entanglement entropy [103,137]. In addition, the purity [62] of the system can be calculated via the reduced density matrix, which is a measure of how mixed the states are. However, the latter does not allow to distinguish the dimensionality of entanglement.

2.1.4.1 Entanglement spectrum

As aforementioned the Schmidt weights c_n allow to quantify the degree of entanglement between the states. The entanglement spectrum of the state $|n\rangle$ is defined by the population given by the Schmidt weights, i.e. $|c_n|^2$.

In the Schmidt decomposition representation, the total wave function of a pure two-body system is given in Eq. 2.8, i.e.

$$|\Psi\rangle = \sum_{n=1}^{N} c_n \, |\phi_n\rangle \otimes |\chi_n\rangle \tag{2.17}$$

with the Schmidt rank N.

One can now consider exemplary two different cases with different entanglement spectra. Firstly, if $|c_1|^2 = |c_2|^2 = 1/2$ and $\sum_{n>2}^{N} |c_n|^2 = 0$, there exist two Schmidt weights with the same value. Accordingly, the total state is maximally entangled in two dimensions. Secondly, if there exists one Schmidt weight, which dominates all others, i.e. $|c_1|^2 \gg \sum_{n>1}^{N} |c_n|^2$, the total state is in good approximation a product state, and the degree of entanglement is close to zero. The ratios between the Schmidt weights is thus a measure of the amount of entanglement over the dimensionality, and accordingly quantifies the degree of entanglement within the system.

2.1.4.2 Entanglement entropy

The entanglement entropy is given as the von Neumann entropy [138, 139] of the reduced density matrix, as

$$S_{\mathrm{vN}}(\rho_\phi) = -\mathrm{Tr}(\rho_\phi \log_2 \rho_\phi) = -\mathrm{Tr}(\rho_\chi \log_2 \rho_\chi) = S_{\mathrm{vN}}(\rho_\chi), \tag{2.18}$$

which corresponds to the Shannon entropy [140] of the entanglement spectrum [141], i.e.

$$S_{\mathrm{S}} = -\sum_{n=1}^{N} |c_n|^2 \log_2 |c_n|^2. \tag{2.19}$$

If the entropy is zero, the system is non-entangled, and the state is separable. Whereas if the entropy has a maximum value of $\log_2 N$, with N as the Hilbert space dimension, the degree of entanglement within the system is maximal.

2.1.4.3 Purity

Before determining the purity, let's derive the reduced density matrix for a bipartite system, which can emerge in photoionization experiments, i.e. an ion+photoelectron system [9, 112, 119, 142–144].

Commonly it is assumed that the wave function of the ion $|\phi_v\rangle$ is fully described by a set of vibrational quantum numbers v, and the wave function of the photoelectron $|\chi_k\rangle$ is described by the kinetic quantum number k.

Thus, the Hilbert space is $N_v \times N_k$ dimensional, and the total wave function is given by the pure total state

$$|\Psi\rangle = \sum_{v=0}^{N_v} \sum_{k=1}^{N_k} c_{v,k} \, |\phi_v\rangle \otimes |\chi_k\rangle \, . \tag{2.20}$$

The density matrix of the ion+photoelectron system is

$$\rho = |\Psi\rangle \langle\Psi| = \sum_{vv',kk'}^{N_v,N_k} c_{v,k} c^*_{v',k'} \, |\phi_v\rangle \langle\phi_{v'}| \otimes |\chi_k\rangle \langle\chi_{k'}| \, , \tag{2.21}$$

and the reduced ionic density matrix is retrieved by taking the trace over the photoelectron coordinates, i.e.

$$\rho_{\mathrm{ion}} = \mathrm{Tr}_{\mathrm{photoelectron}}(\rho) = \sum_{v,v'=0}^{N_v} \sum_{k=1}^{N_k} c_{v,k} c^*_{v',k} \, |\phi_v\rangle \langle\phi_{v'}| \, . \tag{2.22}$$

The diagonal elements of the reduced ionic density matrix $(\rho_{\mathrm{ion}})_{vv}$ represent the population probability of each vibrational state. The off-diagonal elements $(\rho_{\mathrm{ion}})_{vv'}$ are a measure of the coherence between two vibrational states v and v'. [142]

The purity P [62] is given by taking the trace over the squared reduced ionic density matrix, i.e.

$$P = \mathrm{Tr}\left(\rho_{\mathrm{ion}}^2\right) = \sum_{v,v'=0}^{N_v} \sum_{k,k'=1}^{N_k} c_{v,k} c_{v',k}^* c_{v',k'} c_{v,k'}^*. \tag{2.23}$$

The maximum value of the purity is $P_{\mathrm{max}} = 1$. In this case the vibrational states are maximally coherent, all off-diagonal matrix elements are non-zero, i.e. $(\rho_{\mathrm{ion}})_{vv'} > 0$ for all v and v', and the degree of entanglement is zero. The minimum value of the purity is $P_{\mathrm{min}} = 1/N_v$, which corresponds to the case that all vibrational states are equally populated, i.e. $(\rho_{\mathrm{ion}})_{vv} = 1/N_v$ for all v. There is no coherence between the vibrational states, $(\rho_{\mathrm{ion}})_{vv'} = 0$, for all $v \neq v'$, and the system is maximally entangled. [112]

Consequently, an increase of the degree of entanglement between the ion and photoelectron inevitably leads to a decrease of the degree of coherence between the vibrational states. The same conclusion can be derived by calculating the reduced photoelectronic density matrix [112].

2.1.4.4 Mixed states

Quantifying the amount of entanglement for mixed states is much more complex and complicated, since methods are necessary, which allow to distinguish between classical and non-classical correlations. In this thesis mainly pure states occur, thus only a few examples of entanglement measures applicable to mixed states are listed here, and a detailed overview can be found in [103, 145].
Entanglement in mixed states can be quantified for example by entanglement of formation [146], distillable entanglement [147], concurrence [146], logarithmic negativity [148], and entanglement witnesses [149, 150], among others.

In the following only pure states are treated.

As explained before, entanglement plays a crucial role in any experiment involving ionization. Due to the high photon energy of the radiation used in attosecond science, photoionization is a common process occurring in attosecond experiments. This makes it quite likely for entanglement to emerge between different subsystem, for example between an ion and the departing photoelectron. Thus, investigating the role of entanglement in attosecond experiments is an active research topic. An interesting question, for example, is to what extend ion+photoelectron entanglement influences the observability of coherence-based dynamics in an experiment, since an increase of the degree of ion+photoelectron entanglement leads to a decrease of the degree of coherence in the ion as described in sect. 2.1.4.3. In the following chapter, the fundamental principles of attosecond science, the generation of high harmonics, as well as the basic concept of attosecond pump-probe experiments is described, before emphasizing the role of entanglement in those type of experiments.

2.2 Photoionization dynamics and attosecond spectroscopy

In attosecond science the main goal is to study ultrafast nuclear and electronic dynamics in atoms [151–156], molecules [157–162] or condensed matter [163–166]. To experimentally resolve these ultrafast processes, a high temporal resolution is required, which is achieved using short laser pulses in pump-probe experiments [91, 92]. The shortest pulses achieved so far are generated via high-harmonic generation (HHG) [98, 167] leading to pulse duration of as short as 43 attoseconds [168] in the extreme ultra-violet (XUV) to soft-X-ray regime. HHG is a strong-field process, which creates high order harmonics of a driving laser field through non-linear interaction with a medium, which is most commonly a gas [169–171], but can also be a solid [172–176]. HHG requires among other things driving pulses with a short pulse duration, i.e. in the femtosecond (fs) regime, and a high peak intensity of around $10^{14}\,\mathrm{W/cm^2}$ with a high pulse energy of at least a few hundred μJ.

In the following chapters the basic concepts of ultrashort laser pulses, the generation of high harmonics, and their implementation in attosecond pump-probe spectroscopy experiments is described.

An overview of the fundamentals of ultrashort laser pulses and/or high harmonic generation, and their applications can be found for example in [5, 170, 177–179].

2.2.1 Ultrashort laser pulses

The electric field of an ultrashort laser pulse can in general be described in the time domain according to

$$E(t) = \frac{1}{2}\sqrt{I(t)}\exp\left(i\left(\omega_0 t - \varphi(t)\right)\right) + c.c., \tag{2.24}$$

where k is the wavevector, ω_0 is the carrier frequency, $\varphi(t)$ is the temporal phase of the pulse, and $I(t) \propto |A(t)|^2$ is the temporal intensity, which is proportional to the absolute squared of the pulse amplitude $A(t)$. The pulse amplitude can in most cases be approximated as a Gaussian pulse with zero phase, i.e. $A(t) = A_0 \exp(-2\ln 2(t/\Delta\tau)^2)$, where $\Delta\tau$ is the pulse duration, which is given by the full width at half-maximum (FWHM) of the temporal intensity.

Furthermore, the pulse can be represented in the frequency domain in means of a Fourier transform (FT)

$$\begin{aligned} E(\omega) &= \frac{1}{\sqrt{2\pi}}\int_{-\infty}^{+\infty} E(t)\exp(-i\omega t)\mathrm{d}t \\ &= \frac{1}{2}\sqrt{S(\omega)}\exp\left(-i\phi(\omega)\right) + cc., \end{aligned} \tag{2.25}$$

where $S(\omega)$ is the spectral intensity centered around ω_0, and $\phi(\omega)$ is the spectral phase.

Accordingly, the pulse duration $\Delta\tau$, i.e. FWHM of the temporal intensity, and the spectral bandwidth $\Delta\omega$, i.e. the FWHM of the spectral intensity are related through a Fourier transform following

$$\Delta\tau\Delta\omega \geq 2\pi c_B, \tag{2.26}$$

where c_B is a constant, which has for example the value of 0.441 in the case of a Gaussian pulse envelope [177].
The lower limit of Eq. 2.26 can only be achieved if the phase of the pulse is flat, i.e. $\varphi(t) = 0$, and $\phi(\omega) = 0$ for all t and ω. It follows that a 2.7 fs gaussian pulse centered at 800 nm has to have a minimal bandwidth of ~ 370 nm.

In the time domain the phase is defined as

$$\varphi(t) = \arg\left(A(t)\right), \tag{2.27}$$

and can be Taylor expanded around an initial time t_0 leading to

$$\begin{aligned}
\varphi(t) = &\quad \varphi_0 \quad + \sum_{n=1}^{\infty} \frac{\varphi_n (t-t_0)^n}{n!} \\
= &\quad \varphi_0 \quad + \frac{\partial\varphi(t)}{\partial t}\bigg|_{t=t_0} (t-t_0) + \frac{1}{2}\frac{\partial^2\varphi(t)}{\partial t^2}\bigg|_{t=t_0} (t-t_0)^2 \\
&+ \quad \frac{1}{6}\frac{\partial^3\varphi(t)}{\partial t^3}\bigg|_{t=t_0} (t-t_0)^3 + ...,
\end{aligned} \tag{2.28}$$

with $n = 1, 2, 3....$ In Eq. 2.28 the time independent term $\varphi_0 = \varphi(t_0)$ corresponds to the carrier-envelope phase (CEP), which is the phase between the carrier wave and the position of the amplitude envelope of the pulse (cf. Fig. 2.1 (e)).

The first order term $\varphi_1 t$, represents an instantaneous frequency, which leads to a shift in the frequency domain as can be seen in Fig. 2.1 (j). The second order term $\varphi_2 t^2$ corresponds to a linear chirp of the pulse, where a positive chirp means that the pulse frequency linearly increase with time, i.e. $\mathrm{d}\omega/\mathrm{d}t > 0$ (cf. Fig. 2.1 (g)). The third order term $\varphi_3 t^3$ leads to a quadratic chirp, i.e. the pulse frequency changes quadratically with time (cf. Fig. 2.1 (h)).

Equivalent to the time domain, the spectral phase can be Taylor expanded around the carrier frequency ω_0, i.e.

$$\phi(\omega) = \phi_0 + \sum_{n=1}^{\infty} \frac{\phi_n (\omega-\omega_0)^n}{n!}, \tag{2.29}$$

with $n = 1, 2, 3...$, and $\phi_n = \left.\dfrac{\partial^n\phi(\omega)}{\partial\omega^n}\right|_{\omega=\omega_0}$.

The first term ϕ_0 is the same in the time and frequency domain. The first order linear term $\phi_1\omega$ represents the group velocity of the pulse, and accordingly a linear phase in ω leads to a time delay of the pulse. The second order term $\phi_2\omega^2$ is the group delay dispersion (GDD), which leads to an increase of the pulse

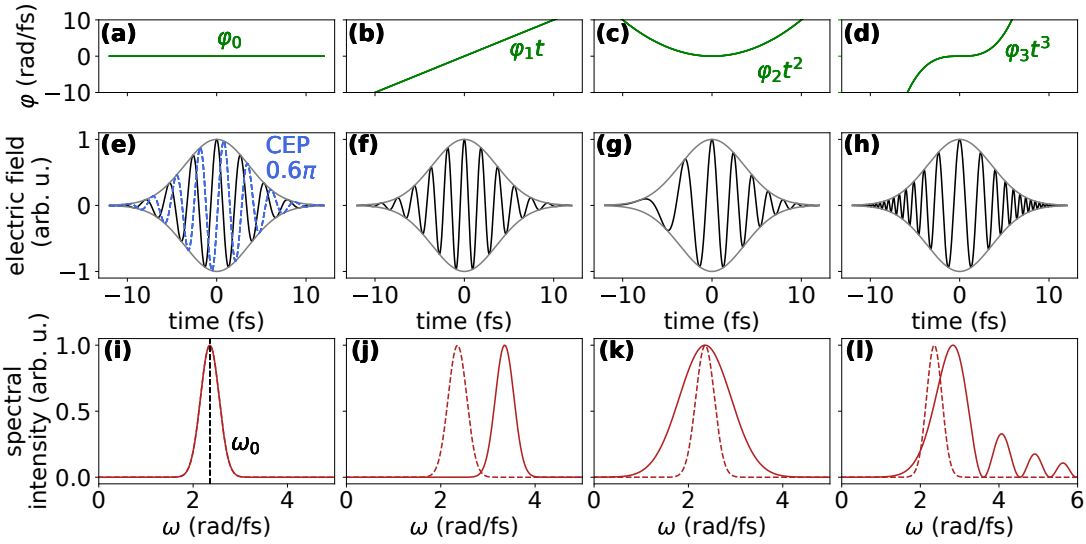

Figure 2.1: Illustration of the electric field of a gaussian pulse with a pulse duration of 6 fs centered at 800 nm, and how different order phase terms φ_n with $n = 0, 1, 2, 3$ affect the temporal properties of the pulse. In addition the spectral intensity of the pulse is shown, by performing a Fourier transform of the time dependent electric field. In (a)-(d) the different order phase terms as a function of time are shown. In (e)-(h) the electric field of the pulse for the different order phase terms is shown, and in (i)-(l) the corresponding Fourier transform of the electric field is plotted. In (e) the electric field of a pulse with a flat phase $\varphi_n = 0$ for $n = 0, 1, 2...$ is shown in black. In addition, the same pulse with a CEP of 0.6π, i.e. $\varphi_0 = 0.6\pi$ is plotted in blue leading to a shift of the carrier wave underneath the envelope in time. In the frequency domain (i) the corresponding spectral intensity is centered at $\omega_0 = 2.35\,\text{rad/fs}$, which corresponds to a wavelength of 800 nm with a FWHM of $\Delta\omega = 0.46\,\text{rad/fs}$, i.e. a bandwidth of 158 nm. In (f) the electric field of the pulse with a non-zero first order phase term φ_1 is shown. A first order phase term in time leads to an instantaneous frequency, and thus to a shift of the central frequency in the frequency domain shown in (j). In (c) the electric field of a pulse with a non-zero second order phase term $\varphi_2 t$ is shown, which give rise to a linear chirp, and thus to a broadening of $\Delta\omega$ in the frequency domain (k). In (h) the electric field of a pulse with a non-zero third order phase term $\varphi_3 t$ is shown, leading to additional frequency components as shown in (l).

duration. The third order term $\phi_3\omega^3$ corresponds to the third-order dispersion (TOD) leading to small pre- or post-pulses in time.

Accordingly, in order to create short driving laser pulses for a sufficient HHG, especially the higher order phase terms have to be zero, i.e $\phi_n = 0$ for $n \geq 2$ for all ω.

2.2.2 High harmonic generation

The first high harmonics were found experimentally by A. McPherson et al. [97], and M. Ferray et al. [98], where a picosecond laser pulse was focused in a rare gas medium, and the emitted light was recorded. They discovered that the emitted light is composed of odd high order harmonics of the driving laser frequency. The spectrum showed few harmonics at low photon energies with fast decreasing intensities (pertubative regime). These harmonics are then subsequently followed by a plateau with constant intensity, and at high energies the harmonics displayed a sharp cut-off.
A. L'Huillier et al. [167], and J. Macklin et al. [180] found a cut-off extending even to the 40th harmonic order.

The formation of a plateau as well as a cut-off at such high photon energies can not be explained by perturbation theory, which describes light-matter interaction by the non-linear polarization of the medium:

$$\vec{P} = \epsilon_0 \left(\chi^{(1)}\vec{E} + \chi^{(2)}\vec{E}^2 + \chi^{(3)}\vec{E}^3 + ... \right), \tag{2.30}$$

where $\chi^{(N)}$ is the N-th order electric susceptibility of the material, ϵ_0 is the vacuum permittivity, and $\vec{E}$ is the electric light field.

After the experimental discovery of high harmonics multiple research groups tried to understand the underlying mechanism of HHG [181–183]. In 1991, A. L'Huillier, K. Schafer, and K. Kulander [184] were able to theoretically reproduce the spectral shape of HHG by numerically solving the time-dependent Schrödinger equation (TDSE). Furthermore, they predicted that HHG comes from a single electron effect.

In 1992, J. L. Krause et al. [185] formulated a scaling law derived empirically from numerical TDSE simulations, which allowed to predict the HHG cut-off energy from atoms and ions, and which was precisionized later [186] to be

$$\Omega_{\max} = 3.17U_p + I_p, \tag{2.31}$$

where I_p is the ionization potential of the atom. The ponderomotive potential U_p corresponds to the kinetic energy of an electron gained in an oscillatory laser field over half an oscillation cycle according to

$$U_p = q^2E_0^2/4m_e\omega_0^2, \tag{2.32}$$

where E_0 is the electric field amplitude, and q and m_e are the charge and mass of the electron. According to Eq. 2.32 a higher cut-off energy can be achieved by

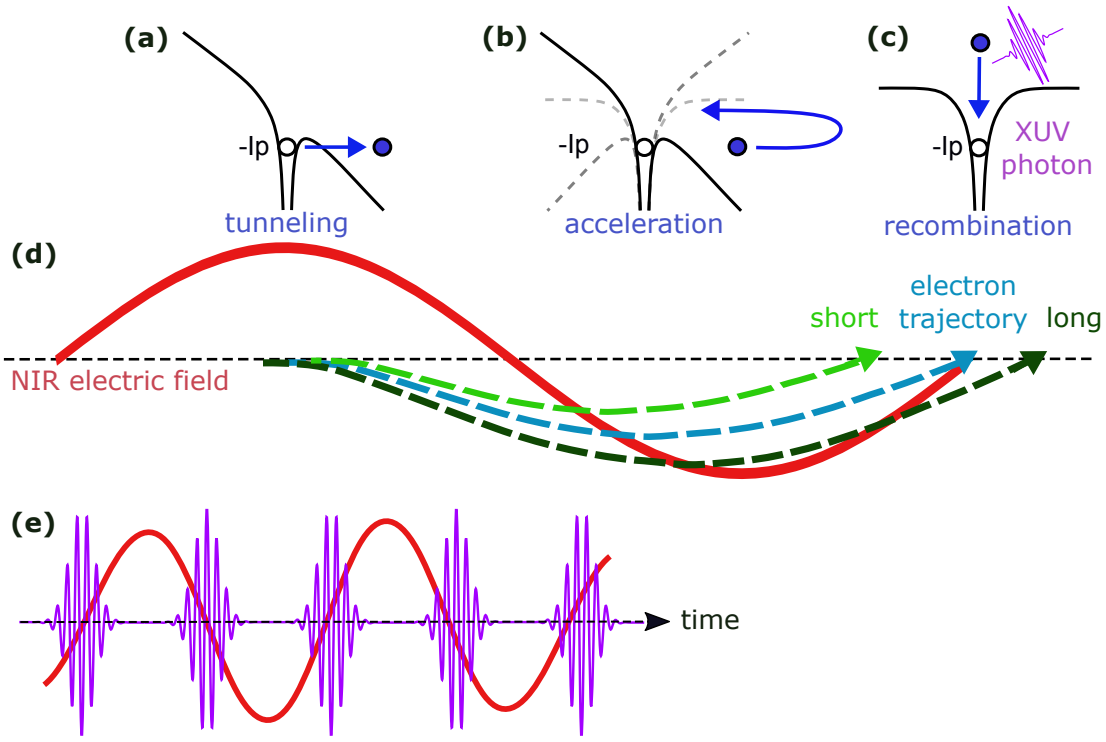

Figure 2.2: Schematic illustration of high harmonic generation. In (a)-(c) the three-step model is described, showing that in a first step the atomic potential is bend by the driving laser electric field shown in (d). After the electron tunnels out, it is accelerated in the laser field, and subsequently recombines again with the ion, releasing it's gained kinetic energy in form of an XUV photon. In (d) the electric field of the driving laser is shown in red. Additional, the schematic electron trajectory leading to the emission of a XUV photon with the highest energy is shown in blue, and the long (dark green) and short (light green) electron trajectories are illustrated, which both lead to the same lower photon energy. In (e) the driving laser field is shown together with the field of the generated attosecond pulse train (APT).

using a longer driving laser wavelength or a higher pulse intensity. However, there are some limitations, since the efficiency of HHG decreases with $\sim \lambda^{-6}$ [187,188], and if the intensity of the driving laser is too high for a given pressure of the HHG gas medium, phase matching throughout the medium is limited [189].

In 1993, Kulander and Schafer [190], Paul Corkum [186], and later Lewenstein et al. [191] introduced the semi-classical three step model explaining the fundamental principle of HHG.

An illustration of the three-step model can be found in Fig. 2.2 (a)-(c). In the first step, in Fig. 2.2 (a) the electric field of the driving laser bends the atomic potential leading to tunnel ionization of the atom. In general tunnel ionization occurs, whenever $\gamma < 1$, where γ is the Keldysh parameter, which is given by $\gamma = \sqrt{I_p/2U_p}$ [192]. In contrary, if $\gamma > 1$ the atom is ionized through multi-photon absorption [192]. In the second step, Fig. 2.2 (b) the free electron is accelerated

away from the ion core gaining kinetic energy while following the electric laser field. As soon as the laser field changes sign the electron is redirected towards the ion. In the third step, Fig. 2.2 (c) the electron recombines with the ion releasing its kinetic energy in form of an XUV photon.

The amount of energy the electron gains while moving in the laser field depends on the time of the tunneling in respect to the extrema of the laser electric field. For all emitted photons with a energy smaller than the maximal possible energy $\Omega_{\max}$, there exist two electron trajectories leading to the same final energy. These trajectories are called short and long trajectories [5], and are shown schematically as light and dark green curves in Fig. 2.2 (d).

The three-step process repeats at every extremum (half-cycle) of the driving electric field (cf. Fig. 2.2 (e)). Consequently, for a few fs driving pulse a train of attosecond pulses (APT) with a distance of half a laser cycle between individual pulses occurs. The interference of the attosecond pulses leads to peaks at odd-number harmonics $\omega = N\omega_0$, with $N = 2n + 1$, in the frequency domain.

It is also possible to create single isolated attosecond pulses (IAP), which was first demonstrated by Hentschel et al. [193]. A detailed description of IAP generation is given in section 4.

2.2.3 Theory of pump-probe spectroscopy

In attosecond pump-probe spectroscopy a XUV pulse photoionizes a target, for example an atom or molecule. The absorption of one XUV photon initiates a time-dependent process in the emerging fragments, for example the launch of a vibrational wave packet in the ion [194–198] or a phase shift of the photoelectron wave packet [151, 199, 200]. The time evolution of these processes can then be probed by the interaction of the system with a NIR pulse.

In Fig. 2.3 (a) the schematic principle of XUV-NIR pump-probe spectroscopy is illustrated. First of all, the attosecond XUV pulse project the initial state of a target, for example an atom or moleclule, onto an intermediate state. Since the bandwidth of the probe pulse is rather large, multiple intermediate states are excited simultaneously, thus creating a coherent superposition of intermediate states. After a variable time delay these states are then projected onto a final state by the NIR probe pulse. The time evolution of the intermediate states can be mapped by scanning the delay between the pump and the probe pulse.

Quantum-mechanical description Similar derivations can be found for example in [89, 92, 194, 201–203].
A quantum-mechanical system with the total wave function $|\Psi(t)\rangle$ is determined by the time-dependent Schrödinger equation (TDSE), i.e.

$$i\hbar\frac{\partial}{\partial t}|\Psi(t)\rangle = \widehat{H}(t)\,|\Psi(t)\rangle\,. \tag{2.33}$$

Here the total Hamiltonian $\widehat{H}$ includes two parts,

$$\widehat{H}(t) = \widehat{H}_0 + \widehat{H}_{\mathrm{MR}}(t). \tag{2.34}$$

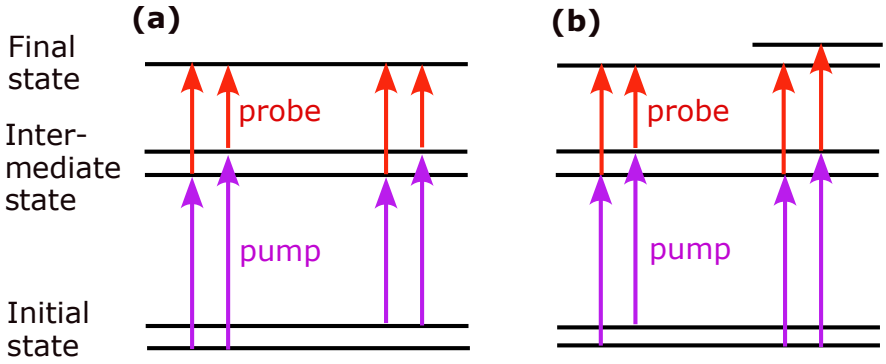

Figure 2.3: Schematic illustration of XUV-NIR pump-probe spectroscopy. The XUV pulse excites/ionizes the target, and projects the initial state onto a coherent superposition of intermediate states. After a certain time delay the NIR probe pulse project the excited states onto a final state. (a) Two different pathways, which originate from the same initial state, and resulting in the same final state. Accordingly the two pathways interfere in the final state. (b) Two different pathways, which do not interfere, because they originate from different initial states or end up in different final states.

The time-independent radiation-free Hamiltonian $\widehat{H}_0$ fully describes the unperturbed system with the eigenstates $|n\rangle$ and eigenvalues E_n, i.e.

$$\widehat{H}_0 \, |n\rangle = E_n \, |n\rangle \, . \tag{2.35}$$

The time-dependent matter-radiation interaction Hamiltonian

$$\widehat{H}_{\mathrm{MR}}(t) = -\widehat{d}\vec{E}_{\mathrm{el}}(t) \tag{2.36}$$

includes the scalar product of the laser electric field $\vec{E}_{\mathrm{el}}(t)$ interacting with the system at time t' and the dipole operator $\widehat{d}$.

The electric field in general contains multiple frequencies ω_q, and is defined as

$$\vec{E}_{\mathrm{el}}(t) = \sum_j \left(\vec{E}_{\mathrm{el},j} f_j(t) \mathrm{e}^{-i\omega_j t} + c.c.\right), \tag{2.37}$$

where $f_j(t)$ is the envelope at each frequency ω_j. In particular, the term $\mathrm{e}^{-i\omega_j t}$ is responsible for the absorption and $\mathrm{e}^{+i\omega_j t}$ for the emission of photons.
The field can now be applied to a pump-probe sequence. Here the pump pulse is centered at time zero, with the envelope $f_q(t)$ and the carrier frequency ω_q. The probe pulse has the envelope f_p, and the carrier frequency ω_p. The probe pulse is delayed by a time τ_D, accordingly its envelope can be written as $f_p(t-\tau_D)$:

$$\begin{aligned} \vec{E}_q(t) &= \left(\vec{E}_q f_q(t) \mathrm{e}^{-i\omega_q t} + c.c.\right), \\ \vec{E}_p(t) &= \left(\vec{E}_p f_p(t-\tau_D) \mathrm{e}^{-i\omega_p (t-\tau_D)} + c.c.\right). \end{aligned} \tag{2.38}$$

The delayed probe pulse has a phase shift in the carrier proportional to τ_D, which ensures that the carrier oscillations remain locked to the shifted envelope while the delay is changed.

Now, one can assume that the pulses are linearly polarized, and thus the dipole operator only includes components parallel to the pump and the probe pulses. Accordingly, the vectors can be dropped for simplicity of notations.

The field-unperturbed solution is described by solving the zero-order TDSE without the laser field, yielding the time-dependent wave function as

$$|\Psi^{(0)}(t)\rangle = \sum_n b_n^{(0)}(t)\,|n\rangle = \sum_n b_n^{(0)}(t_i)\,|n\rangle\,\mathrm{e}^{-iE_n(t-t_i)/\hbar} \tag{2.39}$$

where $b_n(t)$ are the amplitudes to find the system in the eigenstates $|n\rangle$, with the phases given by the energy factors $\mathrm{e}^{-iE_n(t-t_i)/\hbar}$. If the system is initially in its ground state, only $|b_g^{(0)}(t_i)| = 1$ remains, since $|b_{n\neq g}^{(0)}(t_i)| = 0$. It should be noted that in the following atomic units are used, i.e. $m = e = \hbar = 1$.

The interaction of the system with an XUV pump pulse can excite the system to an intermediate excited state $|k\rangle$. The first-order perturbation theory yields

$$b_k^{(1)}(t) \;=\; -i\int_{t_i}^{t} \mathrm{d}t' \mathrm{e}^{-iE_k(t-t')} E_q\,\langle k|\widehat{d}|g\rangle\, f_q(t') \mathrm{e}^{-i\omega_q t'} b_g^{(0)}(t_i) \mathrm{e}^{-iE_g(t'-t_i)}, \tag{2.40}$$

which can be written as

$$b_k^{(1)}(t) \;=\; -i\mathrm{e}^{-iE_k t} b_g^{(0)}(t_i) \mathrm{e}^{iE_g t_i} E_q\,\langle k|\widehat{d}|g\rangle \int_{t_i}^{t} \mathrm{d}t' \mathrm{e}^{+i(E_k-E_g-\omega_q)t'} f_q(t'). \tag{2.41}$$

The initial phase factor in the amplitude of the ground state $b_g^{(0)}(t_i)\mathrm{e}^{iE_g t_i}$ is arbitrary, while the modulus is equal to unity in the zero-order perturbation. Thus, the phase factor does not affect the final observables and can be set to $b_g^{(0)}(t_i)\mathrm{e}^{iE_g t_i} = 1$.

After the end of the pump pulse the excitation amplitude becomes

$$b_k^{(1)}(t) \;=\; -i\mathrm{e}^{-iE_k t} E_q\,\langle k|\widehat{d}|g\rangle \int_{-\infty}^{+\infty} \mathrm{d}t' \mathrm{e}^{+i(E_k-E_g-\omega_q)t'} f_q(t') \tag{2.42}$$

The remaining integral is a Fourier transform of the pump pulse envelope f_q at the frequency $\Delta_{kg} = E_k - E_g - \omega_q$. This corresponds to the complex spectral amplitude $E_q(\omega_{kg})$ of the pump pulse at the transition energy $\omega_{kg} = E_k - E_g$ from the ground state $|g\rangle$ to the intermediate state $|k\rangle$. Accordingly the amplitude can be written as

$$\begin{aligned} b_k^{(1)}(t) &= -i\mathrm{e}^{-iE_k t} E_q(\omega_{kg})\,\langle k|\widehat{d}|g\rangle \\ E_q(\omega_{kg}) &= \int_{-\infty}^{+\infty} \mathrm{d}t' \mathrm{e}^{+i\omega_{kg}t'} E_q \mathrm{e}^{-i\omega_q t'} f_q(t'). \end{aligned} \tag{2.43}$$

Subsequently, a probe pulse with carrier frequency ω_p excites the system from the intermediate state $|k\rangle$ to a final state $|f\rangle$. The excitation amplitude for the pathway $|g\rangle \to |k\rangle \to |f\rangle$ is

$$
\begin{aligned}
b^{(2)}_{f;kg}(t) &= -i\int_{-\infty}^{t} \mathrm{d}t' \mathrm{e}^{-iE_f(t-t')} E_p \mathrm{e}^{-i\omega_p(t'-\tau_D)} f_p(t'-\tau_D)\, \langle f|\widehat{d}|k\rangle\, b^{(1)}_k(t') \\
&= -i\mathrm{e}^{-iE_f t} E_p \mathrm{e}^{i\omega_p\tau_D}\, \langle f|\widehat{d}|k\rangle \int_{-\infty}^{t} \mathrm{d}t' \mathrm{e}^{i(E_f-\omega_p)t'} f_p(t'-\tau_D) b^{(1)}_k(t') \\
&= -\mathrm{e}^{-iE_f t} E_p \mathrm{e}^{i\omega_p\tau_D}\, \langle f|\widehat{d}|k\rangle\, \langle k|\widehat{d}|g\rangle\, E_q(\omega_{kg}) \\
&\quad \times \int_{-\infty}^{t} \mathrm{d}t' \mathrm{e}^{i(E_f-E_k-\omega_p)t'} f_p(t'-\tau_D)
\end{aligned}
\tag{2.44}
$$

After the end of the second pulse the new integration variable $t'' = t' - \tau_D$ is introduced, and the second order amplitude becomes

$$
\begin{aligned}
b^{(2)}_{f;kg}(t) &= -\mathrm{e}^{-iE_f(t-\tau_D)} \mathrm{e}^{-iE_k\tau_D} d_{fk} d_{kg} E_q(\omega_{kg}) \int_{-\infty}^{+\infty} \mathrm{d}t'' \mathrm{e}^{i\omega_{fk}t''} E_p \mathrm{e}^{-i\omega_p t''} f_p(t'') \\
&= -\mathrm{e}^{-iE_f(t-\tau_D)} \mathrm{e}^{-iE_k\tau_D} d_{fk} d_{kg} E_q(\omega_{kg}) E_p(\omega_{fk})
\end{aligned}
\tag{2.45}
$$

where $E_p(\omega_{fk})$ is the complex spectral amplitude of the probe pulse at the frequency $\omega_{fk} = E_f - E_k$ of the transition from the intermediate state $|k\rangle$ to the final state $|f\rangle$, since the remaining integral in Eq. 2.45 corresponds to the Fourier transform of the probe pulse envelope f_p at the frequency $\Delta_{fk} = E_f - E_k - \omega_p$. In addition, the used abbreviations are $d_{fk} = \langle f|\widehat{d}|k\rangle$, and $d_{kg} = \langle k|\widehat{d}|g\rangle$.

Further, one can assume that there exist two pathways involving two intermediate states $|k\rangle$ and $|k'\rangle$, each resulting in the same final state $|f\rangle$. Accordingly, the total population of the final state $|f\rangle$ is given by

$$
\begin{aligned}
|b^{(2)}_f(t)|^2 &= |b^{(2)}_{f;kg}(t) + b^{(2)}_{f;k'g}(t)|^2 \\
&= |b^{(2)}_{f;kg}(t)|^2 + |b^{(2)}_{f;k'g}(t)|^2 + \left[b^{(2)}_{f;kg}(t) b^{(2)*}_{f;k'g}(t) + b^{(2)*}_{f;kg}(t) b^{(2)}_{f;k'g}(t)\right]
\end{aligned}
\tag{2.46}
$$

The first two terms give the probability to populate $|f\rangle$ via $|k\rangle$ or $|k'\rangle$, respectively. The expression in the squared bracket is the interference term between both possible pathways.

Thus, the population is

$$
\begin{aligned}
|b^{(2)}_f(t)|^2 &= D_{fkg}|E_q(\omega_{kg})|^2|E_p(\omega_{fk})|^2 + D_{fk'g}|E_q(\omega_{k'g})|^2|E_p(\omega_{fk'})|^2 + \\
&\quad + E_q(\omega_{kg})E_p(\omega_{fk})E^*_q(\omega_{k'g})E^*_p(\omega_{fk'})\, d_{fk}d_{k'f}d_{kg}d_{gk'}\mathrm{e}^{i(E_{k'}-E_k)\tau_D} \\
&\quad + E^*_q(\omega_{kg})E^*_p(\omega_{fk})E_q(\omega_{k'g})E_p(\omega_{fk'})\, d_{fk'}d_{kf}d_{k'g}d_{gk}\mathrm{e}^{i(E_k-E_{k'})\tau_D}
\end{aligned}
\tag{2.47}
$$

with $d_{k'f} = \langle k'|\widehat{d}|f\rangle$, $d_{gk'} = \langle g|\widehat{d}|k'\rangle$, $D_{fkg} = d_{fk}d_{kf}d_{kg}d_{gk} = |d_{fk}d_{kg}|^2$, and $D_{fk'g} = d_{fk'}d_{k'f}d_{k'g}d_{gk'} = |d_{fk'}d_{k'g}|^2$.

In general, the signal measured in an experiment can involve multiple intermediate states

$$S(t) \;=\; |b_f(t)|^2 = \left| \sum_k b^{(2)}_{f;kg}(t) \right|^2, \tag{2.48}$$

and is dominated by the phase difference between different intermediate states, according to

$$\begin{aligned} S(t) \;\sim\; & \sum_k \sum_{k' \neq k} 2\Re \left\{ E_q(\omega_{kg}) E_p(\omega_{fk}) E_q(\omega_{k'g}) E_p(\omega_{fk'}) \right\} \\ & \times \Re \left\{ d_{fk} d_{k'f} d_{kg} d_{gk'} \right\} \cos((E_{k'} - E_k)\tau_D). \end{aligned} \tag{2.49}$$

The measured signal consists of beat frequencies between pairs of intermediate energy levels of the wave packet, due to the interference between different competing pathways leading to the same final state.

Pathways initiating from different initial states or resulting in different final states do not interfere (cf. Fig. 2.3 (b)), and thus in a measurement the time-dependent information is lost.

Role of entanglement The temporal evolution of a process in an atom or molecule becomes resolvable due to the interference between competing pathways, which depend on the energy difference between the involved intermediate states (cf. Eq. 2.49). For example in the case of photoionization of an atom or molecule, in order to observe these processes, a measurement of the dynamics in the ion (photoelectron) relies on the coherence properties of the ion (photoelectron) intermediate states.

However, as discussed in detail in sect. 2.1, if the ion and the photoelectron are entangled, a possible measurement of the photoelectron (ion) would allow to distinguish between the intermediate states of the ion (photoelectron). Thus, the ion+photoelectron states are in a coherent superposition, but there is no or only limited coherence between the ion (photoelectron) intermediate states. Accordingly, the observed interference signal (i.e. Eq. 2.49) is strongly limited or even absent, and therefore the retrieval of time-dependent information from that measurement is restricted (cf. Fig. 2.4).

In this thesis, two experiments are presented (cf. chapter 6 and 7), where H_2 is ionized by two phase-locked XUV pulses and an NIR pulse, creating an ion+photoelectron bipartite system. In the first and second experiment, different coherence-based dynamics are observed, i.e. the vibrational coherence and electronic coherence, respectively, in H_2^+. It is analyzed how entanglement between the ion and photoelectron limits the observability of these coherences, and in particular how the degree of coherence in the ion and the degree of ion+photoelectron entanglement, respectively, relies on the pulse properties of the ionizing pulses (i.e. pulse delays). Before turning to the main experimental results, in the following chapter, the setup is described, in which the experiments were conducted.

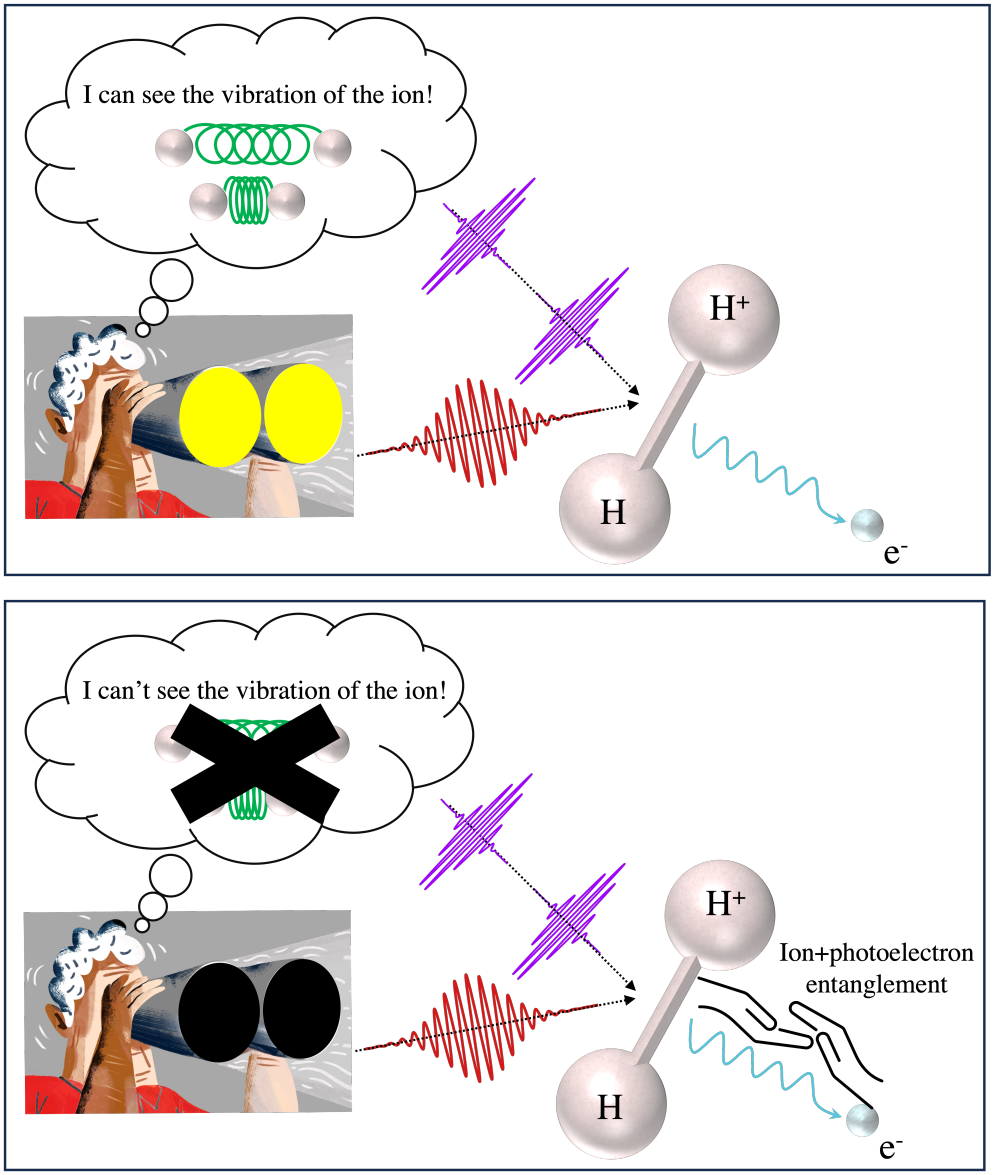

Figure 2.4: Cartoon to illustrate schematically how ion+photoelectron entanglement affects the observability of a coherence-based process, which is in the current case the dynamics of a vibrational wave packet in H_2^+ (cf. chapter 6). Here a bipartite system consisting of an ion and a photoelectron are created through photoionization of H_2 by a pump (here 2 XUV pulses) and probe (here 1 NIR pulse) pulse. An observer now wants to observe the motion of the vibrational wave packed created in the ion, which strongly depends on the vibrational coherence properties of the system. If the ion and photoelectron are not entangled (upper figure), the observer is able detect the dynamics of the wave packet as a function of the pump-probe delay. However, if the ion (in particular the vibrational states of the ion) and the photoelectron are entangled, an observer will have difficulties to see the vibrational wave packet dynamics (lower figure), and can be even completely blind towards it. It should be noted that all pulses are in fact collinear in the actual experiment.

CHAPTER 3

Experimental setup

In the previous chapter the theoretical basics of attosecond pump-probe spectroscopy are introduced, as well as the limiting role of ion+photoelectron entanglement regarding the observability of time-dependent dynamics, which rely on certain coherence properties of the system under investigation. These theoretical predictions are now tested experimentally, by photoionizing hydrogen molecules with a pair of phase-locked XUV pulses, where the coherent superposition of intermediate states in the ion are investigated in correlation with ion+photoelectron entanglement.
In the following chapter the experimental setup, in which these experiments are performed, is described. This beamline was the foundation for a variety of experimental discoveries in the last years [2, 156, 204–207]. The overview of the experimental setup, as well as the description and characterization of the ultrastable Mach-Zehnder interferometer (MZI) are published in Optics Express [1]. Short summaries of the setup can also be found in the other publications associated with this thesis [2, 3].

Publication information

Parts of this chapter are published as

- *Phase-locking of time-delayed attosecond XUV pulse pairs* by L.-M. Koll, L. Maikowski, L. Drescher, M. J. J. Vrakking, and T. Witting in Optics Express, vol. 30, no. 5, pp. 7082–7095 (2022) [1]. DOI: `https://doi.org/10.1364/OE.452018`

  Author contributions: The Mach-Zehnder interferometer (MZI) was developed by L. Maikowski and T. Witting. The experiments were conceived by L.-M. Koll, T. Witting and M. J. J. Vrakking. The MZI was characterized by L.-M. Koll and L. Maikowski. The further experiments were per-

formed and the data was analyzed by L.-M. Koll under the supervision of T. Witting. The manuscript was written by L.-M. Koll and T. Witting with the help and discussion of the other co-authors.

Short summaries of the setup are published in

- *Experimental control of quantum-mechanical entanglement in an attosecond pump-probe experiment* by L.-M. Koll, L. Maikowski, L. Drescher, T. Witting, and M. J. J. Vrakking in Physical Review Letters, vol. 128, no. 4, p. 043201 (2022) [2]. DOI: `https://doi.org/10.1103/PhysRevLett.128.043201`

  Author contributions: The experiments were performed and the data was analyzed by L.-M. Koll under the supervision of T. Witting. The conceptual idea and the theoretical work were developed by M. J. J. Vrakking. The main figures of the manuscript were produced by L.-M. Koll, and the manuscript was written by M. J. J. Vrakking with the help and discussion of the other co-authors.

- *Control of photoelectron-ion entanglement in attosecond laser-induced photoionization of H_2* by L.-M. Koll, T. Witting, and M. J. J. Vrakking in Proceedings of the 8th International Conference on Attosecond Science and Technology (ATTO 8). Springer Proceedings in Physics, vol 300. Springer, pp. 155-165 (2024) [3].
  DOI: `https://doi.org/10.1007/978-3-031-47938-0_15`

  Author contributions: The experiments were performed and the data was analyzed by L.-M. Koll under the supervision of T. Witting. The conceptual idea, the theoretical work and calculations were developed by M. J. J. Vrakking. The manuscript was written by L.-M. Koll and M. J. J. Vrakking, where the part about the experimental results was mainly written by L.-M. Koll, and the part about the theoretical calculations was mainly written by M. J. J. Vrakking.

3.1 Overview

The laser system used in all presented experiments consists of a Ti:Sapphire oscillator, which has the option to operate in the carrier-envelope phase (CEP) stabilized regime [10, 208] using a feed-forward scheme for stabilization [209] (cf. sect. 3.3).

The oscillator pulses are amplified by a multi-stage chirped-pulse amplification (CPA) Ti:Sapphire laser system (Aurora, Amplitude Technologies). Dispersion in the amplification stages are controlled by compression grating and an acousto-optical modulator (DAZZLER [210]).
In addition, an intra-cavity acousto-optical absorber (MAZZLER [211]) is used to actively broaden the pulse spectrum by spectral hole burning [212]. The final

near-infrared (NIR) pulses at a repetition rate of 1 kHz have a center wavelength of 790 nm with an output power of up to 20 W. The final pulse duration is between $20 - 25$ fs (FWHM). Even though higher pulse energies are available, only 3 mJ is used for the experiments described in the following chapters.

In Fig. 3.1 an overview of the experimental setup is shown. For the following experiments few cycle-pulses are required, thus a pulse duration of 20 fs is not sufficiently short (the laser cycle is around 2.6 fs long). A decrease of the pulse duration can be achieved by hollow-core fiber pulse (HCF) compression [4]. Here 1.8 - 2 mJ of the output power are coupled into a 1 m long fused silica waveguide (1002562, Hilgenberg GmbH). The core of the HCF has a diameter of 340 μm. The fiber is filled with neon gas in gradient pressure [213] up to 3 bar. This leads to spectral broadening of the pulses by self-phase modulation [214] increasing the NIR bandwidth up to a full octave (cf. sect. 3.2). The pulse energy after the HCF is 1.4 mJ.

The pulses are subsequently compressed by double angle technology chirped mirrors (PC70, Ultrafast Innovations GmbH) [215, 216] and a pair of fused silica wedges with variable thickness (OA925, Spectra-Physics Vienna). A 3 mm long z-cut potassium dihydrogenphosphate (KDP) crystal compensates for any third-order dispersion obtained during the non-linear compression of the pulses [216, 217]. The compressed pulses are characterized by a spectral shearing interferometer (SEA-F-SPIDER) [218]. The final pulse duration is typically around 5 fs with a gas pressure of 2 bar in the HCF. By increasing the neon gas pressure to 3 bar a pulse duration of 3.2 fs can be achieved, which is quite close to a NIR single-cycle pulse.

Subsequently the pulses are send to a phase-stabilized Mach-Zehnder type interferometer. A beam splitter (BS) splits 80 % of the initial pulse, which are used for the generation of an XUV pump pulse, and the remaining 20 % serve as a NIR probe pulse. It should be noted that for the last experiment, which is described in chapter 7, the setup was modified to a 90 % (pump) - 10 % (probe) splitting ratio. The XUV pump and NIR probe pulse can be delayed relative to each other by a stick-slip piezo stage (SLC-1730-LC-ST, Smaract GmbH). Just below the NIR beam a frequency stable 761 nm cw laser (BrixX 761-10, omicron Laser GmbH) co-propagates through the interferometer to actively stabilize the delay between both interferometric arms. A tilt between the two arms of the cw beam is introduced to create vertical aligned spatial fringes, which are recorded by a CMOS camera. Phase changes are extracted after fast Fourier transform (FFT) processing, generating a feedback signal, which actively stabilizes the interferometer achieving a delay jitter with a standard deviation of $\sigma < 50$ as.

Inside the XUV arm of the main interferometer, a passively and actively stabilized Mach-Zehnder interferometer (MZI) is placed to generate two phase-locked NIR pulses. A detailed description of the MZI is given in section 3.4.

The two phase-locked NIR pulses are then focused by a spherical mirror with a focal length of $f = 750$ mm into a 3 mm long gas cell filled typically with around 40 mbar of argon gas to generate two phase-locked attosecond XUV pulses via HHG. The intensity of the two driving NIR pulses is kept below 1×10^{14} W/cm^2

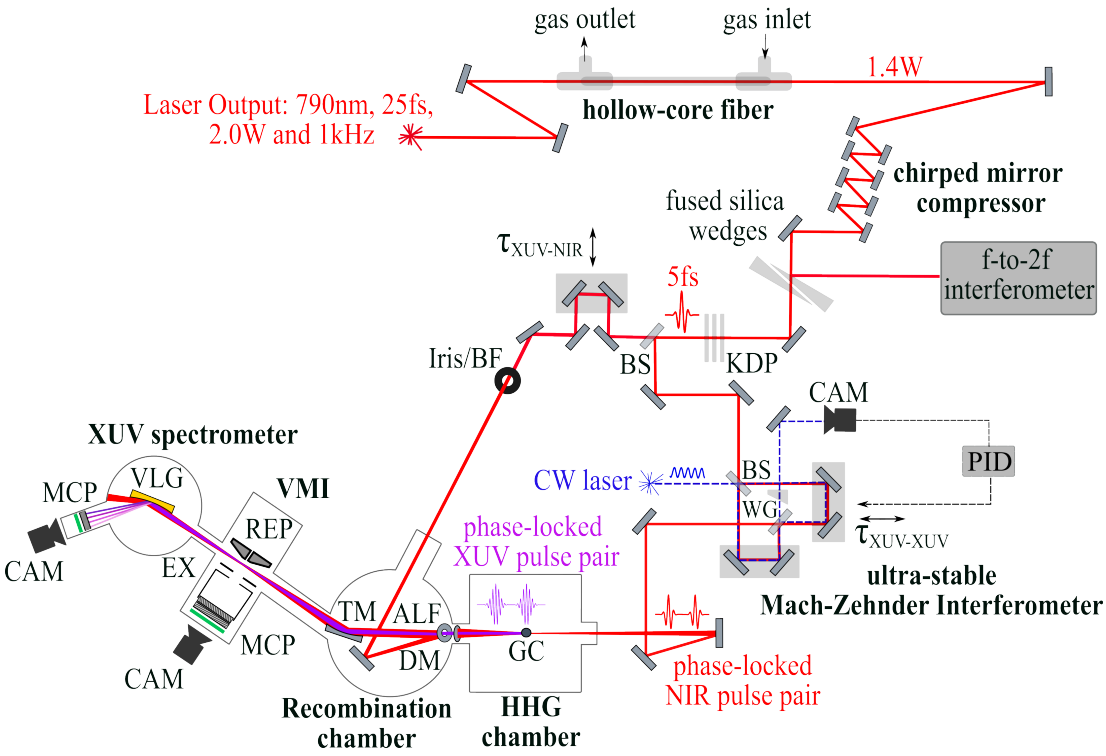

Figure 3.1: Overview of the experimental setup. The NIR laser output pulses propagate through a hollow-core fiber, chirped mirrors, fused silica wedges, and a z-cut potassium dihydrogenphosphate (KDP) crystal leading to a final pulse duration between $3.2 - 5\,\mathrm{fs}$ centered between $770 - 790\,\mathrm{nm}$. Subsequently, the NIR pulses are split by a fused silica beam splitter (BS) in two parts, one part is used for XUV generation and the other part serves as the NIR probe pulse in pump-probe experiments. The HHG driving pulse is send through a passively and actively stabilized Mach-Zehnder interferometer creating a phase-locked NIR pulse pair. The two generated phase-locked XUV pulses are recombined with the NIR probe pulse by a drilled mirror (DM). The recombined pulses are then focused by a toroidal mirror (TM) into a velocity map imaging (VMI) spectrometer. The spectrum of the two XUV pulses is detected by an XUV spectrometer. Abbreviations: BF: bandpass filter, DM: drilled mirror, BS: beam splitter, WG: wedge, CAM: camera, ALF: aluminum filter, EX: Extractor electrode, REP: Repeller, MCP: microchannel plate, VLG: variable line-spacing grating, PID: proportional-integral-derivative feedback.

to ensure that the ionization of the gas medium by the first NIR pulse does not disturb the HHG by the second pulse [219]. After the HHG process the remaining NIR pulse is filtered out by a 200 nm thin aluminium foil (ALF), with a bandpass between 15 eV to 72 eV. In addition, the ALF compensates the GDD induced by HHG (*attochirp*, [220]).

The XUV pulses are then recombined collinearly with the NIR probe pulse by a drilled mirror (DM). With a gold-coated toroidal mirror (TM) the focus of the combined XUV and NIR pulses is then $2f - 2f$ re-imaged into the velocity map imaging (VMI) spectrometer chamber (cf. sect. 3.5). A nozzle integrated in the repeller electrode of the VMI spectrometer [221] ejects a neutral gas medium, which serves as a target of any pump-probe experiments. The polarization of the pulses are in the plane of the detector, and after ionization of the target either the ions or electrons can be detected with a micro-channel plate (MCP) and phosphor screen recorded by a USB3 CMOS camera (ace acA2440-75um, Basler AG). After the VMI chamber the XUV spectra is split into its frequency components by a variable line-space grating (VLG, 001-0640, Hitachi) and the spectra are resolved by a flat-field XUV spectrometer [7].

3.2 Hollow-core fiber pulse compression

As described above, the NIR pulses after the CPA Ti:Sapphire laser system have a pulse duration between $20 - 25$ fs centered at 790 nm (cf. Fig. 3.2). To increase the spectral bandwidth of the pulses, and then subsequently decrease the pulse duration as close as possible to the Fourier limit (cf. Eq. 2.26) to create few- or even single-cycle pulses, the NIR pulses are first send through a hollow-core fiber filled with up to 3 bar of neon gas in a gradient pressure configuration [213]. Pulse compression with a HCF was first demonstrated by Nisoli et a. [4], paving the way to apply this technique to pulses with a variety of different parameters [213, 222–224].
In the HCF the bandwidth of the pulses is increased up to a full octave by the non-linear process of self-phase modulation (SPM) [214].

Equation 2.30 describes the interaction of a medium with an electric field in terms of the non-linear polarization of the medium. The third order polarization term leads to an intensity dependence of the total refractive index

$$n(\omega_{\mathrm{NIR}}, t) = n_0(\omega_{\mathrm{NIR}}) + n_2(\omega_{\mathrm{NIR}}) \cdot I_{\mathrm{NIR}}(t), \tag{3.1}$$

where n_0 is the linear, and $n_2 \cdot I_{\mathrm{NIR}}$ is the non-linear refractive index of the medium, $I_{\mathrm{NIR}}(t)$ is the time-dependent pulse intensity, and ω_{NIR} is the carrier frequency of the NIR electric field.

While the pulse propagates through the medium over a distance l, the time-dependent pulse intensity leads to a change of the refractive index, and thus to a shift of the phase of the pulse.

The NIR phase is given by

$$\phi_{\mathrm{NIR}}(t) = \omega_{\mathrm{NIR}} t - k_{\mathrm{NIR}} z = \omega_{\mathrm{NIR}} t - \frac{\omega_{\mathrm{NIR}}}{c} \cdot n(I_{\mathrm{NIR}}) \cdot l, \tag{3.2}$$

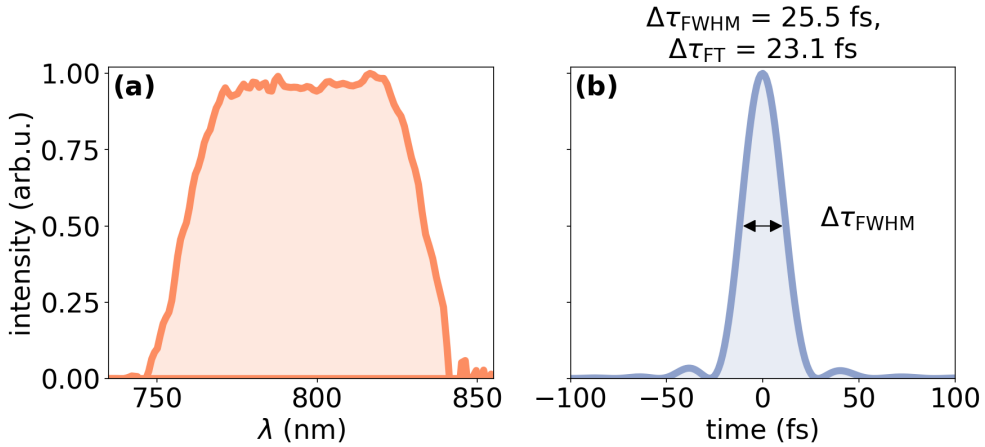

Figure 3.2: (a) Spectrum of the NIR pulse at the output of the CPA Ti:Sapphire laser system, and corresponding (b) pulse in time with a duration of 25.5 fs measured by SPIDER [13], which is close to the Fourier limit of 23.1 fs based on the bandwidth.

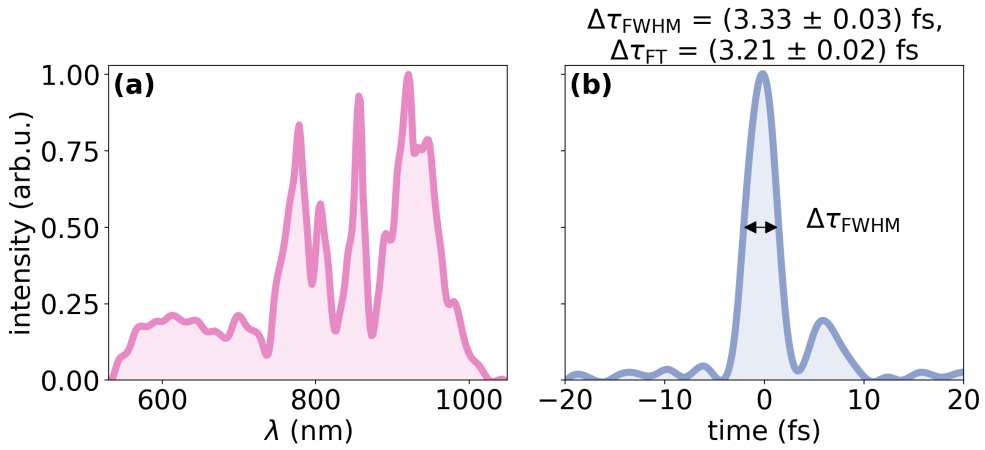

Figure 3.3: (a) Spectrum of the NIR pulse after hollow-core fiber pulse compression. (b) Temporal pulse shape with a duration of 3.3 fs, which is measured at FWHM by SEA-F-SPIDER [218] averaged over ten measurements. Based on the bandwidth, the Fourier limit of the pulse duration is 3.2 fs. Accordingly, a successful pulse compression is achieved, and only the small maximum at 5 fs indicates that the pulse still has a small finite third-order dispersion (TOD).

where c is the speed of light.

As a consequence, the pulse frequency is shifted to lower values at the front of the pulse ($\mathrm{d}I_{\mathrm{NIR}}(t)/\mathrm{d}t > 0$), and to higher frequencies at the back ($\mathrm{d}I_{\mathrm{NIR}}(t)/\mathrm{d}t < 0$), according to

$$\omega_{\mathrm{new}}(t) = \frac{\mathrm{d}\phi_{\mathrm{NIR}}(t)}{\mathrm{d}t} = \omega_{\mathrm{NIR}} - \frac{\omega_{\mathrm{NIR}}}{c} \cdot n_2 \frac{\mathrm{d}I_{\mathrm{NIR}}(t)}{\mathrm{d}t} \cdot l. \tag{3.3}$$

The amount of bandwidth broadening depends on multiple factors, for example the length and the core diameter of the fiber, the input laser intensity or the gas itself, as well as the gas pressure in the fiber [224–226].

After the HCF broadening the NIR pulses are positively chirped, leading to a pulse duration in the picosecond range. Thus, the acquired GDD due to SPM has to be compensated in order to create few-cycle pulses. This is achieved by multiple chirped mirror pairs in double angle configuration [215, 216] followed by a pair of fused silica wedges with variable thickness. The chirped mirrors consist of multiple dielectric-coated layers with varying width. As a result different wavelengths have different penetration depths, i.e. long wavelengths reach deeper into the material than the short ones, which induces a negative chirp on the pulses. In contrary, fused silica has a GDD of $+37\,\mathrm{fs}^2$ for a thickness of 1 mm at 790 nm [227, 228]. Accordingly, the pulses after the chirped mirrors are supposed to have a small negative chirp, which is subsequently controlled by a variable positive chirp induced by the propagation of the beam through the fused silica wedges (cf. sect. 4.1). The third-order dispersion is compensated by a 3 mm thick KDP crystal.

In Fig. 3.3 the spectrum, and the pulse duration of the NIR pulses after HCF compression is shown. The bandwidth of the pulses is increased from initially $750 - 840\,\mathrm{nm}$ to $510 - 1030\,\mathrm{nm}$, which decreases the measured pulse duration from 25.5 fs to 3.3 fs (FWHM) after compression.

3.3 Carrier-envelope phase stability

As described in detail in section 2.2.1, the CEP is the phase between the carrier wave and the position of the amplitude envelope of the pulse (cf. Fig. 3.4). When the CEP is not actively controlled, the phase alternates from pulse to pulse, thus leading to different waveforms for consecutive pulses. For relatively narrowband pulses ($\Delta\omega/\omega_0 \ll 1$, where $\Delta\omega$ is the bandwidth and ω_0 the central frequency of the pulse) a change of the CEP has no measurable physical consequence. However, this changes as soon as the bandwidth of the pulses become large, and the pulses are close to single-cycle in duration. In this regime, a change of the CEP changes significantly the temporal evolution of the few- or single-cycle pulses, e.g. if the CEP jumps by $\pi/2$ an originally cosine-shaped pulse becomes a sine-shaped one, or vice versa (cf. Fig. 3.4).
Accordingly, it is important to stabilize the CEP in any experiment, which requires short pulses.

CEP stabilization already starts in the oscillator. A mode-locked laser produces a train of pulses, which are separated in time by one round trip within the laser cavity. From pulse to pulse the CEP changes by $\Delta\varphi_0$. If now the change of the CEP is $\Delta\varphi_0 = 2\pi/n$ (with n as an integer), every n-th pulse has the same CEP value. A train of pulses leads to a comb in the frequency domain, which typically spans over a full octave in the current system.

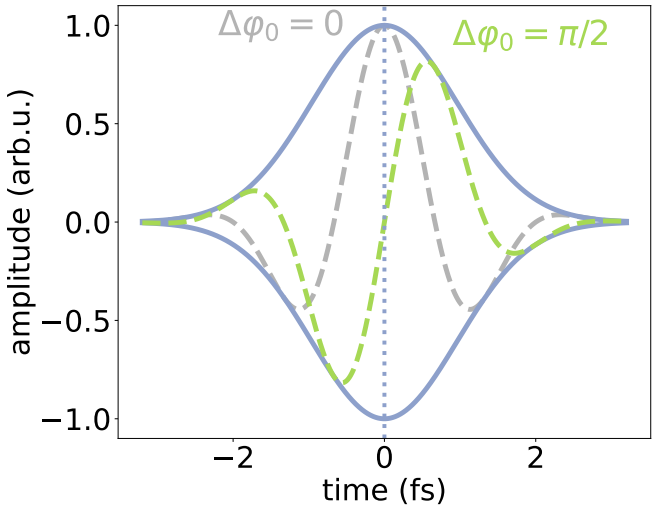

Figure 3.4: Illustration of a 3.2 fs pulse centered at 800 nm with a carrier-envelope phase (CEP) of $\Delta\varphi_0 = 0$, which corresponds to a cosine-shaped pulse (grey dashed line), and a CEP of $\Delta\varphi_0 = \pi/2$, i.e. a sine-shaped pulse (green dashed line).

Each comb frequency is defined by

$$f_i = n f_{\text{rep}} + f_{\text{CEO}}, \tag{3.4}$$

with n as an integer, f_{rep} as the repetition rate, and $f_{\text{CEO}} = f_{\text{rep}}\Delta\varphi_0/2\pi$ corresponds to the carrier-envelope offset (CEO) [229]. Accordingly, if $f_{\text{CEO}} = f_{\text{rep}}/n$ the CEP is the same for every n-th pulse.

The f_{CEO} is measured in terms of f-to-2f interferometry [10]. Thereby a low-frequency comb line f_1 is frequency-doubled (i.e. second harmonic generation, SHG [230]) $f_{\text{SHG}} = 2f_1$, and the beat frequency, i.e. the difference between a high-frequency $f_2 = n_2 f_{\text{rep}} + f_{\text{CEO}}$ (with $n_2 = 2n_1$), and frequency-doubled $2f_1$ comb line is measured with a photodiode, according to

$$2f_1 - f_2 = 2n_1 f_{\text{rep}} + 2f_{\text{CEO}} - (n_2 f_{\text{rep}} + f_{\text{CEO}}) = f_{\text{CEO}}. \tag{3.5}$$

In terms of a feed-forward scheme [209], the measured CEO frequency is subtracted from each spectral line in the comb in an acousto-optic frequency shifter achieving the same phase for each single pulse.

Unfortunately, while the oscillator pulses pass through the amplifier system, the CEP stability degrades substantially, due to the variation of the dispersion of different optical elements caused by vibrations, thermal drifts or energy fluctuations of the pump lasers. To compensate for these additional accumulated CEP instabilities, an additional out-of-loop f-to-2f interferometer [11,12] was built and set up after the chirped mirrors (cf. Fig. 3.1).
In Fig. 3.5 the out-of-loop f-to-2f interferometer is illustrated. A small fraction of the NIR pulse (back reflection of the fused silica wedges) is focused into a 100 μm-thick BBO crystal generating the second harmonic of the NIR spectrum [231].

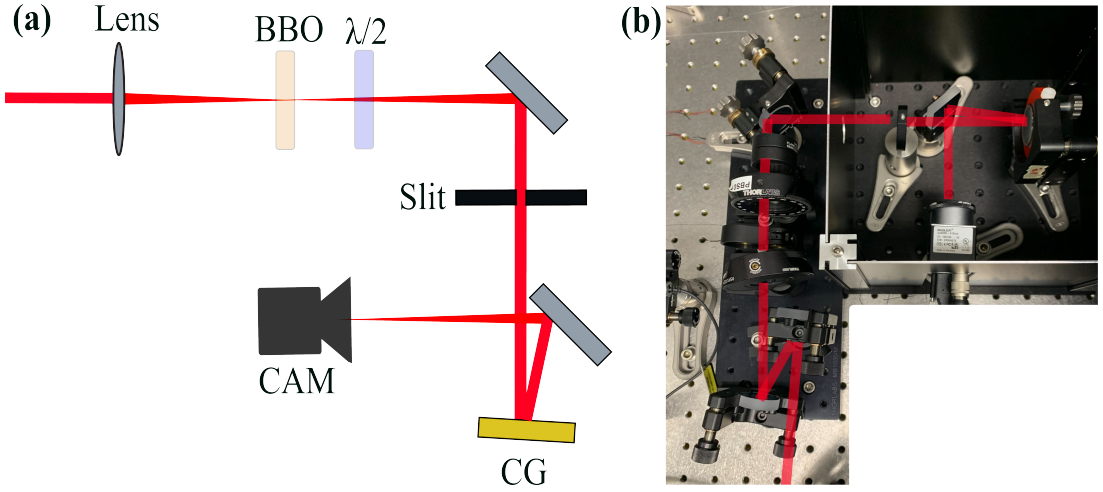

Figure 3.5: Schematic illustration of the f-to-2f interferometer, which was built to measure the carrier-envelope phase (CEP) of the NIR pulse at 1 kHz after the hollow-core fiber (HCF). (a) A small reflection of the NIR pulse is focused into a BBO crystal, and a $\lambda/2$-polarizer. A slit is then re-imaged by a concave grating (CG) into a camera (CAM). (b) Photo of the self-built f-to-2f interferometer.

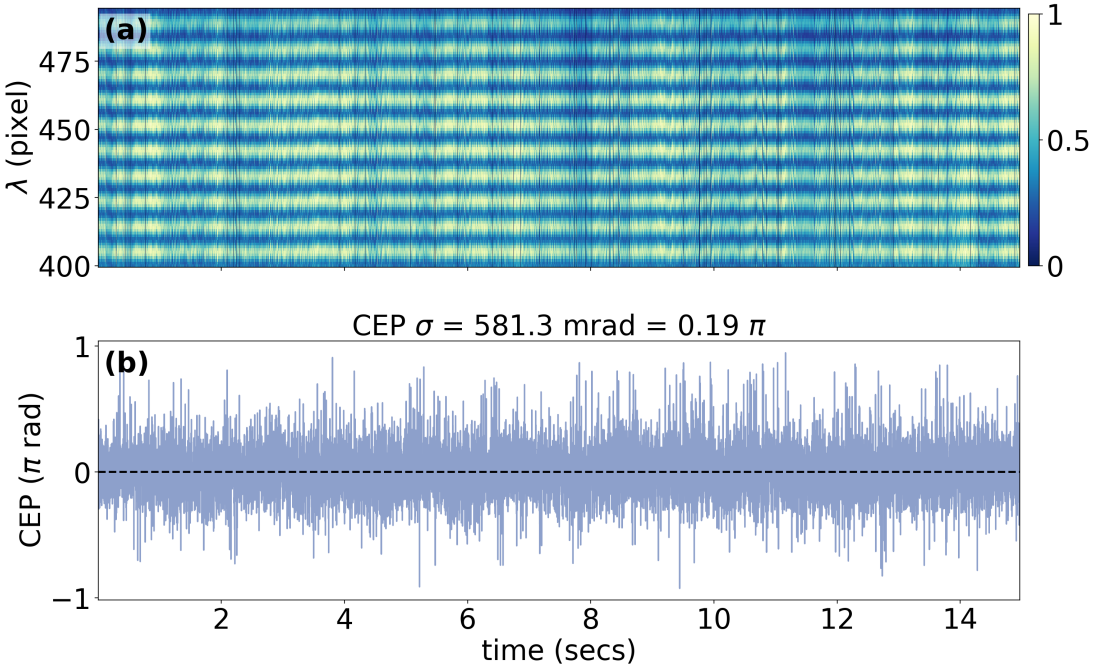

Figure 3.6: (a) Interference fringes of the fundamental and the second harmonic as a function of time. The vertical axis is given as pixel units of the camera, which corresponds in a linear way to the wavelength. (b) Values of the carrier-envelope phase (CEP) as a function of time, which result in an averaged CEP stability of $\sigma = 581.3$ mrad.

After the BBO a $\lambda/2$-polarizer is placed, which is necessary to match the polarization of the fundamental and second harmonic beam [232]. The two beams then pass a slit, and incident on a 320 l/mm concave grating (Zeiss, concave grating polychromator mounting, 264510-2951-624), which focuses both beams into a camera (Basler, acA800-510μm). The camera records CEP-dependent wavelength-resolved fringes (cf. Fig. 3.6 (a)), which emerge due to the interference of the fundamental and the second harmonic in the overlapping frequency region.
The spectrometer is self-built, since it allows to record images at a 1 kHz rate, which is usually not achievable with conventional spectrometers.
With the Takeda algorithm [233] the phase of the spectral fringes is measured shot-by-shot relative to a user-defined set point, which corresponds directly to the relative CEP of the NIR driving pulses according to Eq. 3.5. Thus, an error signal relative to an user-defined set value is generated, and is fed back to the DAZZLER using a feedback loop 234–236. This leads to the compensation of any CEP fluctuations, and the CEP is kept constant over time at a set value.

In Fig. 3.6 (b) the CEP is recorded shot-by-shot for a set value of $\Delta\varphi_{\text{set}} = 0$ over a duration of 15 s. The averaged CEP stability is $\sigma = 581.3$ mrad. The best stability achieved with this setup is $\sigma = 450$ mrad.

3.4 Passively and actively stabilized Mach-Zehnder interferometer

Performing experiments with multiple pulses in the XUV regime received increasing attention in the last years. The main challenge is to create pairs of XUV pulses, without loosing too much pulse intensity or increasing the pulse duration and remaining high phase-stability between the pulses. There are a couple of approaches in literature describing how to achieves this. In general, there are two main techniques, either the XUV beam can be split directly in two identical parts, or the NIR beam is split, and the pair is then used to generate two XUV beams via HHG.

The XUV beam can be split directly with a mirror pair [237–244], which leads to a small delay jitter between the two XUV pulses, since both beams share the same pathway. However, a sharp cut in the spatial profile compromises the quality of the focus, since the XUV beam is split by two halves of a mirror pair. In addition, the beams are non-collinear after the splitting leading to spatial fringes [245].

An alternative method is to split the NIR pulse before the HHG process, which can be done in several ways. A first example is the splitting of the NIR pulse by two pairs of birefringent wedges [246, 247]. The drawback of this method is that it is limited to $>$ 10-cycle pulses, due to the high dispersion difference of the e- and o-axes of the birefringent material.

NIR pulse pairs with shorter time duration can be achieved via spatial wavefront pulse shaping [248], however here the delay range is limited to a few optical cycles. LCD based 4f-line polarization pulse shaping [249] can lead to pulse pairs with a

delay range of up to 120 fs and a high phase-stability, i.e. a delay jitter of 300 zs (zeptoseconds). However, this method suffers from poor transmission, pixelation and satellite pulses, due to phase wrapping artifacts [250].

The easiest way to realize large delay ranges is with a Michelson or Mach-Zehnder interferometer [251–256]. However, the main challenge is to maintain a high phase-stability between the two pulses resulting in a phase-locked XUV pulse pair upon HHG.

In the following section, our self-built Mach-Zehnder interferometer (MZI) is presented, which is few-cycle compatible, has a variable delay range over 400 fs and a delay stability of under 10 as.
The here achieved interferometer with a combination of high stability and flexibility is at the forefront of what is currently feasible.

3.4.1 Technical description

One of the main features of the self-built MZI is the compatibility with few-cycle pulses. Therefore, the beamsplitters used to split the NIR beam and recombine the two pulses again, are custom low-dispersion ultrabroadband coated (Layertec) with a reflectivity $R = 50\,\%$ over a range of $440-1020$ nm, and a < 5 fs dispersion. Losses are reduced and residual surface bend due to unilateral stress to the glass are minimized by coating the backside of the beamsplitter with an antireflection-coating.

The system is passively and actively stabilized to achieve phase stability with attosecond precision between the two interferometer arms. Passive stabilization is introduced by building the interferometer on the smallest possible area on a breadboard measuring 200 by 200 mm. The interferometer arm length is only around ~ 50 mm. The interferometer is decoupled from the main laser table by attaching Viton O-rings at the underside of the MZI. As a consequence the MZI 'floats' on top of the table, which decouples the breadboard from any laser table vibrations around 100 Hz.

The retro-reflecting mirrors of arm A (cf. Fig. 3.7) are mounted on a time-delay stage (piezo stage PIHera P-620.10L, Physik Instrumente), which is attached to a thick stainless steel plate to increase the weight of the stage. Thus, the resonant frequency of the delay stage is shifted below dominant noise sources in the laboratory.

The retro-reflecting mirrors of arm B are mounted to a piezo stick-slip stage (SLC-1730-S, Smaract) with a range of 21 mm. Accordingly, the delay range is extended, and finding the overlap between the two arms becomes more convenient. In addition, a second SLC-1730-S stage in arm B at a 90 degree angle to the first stage gives the possibility to introduce and control a lateral beam offset between the two arms. The two arms can be overlapped with high precision, since the recombining beamsplitter is attached to a piezo mirror mount (Polaris-K05P2, Thorlabs).

The additional degree of freedom, due to the movable beamsplitter, allows for a non-collinear geometry by introducing an angle between the two arms [257]. The

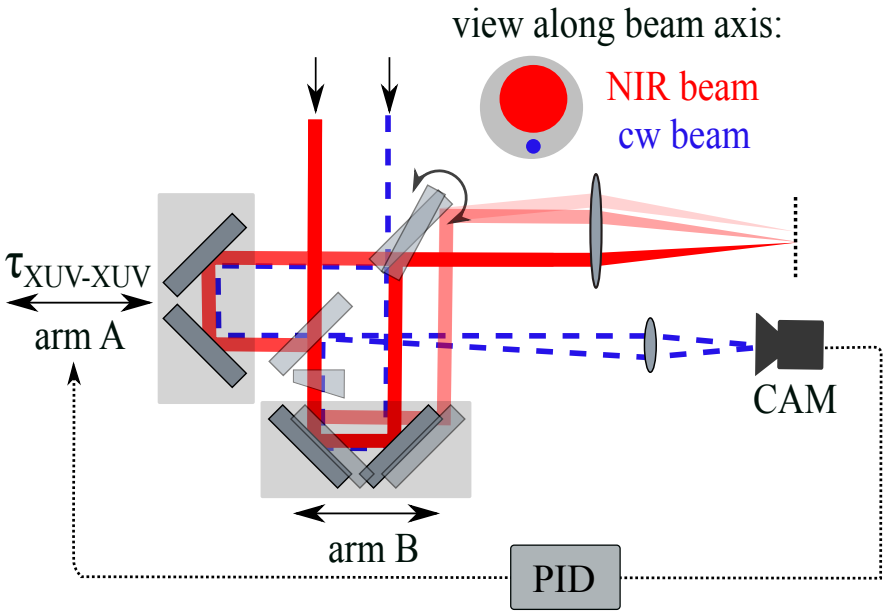

Figure 3.7: Passively and actively stabilized Mach-Zehnder interferometer (MZI) used to create two phase-locked NIR pulses. The two arms can be delayed relative to each other by a piezo stage in arm A (solid red line). A translation stage in arm B allows to control the lateral beam position. The overlap between the pulses is ensured by a second beamsplitter, which can also introduce a tilt angle between both beams, or can be used to operate the interferometer in a non-collinear manner (transparent red line). After the focusing element (here lens), a tilt angle in the beam becomes a lateral shift of the beam and vice versa. Below the NIR pulse a cw laser is co-propagating trough the MZI for active phase stabilization. A wedge placed in arm B introduces a fixed angle between the two cw beams leading to tilt fringes in the overlap, which are recorded by a CMOS camera (CAM). The phase drift is estimated, and a feedback signal is created, and is send to the delay stage in arm A.

combination of a controllable tilt angle with a lateral beam offset enables the adjustment of the angle between the two beams in the far field as well as in the focus. This allows one to switch easily between a collinear and non-collinear geometry, depending on the requirements of the current experiment. In the collinear geometry, for example, Fourier transform experiments with highest interference contrast can be performed. In the non-collinear geometry two independent foci in the HHG chamber can be created leading to two independent HHG sources for two source interferometry.

In conclusion, the flexibility of the MZI allows to perform a variety of interferometry experiments [258–261] and Fourier transform experiments [251–253,255,256]. In the work presented in this thesis, the MZI is always used in a collinear geometry.

3.4.2 Phase stability of NIR pulse pair

A short term delay stability of the pulse pair between $\sigma = 5$ and 10 as is achieved by passive stabilization. However, the delay will slowly drift over time, due to air currents as well as thermal effects, since the different optical elements in the MZI have different thermal expansion coefficients (cf. Fig. 3.8 (a)).

This is why active phase stabilization is introduced, which is achieved by a frequency stable cw laser (Cobolt Blues, Hübner Photonics) co-propagating through the interferometer (just below the NIR pulse) as an absolute path length reference.

The center wavelength of the cw laser is 473.36 nm with a linewidth of < 1 MHz, and a > 8 hours stability of < 1 pm (0.001 nm). The cw laser propagates through the interferometer in the opposite direction as the NIR beam, i.e. entering through the backside of the recombination beamsplitter and exiting through the beamsplitter the NIR pulse enters. The cw beam is reflected off and transmitted through the same optics (two beamsplitter, four silver mirrors) as the NIR pulse.

In arm B a wedge is placed at a 30 arcmin face angle just below the NIR beam to introduce a small angle α between both cw arms. This leads to a difference of the wavevectors in the x-direction $\Delta k_{x,cw} = k_{z,cw} \sin \alpha$, where $k_{z,cw}$ is the wavevector along the propagation direction of the laser beam. The plane of the wedge is re-imaged by a lens onto a CMOS camera recording the emerging tilt fringes. Accordingly, the beam is $\cos(\phi_\tau + \Delta k_{x,cw} x)$ modulated leading to spatial fringes, where ϕ_τ is the phase shift, which is due to a slow drift of the delay over time. Via FFT processing using the Takeda algorithm [233], the phase jitter term ϕ_τ can be extracted. This phase jitter leads to an error-signal, i.e. a phase difference to an user-defined set point. The error-signal is then send to a software proportional differential (PID) controller, which controls the delay $\tau_{\text{XUV-XUV}}$ (cf. arm A in Fig. 3.7).

To scan the time delay between the two NIR pulses, and accordingly the two XUV pulses, the set delay $\tau_{\text{XUV-XUV}}$ is converted to a phase $\phi_\tau = \tau_{\text{XUV-XUV}}/T_{\text{cw}} 2\pi$, where T_{cw} is the period of the cw laser. The piezo stage is moved slowly at a 20 Hz servo rate ensuring a continuously phase tracking, and avoiding any vibrations. The absolute time zero $\tau_{\text{XUV-XUV}} = 0$ is found by scanning the XUV spectrum as a function of $\tau_{\text{XUV-XUV}}$ before each experimental campaign.

To successfully sample an XUV spectrum up to $E_{\max} = 100$ eV a minimal delay stepsize of $\delta\tau_{\min} = \lambda_{\min}/2c = 20$ as (Whittaker-Nyquist-Shannon sampling theorem), i.e. a minimal wavelength of $\lambda_{\min} = 12.4$ nm is required. Accordingly, a delay stability with a 1-σ jitter of 10 as is aimed for. In the case of a 473 nm cw laser this corresponds to a phase stability of 40 mrad. The cw laser has a phase detection noise given by $\delta\phi = \pi/\sqrt{N/2} = 2\,\mu$rad, with $N = 5 \cdot 10^{12}$ being the per frame detected photons at a 1.5 kHz detection rate, and 3 mW laser power. This leads to a wavelength error of $\delta\lambda = 1$ pm, which can be converted to a delay error of $\Delta\tau\delta\lambda/\lambda = 0.8$ as for a delay range of $\Delta\tau = 400$ fs. Thus, any delay jitters due to the phase detection noise of the cw laser are negligible.

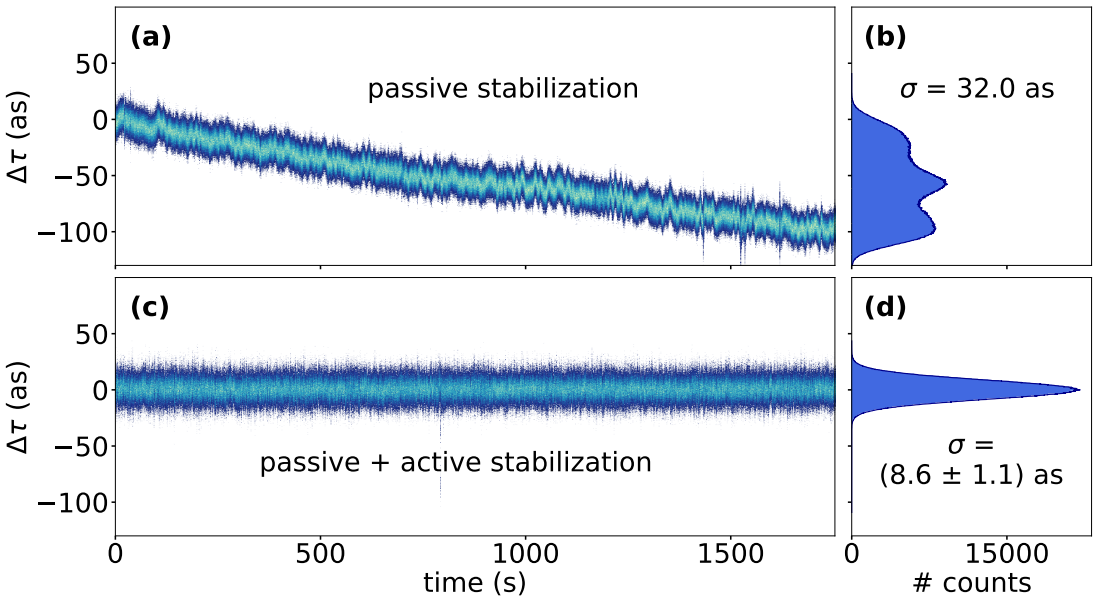

Figure 3.8: Investigation of the phase drift of the interferometer by measuring the cw fringes over time with (a) passive stabilization, and (c) passive + active stabilization of the Mach-Zehnder interferometer. (b) and (d) are the corresponding phase jitter histograms.

In Fig. 3.8 the fringe pattern of the cw beam is recorded for over half an hour to investigate the stability of the MZI in the case of the different stabilization schemes. In Fig. 3.8 (a) the interferometer is only passively stabilized resulting in a short term jitter of $\sigma < 10\,\text{as}$, however the delay drifts over many attoseconds in a short amount of time. Thus the overall delay jitter becomes $\sigma = 32\,\text{as}$. In Fig. 3.8 (b) the active feedback is turned on leading to a delay jitter of $\sigma = (8.6 \pm 1.1)\,\text{as}$ rms without any time-dependent drifts, and which is below the aimed for 1-σ jitter of 10 as.

In conclusion, the combination of the passive and active stabilization leads to an absolute phase-lock of 6 to 9 as rms. This phase-stability is kept stable for many hours of measuring, scanning over multiple delay points.

3.4.3 Stability and phase dependence of the XUV pulse pair

The two phase-locked NIR pulses propagating through the Mach-Zehnder interferometer are used to generate two phase-locked XUV pulses via HHG.
In Fig. 3.9 (a) and (b) the XUV spectra for two different delays $\tau_{\text{XUV-XUV}}$ are shown. The spectra exhibit the typical HHG features, i.e. broad peaks at an odd multiple of the NIR driving laser frequency. In addition the spectra show a $\cos(\omega_{\text{XUV}}\tau_{\text{XUV-XUV}})$-modulation, due to the interference of the two pulses, with a fringe period $\delta\omega_{\text{XUV}} = 2\pi/\tau_{\text{XUV-XUV}}$ inversely proportional to the time delay (cf. sect. 5.1). Note, that the fringe contrast is reduced by the limited resolution of the XUV spectrometer, especially at higher photon energies. For a photon energy

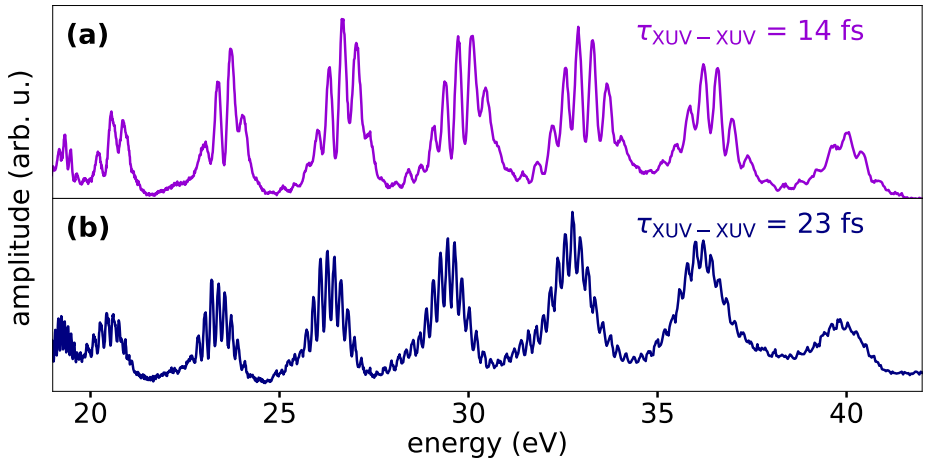

Figure 3.9: a) and (b) XUV spectra for two different XUV-XUV time delays, which are measured with the XUV spectrometer.

of 12.36 eV the resolution is approximately 25 meV, and becomes lower for higher photon energies [206].

To validate that the high phase stability between the two NIR pulses is remained throughout the HHG process, the phase jitter of the XUV fringes for a delay of $\tau_{\text{XUV-XUV}} = 26.5\,\text{fs}$ is investigated over time (cf. Fig. 3.10 (a)). The phase, i.e. delay jitter of each harmonic is extracted using the Takeda algorithm [233]. In Fig. 3.10 (b) the retrieved delay values are shown for the harmonics $q = 17 - 27$. The corresponding standard deviations are $\sigma = 5.7, 5.9, 7.4, 5.7, 6.9, 5.5\,\text{as}$, which result in an averaged delay jitter of $\sigma = (6.2 \pm 0.7)\,\text{as}$. As expected the dynamics of the delay values as a function of the acquisition time are in good approximation the same for all harmonics. Accordingly, this measurement validates that the high phase stability of the two NIR pulses remained throughout the HHG leading to a phase-locked XUV pulse pair.

Furthermore, the phase dependence of the XUV pulse pairs on the phase of the two NIR pulses is investigated. The two interfering NIR pulses create two interfering XUV pulses, according to

$$E_{\text{NIR,A}}(t)e^{i\phi_{\text{NIR,A}}} + E_{\text{NIR,B}}(t)e^{i\phi_{\text{NIR,B}}} \longrightarrow E_{\text{XUV,A}}(t)e^{i\phi_{\text{XUV,A}}} + E_{\text{XUV,B}}(t)e^{i\phi_{\text{XUV,B}}}, \tag{3.6}$$

where $E_{\text{NIR,A}}(t)$ and $E_{\text{NIR,B}}(t)$ are the NIR electric fields, and $E_{\text{XUV,A}}(t)$ and $E_{\text{XUV,B}}(t)$ are the electric fields of the two XUV pulses.

In the HHG medium the driver NIR laser and the generated harmonics move with different phase velocities, since $v_{\text{phase}} = \lambda\nu = \omega/k$, where k is the wavevector. Thus, the phase velocity of the NIR pulse is given by $v_{\text{NIR}} = \omega_{\text{NIR}}/k_{\text{NIR}}$, and accordingly for the q-th harmonic the phase velocity is $v_q = \omega_{\text{q,XUV}}/k_q = q\omega_{\text{NIR}}/k_q$. To create attosecond XUV pulses, all rays of XUV light generated at different positions in the HHG medium have to interfere constructively. Accordingly, the phase matching condition $\Delta k_q = k_q - qk_{\text{NIR}} = 0$ has to be fulfilled [189]. Thus, the phases $\phi_{\text{XUV,A/B}}$ of the two XUV pulses depend on the phases $\phi_{\text{NIR,A/B}}$ of the

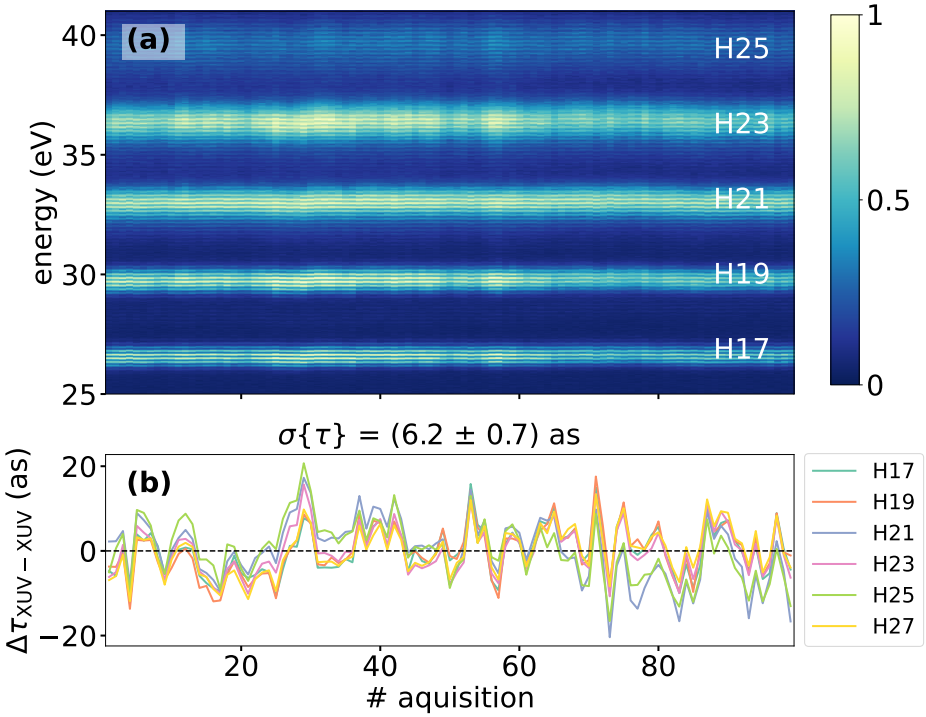

Figure 3.10: XUV pulse pair phase stability validated by measuring the XUV spectra over time. (a) XUV pulse spectra at a delay of $\tau_{\text{XUV-XUV}} = 26.5\,\text{fs}$ acquired for a set of 100 images averaged over 5 s. (b) Delay jitter of each harmonic q, which are extracted with the Takeda algorithm.

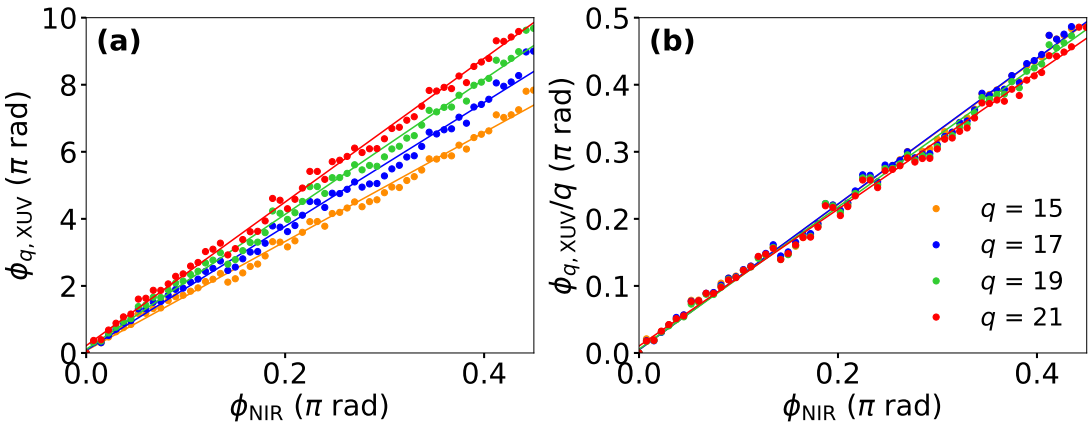

Figure 3.11: Experimental test of the phase transfer from the NIR pulses to the XUV pulses. (a) Phase change of the different harmonic orders $\Delta\phi_{q,\text{XUV}} = \phi_{q,\text{XUV,A}} - \phi_{q,\text{XUV,B}}$ by scanning the NIR phase ϕ_{NIR} over a range of $0.45\,\pi$rad. The measured data points $\Delta\phi_{q,\text{XUV}}$ are given as dots and the linear fit is shown as a line. (b) Phase of the different harmonics normalized by the harmonic order q.

NIR pulse pair according to $\phi_{q,\mathrm{XUV,A/B}} = q \times \phi_{\mathrm{NIR,A/B}}$. A delay scan between the two NIR pulses, i.e. a scan of the NIR phase $\Delta\phi_{\mathrm{NIR}} = \phi_{\mathrm{NIR,A}} - \phi_{\mathrm{NIR,B}}$ leads to a phase difference between the two XUV pulses $\Delta\phi_{q,\mathrm{XUV}} = \phi_{q,\mathrm{XUV,A}} - \phi_{q,\mathrm{XUV,B}}$ for each delay point $\tau_{\mathrm{XUV\text{-}XUV}}$.

The phase values $\phi_{q,\mathrm{XUV}}$ can be extracted for the harmonics individually, which is shown in Fig. 3.11 (a). As the NIR phase increases, i.e. for longer $\tau_{\mathrm{XUV\text{-}XUV}}$, the phases of the harmonics also increase, and the slopes become steeper for higher harmonic orders q. In Fig. 3.11 (b) the order normalized harmonic phases $\phi_{q,\mathrm{XUV}}/q$ are plotted showing that the phase ϕ_{NIR} of the NIR pulse is transferred to the q-th harmonic according to $\phi_{q,\mathrm{XUV}} = q \times \phi_{\mathrm{NIR}}$. The linear fits shown in Fig. 3.11 (b) result in slopes of $1.084, 1.087, 1.060, 1.020$ for the harmonics $q = 15$ to 21. As expected the slopes are close to 1. This validates the phase dependence of the XUV pulse pair on the phase of the NIR pulse pair.

3.5 Velocity map imaging spectrometer

In the experiments presented in this thesis, atomic and molecular dynamics are investigated. Accordingly, the setup needs to provide the possibility to measure the momenta of photoelectrons and ions. As described in section 3.1 this is realized by a velocity map imaging (VMI) spectrometer [6]. Detailed descriptions of the given VMI can be found in [162, 262].
The gas target of interest is ionized by the XUV+NIR pulses in the focus in the center of the VMI chamber (cf. Fig. 3.12). The charged particle exhibit a three-dimensional (3D) distribution, which is projected via an electrostatic lens onto a 2D detector. The VMI imaging apparatus consists of an repeller and extractor electrode, as well as a flight tube. The repeller has an incorporated $50\,\mu$m diameter nozzle [221], which provides the gas target (cf. Fig. 3.1).
The gas nozzle is pulsed, i.e. opens and closes at the same frequency as the laser pulses arrive, providing a fresh target for each laser shot. An electrostatic lens is achieved by applying voltages to the electrodes. By changing the polarity of the voltages, either the ions or photoelectrons are detected.
To protect the trajectories of the charged particles from distortion due to external magnetic fields, the system is covered with a μ-metal shield.
The charged particle detector consists of a dual micro-channel plate (MCP) stack as an particle amplifier, a phosphor screen, and a USB3 CMOS camera, which records the position of the particle impact. The MCP consists of a 1 mm thick dielectric plate with many small channels leading in a small angle from the one side to the other side of the plate [263]. The channels are made out of an electrical resistant material, mostly glass with semiconducting walls. In addition, a 1 kV accelerating voltage is applied at the front and back side of the MCP. If a charged particle incidents on one of these channel walls an avalanche of secondary electrons is produced. The amplified signal then interacts with a phosphore screen and the resulting fluorescence signals are recorded by a camera.
From the recorded 2D projection of the charged particles, the 3D momentum distribution can be retrieved with an inverse-Abel transform [14], since it is cylin-

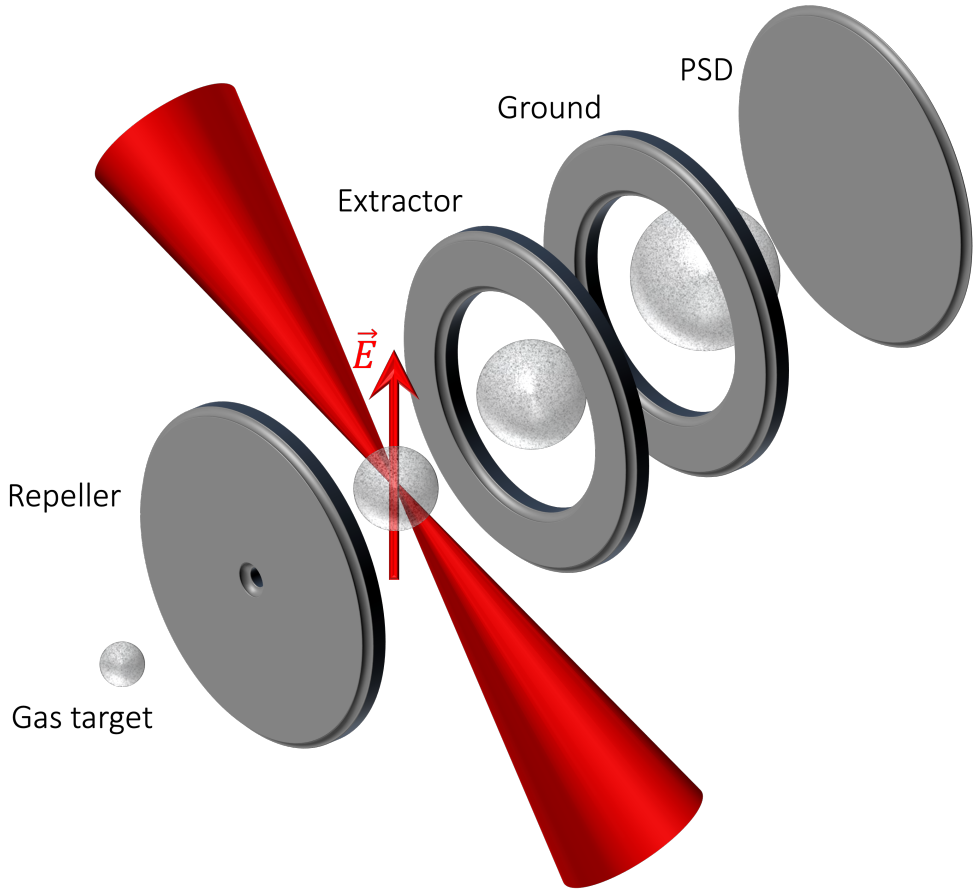

Figure 3.12: Schematic illustration of the VMI imaging system. A gas target is ejected through a repeller integrated nozzle into the VMI chamber, where the gas is ionized by the laser beam. Depending on the polarity of the voltages applied to the repeller and extractor electrodes, either the ions or photoelectrons are accelerated towards a phosphor detector (PSD), i.e. MCP + phosphor screen, re-imaging the 3D velocity distribution of the particles onto a 2D detector.

drically symmetric, and the symmetry axis is parallel to the laser polarization, which is in the plane of the detector.

3.5.1 Abel inversion

The wave function of an hydrogen-like atom, i.e. an atom with a single valence electron can be described as [132]

$$\Psi_{nlm}(r,\theta,\phi) = R_{nl}(r)Y_{lm}(\theta,\phi), \tag{3.7}$$

where R is a radial function, Y_{lm} are spherical harmonics of degree l and order m. The polar angle θ can take values between 0 and π, whereas $0 \leq \phi \leq 2\pi$. The principle quantum number is given by $n = 1, 2, 3...$, with the orbital angular momentum of $l = 0, 1, 2, ..., n-1$. The magnetic quantum number m, i.e. the

projection of the orbital angular momentum on the z-axis can take values between $m = -l, ..., l$.
It should be noted that the Schrödinger equation $\mathbf{H}\Psi = E\Psi$ can only be solved exactly for hydrogen-like atoms, and thus systems with multiple electrons or atoms require approximation methods (e.g. Hartree-Fock method [264–266]).

In multi-photon ionization processes the angular distribution of an ion or photoelectron momentum can be described as a superposition of Legendre polynomials [267–271]. This gives a direct physically meaningful interpretation, since Legendre polynomials are spherical harmonics with $m = 0$. The magnetic quantum number can be set to zero, since the 3D momentum distribution is cylindrically symmetric. The order of the multi-photon process determines the highest order of the polynomial involved [270].

Accordingly, the cylindrically symmetric 3D momentum distribution of the charged particles is given by

$$P_{3D}(v_{3D}, \cos(\theta_{3D})) = 2\pi v_{3D}^2 \sum_L \alpha_{3D,L} P_L(\cos(\theta_{3D})), \tag{3.8}$$

where $P_L(\cos(\theta_{3D}))$ is the L-th order Legendre polynomial, v_{3D} is the velocity, and θ_{3D} is the angle between the particles velocity and the laser polarization direction. The coefficient $\alpha_{3D,L}$ depends on the dynamics of the photoionization process, the atomic or molecular orbital, the spatial distribution of the sample and the photoionizing energy. [267–271]

The velocity distribution is given by

$$P_{3D}(v_{3D}) = 4\pi v_{3D}^2 \alpha_{3D,L=0}, \tag{3.9}$$

where $\alpha_{3D,L=0}$ is the angle-integrated coefficient, and the kinetic energy distribution is

$$P_{3D}(E_{3D}) = (4\pi/m) v_{3D} \alpha_{3D,L=0}, \tag{3.10}$$

where m is the mass.

The angular distribution is given by higher order Legendre polynomials, and is expressed by the so called anisotropy or asymmetry parameter $\beta_{L,v_{3D}}$, i.e.

$$\begin{aligned} \beta_{2,v_{3D}} &= \alpha_{3D,L=2}/\alpha_{3D,L=0} \\ \beta_{4,v_{3D}} &= \alpha_{3D,L=4}/\alpha_{3D,L=0} \\ \beta_{6,v_{3D}} &= \alpha_{3D,L=4}/\alpha_{3D,L=0} \\ &\vdots \end{aligned} \tag{3.11}$$

For example, β_2 can have values between $[-1, 2]$ [269, 270], where $\beta_2 = -1$ corresponds to a particle ejection orthogonal to the laser polarization, $\beta_2 = 0$ presents an uniformal emission, and $\beta_2 > 0$ results from an emission along the laser polarization. Odd-order asymmetry parameters can occur when for example the ionizing pulses are circularly polarized or the molecule under investigation is chiral [270].

The 2D momentum distribution can be expressed in the same manner, and is related to the 3D distribution by means of a matrix multiplication [272]:

$$\begin{aligned} \vec{b}_{2D} = &\quad \mathbf{M} \cdot \vec{a}_{3D} \\ \vec{a}_{3D} = &\quad \mathbf{M}^{-1} \cdot \vec{b}_{2D} \end{aligned} \tag{3.12}$$

Note that the matrix $\mathbf{M}$ only depends on the maximum value of the velocity $v_{2D/3D}$, i.e. the 2D/3D radius of the VMI images (the number of pixels from the center of the image ($v = 0$) to the edge ($v = max$)) and the highest occurring Legendre order L_{max}. Consequently, the matrix $\mathbf{M}$ has to be determined only once and can be used for all subsequent inversions.

In most of the experiments presented in this thesis, the algorithm rBASEX [273, 274] is used to invert the recorded VMI images.

chapter 4

Isolated attosecond pulses

In this chapter, a more detailed overview of the steps necessary to generate isolated attosecond pulses (IAPs) is given. In particular, the occurring challenges are emphasized by explaining how dispersion as well as the carrier-envelope phase (CEP) of the driving NIR pulses affects the generation of IAPs. In the last section, a pump-probe scheme is presented, which allows one to verify if an IAP is successfully created.

As described in detail in section 2.2.2, HHG leads to the emission of an attosecond pulse every half-cycle of the driving pulse. The interference of multiple attosecond pulses in a train results in distinct harmonics in the frequency domain at odd-multiple of the driver frequency. However, some experiments require a single isolated attosecond pulse (IAP) with a continuous spectrum over a large bandwidth.

In general, there exist different methods of IAP generation. Firstly, the driving laser pulse can be compressed close to a single-cycle. If the electric field strength exceeds the ionization potential of the atom only once, one attosecond pulse is generated at the maximum of the driving pulse. This can be achieved by shaping the driving pulse cosine-like (cf. Fig. 3.4). Accordingly, stabilizing the CEP is crucial, since $\Delta\varphi_0 = \pi/2$ would lead to a sine-shaped pulse, and thus to the emission of two attosecond pulses. This so called cut-off method was first demonstrated in [275–277].
In the following years other methods were discovered, which allow to use driving pulses with longer pulse duration. The first example is polarization gating [278–282]. In this case the initially linear polarized pulse is split by a quartz plate into two delayed and orthogonal polarized pulses. A $\lambda/4$-plate then creates two elliptically polarized pulses with opposite helicity. In general circular polarized light can not generate harmonics, because the freed photoelectrons will never

come back to the ions. However, an elliptically polarized field exhibits exactly one linearly polarized cycle, which can generate an IAP.
The main problem of the cut-off method, and of polarization gating is the low efficiency, and the corresponding low XUV intensity.
Slightly more efficient methods are double optical gating [283], generalized double optical gating [284], and attosecond lighthouse effect [285].
Another scheme is ionization gating [286–290], which confines the XUV pulse generation to the leading edge of the pulse by highly ionizing the HHG gas medium when the driving pulse intensity becomes sufficiently large. The time-dependent intensity increase at the beginning of the driving pulse induces a steady increase of the ionization level in the HHG gas, which at one point rises above the critical level for HHG. This leads to a loss of phase-matching [291], and thus a suppression of HHG at that point.
A comparison of the IAP, and driving NIR pulse properties between the different generation methods can be found in [292].

In this thesis, the NIR driving pulses are compressed close to single-cycle, i.e. to 3.2 fs centered at 770 nm. The CEP is stabilized to ensure a cosine-shape, leading ideally to the generation of a single IAP emitted at the maximum of the NIR electric field. In addition, the NIR intensity is high enough to highly ionize the HHG gas medium, and thus ionization gating is achieved suppressing the HHG generation after the maximum of the NIR pulse envelope.

4.1 Dispersion dependency of XUV pulse

Few-, and especially single-cycle pulses are extremely sensitive to small dispersion changes in the beam path. Accordingly, before every measurement the dispersion in the beam path has to be adjusted to ensure a NIR driving pulse with zero GDD, and thus a NIR pulse duration of around 3.2 fs.

This is achieved by measuring the XUV spectra ($\tau_{\text{XUV-XUV}} = 0\,\text{fs}$) as a function of the position of the fused silica wedges relative to each other (cf. Fig. 3.1). The position of the first wedge is fixed, whereas the second wedge is attached to a motorized stage, which allows to move the position of the second wedge parallel to the first one. Accordingly, by scanning the position of the wedges the amount of fused silica the NIR pulse has to propagate through is de- or increasing.

In Fig. 4.1 the XUV spectrum ($\tau_{\text{XUV-XUV}} = 0\,\text{fs}$) as a function of the wedge position is shown. When the wedge position is increase, the second wedge moves out of the beam path, and the amount of fused silica is decreased. The fused silica wedges have an angle of 2.48°, and thus a position change of +1 mm decreases the amount of fused silica by 0.04 mm leading to a GDD decrease of $1.54\,\text{fs}^2$ for a 770 nm beam.

In Fig.4.1 (a) it can be seen that the cutoff energy, the intensity and the continuity of the spectrum strongly depends on the wedge position, i.e. the amount of fused silica, and thus the induced GDD. If the NIR pulse is properly compressed the GDD is zero, the pulse is close to a single-cycle pulse, and thus only one IAP

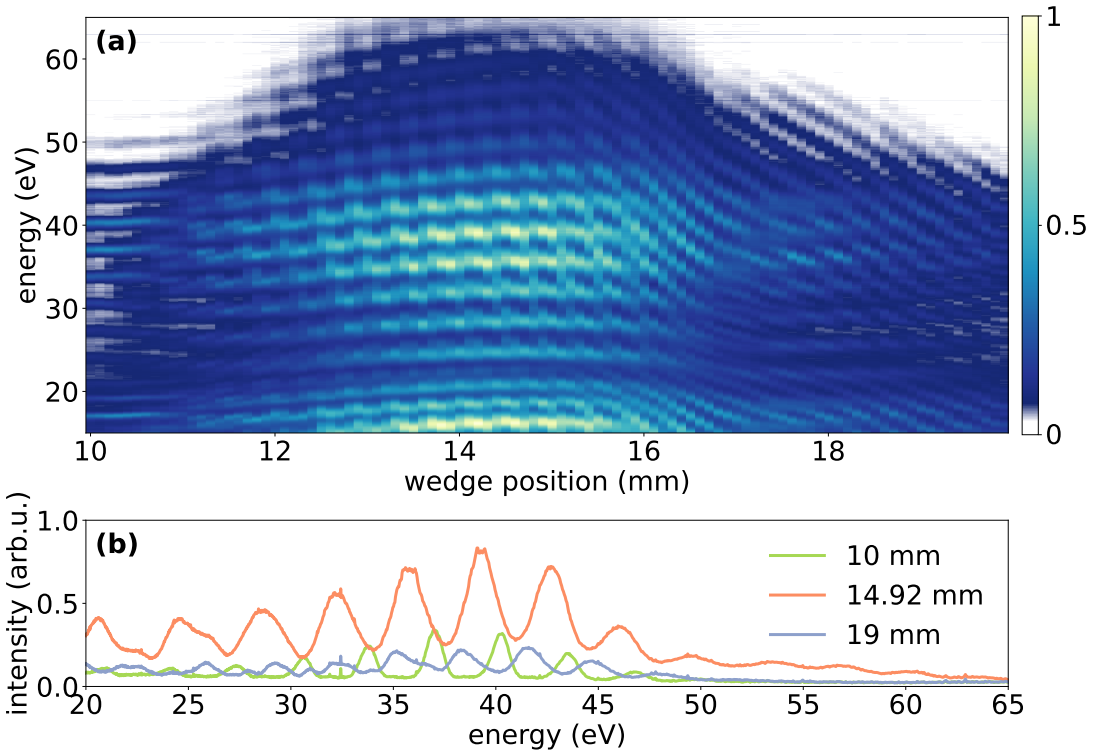

Figure 4.1: XUV spectra as a function of the wedge position, i.e. the amount of fused silica in the NIR beam path, which controls the NIR pulse compression and IAP (isolated attosecond pulse) generation, respectively. (a) Dependence of the XUV cutoff, spectral shape and intensity on the induced GDD (group delay dispersion) by increasing or decreasing the amount of fused silica in the beam path (increase of wedge position correspond to a decrease of the amount of fused silica). (b) XUV spectra for three different wedge positions. A position of 10 mm (green) correspond to a positively chirped NIR driving pulse, 14.92 mm (orange) a non-chirped pulse, and 19 mm (blue) a negatively chirped pulse.

is generated at the maximum of the driving pulse during HHG. This leads to a continuous XUV spectrum with a high cutoff energy.

In Fig.4.1 (b) the XUV spectra for three different wedge positions are shown. The best pulse compression is achieved for a wedge position of 14.92 mm, leading to a continuous spectrum with a high cutoff energy of around 65 eV. On top of the continuous spectrum harmonic peaks are observable for an energy ≤ 50 eV, which is due to the interference with a small pre-IAP. The magnitude of the second IAP is small enough to not sufficiently influence any experimental results. A fringe contrast of 50% already occurs, when the second IAP has a peak intensity of 5% of the main IAP.

At a wedge position of 10 mm the amount of fused silica is maximal, the NIR driving pulse is positively chirped, and the XUV spectrum exhibits distinct harmonics. The XUV intensity is substantially decreased and the cutoff energy is

much lower compared to the non-chirped case, since the chirp increased pulse duration results in a much smaller maximum electric field peak amplitude [293].

At a position of 19 mm the fused silica amount is minimal, the NIR driving pulse is negatively chirped leading to a continuous spectrum with a low intensity.

The dependence of the harmonic's bandwidth on the sign of the chirp has been studied in [293–296], and its origin can be found in the *harmonic chirp* [297]. As described above, HHG occurs at every half-cycle of the NIR driving pulse. If the driving pulse is positively chirped, the pulse frequency ω_{NIR} and the intensity I_{NIR} increase in time. Accordingly, the ponderomotive potential given by Eq. 2.32, i.e. $U_p \sim I_{\mathrm{NIR}}/\omega_{\mathrm{NIR}}^2$ stays constant over the duration of the pulse, and the harmonics are always emitted around the center of each NIR half-cycle. The interference of all attosecond pulses with constant phase relations between individual harmonics in consecutive pulses, lead to narrow harmonic peaks in the frequency domain. If however the pulse is negatively chirped, the frequency decreases while the intensity increases in time. As a consequence Eq. 2.32 increases over the duration of the pulse, and the harmonics are emitted earlier in time with increasing NIR half-cycle order. The interference of all pulses, which now have a decreasing phase relation between individual harmonics in consecutive pulses, result in broad harmonics in the frequency domain.

4.2 Carrier-envelope phase dependency of XUV pulse

Once the NIR pulse is properly compressed, the CEP value has to be set, and kept stable, so that a cosine-shaped NIR pulse is given at all times. In Fig. 4.2 the XUV spectrum ($\tau_{\text{XUV-XUV}} = 0\,\mathrm{fs}$) is shown as a function of the set CEP value $\Delta\varphi_0$, which is controlled by the DAZZLER as described in section 3.3. The XUV cutoff energy alternates as a function of the CEP repeating whenever the CEP changes by π.

The highest harmonic energy emitted at an half-cycle of the NIR driving pulse is called half-cycle cutoff (HCO) energy, which depends on the NIR electric field strength at that particular half-cycle (cf. Eq. 2.32) [286,291,298,299]. The highest cutoff energy overall emerges at the half-cycle at the maximum of the NIR pulse envelope, leading to a photon energy Ω_{max} according to Eq. 2.31. Neighboring half-cycles produce photons with a lower cutoff energy, i.e. $\Omega < \Omega_{\mathrm{max}}$.

In Fig. 4.2 at a CEP of $\Delta\varphi_0 = 0$ the XUV spectrum exhibits the highest cutoff energy. Thus, the NIR driving pulse is cosine-shaped exhibiting one dominant half-cycle at the maximum of the NIR pulse envelope, which generates one IAP with a maximal harmonic cutoff energy Ω_{max}. In contrast, at $\Delta\varphi_0 = \pi/2$ the NIR driving pulse is sine-shaped exhibiting two prominent half-cycles with less electric field strength compared to the former case, which leads to XUV photons with an energy according to $\Omega_{\mathrm{min}} < \Omega_{\mathrm{max}}$. Thus, by changing the CEP the HCO is gradually altered between the two extrema $\Omega_{\mathrm{min}} \leq \Omega \leq \Omega_{\mathrm{max}}$.

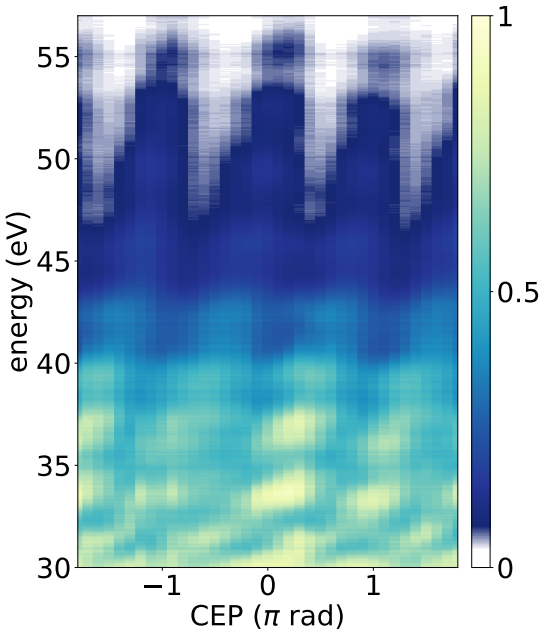

Figure 4.2: XUV spectrum ($\tau_{\text{XUV-XUV}} = 0\,\text{fs}$) as a function of the carrier-envelope phase (CEP) to illustrate the dependence of the harmonic cutoff energy on the sub-cycle evolution of the NIR driving pulse.

In general, a measurement of the shift of the individual HCOs as a function of CEP allows one to determine the time-dependent ponderomotive potential U_p over a portion of the driving laser pulse, and thus the driver pulse duration, and intensity can be retrieved, which was demonstrated in [286, 291, 298, 299].

4.3 Attosecond pulse streaking vs RABBITT

To clarify once and for all if an IAP or an APT is generated, a pump-probe experiment in a neutral atom can be performed. The atom is ionized by absorption of 1-XUV-photon, leading to photoelectrons with a kinetic energy distribution depending on the initial XUV spectrum. Subsequently, the photoelectrons interact with a time-delayed NIR probe pulse, alternating the kinetic energy of the photoelectron.

RABBITT [301–303] Assumingly the XUV beam is an attosecond pulse train (APT) with distinct individual harmonics in the frequency domain. Consequently, the photoelectrons after XUV ionization have a distinct kinetic energy distribution following the shape of the XUV spectrum according to

$$E_{\text{e}^-,\text{XUV}} = \hbar\omega_q - \text{IP}, \tag{4.1}$$

where $q = 2n \pm 1$ is the harmonic order, with n as an integer. These contributions are called *harmonic bands* (cf. Fig. 4.3 (a)).

The interaction with the NIR pulse during the temporal overlap of both pulses leads to a shift of the photoelectron energy, and to the appearance of so called

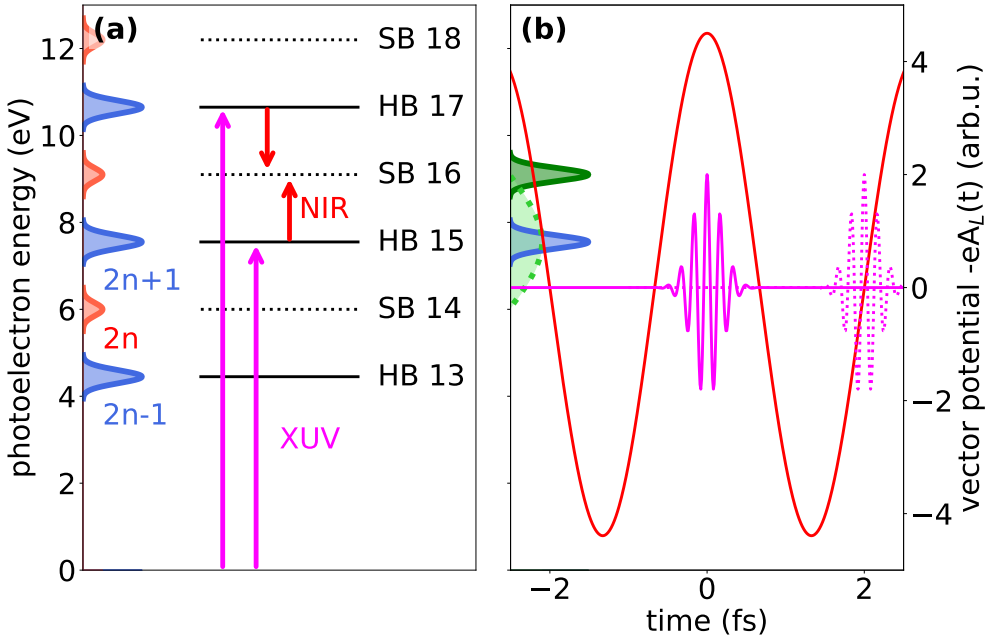

Figure 4.3: Schematic illustration of a (a) RABBITT measurement, and (b) streaking measurement. In (a) an attosecond pulse train (APT) ionizes neutral argon atoms leading to a photoelectron yield (blue peaks) with an energy distribution following the XUV spectrum. Accordingly, harmonic bands (HB) at an energy of $E_{2n\pm1} = \hbar\omega_{2n\pm1} - \mathrm{IP}$ appear due to XUV ionization (argon ionization potential $\mathrm{IP_{Ar}} = 15.7\,\mathrm{eV}$ [300]). The interaction of the system with the NIR probe pulse leads to the absorption or emission of a NIR photon ω_{NIR} by the photoelectron. Accordingly sidebands (SB) emerge, i.e. photoelectron contributions at an energy of $E_{2n} = \hbar\omega_{2n} - \mathrm{IP}$ (red peaks). The interference of two quantum pathways resulting in the same SB induces a $\tau_{\mathrm{XUV\text{-}NIR}}$-dependent oscillation of the photoelectron yield with a period given by the cycle period of the NIR probe pulse. In (b) the argon atom is ionized by an single isolated attosecond pulse (IAP). When the XUV pulse coincides with the maximum of the NIR vector potential (purple solid line), i.e. a zero-crossing of the electric field, the photoelectron yield generated by XUV ionization (blue peak) is shifted to higher energies (green peak). In contrary, when the XUV is temporally overlapped with a zero-crossing of the vector potential (purple dashed line), the initial photoelectron energy distribution (green peak) is broadened (light green peak).

sidebands (SB) at a kinetic energy of

$$E_{\mathrm{e}^-,\mathrm{XUV+NIR}} = \hbar\omega_{2n} - \mathrm{IP}, \tag{4.2}$$

with n as an integer. The SB are located energetically in between two harmonic bands $q_1 = 2n + 1$, and $q_2 = 2n - 1$. The signal of the SB oscillate as a function of the pump-probe delay $\tau_{\mathrm{XUV\text{-}NIR}}$ with a period $T = \pi/2\omega_{\mathrm{NIR}}$ given by the fundamental of the NIR probe pulse ω_{NIR}. The SB oscillate, due to the interference of two quantum pathways ($E_{2n+1} - \hbar\omega_{\mathrm{NIR}}$, and $E_{2n-1} + \hbar\omega_{\mathrm{NIR}}$) resulting in photoelectrons with the same kinetic energy E_{2n}. This is illustrated schematically in Fig. 4.3 (a).

This pump-probe technique is called RABBITT (Reconstruction of Attosecond Beating By Interference of Two photon Transitions), which allows to retrieve the underlying pulse properties of an APT, as the relative phase and intensity between the harmonics can be extracted [301–303].

Attosecond streaking [276, 304–307] In contrary, if the XUV beam is a single isolated attosecond pulse (IAP), the photoelectron kinetic energy spectrum is continuous after XUV ionization, and an interaction with the NIR pulse can lead to the following:

At $\tau_{\mathrm{XUV\text{-}NIR}}$, where the IAP is temporally overlapped with a zero-crossing of the NIR electric field (maximum of vector potential), the photoelectron yield is shifted to higher energies by the amount associated with the change in the photoelectron momentum at the detector, i.e.

$$p_{\mathrm{e}^-,\mathrm{XUV+NIR}} = p_{\mathrm{e}^-,\mathrm{XUV}}(t) - eA_{\mathrm{NIR}}(t), \tag{4.3}$$

where $A_{\mathrm{NIR}}(t)$ is the vector potential of the electromagnetic field of the NIR pulse, which is related to its electric field $F_{\mathrm{NIR}}(t)$ as follows: $F_{\mathrm{NIR}}(t) = -\partial A_{\mathrm{NIR}}(t)/\partial t$. Further, e is the corresponding unit vector, and $p_{\mathrm{e}^-,\mathrm{XUV}}$ is the photoelectron momentum after ionization by the XUV pulse (cf. Fig. 4.3 (b)). Thus, ionization at the zero-crossing of the electric field corresponds to the maximum of the vector potential, and the maximum shift in the photoelectron velocity and energy at the detector.

However, at a temporal overlap of the IAP with a maximum of the NIR electric field (zero-crossing of vector potential) leads to an increase of the bandwidth of the photoelectron energy. In this case the photoelectrons before the maximum of the electric field (zero-crossing of vector potential) are decelerated, and the photoelectrons after the maximum (zero-crossing) are accelerated, thus the bandwidth of the photoelectron energy distribution is increased without shifting its initial energy.

This pump-probe scheme is called attosecond streaking, which allows to retrieve the CEP, intensity and chirp of an IAP [276, 304–307].

In the following experiment, the goal is not to fully reconstruct the temporal XUV pulse structure, but rather to investigate the influence of the CEP on HHG. If

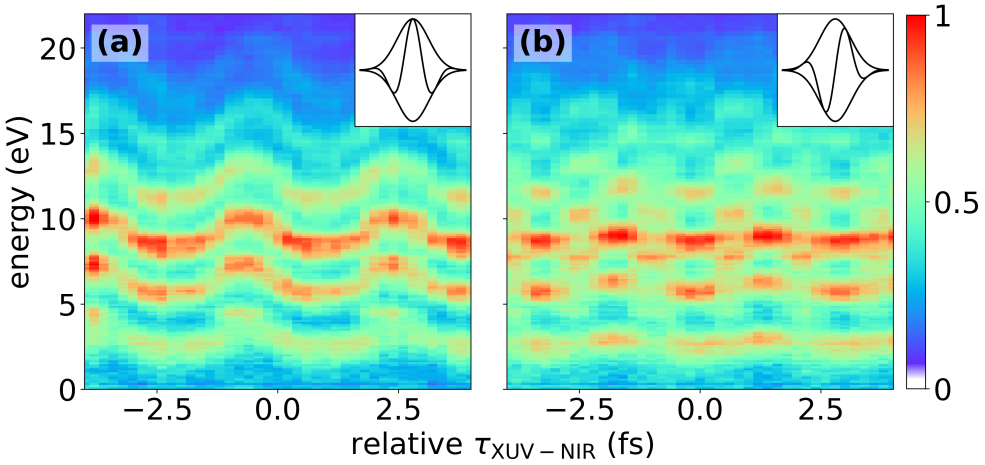

Figure 4.4: Photoelectron yield created by ionizing argon atoms with only XUV pulse A for two different settings of the carrier-envelope phase (CEP), i.e. (a) $\Delta\varphi_0 = 0$, and (b) $\Delta\varphi_0 = \pi$. A NIR probe pulse (25 fs pulse duration, centered at 800 nm with a bandwidth of 40 nm) interacts with the photoelectrons after $\tau_{\text{XUV-NIR}}$ alternating their kinetic energy. The photoelectrons are recorded with the VMI spectrometer averaging over 5000 laser shots. The raw VMI images are Abel inverted using rBASEX [273, 274] for a delay range of over 8 fs with a stepsize of 0.2 fs. The CEP stability is 550 mrad. The inset of the images show in (a) a cosine-, and (b) sine-shaped NIR pulse with a pulse duration of 3.2 fs centered at 800 nm, leading to an (a) IAP and (b) APT, respectively.

the photoelectron spectrum as a function of $\tau_{\text{XUV-NIR}}$ exhibits the same dynamic as in a streaking measurement, the NIR pulse is cosine-shaped, and a single IAP is generated. In contrast, if the photoelectron spectrum shows the same behavior as in a RABBITT measurement, an APT is generated, and accordingly the NIR driving pulse is sine-shaped.

In Fig. 4.4 the photoelectron spectrum emerging due to the XUV ionization (using only one of the XUV pulses, i.e. pulse A) of neutral argon gas as a function of $\tau_{\text{XUV-NIR}}$, and the kinetic energy is shown for two different CEP settings. In Fig. 4.4 (a) the CEP is set to $\Delta\varphi_0 = 0$, and the photoelectrons shift up and down in energy as a function of $\tau_{\text{XUV-NIR}}$ resembling a streaking trace. In Fig. 4.4 (b) the CEP is set to $\Delta\varphi_0 = \pi/2$, the photoelectron yield shows a clear oscillation of the harmonic bands at $E_{2n+1} = \hbar\omega_{2n+1} - \text{IP}$, and sidebands at $E_{2n} = \hbar\omega_{2n} - \text{IP}$ with n as an integer as a function of $\tau_{\text{XUV-NIR}}$ following the dynamics of a RABBITT trace.

In conclusion, by changing the CEP of the driving NIR pulse by $\pi/2$, one can switch between an IAP and APT. It has to be noted, that the streaking trace in Fig. 4.4 (a) is not perfectly continuous, but shows harmonic peaks on top of the continuous part. This indicates that in addition to the main IAP, there exists a small pre-IAP generated at the half-cycle prior to the half-cycle at the maximum of the NIR envelope [308]. The contrast of the fringes in the photoelectron spec-

trum is around 50% leading to a pre-pulse with approximately 5% of the intensity of the main IAP, which is consistent with the observation made in sect. 4.1. The intensity of the pre-pulse is much smaller compared to the main one, so that the second IAP does not disturb the experimental results.

CHAPTER 5

Fourier transform spectroscopy

Multidimensional spectroscopy is a well established method in the visible to infrared spectral range, where collective dynamics and correlations in matter are explored by using a sequence of phase-locked femtosecond pulses [309–318]. In these experiments a non-linear signal is measures as a function of the pump-probe delay, and the Fourier transform of this signal gives insight into the frequency-dependent dynamics, which are related to the interaction of the system with the pump and/or probe pulse. The coupling between different quantum states are revealed, since all non-linear optical signals are recorded at the same time. Recently multidimensional spectroscopy started to become an important tool in attosecond science, where either an XUV pulse is combined with multiple NIR pulses [319] or where multiple XUV sources are established [237, 242–244, 254]. These methods allow for linear and non-linear Fourier transform spectroscopy [238, 240, 251–253, 255, 256, 320–322], attosecond-gated interferometry [323], measuring the temporal coherence of XUV radiation [241] or their pulse duration in means of non-linear autocorrelation [239]. In addition, first advances were made to extend the two XUV pulse generation scheme to solids to gain deeper insight into the underlying dynamics [166].

In the following chapter, different Fourier Transform spectroscopy experiments are presented. Firstly, the autocorrelation signal of the two phase-locked NIR, and XUV pulses is investigated in detail to fully understand the dynamics and implications, due to the generation of high harmonics with two phase-locked collinear NIR pulses. In addition, the two XUV pulses are used in a Fourier transform spectroscopy experiment measuring the Rydberg energies in helium. This experiment demonstrates the high stability and accuracy of the self-developed Mach-Zender interferometer, and it highlights the high variety of possible applications

of this setup. The main results of the latter experiment are published in Optics Express [1]. A further investigation of NIR, and XUV autocorrelation measurements in the collinear and non-collinear geometry of the self-built MZI can be found in the master thesis of Laura Maikowski [8].

Publication information

Parts of this chapter are published in *Phase-locking of time-delayed attosecond XUV pulse pairs* by L.-M. Koll, L. Maikowski, L. Drescher, M. J. J. Vrakking, and T. Witting in Optics Express, vol. 30, no. 5, pp. 7082–7095 (2022) [1]. DOI: `https://doi.org/10.1364/OE.452018`

Author contributions: The Mach-Zehnder interferometer (MZI) was developed by L. Maikowski and T. Witting. The experiments were conceived by L.-M. Koll, T. Witting and M. J. J. Vrakking. The MZI was characterized by L.-M. Koll and L. Maikowski. The further experiments were performed and the data was analyzed by L.-M. Koll under the supervision of T. Witting. The manuscript was written by L.-M. Koll and T. Witting with the help and discussion of the other co-authors.

5.1 Autocorrelation measurements

An autocorrelation measurement can reveal the underlying spectral information of an optical pulse by measuring and Fourier transforming the delay-dependent interference signal of the original pulse with a delayed replica of itself.
The first-order autocorrelation function [324] of two identical pulses is

$$S^{(1)}(\tau) = \int_{-\infty}^{+\infty} \left|E(t) + E(t-\tau)\right|^2 dt, \tag{5.1}$$

where $E(t)$ is the electric field of the pulses, and τ is the time delay between them. Equation (5.1) can be further expressed as

$$S^{(1)}(\tau) = \int_{-\infty}^{+\infty} dt \left(\left|E(t)\right|^2 + \left|E(t-\tau)\right|^2 + 2\left|E(t)\right|\left|E(t-\tau)\right| \cos\left(\omega \cdot \tau + \phi\right) \right), \tag{5.2}$$

where ω is the frequency of the pulses, and ϕ the relative phase between them. According to Eq. (5.2) the spectrum of two interfering pulses shows a $\cos(\omega\tau)$-modulation with a fringe period of $\delta\omega = 2\pi/\tau$. In Fig. 5.1 the simulated interference signal for two collinear gaussian beams at a center frequency of 26 eV is shown for three different time delays τ. The spectral fringe spacing decreases with increasing τ.

5.1.1 Collinear NIR pulse pair

Firstly, an autocorrelation measurement of the two collinear NIR pulses passing through the MZI is performed to retrieve the underlying spectral NIR pulse in-

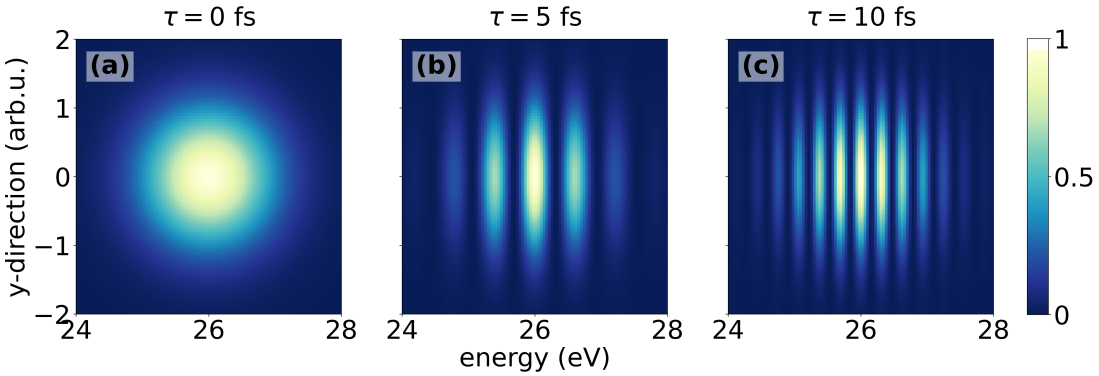

Figure 5.1: Exemplary calculation of the interference signal of two identical gaussian beams with mean energies of 26 eV. This signal is an exemplary spectrum, which is expected to be measured in a similar shape with the XUV spectrometer. The signal is plotted as a function of the pulse energy and the spatial coordinate of the beam for three different time delays τ. For $\tau > 0$ fs a fringe modulation along the energy axis is observed, where the fringe spacing becomes narrower for longer delays.

formation. This measurement was performed in the scope of Laura Maikowski's master thesis [8], and the results can also be found in chapter 4.1 of her thesis.

In Fig. 5.2 (a) the autocorrelation signal of the two interfering NIR pulses is shown. The time delay $\tau_{\text{NIR-NIR}}$ is scanned from -100 fs to 100 fs in $\delta\tau_{\text{NIR-NIR}} = 200$ as steps, and the intensity of the two interfering beams is recorded with a CMOS camera (asA1929-25 μm, Basler AG) after the MZI. The interferogram is thus retrieved by spatially integrated the intensity distribution for each delay point. A Fourier transform (FT) of the measured autocorrelation signal retrieves the NIR frequency spectrum. In Fig. 5.2 (b) the result of the FT is compared with the spectrum of both pulses (arm A and B) separately measured with a spectrometer (Ocean Optics, FLAME-S-VIS-NIR). The FT energy resolution is $\delta E = 0.02$ eV according to the Whittaker–Nyquist–Shannon sampling theorem [325] ($\delta E = h/\Delta\tau_{\text{NIR-NIR}}$, with $\Delta\tau_{\text{NIR-NIR}} = 200$ fs). As a consequence, the resolution of the spectrum retrieved via autocorrelation measurement, and the two spectra recorded by the spectrometer (resolution of the spectrometer $\delta E_{\text{spec}} = 0.003$ eV) depict slight, but negligible differences.

5.1.2 Collinear XUV pulse pair

In this section, the interferogram of two collinear phase-locked XUV pulses is investigated.

Coherence time In general, the quality of an interferogram relies first of all on the coherence length of the pulses, however it also depends on the coherence properties of the interferometer, and the detection scheme itself, which are defined by for example the stability of the setup, as well as the resolution of the detector. So for example to sample a cutoff energy of the harmonics of around $E_{\text{max}} =$

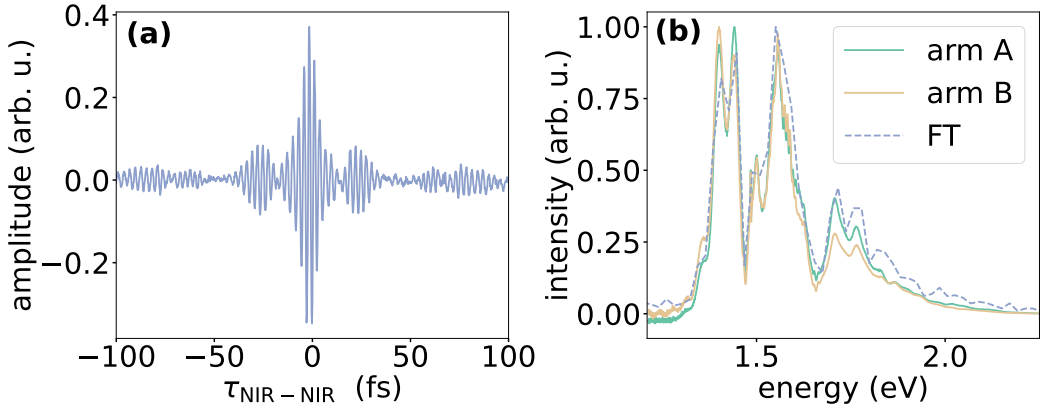

Figure 5.2: (a) Autocorrelation measurement of the two phase-locked NIR pulses. (b) Reconstruction of the NIR spectrum by performing a Fourier transform (FT) of the autocorrelation signal (blue dashed line) compared with the NIR spectrum of the two individual pulses of the interferometer measured with a spectrometer (green and orange line). This data was taken in the scope of Laura Maikowski's master thesis [8], and can also be found in chapter 4.1 of her thesis.

45 eV a 1-σ-delay stability of 22 as is required. The coherence time of a pulse is given by $t_{\mathrm{coh}} \approx 2\pi/\Delta\omega_{\mathrm{XUV}}$ [324], which is determined by the bandwidth of the pulses $\Delta\omega_{\mathrm{XUV}}$. In the current setup the XUV spectrometer is wavelength resolved, with a resolution much smaller than the bandwidth of the pulses, i.e. $\delta\omega_{\mathrm{Spec}} << \Delta\omega_{\mathrm{XUV}}$. Accordingly, the coherence time of the detected signal is not given solely by the bandwidth of the pulses, but is rather determined by the resolution of the spectrometer. As aforementioned the resolution of the XUV spectrometer is 25 meV for a photon energy of 12.36 eV [206] becoming less for higher energies. Now one can assume an averaged spectral resolution of 40 meV, which corresponds to a coherence time of $t_{\mathrm{coh}} \approx 2\pi/\delta\omega_{\mathrm{Spec}} \approx 100$ fs. In other words, at $\tau_{\mathrm{XUV\text{-}XUV}} \geq 100$ fs the spectral fringe modulation of the XUV spectrum becomes so narrow, that multiple fringes fall within one pixel of the camera, and thus can not be resolved anymore.

If however, the two XUV pulses not only interact with themselves, but also with an atomic or molecular resonance, the temporal coherence of the measured signal increases. The resonance introduces a "memory" in the system, and since an atomic or molecular resonance normally has a much narrower bandwidth than the XUV pulses or as the spectral resolution of any detector, the coherence length of the measured signal is defined by the energetic width of the resonance (cf. experiment presented in the next section 5.2).

Autocorrelation function of two XUV pulses If the two XUV pulses are generated independently, Eq. 5.1 can be written as

$$S_q^{(1)}(\tau_{\mathrm{XUV\text{-}XUV}}) = \int_{-\infty}^{+\infty} \left| E_{\mathrm{q,XUV}}(t) + E_{\mathrm{q,XUV}}(t - \tau_{\mathrm{XUV\text{-}XUV}}) \right|^2 dt, \tag{5.3}$$

where $E_{\mathrm{q,XUV}}(t)$ is the q-th harmonic electric field.

However, for sufficient small $\tau_{\text{XUV-XUV}}$ the two driving NIR pulses interfere in the focus during the HHG [219, 253, 326]. Consequently, the two XUV pulses are not created independently, and Eq. 5.3 has to be modified.

Thus, the first-order becomes a high-order autocorrelation function of the NIR driving pulses [253], i.e.

$$S_q^{(p)}(\tau_{\text{XUV-XUV}}) = \int_{-\infty}^{+\infty} \left| \left(E_{\mathrm{NIR}}(t) + E_{\mathrm{NIR}}(t - \tau_{\text{XUV-XUV}}) \right)^p \right|^2 dt, \qquad (5.4)$$

where $E_{\mathrm{NIR}}(t)$ is the electric field of the NIR pulses, and p is the effective order of nonlinearity. As a result the total NIR laser intensity oscillates as a function of $\tau_{\text{XUV-XUV}}$ with a period of $T_{\mathrm{osci}} = 2\pi/\omega_{\mathrm{NIR}}$, and thus the amount of generated XUV radiation is altered.

The measured interferogram of the XUV pulse pair as a function of $\tau_{\text{XUV-XUV}}$ is shown in Fig. 5.3 (a). It should be noted that the harmonics in this experiment are generated by a 3.2 fs NIR pulse, thus leading to a broad continuous harmonic spectrum (cf. Fig. 5.3 (a) white inset). The optical frequency axis corresponds to the frequency given by the XUV spectrometer. The XUV spectrum is recorded for a delay range of $\Delta\tau_{\text{XUV-XUV}} = 150\,\mathrm{fs}$ in steps of $\delta\tau_{\text{XUV-XUV}} = 25\,\mathrm{as}$.

The interference signal exhibits a strong modulation of the XUV intensity around delay zero, which fades out with larger delay and disappears completely for $\tau_{\text{XUV-XUV}} \geq 100\,\mathrm{fs}$. This delay corresponds to the limit of the coherence time of the measured signal given by the resolution of the XUV spectrometer. Below $\tau_{\text{XUV-XUV}} < 40\,\mathrm{fs}$ the spectral fringe modulation of the XUV spectrum can be seen as horizontal stripes. In addition, the higher the XUV intensity, the higher is the cutoff energy, which is directly correlated to the intensity of NIR driving pulse.

The Fourier transform of the interferogram along $\tau_{\text{XUV-XUV}}$ is shown in Fig. 5.3 (b). The most pronounced signal is independent of the optical frequency, and occurs at around 1.6 eV, which is in good approximation the photon energy of the NIR driving pulse.
In addition, contributions at high frequencies emerge, which depend linearly on the optical frequency, i.e. $\omega_{\mathrm{opt}} = \omega_{\mathrm{FT}}$, and can be assigned to the frequencies of the individual harmonics ω_q. Furthermore multiple artifact peaks to the left and right side of the harmonic peaks occur at a distance, which is a multiple of the NIR driving frequency $\omega_q \pm n \cdot \omega_{\mathrm{NIR}}$, with n as an integer. The artifact peaks as well as the strong signal at $\sim 1.6\,\mathrm{eV}$ are due to the fact, that the two driving NIR pulses interfere in the focus during the HHG process [253].

The oscillation of XUV photon flux, due to the NIR pulse interference can be seen in detail in Fig. 5.4, where the interferogram shown in Fig. 5.3 (a) is summed over the optical frequency between 20 eV and 40 eV. The XUV intensity is shown for three different delay ranges, and is fitted to a cosinusoidal function to retrieve the period of the $\tau_{\text{XUV-XUV}}$-dependent oscillation of the harmonic flux, i.e. T_{HHG}.

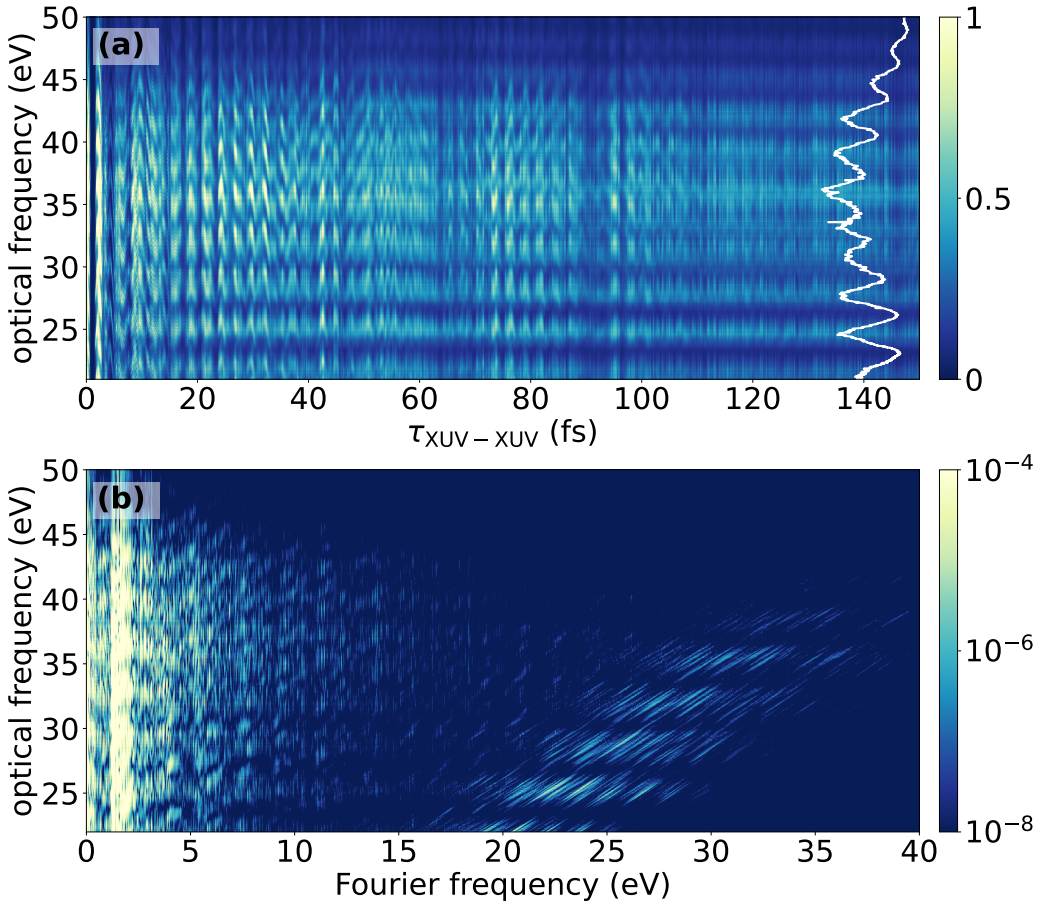

Figure 5.3: (a) Interference signal of two phase-locked XUV pulses created by HHG with two collinear phase-locked NIR pulses. The spectrum plotted in white corresponds to the HHG spectrum recorded with the XUV spectrometer at $\tau_{\text{XUV-XUV}} = 145\,\text{fs}$. (b) Fourier transform of the interference signal shown in (a). There is a strong contribution at around 1.6 eV visible corresponding to the NIR driving frequency, as well as a signal at high frequencies, which can be assigned to the frequencies of the individual harmonics in the pulse spectrum. In addition artifact peaks appear to the left and right side of the main harmonics. These artifacts are due to a $\tau_{\text{XUV-XUV}}$-dependent modulation of the harmonic yield.

At $\tau_{\text{XUV-XUV}} = 0\,\text{fs}$ the intensity of the harmonic flux is maximal, whereas it is minimal for $\tau_{\text{XUV-XUV}} \sim \pm 1.4\,\text{fs}$ (cf. Fig. 5.4 (a)). As $\tau_{\text{XUV-XUV}}$ increases the intensity of the maxima decreases until it reaches a value of $1/4 \cdot I_{\text{max}}(\tau_{\text{XUV-XUV}} = 0\,\text{fs})$. The intensity of the minima increase with increasing $\tau_{\text{XUV-XUV}}$ until at $\tau_{\text{XUV-XUV}} \geq 100\,\text{fs}$ the signal becomes delay independent with a constant intensity of $1/4 \cdot I_{\text{max}}(\tau_{\text{XUV-XUV}} = 0\,\text{fs})$. The harmonic yield oscillates with a period of $T_{\text{HHG}} = (2.84 \pm 0.02)\,\text{fs}$, which corresponds to an energy of 1.5 eV, i.e. in good approximation the NIR photon energy.

In Fig. 5.4 (c) for $\tau_{\text{XUV-XUV}} \geq 15\,\text{fs}$ the XUV intensity has a comparable oscillation period of $T_{\text{HHG}} = (2.78 \pm 0.01)\,\text{fs}$. However, in Fig. 5.4 (b) for $5\,\text{fs} \leq$

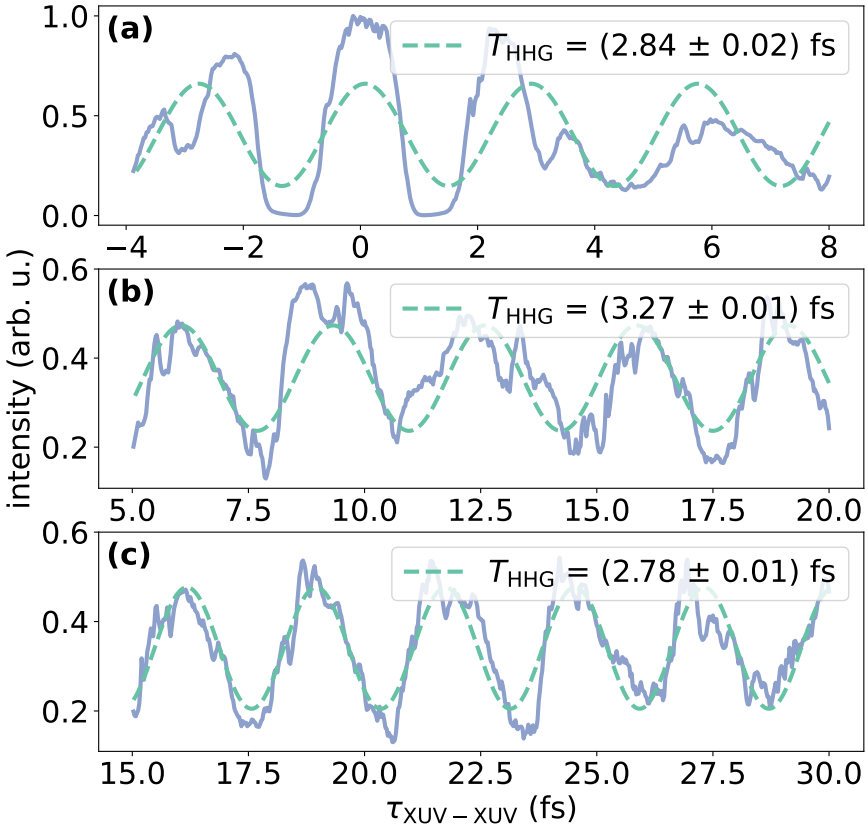

Figure 5.4: Normalized XUV intensity as a function of $\tau_{\text{XUV-XUV}}$ for three different delay ranges. The intensity is retrieved by summing over the recorded XUV spectrum between 20 eV and 40 eV. The harmonic yield oscillates along $\tau_{\text{XUV-XUV}}$ with the period T_{HHG} (see inset), which is retrieved by fitting the intensity to a cosinusoidal curve (dashed green line).

$\tau_{\text{XUV-XUV}} \leq 20\,\text{fs}$ the harmonic yield oscillates with a slightly longer period of $T_{\text{HHG}} = (3.27 \pm 0.01)\,\text{fs}$. This time corresponds to an energy of 1.26 eV, and a wavelength of 980 nm, which is at the upper limit of the NIR bandwidth ($\sim 510 - 1030\,\text{nm}$). In this delay range predominantly the tail of the first NIR pulse interferes with the leading part of the second NIR pulse. Commonly these close to single-cycle pulses have a flat zero phase at the center of the pulse, but have a small non-zero phase at the edges (cf. Fig. 3.3). If the period in this delay range is defined by the dominant frequency within the tails, depending on the tails chirps, this could possibly result in a de- or increase of T_{HHG}.

To investigate the ω_{NIR}-modulation of the signal in more detail, in Fig. 5.5 the Fourier spectrum at low frequencies is shown as a function of the two pulse delay $\tau_{\text{XUV-XUV}}$, which is retrieved by performing a Gabor analysis [327]. This representation allows to disentangle the temporal evolution of the ω_{NIR}-component. It can be seen that for small delays $\tau_{\text{XUV-XUV}} < 25\,\text{fs}$ the Fourier spectrum exhibits a strong peak at the NIR driving frequency ω_{NIR}. In this temporal region the interference of the two NIR pulses during HHG is maximal, and consequently the XUV interferogram is fully determined by Eq. 5.4. As the time delay between

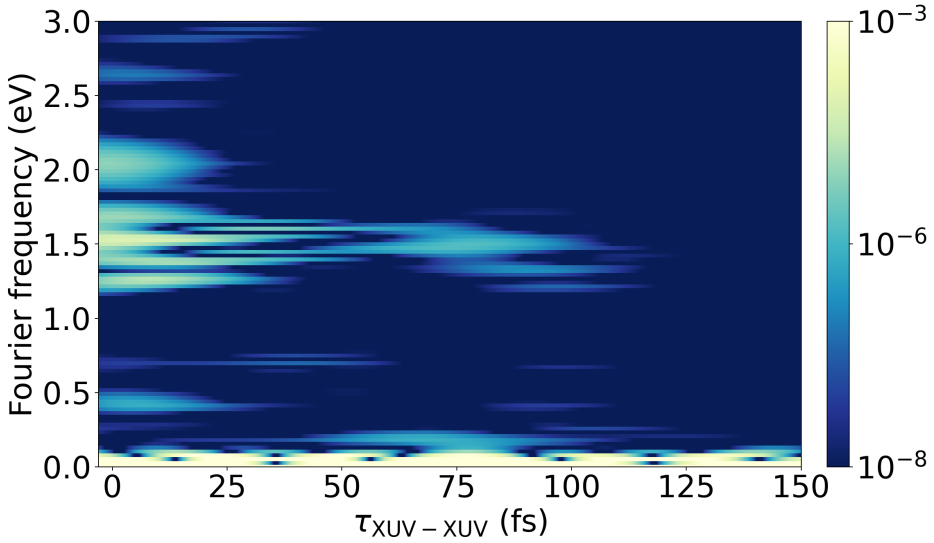

Figure 5.5: Fourier spectrum as a function of $\tau_{\text{XUV-XUV}}$ to visualize the time dependence of the low frequency components. Therefore, the recorded XUV spectrum is summed between 20 eV and 40 eV, and Fourier transformed with a window function with a width of 15 fs (Gabor analysis [327]).

the two pulses increase ($25\,\text{fs} \lesssim \tau_{\text{XUV-XUV}} \lesssim 65\,\text{fs}$), the NIR interference modulation decreases, and the XUV interferogram can be described by a combination of Eq. 5.4 and Eq. 5.3. This leads to a ω_{NIR}-modulation of the harmonics signals, and to artifact peaks at $\omega_q \pm \omega_{\text{NIR}}$ in the Fourier spectrum.

In Fig. 5.5 this can be seen as a slight decrease of the strength of the ω_{NIR}-contribution. At $\tau_{\text{XUV-XUV}} \sim 65\,\text{fs}$ the signal strength of the ω_{NIR}-contribution increases again, which is due to the interference of a small pre-pulse with one of the main pulses in the HHG. Only at long delays $\tau_{\text{XUV-XUV}} \gtrsim 100\,\text{fs}$ the two pulses are far enough apart, that the second NIR pulse is not affected by the first or pre-pulse during the HHG process. Consequently the two XUV pulses are generated independently, and the XUV interferogram can be described by Eq. 5.3. However, this delay is already at the limit of the coherence time of the interference signal.

Accordingly, the reconstruction of the XUV spectrum by means of an autocorrelation measurement as it is done for the NIR spectrum in the previous section, is strongly limited by the ω_{NIR}-modulation of the harmonic signal, and consequently the appearance of multiple artifact peaks in the Fourier spectrum. The amount of artifact peaks can be reduced or even completely depleted, if the MZI is used in a non-collinear geometry [8, 253], and thus realizing two independent foci in the HHG chamber. In that case the Fourier transform spectrum of the two interfering pulses exhibits no artifact peaks if the distance between the two foci is sufficiently large. Accordingly the XUV interference signal can be described by a first-order autocorrelation function, i.e. Eq. 5.3 for all $\tau_{\text{XUV-XUV}}$, allowing to reconstruct the underlying XUV spectral information.

However, the use of the MZI in a non-collinear geometry brings other challenges, as for example the two foci do not overlap in the VMI spectrometer, due to the $2f-2f$ re-imaging of the HHG foci in the current setup. Furthermore, the temporal fringes due to the two pulse delay overlap with spacial fringes due to the induced angle between both beams, which can make the data analysis rather complicated.

Thus, in this thesis the MZI is always used in a collinear geometry avoiding the delays $\tau_{\text{XUV-XUV}}$ close to 0 fs, to avoid the region with the strongest NIR-NIR interference modulation.

5.2 Excitation of the Rydberg states of helium

In this section, a Fourier transform spectroscopy experiment is presented, which determines the accuracy, and the long term stability of the passively and actively stabilized Mach-Zehnder interferometer, by retrieving the Rydberg energies of helium. These energies are very well known, and therefore present a perfect physical verification of the absolute accuracy of the MZI. The main results shown in this section are published in Optics Express [1].

5.2.1 Experimental results

In the current experiment the two phase-locked XUV pulses (two attosecond pulse trains, 5 fs NIR driving pulses) are focus into a neutral helium gas jet, which is located in the VMI chamber. The spectrum of the two XUV pulses is shown in Fig. 3.9 for two different $\tau_{\text{XUV-XUV}}$.

In Fig. 5.6 a schematic illustration of the energy levels of helium is shown, as well as possible population transfers induced by the XUV pulse pair, and NIR probe pulse. The ionization potential (IP) of helium is $\sim 24.6\,\text{eV}$ [328], thus each harmonic with an order $q \geq 17$ has enough photon energy $\omega_{q\geq 17}$ to directly ionize the helium atoms. Moreover, the photon energies of harmonics $q = 13$, and $q = 15$ are sufficient to populate different Rydberg states, i.e. harmonic $q = 13$ can excite the 1s2p state, whereas harmonic $q = 15$ can populate the 1s4p state and the ones above. The Rydberg state 1s3p is not populated, since there are no XUV photons with this energy.

As described in the previous chapter, the XUV spectra exhibits a modulation, which is inversely proportional to the time delay $\tau_{\text{XUV-XUV}}$ between the two XUV pulses. As a consequence, the spectral intensity for a given ω_{XUV} oscillates with $\tau_{\text{XUV-XUV}}$. For a time delay of $\tau_{\text{XUV-XUV}} = n\pi/\omega_{\text{XUV}}$, with n as an integer the spectral intensity is maximal, whereas for $\tau_{\text{XUV-XUV}} = (n + 1/2)\pi/\omega_{\text{XUV}}$ it is zero. Consequently, the population of the Rydberg states oscillate as a function of $\tau_{\text{XUV-XUV}}$.
The exited Rydberg states are subsequently ionized by a NIR probe pulse delayed by 1 ps relative to the second XUV pulse B, which is fixed in time (for $\tau_{\text{XUV-XUV}} > 0\,\text{fs}$ XUV pulse A comes prior to XUV pulse B). With the VMI spectrometer the photoelectrons are then measured as a function of $\tau_{\text{XUV-XUV}}$. One

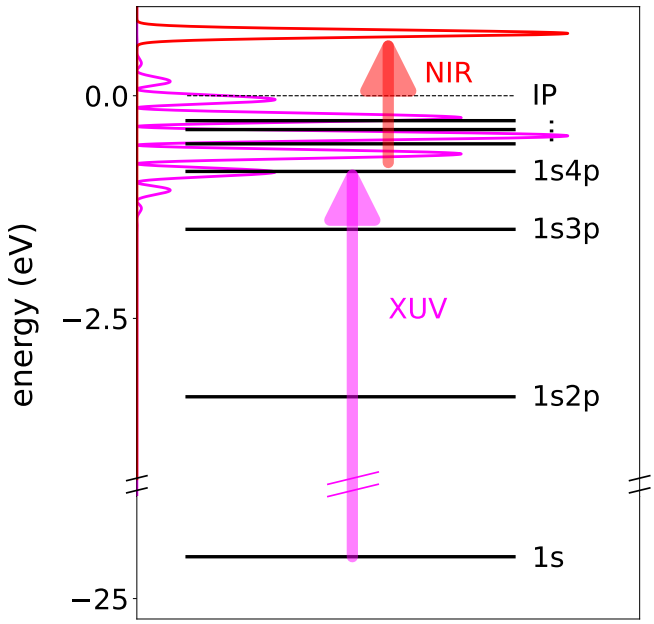

Figure 5.6: Schematic illustration of energy levels in helium. The Rydberg states are populated by harmonic $q = 13$, and 15, and are subsequently ionized by the NIR pulse (red). The XUV spectrum (purple) exhibit a fringe pattern with a spacing inversely proportional to $\tau_{\text{XUV-XUV}}$. Accordingly, the population of the Rydberg states depend on $\tau_{\text{XUV-XUV}}$. The data for the energy levels are taken from [328].

VMI image is integrated over 5000 laser shots and is Abel inverted using the rBASEX method [273, 274].

In Fig. 5.7 (a) an example of a raw VMI image is shown, and in Fig. 5.7 (b) the corresponding inverted image is illustrated. The main contribution in the data are several bands becoming narrower to the edge of the picture, which are due to direct 1-XUV-photon ionization. These bands are a representation of the initial XUV spectrum, and have an energy according to $E_{e^-} = \hbar\omega_{\text{XUV}} - \text{IP}$. In Fig. 5.7 (c) a magnified view of the bands of the inverted VMI image is shown, which reveals a $\tau_{\text{XUV-XUV}}$-dependent fringe modulation corresponding to the fringe pattern of the XUV spectrum. The fringes are only resolvable at low energies and $\tau_{\text{XUV-XUV}} \lesssim 20\,\text{fs}$, due to the fact that the resolution of the VMI detector decreases towards higher energies.

The photoelectron signals, which result from direct 1-XUV-photon ionization are not of interest here, and rather the signal corresponding to the two-color ionization (excitation of the Rydberg states by absorption of 1-XUV-photon followed by ionization of the atom through the absorption of 1-NIR-photon) is investigated. The corresponding features show up as sharp lines close to the center of the VMI image.

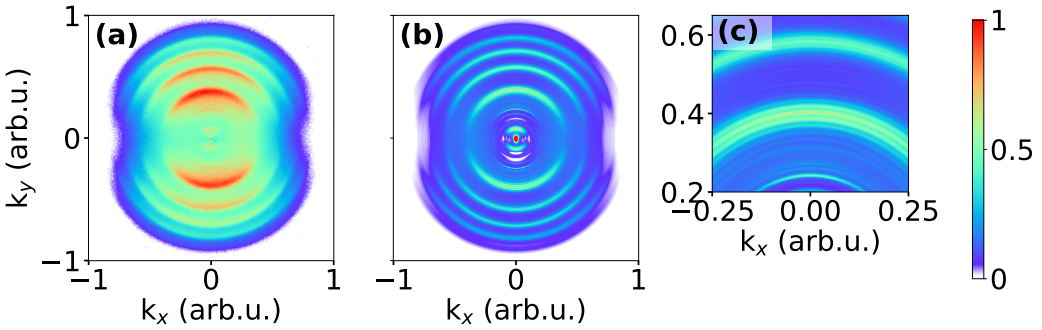

Figure 5.7: (a) Measured VMI image of the momentum resolved photoelectron fragment yield. (b) Abel inverted image of the recorded image shown in (a) using the rBASEX method [273, 274]. (c) Magnified view of (b) to emphasize the fringe modulation, due to the delay between the two XUV pulses, with a fringe spacing according to $\delta\omega_{\text{XUV}} = 2\pi/\tau_{\text{XUV-XUV}}$ with $\tau_{\text{XUV-XUV}} = 15\,\text{fs}$.

As described in sect. 3.5.1 the 3D photoelectron momentum distribution can be expressed by a superposition of Legendre polynomials as

$$\begin{aligned} P(p_{e^-}, \tau_{\text{XUV-XUV}}, \cos\theta) \;=\; & \beta_0(p_{e^-}, \tau_{\text{XUV-XUV}}) \times \\ & \{1 + \beta_2(p_{e^-}, \tau_{\text{XUV-XUV}}) P_2(\cos\theta) + \\ & \beta_4(p_{e^-}, \tau_{\text{XUV-XUV}}) P_4(\cos\theta)\}\,, \end{aligned} \tag{5.5}$$

where θ is the angle between the polarization of the XUV+NIR beams and the photoelectron momentum p_{e^-} . The particle velocity distribution is $\beta_0(p_{e^-}, \tau_{\text{XUV-XUV}})$, and the photoelectron angular distributions are $\beta_{2,4}(p_{e^-}, \tau_{\text{XUV-XUV}})$, respectively. Since the ionization of the Rydberg states is a two-photon process, the signal of the photoelectrons can be fully described by $\beta_L(p_{e^-}, \tau_{\text{XUV-XUV}})$ with $L = 0, 2, 4$.

5.2.1.1 Broadband NIR probe pulse

In the first measurement campaign the VMI images are recorded for a delay range of $\Delta\tau_{\text{XUV-XUV}} = 250\,\text{fs}$ in $\delta\tau_{\text{XUV-XUV}} = 25\,\text{as}$ steps. The NIR probe pulse has a pulse duration of $\sim 5\,\text{fs}$, centered at 790 nm.

In Fig. 5.8 (a)-(c) the different parameters $\beta_{0,2,4}(p_{e^-}, \tau_{\text{XUV-XUV}})$ are shown as a function of $\tau_{\text{XUV-XUV}}$, and the photoelectron momentum (in arbitrary units). In Fig. 5.8 (b)&(c) the photolines of the 1s2p, 1s4p, and 1s5p Rydberg states are clearly visible, and the intensities of these photoelectron signals oscillate as a function of $\tau_{\text{XUV-XUV}}$. In Fig. 5.8 (a) the angle integrated $\beta_0(p_{e^-}, \tau_{\text{XUV-XUV}})$ does not show the photolines as clearly, and the contributions of the different states largely overlap.

The corresponding Fourier transform power spectra (FTPS) $\text{FS}_{\beta_{0,2,4}}(p_{e^-}, \omega_{\text{FT}})$ with ω_{FT} as the Fourier frequency, are shown in Fig. 5.8 (d)-(e), where the time-dependent signal in Fig. 5.8 (a)-(c) is Fourier transformed along $\tau_{\text{XUV-XUV}}$. The

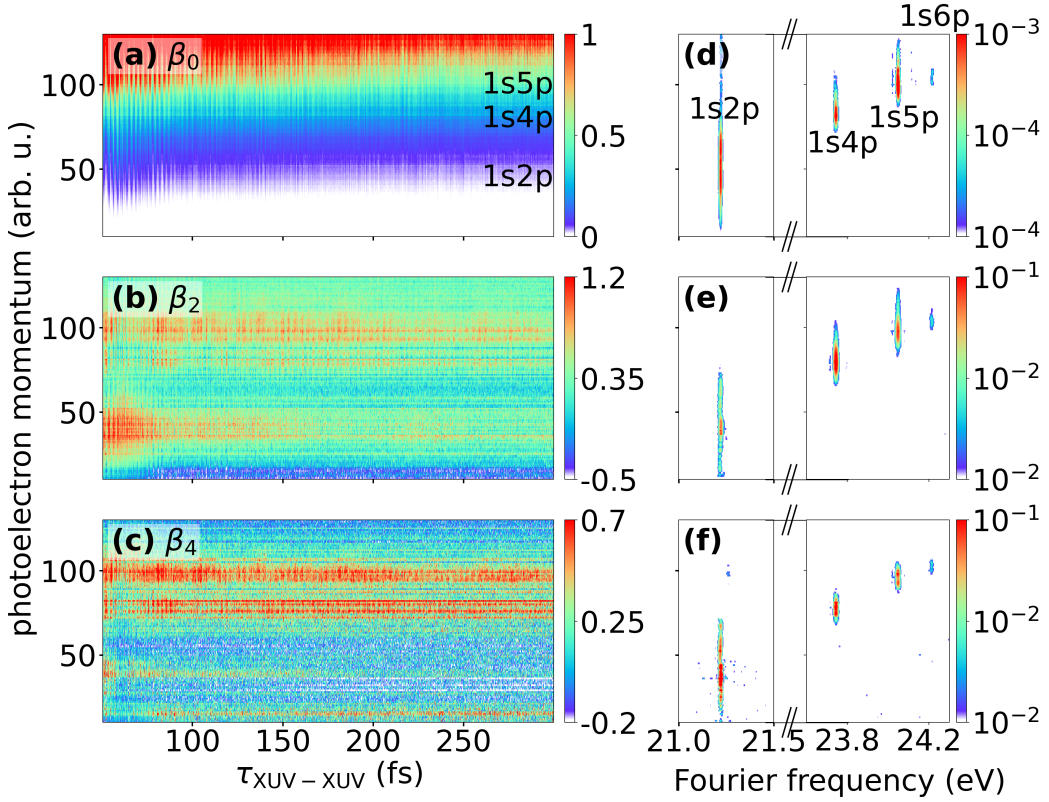

Figure 5.8: Photoelectron yield as a function of $\tau_{\text{XUV-XUV}}$ emerging due to the excitation of neutral helium atoms by the phase-locked XUV pulse pair, and ionization by a broadband NIR pulse 1 ps later. (a)-(c) $\beta_L(p_{e^-}, \tau_{\text{XUV-XUV}})$ parameters with $L = 0, 2, 4$ as a function of $\tau_{\text{XUV-XUV}}$. The vertical axis is given in pixel units of the CCD camera recording the VMI images, which correspond to the photoelectron momentum in arbitrary units. (d)-(e) Corresponding Fourier transform power spectra (FTPS) $\text{FS}_{\beta_{0,2,4}}(p_{e^-}, \omega_{\text{FT}})$. The peaks in the FTPS can be assigned to the excitation energies ω_{Ryd} of different Rydberg states in a helium atom.

pronounced peaks in the FTPS appear around 24 eV corresponding to the excitation energies ω_{Ryd} of the 1s2p, 1s4p, 1s5p, and 1s6p Rydberg states in helium. The signal of the peaks overlap along the photoelectron momentum, due to the broad bandwidth of the NIR probe pulse. The FTPS $\text{FS}_{\beta_{0,2,4}}(p_{e^-}, \omega_{\text{FT}})$ of all three $\beta_{0,2,4}(p_{e^-}, \tau_{\text{XUV-XUV}})$ parameters agree well, which confirms that the photoelectron signal corresponding to the Rydberg states, originate from a two-photon process.

In Fig. 5.9 the normalized momentum-integrated FTPS of all three $\beta_{0,2,4}(p_{e^-}, \tau_{\text{XUV-XUV}})$ are shown. The main signal shows the aforementioned four peaks corresponding to the different Rydberg states. The Fourier frequencies of the four peaks are in good agreement with literature values [329], as listed in table 5.1.

The FWHM of the different Rydberg peaks is given in table 5.1 third column and is between 17.25 meV and 18.64 meV. The errorbars of the Fourier frequency, and the FWHM are derived by the standard deviation of the experimental data for

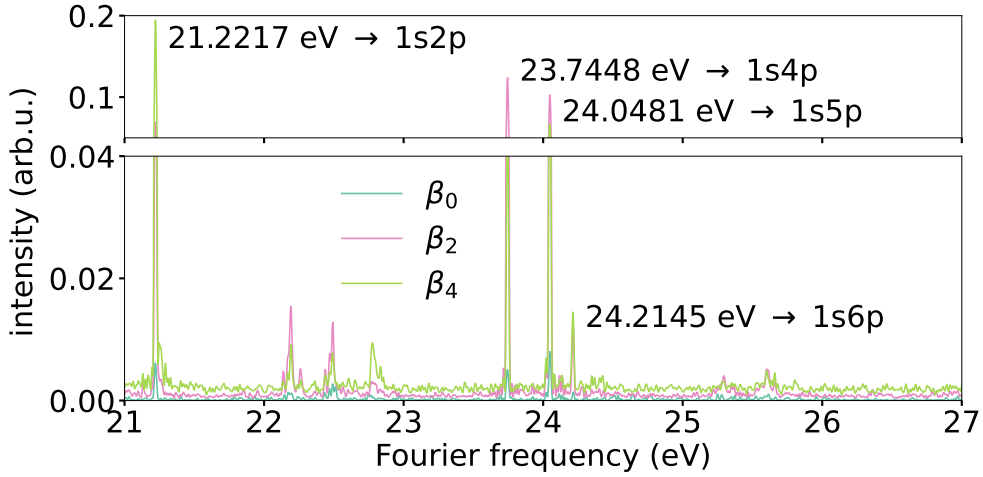

Figure 5.9: Normalized momentum-integrated FTPS $\mathrm{FS}_{\beta_{0,2,4}}(p_{e^-}, \omega_{\mathrm{FT}})$ for the different $\beta_{0,2,4}(p_{e^-}, \tau_{\text{XUV-XUV}})$ parameters. In addition to the main Rydberg peaks at ω_{Ryd}, artifact peaks at $\omega_{\mathrm{Ryd}} \pm 1.6\,\mathrm{eV}$ appear.

Rydberg state	Fourier frequency ω_{FT} (eV)	FWHM (meV)	ω_{Ryd} (eV) [329]
1s2p	21.2217 ± 0.0004	17.35 ± 0.61	21.2180
1s4p	23.7448 ± 0.0002	18.64 ± 1.07	23.7421
1s5p	24.0481 ± 0.0001	17.56 ± 0.31	24.0458
1s6p	24.2145 ± 0.0014	17.89 ± 1.67	24.2110

Table 5.1: Fourier frequencies of the Rydberg states in helium found in the experimental data by exciting the atoms with two phase-locked XUV pulses, and subsequently ionizing the atom with a broadband NIR pulse. In the last column the experimental found energies are compared with the corresponding literature values ω_{Ryd} [329].

the three different $\beta_{0,2,4}(p_{e^-}, \tau_{\text{XUV-XUV}})$ parameters. According to the Whittaker-Nyquist-Shannon sampling theorem [325] $\delta E = h/\Delta\tau_{\text{XUV-XUV}}$ the expected FWHM is 16.5 meV for a delay range of 250 fs, which is smaller than the found FWHM.
The average of the deviation of the experimentally retrieved energies of the Rydberg states from the literature values is 0.013%.

The accuracy found in this experiment can be improved by using a narrowband NIR probe pulse to disentangle the photolines along the momentum in the time domain, and thus to isolate the individual peaks in the Fourier domain, as described in detail in the next section.

5.2.1.2 Narrowband NIR probe pulse

In this experiment the bandwidth of the NIR probe pulse is limited by transmitting the pulse through a 25 nm bandwidth interference filter centered at 800 nm

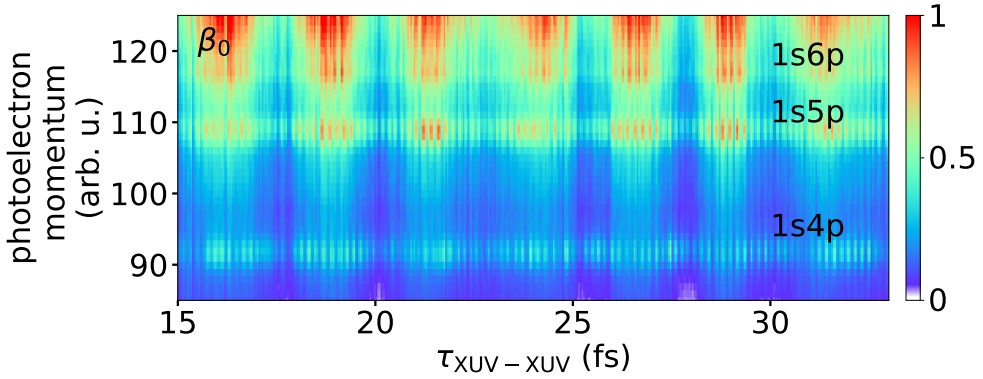

Figure 5.10: $\beta_0(p_{e^-}, \tau_{\text{XUV-XUV}})$ as a function of $\tau_{\text{XUV-XUV}}$, and the photoelectron momentum zoomed in to highlight the oscillation of the photoelectron yield as a function of the pulse delay. The vertical axis is given in pixel units of the CCD camera, which records the VMI images, and which correspond to the photoelectron momentum in arbitrary units.

(leading to a pulse duration of approximately 38 fs). The VMI images are recorded over a delay range of $\Delta\tau_{\text{XUV-XUV}} = 280\,\text{fs}$ in $\delta\tau_{\text{XUV-XUV}} = 25\,\text{as}$ steps.

In Fig. 5.10 $\beta_0(p_{e^-}, \tau_{\text{XUV-XUV}})$ is shown as a function of $\tau_{\text{XUV-XUV}}$, and the photoelectron momentum in arbitrary units. The figure zooms into a small portion of the delay range to highlight the oscillation of the photoelectron yield as a function of $\tau_{\text{XUV-XUV}}$. The photolines of the 1s4p, 1s5p, and 1s6p are pronounced, and disentangled from each other. Clearly the photoelectron yield oscillates with a period given by $2\pi/\omega_{\text{XUV=Ryd}}$, overlapped by a second oscillation with a longer period of $2\pi/\omega_{\text{NIR}}$, which is due to the NIR-NIR interference during the HHG process as described in detail in the previous sect. 5.1.

In Fig. 5.11 (a)-(c) the parameters $\beta_{0,2,4}(p_{e^-}, \tau_{\text{XUV-XUV}})$ are shown as a function of the photoelectron momentum (arbitrary units), and $\tau_{\text{XUV-XUV}}$. In Fig. 5.11 (d)-(e) the corresponding FTPS $\text{FS}_{\beta_{0,2,4}}(p_{e^-}, \omega_{\text{FT}})$ are displayed. The photolines in the time domain, and the peaks in the frequency domain correspond to the excitation energies ω_{Ryd} of the 124p, 1s5p, 1s6p, and 1s7p Rydberg states (the last one only visible in the Fourier domain). The photolines are well separated, and the peaks in the Fourier domain not only occur at a defined Fourier frequency, but also a defined photoelectron momentum. This allows for a 1-to-1 relation between the measured photoelectron momentum and the helium Rydberg excitation energies ω_{Ryd}. This is in contrast to the former experiment (cf. Fig. 5.8), where the broad bandwidth of the NIR pulse leads to an overlap of the signal along the photoelectron momentum. A signal corresponding to the energy of the 1s2p Rydberg state is not observed in this experiment, since the NIR probe pulse has not enough photon energy to ionize the atom from this state. The FTPS of all three $\beta_{0,2,4}(p_{e^-}, \tau_{\text{XUV-XUV}})$ parameters agree nicely.

In Fig. 5.12 the normalized momentum-integrated FTPS $\text{FS}_{\beta_{0,2,4}}(p_{e^-}, \omega_{\text{FT}})$ of all three $\beta(p_{e^-}, \tau_{\text{XUV-XUV}})$ are shown. The main peaks correspond to the energy

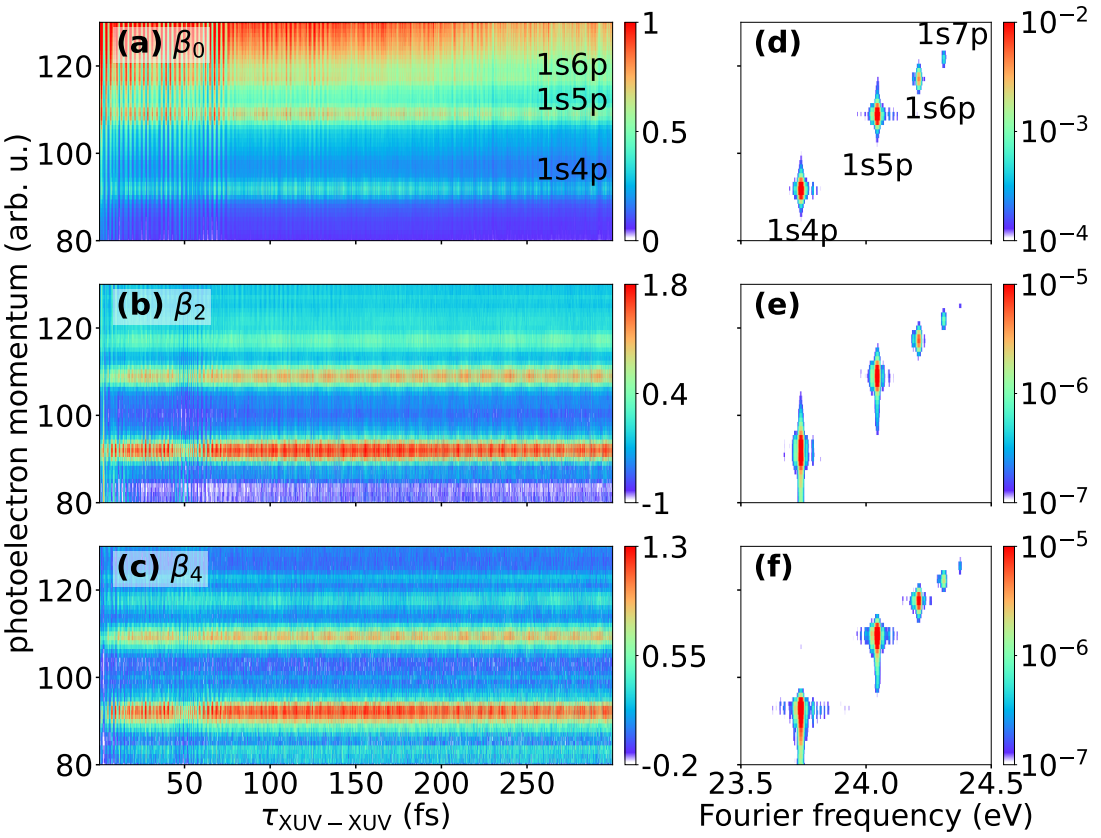

Figure 5.11: Photoelectron fragment yield created by two-XUV-pulse excitation of neutral helium, and subsequent ionization of the atom by a narrowband NIR pulse after 1 ps. (a)-(c) $\beta_{0,2,4}(p_{e^-}, \tau_{\text{XUV-XUV}})$ as a function of $\tau_{\text{XUV-XUV}}$, and the photoelectron momentum (arbitrary units) given in pixel units of the CCD camera recording the VMI images. (c)-(d) Corresponding Fourier transform power spectra (FTPS) $\text{FS}_{\beta_{0,2,4}}(p_{e^-}, \omega_{\text{FT}})$ retrieved by Fourier transforming the signal in (a)-(c) along $\tau_{\text{XUV-XUV}}$. The spectra exhibit pronounced peaks, which can be assigned to the energies of different helium Rydberg states ω_{Ryd}.

of the aforementioned Rydberg states, which are in good agreement with the literature values presented in table 5.2.

Here one has to note, that prior to the experiment the exact wavelength λ_{cw} of the blue cw laser was not known, leading to a small offset of the peaks in the Fourier frequency, since λ_{cw} is actively used to control and scan the time delay between the two XUV pulses (cf. sect. 3.4.2). However, λ_{cw} can be determined by minimizing χ^2, i.e. the summed squared deviations of the experimentally found Fourier peaks from the literature values, and thus the overall offset can be corrected. The cw wavelength is found to be $\lambda_{\text{cw}} = 473.36\,\text{nm}$. This offset is also subtracted from the peaks found in the previous experiment.

The FWHM of the different Rydberg peaks (cf. table 5.1 third column) is between 14.39 meV and 15.18 meV, which agrees nicely with the expected FWHM of 14.8 meV for a delay range of 280 fs (Whittaker-Nyquist-Shannon sampling the-

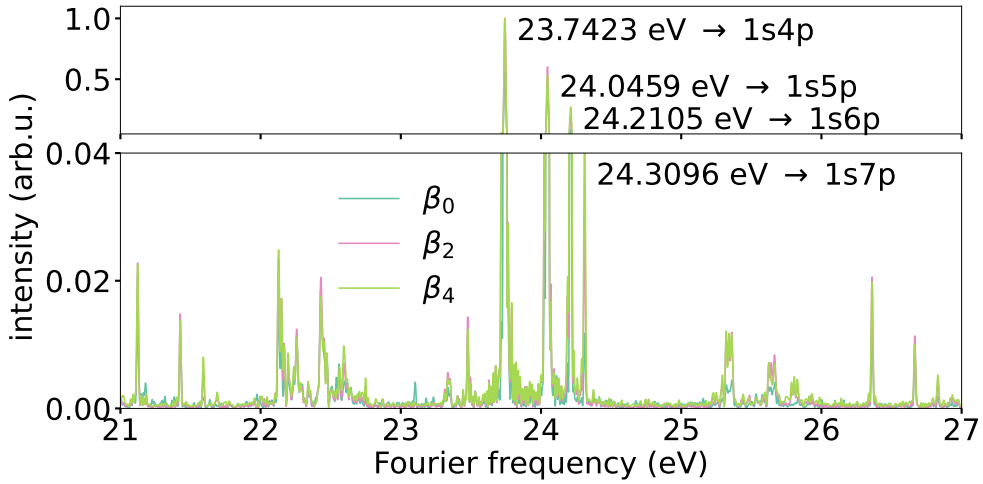

Figure 5.12: Normalized momentum-integrated FTPS $\mathrm{FS}_{\beta_{0,2,4}}(p_{e^-}, \omega_{\mathrm{FT}})$ of $\beta_{0,2,4}(p_{e^-}, \tau_{\text{XUV-XUV}})$. The main peaks ω_{Ryd} correspond to the energies of a series of Rydberg states in helium. In addition artifact peaks at $\omega_{\mathrm{Ryd}} \pm 1.6\,\mathrm{eV}$ and $\omega_{\mathrm{Ryd}} \pm 2.62\,\mathrm{eV}$ appear.

Rydberg state	Fourier frequency ω_{FT} (eV)	FWHM (meV)	ω_{Ryd} (eV) [329]
1s4p	23.7423 ± 0.0004	15.18 ± 0.27	23.7421
1s5p	24.0459 ± 0.0003	14.55 ± 0.04	24.0458
1s6p	24.2105 ± 0.0001	14.47 ± 0.08	24.2110
1s7p	24.3096 ± 0.0009	14.39 ± 0.56	24.3107

Table 5.2: Experimental found Fourier frequencies of the Rydberg states in helium retrieved by first exciting the atoms with two XUV pulses, and subsequently ionizing the atoms with a narrowband NIR probe pulse. The experimentally found values are compared with the literature ω_{Ryd} [329].

orem [325] $\delta E = h/\Delta\tau_{\text{XUV-XUV}}$). The error bars of the Fourier frequency and the FWHM are once more calculated by the standard deviation of the experimental data for all three $\beta_{0,2,4}(p_{e^-}, \tau_{\text{XUV-XUV}})$ parameters. The mean of the deviation of the experimentally found energies of the Rydberg states from the literature values is 0.002%, which is much better than in the former case with a broadband NIR probe pulse. The found value of 0.002% can thus be regarded as the absolute accuracy of the delay axis.

Analysis of the artifact peaks In the FTPS $\mathrm{FS}_{\beta_{0,2,4}}(p_{e^-}, \omega_{\mathrm{FT}})$ additional peaks at $\omega_{\mathrm{Ryd}} \pm 1.6\,\mathrm{eV}$ and $\omega_{\mathrm{Ryd}} \pm 2.62\,\mathrm{eV}$ are visible (cf. Fig. 5.12). The first set of peaks occur at Fourier energies of $(22.1401 \pm 0.0007, 22.4417 \pm 0.0004, 22.5978 \pm 0.0015)\,\mathrm{eV}$ and $(25.3562 \pm 0.0019, 25.6549 \pm 0.0003, 25.8393 \pm 0.0006)\,\mathrm{eV}$, corresponding to somewhat broadened replicas of the three most pronounced Rydberg states 1s4p, 1s5p and 1s6p displaced by $(1.612 \pm 0.009)\,\mathrm{eV}$, respectively. This energy difference is in good approximation the central photon energy of the NIR laser, which indicates a ω_{NIR}-modulation of the experimental measured signal. As

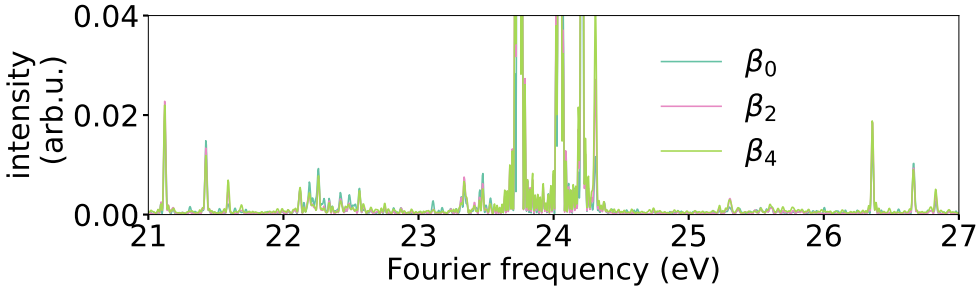

Figure 5.13: Normalized momentum-integrated FTPS $\mathrm{FS}_{\beta_{0,2,4}}(p_{e^-}, \omega_{\mathrm{FT}})$ of $\beta_{0,2,4}(p_{e^-}, \tau_{\text{XUV-XUV}})$ after Fourier transforming only the signal, which is recorded at $\tau_{\text{XUV-XUV}} \geq 80\,\mathrm{fs}$.

described in detail in the previous section 5.1.2, the NIR laser intensity oscillates in the focus of the HHG medium as a function of $\tau_{\text{XUV-XUV}}$, and consequently the XUV photon flux oscillates correspondingly [253, 326].

Thus, the $\tau_{\text{XUV-XUV}}$-dependent amplitude of the XUV field given by Eq. 5.4 is imprinted on the photoelectron momentum distribution. For simplicity, lets consider the modulation of the XUV field at the helium Rydberg transition frequency ω_{Ryd}. The amplitude of the XUV field at ω_{Ryd} can be Fourier transformed along $\tau_{\text{XUV-XUV}}$. The signal in the FTPS is then given by

$$S^{(p)}(\omega_{\mathrm{Ryd}}, \tau_{\text{XUV-XUV}}) = \left| \left[\int_{-\infty}^{+\infty} \left(E_{\mathrm{NIR}}(t) + E_{\mathrm{NIR}}(t - \tau_{\text{XUV-XUV}}) \right)^p e^{i\omega t} dt \right]_{\omega=\omega_{\mathrm{Ryd}}} \right|^2 \tag{5.6}$$

and oscillates with ω_{Ryd}, leading to a peak at the helium transition frequency ω_{Ryd} in the FTPS.

In addition, the main signal carries a modulation with ω_{NIR} (cf. Fig. 5.10), which leads to artifact peaks at a distance of $\omega_{\mathrm{Ryd}} \pm \omega_{\mathrm{NIR}}$. The ω_{NIR}-modulation of the photoelectron fragment yield can be seen in Fig. 5.11 (a)-(c) for small $\tau_{\text{XUV-XUV}} \lesssim 10\,\mathrm{fs}$, and a similar ω_{NIR}-modulation of the yield appears at $\tau_{\text{XUV-XUV}} \sim 50\,\mathrm{fs}$, which is due to the interference of one of the main pulses with a small pre-pulse, that arrives 50 fs before the main pulse. The artifact peaks substantially decrease, and even disappear when the data with the strongest ω_{NIR}-modulation is excluded from the FT processing. This can be seen in Fig. 5.13, where the normalized momentum-integrated FTPS $\mathrm{FS}_{\beta_{0,2,4}}(p_{e^-}, \omega_{\mathrm{FT}})$ of $\beta_{0,2,4}(p_{e^-}, \tau_{\text{XUV-XUV}})$ is shown, after Fourier transforming only the measured photoelectron fragment yield for $\tau_{\text{XUV-XUV}} \geq 80\,\mathrm{fs}$.

The next sequence of peaks emerge at $(21.1262 \pm 0.0023,\ 21.4280 \pm 0.0004,\ 21.5968 \pm 0.0007)$ eV and $(26.3635 \pm 0.0005,\ 26.6689 \pm 0.0007,\ 26.8380 \pm 0.0014)$ eV, which is consistent with the energies of the Rydberg states displaced by $\pm(2.620 \pm 0.005)$ eV. This energy corresponds to the central wavelength of the blue cw laser (473.24 ± 0.83) nm, which actively stabilizes the MZI. As described in sect. 3.4.2 the set time delay $\tau_{\text{XUV-XUV}}$ is converted to a phase $\phi_\tau = \tau_{\text{XUV-XUV}}/2\pi T_{\mathrm{cw}}$, which depends on the cw laser period T_{cw}, and thus on the wavelength of the stabi-

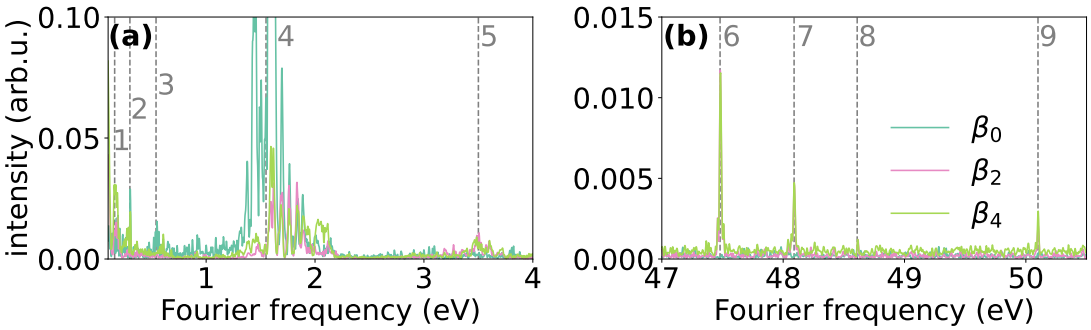

Figure 5.14: Normalized momentum-integrated FTPS $\mathrm{FS}_{\beta_{0,2,4}}(p_{e^-}, \omega_{\mathrm{FT}})$ of $\beta_{0,2,4}(p_{e^-}, \tau_{\text{XUV-XUV}})$ zoomed into (a) the low Fourier frequency region, and (b) the high Fourier frequency region to visualize additional peaks occurring in the FTPS.

lization laser. The set delay, i.e. phase is then fed into a PID controller, and is reached slowly by scanning over multiples of $2\pi T_{\mathrm{cw}}$.

Ideally, the set phase ϕ_τ and the actual phase ϕ_{actual}, i.e. the phase read out by the interference of the two arms of the cw laser are identical. However, in reality the actual delay position ϕ_{actual} can have a finite phase-dependent deviation from the set delay ϕ_τ, i.e. $\phi_{\mathrm{actual}} \neq \phi_\tau$. In the current case the actual phase has a small random (rnd) modulo-2π modulation depending on the wavelength of the blue cw laser, i.e. $\phi_{\mathrm{actual}} = \phi_\tau + rnd \cdot \phi_\tau (\mathrm{mod} 2\pi)$. This modulation leads to artifact peaks at $\omega_{\mathrm{Ryd}} \pm 2.62\,\mathrm{eV}$. It should be noted that the intensities of the artifact peaks are at least two orders of magnitude smaller than the Rydberg peaks, and thus do not jeopardize the practicality of the setup.

FTPS at high and low energy In Fig. 5.14 the normalized momentum-integrated FTPS $\mathrm{FS}_{\beta_{0,2,4}}(p_{e^-}, \omega_{\mathrm{FT}})$ of $\beta_{0,2,4}(p_{e^-}, \tau_{\text{XUV-XUV}})$ are shown in (a) at low, and in (b) at high Fourier frequencies.

In Fig. 5.14 (a) the most pronounced peak is labeled as peak 4 at an energy corresponding to the photon energy of the NIR probe pulse centered at $\sim 1.55\,\mathrm{eV}$. Peak 1, and 2 have an energy of $(0.1699 \pm 0.0014)\,\mathrm{eV}$ and $(0.2954 \pm 0.0017)\,\mathrm{eV}$, respectively, which corresponds in good approximation to the energy of the quantum beat between state 1s5p and 1s6p, i.e. $\Delta E_{\text{5p-6p}} = 0.1652$ [329], and the quantum beat of the 1s4p and 1s5p Rydberg states, i.e. $\Delta E_{\text{4p-5p}} = 0.3037$ [329], respectively. Peak 3 emerges at $(0.5453 \pm 0.0051)\,\mathrm{eV}$, which is close to the energy of the quantum beat between the 1s4p and 1s7p state, i.e. $\Delta E_{\text{4p-7p}} = 0.5686$ [329]. Peak 5 appears at a center energy of $(3.2768 \pm 0.0020)\,\mathrm{eV}$, which is approximately twice the NIR photon energy.

In Fig. 5.14 (b) the first three peaks labeled as 6, 7, and 8 occur at an energy of $(47.4850 \pm 0.0028)\,\mathrm{eV}$, $(48.0925 \pm 0.0028)\,\mathrm{eV}$, and $(48.6152 \pm 0.0006)\,\mathrm{eV}$, which are twice the energies of the 1s4p, 1s6p, and 1s7p Rydberg states, respectively. Peak 9 has an energy of $(50.1021 \pm 0.0032)\,\mathrm{eV}$, which corresponds to an artifact peak at $2 \cdot \omega_{\text{1s4p}} + 2.6\,\mathrm{eV}$.

The harmonic peaks with energies of twice the energies of the Rydberg states or twice the NIR photon energy are artifact peaks due to the Fourier transform.

5.3 Conclusion

In this chapter, different Fourier transform spectroscopy experiments are presented. The autocorrelation measurements of the NIR pulse pair as well as XUV pulse pair allowed to retrieve the underlying spectral information of the pulses. In addition, the dynamics, and consequences occurring due to the inference of the two phase-locked driving NIR pulses during HHG are investigated. In general, the phase-locked pair of attosecond pulses can be scanned over a 400 fs delay range with a sub-10-as residual jitter. Hence, with another Fourier transform spectroscopy experiment the well known helium Rydberg energies are measured with an absolute accuracy of 0.002%. This paves the way to use this setup for experiments investigating the implications of entanglement in bipartite quantum systems, as is described in the next chapters.

chapter 6

Ion+photoelectron entanglement vs vibrational coherence

In the next chapters the main experimental results of this thesis are presented, where the crucial role of entanglement between different subsystems in attosecond pump-probe experiments is investigated. In the following experiment, the vibrational wave packet dynamics in H_2^+ formed during the ionization of H_2 by two-phase locked XUV pulses are analyzed. In particular, it is studied how the observability of the coherence-based vibrational dynamics in the ion is limited by entanglement between the ion and the departing photoelectron, created during the photoionization process. In particular, the vibrational states of the ion are entangled with the kinetic energy of the photoelectron. It is further analyzed how the degree of vibrational coherence in the ion and the degree of ion+photoelectron entanglement, respectively, depend on the delay between the two ionizing XUV pulses, and how the degree of entanglement can be quantified.

The main results presented here are published in Physical Review Letters [2], and the Proceedings of the ATTO 8 conference [3]. The accompanying theoretical work was performed by M. J. J. Vrakking, and can be found in [9], and [143]. Recently a paper by Y. Nabekawa et. al [144] was published, which extends the aforementioned theoretical work by solving the time-dependent Schrödinger equation (TDSE) analytically.

Publication information

Parts of this chapter are published in

- *Experimental control of quantum-mechanical entanglement in an attosecond pump-probe experiment* by L.-M. Koll, L. Maikowski, L. Drescher, T. Witting, and M. J. J. Vrakking in Physical Review Letters, vol. 128, no. 4, p. 043201 (2022) [2]. DOI: `https://doi.org/10.1103/PhysRevLett.128.043201`

  Author contributions: The experiments were performed and the data was analyzed by L.-M. Koll under the supervision of T. Witting. The conceptual idea and the theoretical work were developed by M. J. J. Vrakking. The main figures of the manuscript were produced by L.-M. Koll, and the manuscript was written by M. J. J. Vrakking with the help and discussion of the other co-authors.

- *Control of photoelectron-ion entanglement in attosecond laser-induced photoionization of H_2* by L.-M. Koll, T. Witting, and M. J. J. Vrakking in Proceedings of the 8th International Conference on Attosecond Science and Technology (ATTO 8). Springer Proceedings in Physics, vol 300. Springer, pp. 155-165 (2024) [3].
  DOI: `https://doi.org/10.1007/978-3-031-47938-0_15`

  Author contributions: The experiments were performed and the data was analyzed by L.-M. Koll under the supervision of T. Witting. The conceptual idea, the theoretical work and calculations were developed by M. J. J. Vrakking. The manuscript was written by L.-M. Koll and M. J. J. Vrakking, where the part about the experimental results was mainly written by L.-M. Koll, and the part about the theoretical calculations was mainly written by M. J. J. Vrakking.

6.1 Vibrational wave packet and bond-softening

In the current experiment two phase-locked attosecond pulse trains (APTs) (cf. Fig. 3.9 in chapt. 3) are used to ionize H_2 creating a coherent superposition of vibrational states in the $1s\sigma_g$ state of H_2^+ (cf. Fig. 6.1). The emerging vibrational wave packet then oscillates within the $1s\sigma_g$ potential curve until a NIR probe pulse dissociates the molecule. The dynamics of a vibrational wave packet in the $1s\sigma_g$ state of H_2^+ upon XUV ionization were first investigated by Kelkensberg et al. [196]. General descriptions and investigations of vibrational wave packet dynamics in different molecules can be found in [194, 330–338]. The following equations, and corresponding explanations are based on these references.

Vibrational wave packet In general, a vibrational wave packet represents a coherent superposition of intermediate ionic states, which can be expressed as

$$|\psi_v(t)\rangle = \sum_v b_v |v\rangle \exp(-iE_v t/\hbar), \tag{6.1}$$

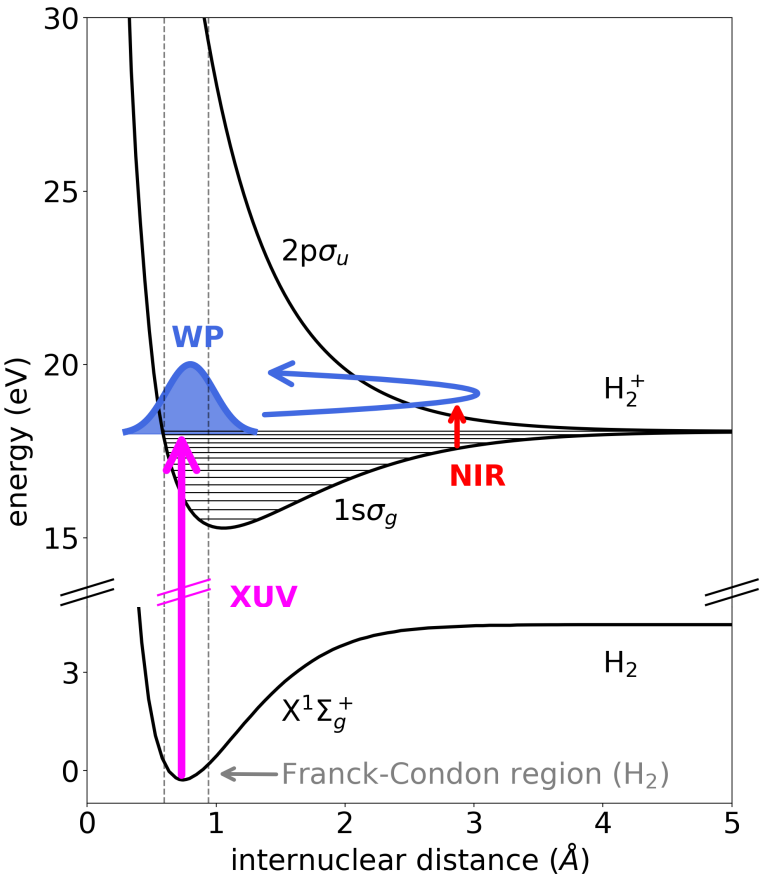

Figure 6.1: Illustration of the XUV+NIR dissociative ionization of a hydrogen molecule. The XUV pulse launches a vibrational wave packet (WP) in the $1s\sigma_g$ state of H_2^+, which is subsequently projected onto the repulsive $2p\sigma_u$ state by the NIR pulse, leading to H^++H dissociation (here: low NIR laser intensity). The bandwidth of the XUV pulses in the current experiment is between 15 and 42 eV, and is thus high enough to excite all vibrational states. The NIR pulse is approximately 5 fs long, and it's photon energy is centered at 1.55 eV (red arrow). Consequently, the probe pulse can only probe the highest vibrational states at the outer turning point of the $1s\sigma_g$ potential. The data points for the $X^1\Sigma_g^1$, and $1s\sigma_g$ potential curve in H_2 and H_2^+, respectively, as well as the $2p\sigma_u$ potential curve are taken from [339]. The Franck-Condon region[1]corresponds to the H_2 vibrational ground state $v_g = 0$. The vibrational energy levels are calculated according to Eq. 6.3 with the constants from [340].

where $|v\rangle$ is the wave function of the vibrational state v with the energy E_v, and b_v is a constant coefficient. The NIR probe pulse now projects these intermediate vibrational states after a variable time t to a final state $|f\rangle$. The detailed derivation of such a pump-probe scheme can be found in sect. 2.2.3. The final detected signal is given according to Eq. 2.49 by

$$S(t) \sim \sum_{v,v' \neq v} 2p_v p_{v'} \cos((E_v - E_{v'})t/\hbar), \tag{6.2}$$

where $p_v = \Re\left\{E_q(\omega_{vg})E_p(\omega_{fv})\,\langle f|\vec{d}|v\rangle\,\langle v|\vec{d}|g\rangle\right\}$, which describes the transition of the system from an initial ground state $|g\rangle$ to an intermediate ionic state $|v\rangle$ by absorbing a photon of the pump pulse with an energy of $\omega_{vg} = E_v - E_g$, and subsequently the transition from $|v\rangle$ to a final state $|f\rangle$ by absorbing a photon of the probe pulse with an energy of $\omega_{fv} = E_f - E_v$. Here $E_q(\omega_{vg})$, and $E_p(\omega_{fv})$ are the spectral amplitudes of the pump and probe pulse, respectively, at the frequencies ω_{vg}, and ω_{fv}. The dipole operator is $\vec{d}$.

It should be noted that the system starts in one common ground state, and ends up in one final state. However, multiple intermediate vibrational states can be excited simultaneously, due to the broad bandwidth of the XUV pulses (here: $15-42\,\mathrm{eV}$). Consequently, the measured signal consists of beat frequencies between pairs of intermediate vibrational levels.

In H_2^+ the $1s\sigma_g$ energy potential well can be approximated as an anharmonic oscillator (i.e. Morse potential [342]), with energy levels at

$$E_v = \hbar\omega_{\mathrm{vib}}(v - \alpha v^2), \tag{6.3}$$

where ω_{vib} is the fundamental frequency, and α is the anharmonicity parameter ($\omega_{\mathrm{vib}} = 2321.7\,\mathrm{cm}^{-1}$ and $\omega_{\mathrm{vib}}\alpha = 66.2\,\mathrm{cm}^{-1}$ [340]). The energy difference between consecutive vibrational levels decreases with increasing v, and Eq.6.3 is valid until an upper limit $v_{\max}$, where $E_{v_{\max}+1} - E_{v_{\max}} \leq 0$.

Each vibrational eigenstate evolves in time with a particular phase factor $\phi_v(t) = E_v t/\hbar$, given by the state's energy. The phase of the quantum beats between the two vibrational states v and v' is given by

$$\phi_{v,v'}(t) = (E_v - E_{v'})t/\hbar = 2\pi\frac{t}{T_{\mathrm{rev}}}\left(\frac{v-v'}{\alpha} - v^2 + (v')^2\right), \tag{6.4}$$

and the vibrational period of the quantum beat $\Delta E_{v,v'}$ is $\Delta t = 2\pi\hbar/\Delta E_{v,v'}$, which is for example $\Delta t_{8,9} = 28.5\,\mathrm{fs}$ for $\Delta E_{8,9} = 0.16\,\mathrm{eV}$. After a few vibrational periods, the initially well localized wave packet dephases, since ≥ 3 states contribute and

[1]The Franck-Condon principle [341] states that the excitation from one vibrational level to another is more probable the more the wave functions overlap. In general, the total molecular wave function can be expressed as a superposition of an electronic $|\phi_e\rangle$ and vibrational $|\phi_v\rangle$ wave function, i.e. $|\Phi\rangle = |\phi_e\rangle\,|\phi_v\rangle$. The probability amplitude of the transition from $|\Phi\rangle$ to $|\Phi'\rangle$ is given by $P \propto \langle\phi'_e|\widehat{d}|\phi_e\rangle\,\langle\phi'_v|\phi_v\rangle$. The term $\langle\phi'_v|\phi_v\rangle$ describes the overlap between the initial and final state of the vibrational wave function, and is known as the Franck-Condon factor. In other words a transition with a minimal change in the nuclear coordinates is favored.

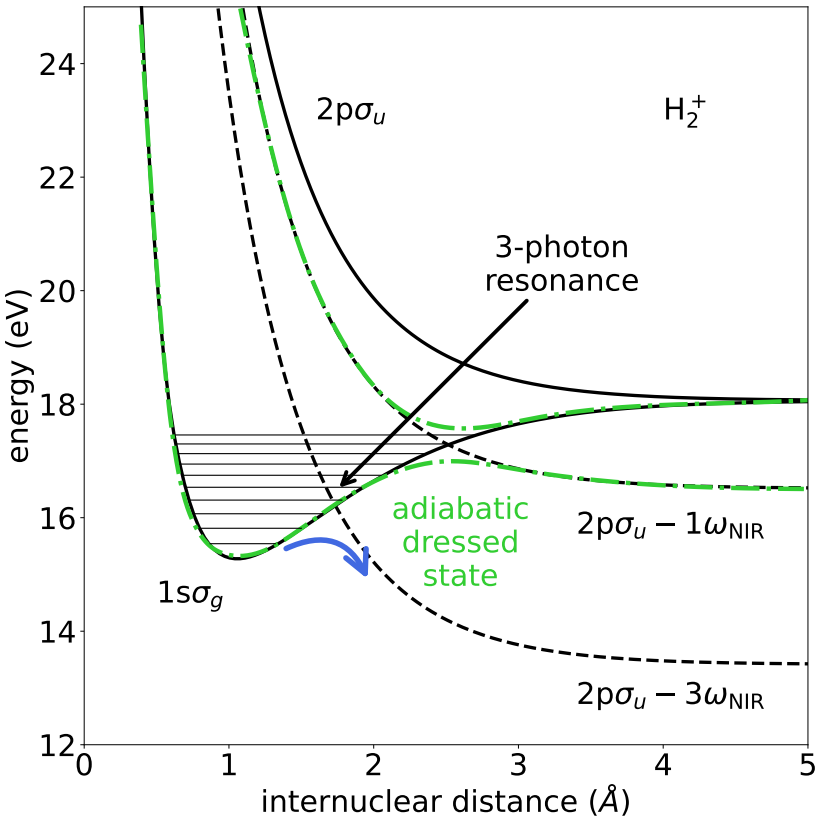

Figure 6.2: Illustration of the bond softening process in a hydrogen molecule. At high NIR probe laser intensities the molecule becomes "dressed" in photons (dashed line), leading to adiabatic dressed states (green dashed line, only approximated for low TW/cm^2 intensity), which results in new dissociation pathways. The NIR photon energy is $\omega_{\mathrm{NIR}} = 1.55\,\mathrm{eV}$. The data points for the $1s\sigma_g$, and $2p\sigma_u$ potential curves are taken from [339], and the vibrational energy levels are calculated after Eq. 6.3 with the constants from [340].

the energy difference $\Delta E_{v,v'}$ between consecutive vibrational levels is not constant.

The revival time of the wave packet, i.e. the time after the wave packet reaches again its initial phase is given by $T_{\mathrm{rev}} = 2\pi/\omega_{\mathrm{vib}}\alpha$, which is $T_{\mathrm{rev}} \approx 509\,\mathrm{fs}$ in the case of H_2^+. Prior to a full wave packet revival, the wave packet can break into sets of sub-wave packets at times of $t/T_{\mathrm{rev}} = n/m$, with n and m as integers. At these fractional revival times the vibrational eigenfunctions have a defined phase between each other in such a way that the total wave function behaves as two interfering wave packets with a certain phase $\Delta\phi$ between them.
For example at a half-revival time $t = T_{\mathrm{rev}}/2$, a wave packet made out of all even-v eigenstates is phase shifted by $\Delta\phi = \pi$ in respect to a wave packet consisting of all odd-v eigenstates, and as a result the total vibrational wave packet is phase shifted by π compared to the initial total wave packet at $\Delta\phi = 0$.

A fractional revival occurs at for example $t = T_{\mathrm{rev}}/4$. Here the phase shift is $\Delta\phi = \pi/2$, and the wave packet is split into two sub-wave packets, resulting in the same probability to find the wave packet at the inner turning point as well as the outer turning point of the potential.

Bond softening The created vibrational wave packet oscillates between the inner and outer turning point of the $1s\sigma_g$ potential curve, until after a variable time delay $\tau_{\text{XUV-NIR}}$ the NIR probe pulse projects the wave packet onto the repulsive $2p\sigma_u$ state leading to the H^++H dissociation of the H_2^+ molecule. If the NIR laser intensity is high enough typically around and above $10^{13}\,\mathrm{Wcm^{-2}}$ the dissociation occurs via the process of bond softening [343–348], which is beyond the derivation in section 2.2.3.

Bond softening describes the effect that the energy of the potential curves in H_2^+ are altered in the presence of an intense laser field, i.e. the molecular states become "dressed" in photons. In Fig. 6.2 the basic mechanism of bond softening with a laser center frequency of $\omega_{\mathrm{NIR}} = 1.55\,\mathrm{eV}$ is illustrated. Due to the high laser intensity the molecule constantly absorbs and re-emits photons leading to a $n\omega_{\mathrm{NIR}}$ shift (with n as an integer) of the potential curves, which is shown for the two cases $2p\sigma_u - 1\omega_{\mathrm{NIR}}$, and $2p\sigma_u - 3\omega_{\mathrm{NIR}}$ in Fig. 6.2. The crossing of the dressed states with the $1s\sigma_g$ potential curve corresponds to a 1-photon and 3-photon resonance, respectively. In order to calculate the new energy curves of the system in the presence of the laser field, the perturbation has to be included in the Hamiltonian, which commonly introduces off-diagonal matrix elements. The eigenvalues of the perturbed system are calculated by diagonalising the matrix. As a result, at a former crossing point two eigenvalues are found, turning the crossing into avoided crossings, which leads to new adiabatic dressed states in the perturbed system [349–351]. The gap in between the two resulting dressed states becomes larger the higher the laser intensity is for a given photon energy [345, 347]. As the vibrational wave packet propagates within the $1s\sigma_g$ potential, and eventually reaches a crossing point, the molecule dissociates along the adiabatic dressed state by absorbing one or more NIR photons. This leads to H^+ fragments with higher kinetic energies than in the case of a NIR probe pulse with low intensity, and thus dissociative ionization without bond softening.

For example in Fig. 6.2 the adiabatic dressed state at a 1-photon resonance leaves all vibrational levels $v \geq 6$ unbound. Accordingly, the H^+ fragments with the lowest kinetic energy observed initiate from $v = 6$, with an energy of $E_{H^+} = 1/2(E_{v=6} - \mathrm{IP}_{H_2^+} + \omega_{\mathrm{NIR}}) = 0.21\,\mathrm{eV}$, where $\mathrm{IP}_{H_2^+} = 18.1\,\mathrm{eV}$ [352] is the dissociative ionization threshold, $\omega_{\mathrm{NIR}} = 1.55\,\mathrm{eV}$, and $E_{v=6} = 16.96\,\mathrm{eV}$ (calculated after Eq. 6.3 with the constants from [340]). Without bond softening H^+ fragments from $v = 6$ wouldn't even be observed in the current case, since in order to project the vibrational eigenfunction from $v = 6$ to the $2p\sigma_u$ state at the outer turning point of the $1s\sigma_g$ potential a photon energy of 2.4 eV is necessary.

6.2 Experimental results

In this experiment, two phase-locked APTs, created via HHG by two identical phase-locked NIR pulses with a pulse duration of 5 fs, are used to ionize hydrogen molecules. An example of the XUV spectra can be found in Fig. 3.9 in chapt. 3 for two different $\tau_{\text{XUV-XUV}}$, showing an XUV energy up to 42 eV with a fringe modulation $\delta\omega_{\text{XUV}} = 2\pi/\tau_{\text{XUV-XUV}}$ inversely proportional to the XUV pulse delay.

The two XUV pulses are scanned over a range of 11 fs to 102 fs in $\delta\tau_{\text{XUV-XUV}} = 3$ fs steps. The lower limit of $\tau_{\text{XUV-XUV}}$ is chosen in a way, that the regime is avoided where the interference of the two driving NIR pulses during the HHG process is most pronounced (cf. section 5.1.2). The upper limit is restricted by the total duration of the whole measurement. The delay $\tau_{\text{XUV-XUV}}$ is measured relative to XUV pulse B, which is fixed in time. For $\tau_{\text{XUV-XUV}} > 0$ fs XUV pulse A comes prior to XUV pulse B.
The NIR probe pulse has a pulse duration of $\sim$ 5 fs, a center wavelength of 790 nm, and an intensity of $\sim 10^{13}$ W/cm^2. The time delay $\tau_{\text{XUV-NIR}}$ is measured in respect to the fixed XUV pulse B. For $\tau_{\text{XUV-NIR}} < 0$ fs the NIR probe pulse comes prior to the XUV pulse B. The pump-probe delay is scanned in a certain range between -100 fs and 800 fs in $\delta\tau_{\text{XUV-NIR}} = 4$ fs steps.
After the XUV+NIR dissociative ionization of the hydrogen molecules, the H^+ ions are measured using the VMI spectrometer. Each image is recorded for 2000 laser shots as a function of $\tau_{\text{XUV-XUV}}$ and $\tau_{\text{XUV-NIR}}$ repeated for up to 8 pump-probe scans.
In Fig. 6.3 (a) a recorded VMI image is shown. The H^+ momentum distribution exhibits a signal at the center of the image, which results from direct dissociative ionization from the $1s\sigma_g$ potential by a single XUV photon, and is independent of the NIR probe pulse. The high XUV photon energy allows to populate all vibrational states within the $1s\sigma_g$ potential creating a vibrational wave packet, which starts to oscillate between the inner and outer turning point of the potential.
Firstly, the $1s\sigma_g$ potential is bonding and the vibrational wave packet seems to be trapped without the interaction with a probe pulse. However, with a certain probability the vibrational wave packet can tunnel out at the outer turning point of the potential, and the molecule can dissociate into fragments with low kinetic energy, which results in the signal shown at the center of the VMI image. This signal is used to normalize each VMI image, since it depends linearly on the density of the H_2 gas, and the XUV photon flux.
The 3D H^+ momentum distribution is retrieved by Abel inversion [14] (cf. section 3.5.1). The corresponding inverted VMI image is shown in Fig. 6.3 (b). The probability distribution can be expressed as a superposition of Legendre polynomials, and since the XUV+NIR dissociative ionization is a two-photon process, the distribution is given by

$$\begin{aligned} P\left(v_{H^+}, \cos\theta, \tau_{XX}, \tau_{XN}\right) &= \beta_0\left(v_{H^+}, \tau_{XX}, \tau_{XN}\right) \\ &\quad \times \left[1 + \beta_2\left(v_{H^+}, \tau_{XX}, \tau_{XN}\right) P_2\left(\cos\theta\right)\right. \\ &\quad \left. + \beta_4\left(v_{H^+}, \tau_{XX}, \tau_{XN}\right) P_4\left(\cos\theta\right)\right], \end{aligned} \tag{6.5}$$

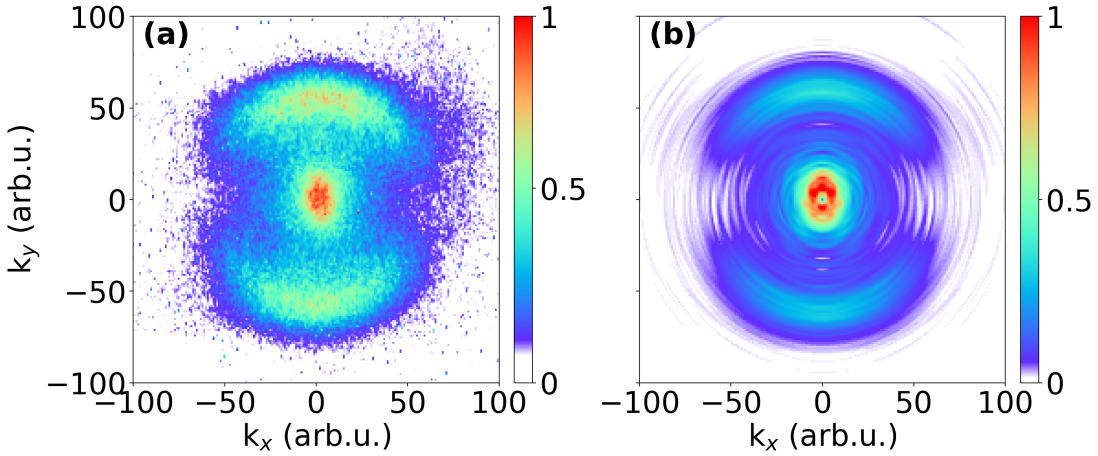

Figure 6.3: (a) Measured VMI image of the H^+ fragment yield. (b) Abel-inverted H^+ VMI image, corresponding to a cut through the 3D momentum distribution.

where $\tau_{XX} = \tau_{XUV\text{-}XUV}$ and $\tau_{XN} = \tau_{XUV\text{-}NIR}$. Furthermore $P_2(\cos\theta)$ and $P_4(\cos\theta)$ are the Legendre polynomials of the 2nd and 4th order.

In Fig. 6.4 (a) the H^+ fragment yield summed over a small region (30 pixels) around $k_x = 0$ at a delay of $\tau_{XUV\text{-}XUV} = 22\,\text{fs}$ and as a function of $\tau_{XUV\text{-}NIR}$ is shown to illustrate the vibrational dynamic of the molecule. It can be seen that for $\tau_{XUV\text{-}NIR} < -22\,\text{fs}$, i.e. the NIR probe pulse comes prior to both XUV pulses, the VMI images show mainly a contribution at the center (cf. Fig. 6.4 (b)). Since the NIR pulse is too weak to ionize the H_2 molecule, only H^+ fragments resulting from direct dissociative ionization by the XUV pulses are observed. For a delay of $\tau_{XUV\text{-}NIR} \geq 0\,\text{fs}$, i.e. the probe pulse comes at the same time or after the pump pulses, the interaction of the NIR pulse with the XUV ionized H_2^+ then leads to the dissociation of the molecule on the $2p\sigma_u$ potential.

In Fig. 6.4 (c) the H^+ fragments resulting from the two-color dissociative ionization can be seen at high momenta (half-ring shaped signal). The XUV+NIR dissociative ionization signal oscillates as a function of $\tau_{XUV\text{-}NIR}$ with a period of $T_{vib} \sim 30\,\text{fs}$ for $\tau_{XUV\text{-}NIR} \geq 0\,\text{fs}$ (cf. Fig. 6.4 (a)). The dissociation of the vibrational wave packet only occurs at the outer turning point of the $1s\sigma_g$ potential curve, due to the limited NIR photon energy. Accordingly, the period T_{vib} corresponds to the time the vibrational wave packet needs for one full oscillation within the $1s\sigma_g$ potential. After a few clearly visible oscillations, the vibrational structure of the wave packet washes out at $\tau_{XUV\text{-}NIR} \sim 100\,\text{fs}$, and revives again at $\tau_{XUV\text{-}NIR} \sim 250\,\text{fs}$. Accordingly in Fig. 6.4 (a) the dephasing and rephasing of the vibrational wave packet can be observed. The delay of the first occurring revival $\tau_{XUV\text{-}NIR} \sim 250\,\text{fs}$ agrees nicely with the calculated half-revival time in H_2^+ of $T_{rev}/2 = 254.5\,\text{fs}$.

Main experimental results The main experimental results are presented in Fig. 6.5, showing the experimentally retrieved $\beta_0(v_{H^+}, \tau_{XX}, \tau_{XN})$ parameter

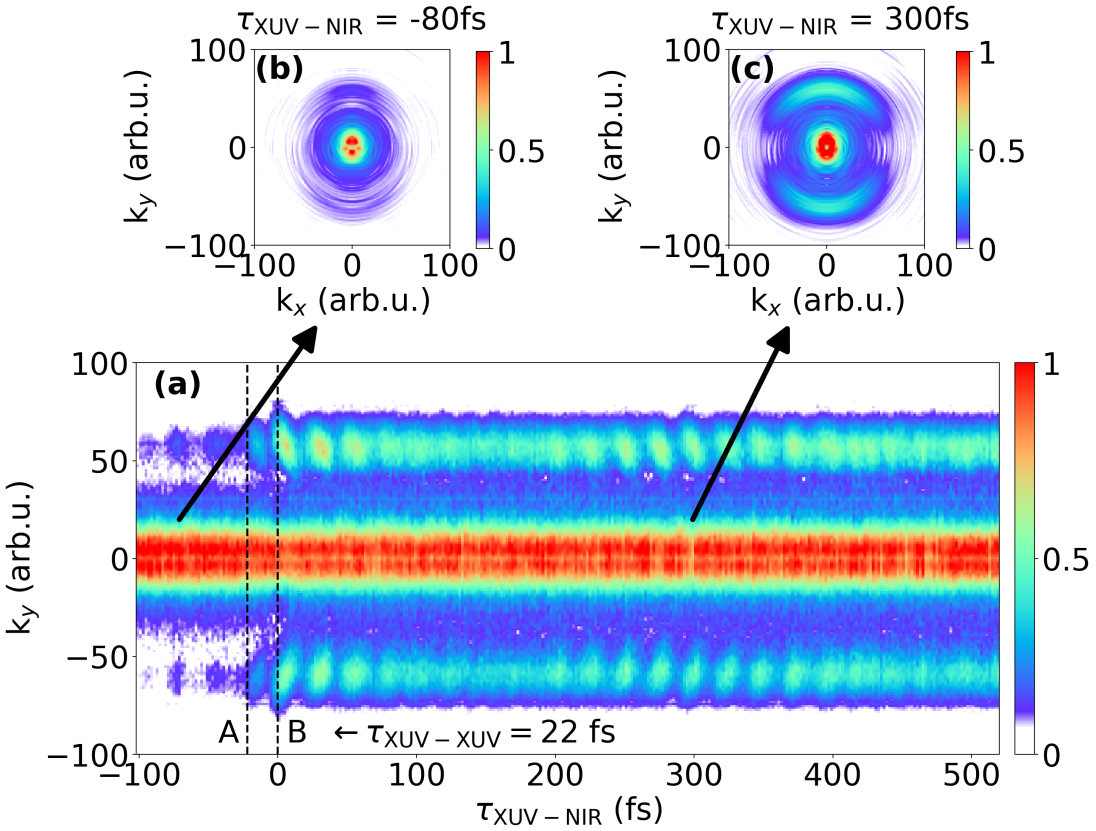

Figure 6.4: H^+ fragment yield as a function of the pump-probe delay for $\tau_{\text{XUV-XUV}} = 22\,\text{fs}$ exemplary. (a) Inverted VMI image summed over a small region of 30 pixels around $k_x = 0$ as a function of $\tau_{\text{XUV-NIR}}$, which highlights the dependence of the different H^+ contributions on the delay. The vertical axis is given in pixel units of the CCD camera, which is linearly related to the H^+ momentum. The two dashed vertical lines show the position of the two XUV pulses A and B, where B is fixed in time. (b) and (c) Inverted VMI image for $\tau_{\text{XUV-NIR}} = -80\,\text{fs}$, and 300 fs, showing that the contribution at high momentum (H^+ fragments resulting from XUV+NIR dissociative ionization) only occurs if the NIR pulse comes at the same time or after the XUV pulse ($\tau_{\text{XUV-NIR}} \geq 0\,\text{fs}$).

as a function of $\tau_{\text{XUV-NIR}}$ and v_{H^+} for different $\tau_{\text{XUV-XUV}}$. In Fig. 6.5 (a)-(d) $\beta_0\,(v_{H^+}, \tau_{\text{XX}}, \tau_{\text{XN}})$ is shown exemplary for four different delays, i.e. $\tau_{\text{XUV-XUV}} =$ 29 fs, 35 fs, 44 fs and 56 fs. Here again the oscillation of the vibrational wave packet with a period of $\sim 30\,\text{fs}$, as well as dephasing and rephasing of the wave packet every $\sim 250\,\text{fs}$ is clearly visible. The delay dependent signal is then Fourier transformed along $\tau_{\text{XUV-NIR}}$, and the corresponding Fourier transform power spectra (FTPS) $\text{FS}_{\beta_0}(v_{H^+}, \tau_{\text{XX}}, \omega_{\text{FT}})$, with ω_{FT} as the Fourier frequency, is shown in Fig. 6.5 (e)-(h).

The FTPS is dominated by nearest- and next-nearest-neighbor quantum beats $\Delta E_{v,v'} \equiv \Delta E(v, v')$, which are due to the interference of the dissociative ionization pathways involving the two vibrational states v and v'. The most pronounced

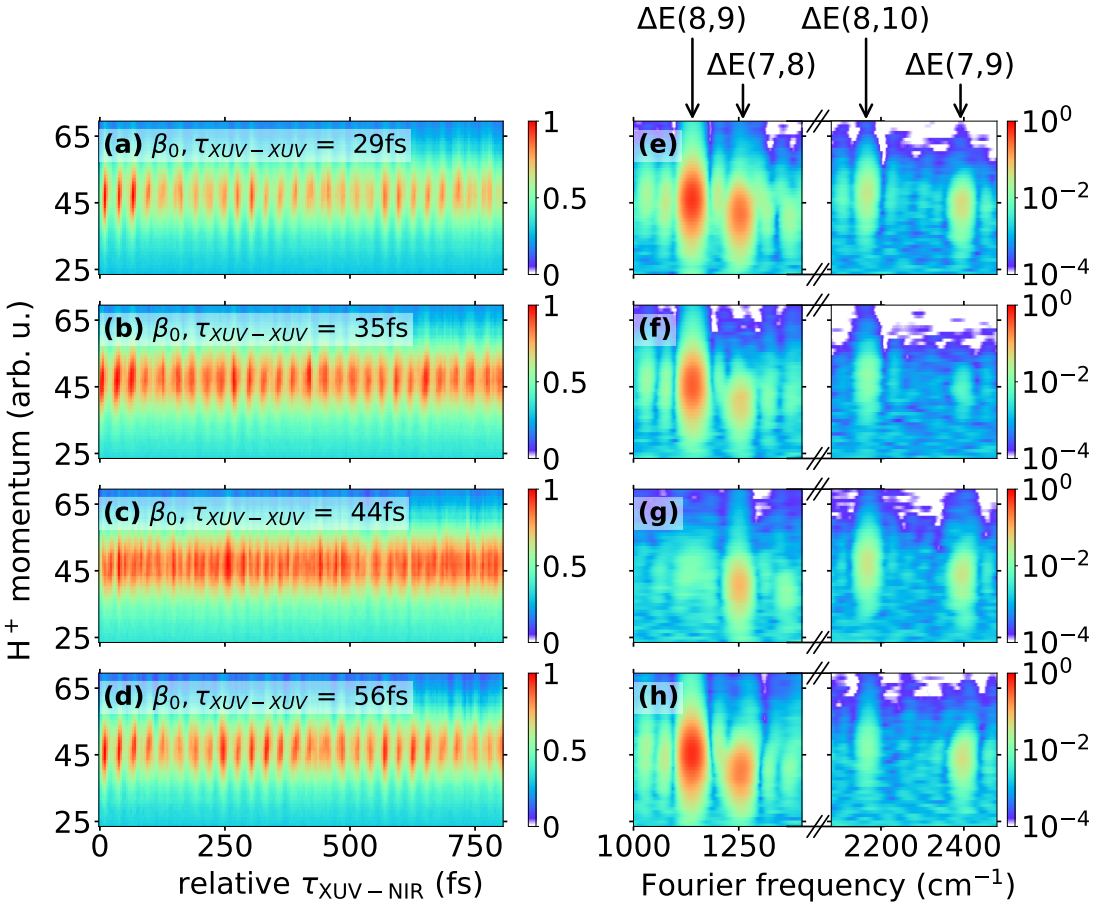

Figure 6.5: Measurement of the vibrational wave packet dynamics upon ionization of H_2 by two phase-locked XUV pulses with a time delay of $\tau_{\text{XUV-XUV}} = 29\,\text{fs}$, 35 fs, 44 fs, and 56 fs. (a)-(d) $\beta_0\,(v_{H^+}, \tau_{XX}, \tau_{XN})$ parameter retrieved by Abel inversion of the measured VMI images. The vertical axis corresponds to the H^+ velocity in arbitrary units, which is given in pixel units of the CCD camera recording the VMI images. Each figure shows the averaged trace over four consecutive pump-probe scans. (e)-(h) Fourier transform power spectra $\text{FS}_{\beta_0}(v_{H^+}, \tau_{XX}, \omega_{FT})$ of the corresponding $\beta_0\,(v_{H^+}, \tau_{XX}, \tau_{XN})$ parameter retrieved by Fourier transforming the data in (a)-(d) along $\tau_{\text{XUV-NIR}}$. Each figure shows the averaged FTPS of four consecutive pump-probe scans. Pronounced quantum beats $\Delta E(v, v')$ are visible, which are due to the interference of dissociative ionization pathways involving the two vibrational states v and v'. The found frequency $\omega_{\text{FT, XUV-NIR}}$ of each quantum beat is listed in table 6.1 in column 2.

quantum beats are assigned to nearest-neighbor vibrational level (8,9), (7,8), and next-nearest-neighbor vibrational states (8,10), (7,9) by comparing the found values to the literature [353]. As aforementioned, the XUV photon energy is high enough to populate all vibrational states, however the population probability decreases with increasing v, due to the Franck-Condon principle [341]. Accordingly the measured signal decreases with increasing v, limiting the highest observable quantum beat. On the other hand, the lowest vibrational states, which can be observed is defined by the NIR probe bandwidth and intensity, and is $v = 7$ in the current experiment, which agrees in good approximation with the theoretical prediction of bond softening (cf. Fig. 6.2).

The Fourier frequencies $\omega_{\text{FT,XUV-NIR}}$ of the different experimentally observed quantum beats can be found in column 2 in table 6.1, where they are compared to the literature values in the last column. In addition, the dynamics of the vibrational wave packet can be compared for the four different $\tau_{\text{XUV-XUV}}$. It can be seen that the oscillatory structure is different in the first three cases (cf. Fig. 6.5 (a)-(c)), whereas the structure in Fig 6.5 (a), and (d) are comparable. In the FTPS (cf. Fig. 6.5 (e)-(h)) the strength of the nearest- and next-nearest-neighbor quantum beats for the four different $\tau_{\text{XUV-XUV}}$ can be compared. In the first three cases (cf. Fig. 6.5 (e)-(g)) the strength of the nearest-neighbor quantum beats decrease with increasing $\tau_{\text{XUV-XUV}}$. In Fig. 6.5 (h) the strength of the nearest-neighbor quantum beats is comparable to the ones in Fig. 6.5 (e).
The strength of the next-nearest-neighbor quantum beats are comparable for the delays $\tau_{\text{XUV-XUV}} = 29\,\text{fs}$, and 44 fs, as well as $\tau_{\text{XUV-XUV}} = 35\,\text{fs}$, and 56 fs, whereas the signal of the next-nearest-neighbor quantum beats at $\tau_{\text{XUV-XUV}} = 35\,\text{fs}$, and 56 fs is decreased in intensity compared to $\tau_{\text{XUV-XUV}} = 29\,\text{fs}$, and 44 fs.

Fourier Peak	$\omega_{\text{FT,XUV-NIR}}$ (cm^{-1}) (Fig. 6.5)	$T_{\text{FT,XUV-NIR}}$ (fs) (Fig. 6.5)	$\omega_{\text{FT,XUV-XUV}}$ (cm^{-1}) (Fig. 6.6,6.9)	Assignment (v, v')	Literature value [353] (cm^{-1})
A	1138 ± 7	29.3 ± 0.3	1141 ± 7	$(8, 9)$	1130.1
B	1252 ± 7	26.6 ± 0.3	1259 ± 6	$(7, 8)$	1262.5
C	2168 ± 16	15.3 ± 0.2	2167 ± 11	$(8, 10)$	2127.8
D	2396 ± 17	13.9 ± 0.2	2387 ± 13	$(7, 9)$	2392.6

Table 6.1: Comparison of the experimentally obtained Fourier frequencies with the literature values [353]. In column 2 $\omega_{\text{FT,XUV-NIR}}$ is the Fourier frequency retrieved by Fourier transform of the pump-probe scan, and integrating $\text{FS}_{\beta_0}(v_{\text{H}^+}, \tau_{\text{XX}}, \omega_{\text{FT}})$ over v_{H^+}, using the data for only β_0 (see Fig. 6.5), and in column 3 the found $\omega_{\text{FT,XUV-NIR}}$ are converted into the corresponding oscillation periods $T_{\text{FT,XUV-NIR}}$. In column 4 $\omega_{\text{FT,XUV-XUV}}$ is retrieved by fitting the peak intensities of the FTPS as a function of $\tau_{\text{XUV-XUV}}$ to a sinusoidal curve (see Fig. 6.6, and Fig. 6.9).

A pump-probe scan as shown in Fig. 6.5 is carried out for $\tau_{\text{XUV-XUV}}$ between 11 fs and 102 fs in 3 fs steps. The intensities of the different quantum beats are then determined as a function of $\tau_{\text{XUV-XUV}}$, which is shown in Fig. 6.6. The

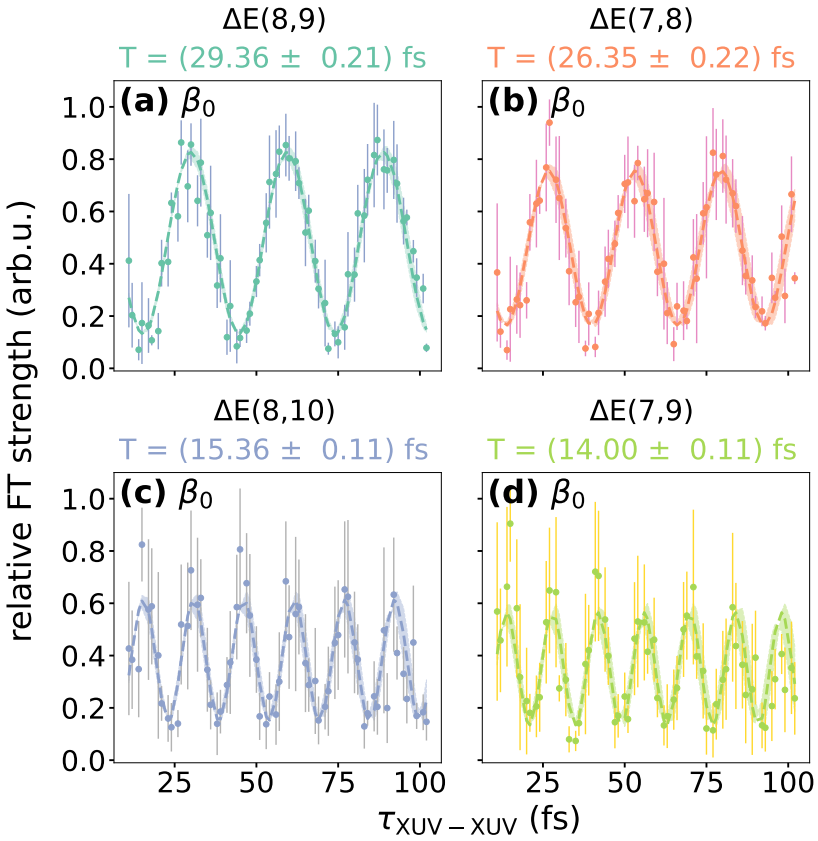

Figure 6.6: Intensity of the four quantum beats found in the Fourier transform power spectrum as a function of $\tau_{\text{XUV-XUV}}$. The FTPS intensities $\text{FS}_{\beta_0}(v_{\text{H}^+}, \tau_{\text{XX}}, \omega_{\text{FT}})$ of the β_0 $(v_{\text{H}^+}, \tau_{\text{XX}}, \tau_{\text{XN}})$ parameter are shown for (a) the nearest-neighbor quantum beat $\Delta E(8,9)$, where ω_{FT} corresponds to the energy difference between vibrational state $v = 8$ and $v' = 9$, (b) the nearest-neighbor quantum beat $\Delta E(7,8)$, where ω_{FT} corresponds to the energy difference between vibrational state $v = 7$ and $v' = 8$, (c) the next-nearest-neighbor quantum beat $\Delta E(8,10)$, where ω_{FT} corresponds to the energy difference between vibrational state $v = 8$ and $v' = 10$, and (d) the next-nearest-neighbor quantum beat $\Delta E(7,9)$, where ω_{FT} corresponds to the energy difference between vibrational state $v = 7$ and $v' = 9$. The experimental data are shown as points, and are fitted to a sinusoidal curve $(A + B\sin(2\pi(\tau_{\text{XUV-XUV}} - \tau_c)/T)$ with the fit parameters $A, B, \tau_c, T)$, which is given as a dashed line. The standard deviation of the fit parameters is presented as a shaded area. The oscillation period T retrieved by the fit is shown at the top of each figure, and the corresponding oscillation frequency $\omega_{\text{FT,XUV-XUV}}$ is listed in column 4 in table 6.1.

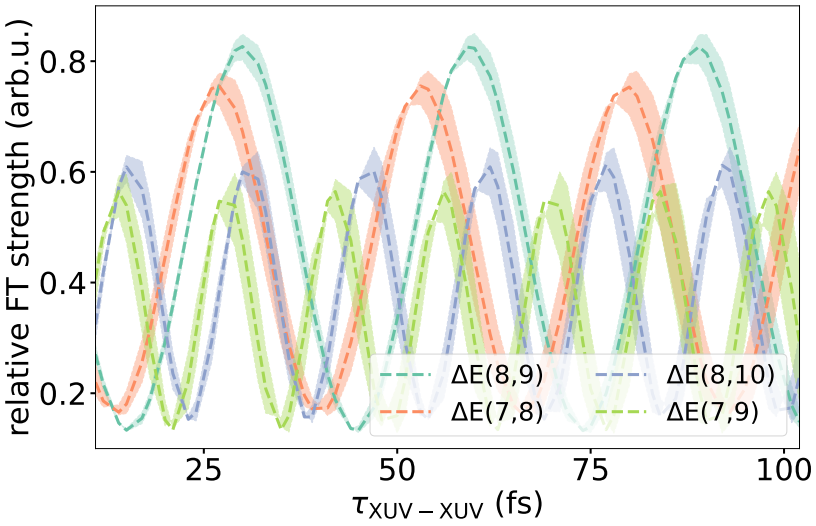

Figure 6.7: Sinusoidal curve fit of the intensities $\mathrm{FS}_{\beta_0}(v_{\mathrm{H}^+}, \tau_{\mathrm{XX}}, \omega_{\mathrm{FT,XUV\text{-}XUV}})$ of the $\beta_0\,(v_{\mathrm{H}^+}, \tau_{\mathrm{XX}}, \tau_{\mathrm{XN}})$ parameter for all four quantum beats $\Delta E(8,9)$, $\Delta E(7,8)$, $\Delta E(8,10)$, and $\Delta E(7,9)$ as in Fig. 6.6 to compare the phase and amplitude of the individual quantum beat oscillations. The shaded area is the standard deviation of the fit parameters. The data points and corresponding error bars are not plotted here to make the comparison more convenient.

intensities of the quantum beats oscillate as a function of $\tau_{\mathrm{XUV\text{-}XUV}}$ with a period, which is inversely proportional to the frequency of the individual quantum beats $\omega_{\mathrm{FT,XUV\text{-}XUV}}$, i.e. the energy difference between the two involved vibrational states $\Delta E(v, v')$. The period of the oscillation for each quantum beat is shown on top of each figure, and is retrieved by a sinusoidal curve fit of the experimental data points.

In Fig. 6.7 the fit of the experimental data points of $\beta_0\,(v_{\mathrm{H}^+}, \tau_{\mathrm{XX}}, \tau_{\mathrm{XN}})$ is compared for the different quantum beats. It can be seen that the minimum for all quantum beats is in good approximation the same. Furthermore the amplitude, and consequently the contrast between the minimum and maximum value of the intensity of the nearest-neighbor quantum beats is higher than for the next-nearest-neighbor quantum beats. This is expected since the probability for two vibrational states to be in a coherent superposition should decrease the more consecutive vibrational states are in between them.
In addition, it seems that the amplitude of the quantum beat $\Delta E(8,9)$ is slightly higher than for $\Delta E(7,8)$, as well as the amplitude of $\Delta E(8,10)$ is slightly higher than for $\Delta E(7,9)$. However given the error bars of the data points in Fig. 6.5 these small differences are insignificant.
For small $\tau_{\mathrm{XUV\text{-}XUV}}$ the nearest-neighbor as well as next-nearest-neighbor quantum beats, respectively, oscillate in phase, however the nearest-neighbor quantum beat oscillation is shifted by π compared to the next-nearest neighbor quantum beat oscillation. With increasing $\tau_{\mathrm{XUV\text{-}XUV}}$ the phase difference between the nearest-neighbor and next-nearest-neighbor quantum beat oscillations, re-

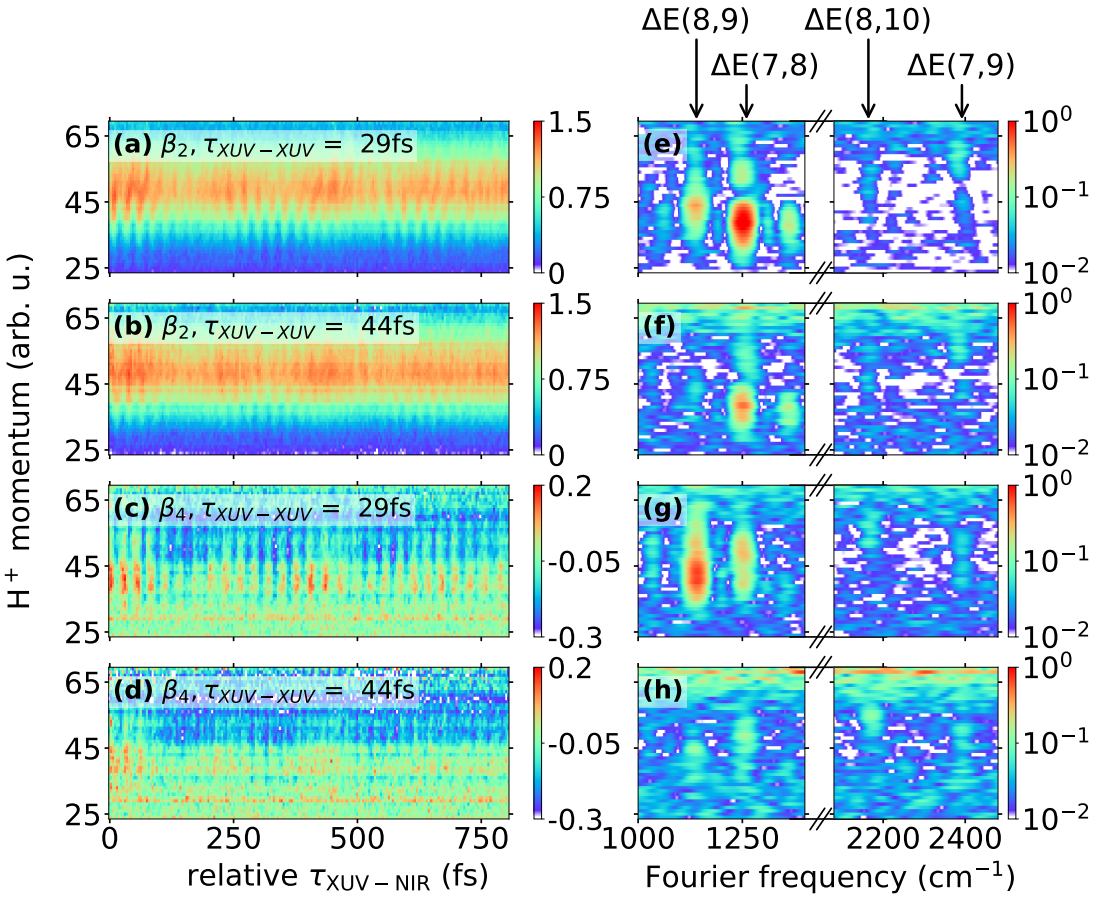

Figure 6.8: Vibrational wave packet dynamic for $\tau_{\text{XUV-XUV}} = 29\,\text{fs}$, and 44 fs. (a)-(b) $\beta_2\,(v_{\text{H}^+}, \tau_{\text{XX}}, \tau_{\text{XN}})$, and (c)-(d) $\beta_4\,(v_{\text{H}^+}, \tau_{\text{XX}}, \tau_{\text{XN}})$ parameter retrieved through Abel inversion of the raw VMI images. The vertical axis corresponds to the H^+ momentum, and is given in pixel units of the CCD camera. Each figure shows the averaged trace over four consecutive pump-probe scans. (e)-(h) shows the corresponding Fourier transform power spectra $\text{FS}_{\beta_{2,4}}(v_{\text{H}^+}, \tau_{\text{XX}}, \omega_{\text{FT}})$, which shows pronounce quantum beats $\Delta E(v, v')$ between nearest- and next-nearest neighbor vibrational states. Each figure shows the averaged FTPS of four consecutive scans.

spectively, increase. At the longest measured delay $\Delta E(8, 10)$ and $\Delta E(7, 9)$ are shifted by π relative to each other.

In addition to $\beta_0\,(v_{\text{H}^+}, \tau_{\text{XX}}, \tau_{\text{XN}})$, the $\beta_2\,(v_{\text{H}^+}, \tau_{\text{XX}}, \tau_{\text{XN}})$, and $\beta_4\,(v_{\text{H}^+}, \tau_{\text{XX}}, \tau_{\text{XN}})$ parameters can be investigated as a function of $\tau_{\text{XUV-NIR}}$ and $\tau_{\text{XUV-XUV}}$. In Fig. 6.8 (a)-(d) the $\beta_{2,4}\,(v_{\text{H}^+}, \tau_{\text{XX}}, \tau_{\text{XN}})$ parameters are shown for $\tau_{\text{XUV-XUV}} = 29\,\text{fs}$, and 44 fs, and in Fig. 6.8 (e)-(h) the corresponding FTPSs $\text{FS}_{\beta_{2,4}}\,(v_{\text{H}^+}, \tau_{\text{XX}}, \omega_{\text{FT}})$ are plotted. The delays of $\tau_{\text{XUV-XUV}} = 29\,\text{fs}$, and 44 fs are chosen, since in Fig. 6.5 the oscillatory structures of the vibrational wave packet is most different for these two delays.

It can be seen that $\beta_2\,(v_{\text{H}^+}, \tau_{\text{XX}}, \tau_{\text{XN}})$, as well as $\beta_4\,(v_{\text{H}^+}, \tau_{\text{XX}}, \tau_{\text{XN}})$ show again the oscillation of the vibrational wave packets within the $1\text{s}\sigma_{\text{g}}$ potential, as well as

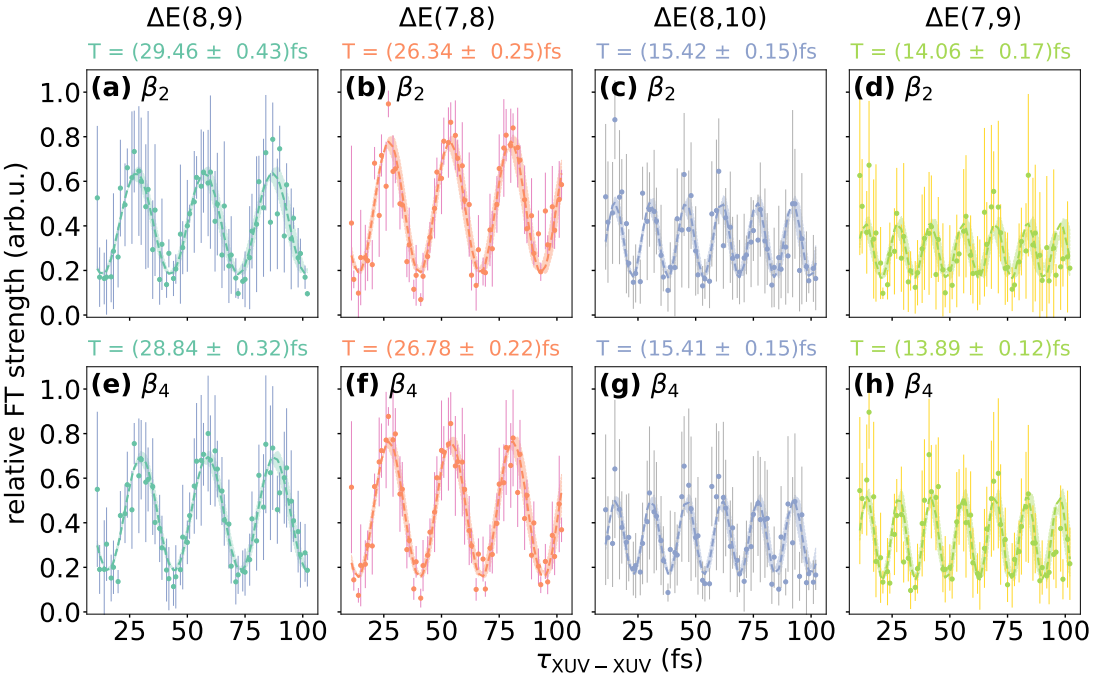

Figure 6.9: Intensity of the nearest- and next-nearest-neighbor quantum beats from the FTPS as a function of $\tau_{\text{XUV-XUV}}$. From the upper to the lower row the FTPS intensities $\text{FS}_{\beta_{2,4}}(v_{\text{H}^+}, \tau_{\text{XX}}, \omega_{\text{FT}})$ of the $\beta_{2,4}(v_{\text{H}^+}, \tau_{\text{XX}}, \tau_{\text{XN}})$ parameters are shown for (a)&(e) the quantum beat $\Delta E(8,9)$, where ω_{FT} corresponds to the energy difference between vibrational state $v = 8$ and $v' = 9$, (b)&(d) $\Delta E(7,8)$, (c)&(g) $\Delta E(8,10)$, and (d)&(h) $\Delta E(7,9)$. The measured data is shown as points and are fitted to a sinusoidal curve $(A + B\sin(2\pi(\tau_{\text{XUV-XUV}} - \tau_c)/T)$ with the fit parameters A, B, τ_c, T, and shown as a dashed line). The standard deviation of the fit parameters is illustrated as a shaded area. The fit retrieved oscillation periods T are shown at the top of the figures, and the corresponding oscillation frequency $\omega_{\text{FT,XUV-XUV}}$ is listed in column 4 in table 6.1.

the dephasing and rephasing of the wave packet, in agreement with the behavior observed for $\beta_0(v_{\text{H}^+}, \tau_{\text{XX}}, \tau_{\text{XN}})$. Furthermore the $\tau_{\text{XUV-XUV}}$-dependent observation in the FTPS of the three parameters $\text{FS}_{\beta_{0,2,4}}(v_{\text{H}^+}, \tau_{\text{XX}}, \omega_{\text{FT}})$ agree nicely, i.e. the strength of the signal of the nearest-neighbor quantum beats decrease from a delay of $\tau_{\text{XUV-XUV}} = 29\,\text{fs}$ to 44 fs, whereas the strength of the next-nearest-neighbor quantum beats stay comparable.

In Fig. 6.9 the strength of the different quantum beats is plotted for $\beta_{2,4}(v_{\text{H}^+}, \tau_{\text{XUV-XUV}}, \tau_{\text{XUV-NIR}})$ as a function of $\tau_{\text{XUV-XUV}}$, in the same manner as in Fig. 6.6 for $\beta_0(v_{\text{H}^+}, \tau_{\text{XX}}, \tau_{\text{XN}})$. Again the intensities of the quantum beats oscillate as a function of $\tau_{\text{XUV-XUV}}$, with a period which is inversely proportional to the frequency of the individual quantum beats $\omega_{\text{FT,XUV-XUV}}$ corresponding to the energy difference between the two vibrational states $\Delta E(v, v')$. The periods are retrieved from a sinusoidal curve fit of the data, and are shown at the top of each figure.

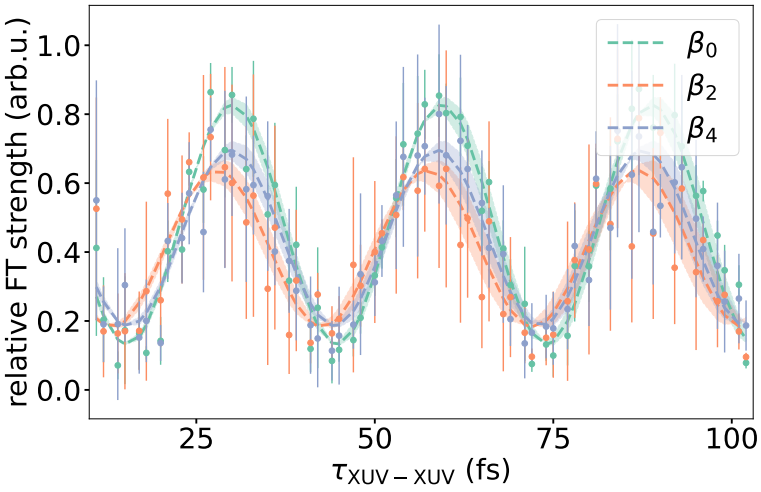

Figure 6.10: Comparison of the normalized intensities $\mathrm{FS}_{\beta_{0,2,4}}(v_{H^+}, \tau_{XX}, \omega_{FT})$ of all three $\beta_L(v_{H^+}, \tau_{XX}, \tau_{XN})$ parameters $(L = 0, 2, 4)$ as a function of $\tau_{\text{XUV-XUV}}$ for the quantum beat $\Delta E(8, 9)$. The dashed line is the sinusoidal curve fit of the data points with the shaded area as the standard deviation of the fit parameters.

The values for $\omega_{\text{FT,XUV-XUV}}$ are presented in column 4 of table 6.1 after a weighted averaging of the found values for the different $\beta_{0,2,4}(v_{H^+}, \tau_{\text{XUV-XUV}}, \tau_{\text{XUV-NIR}})$ parameters. The values show a nice agreement with the literature.

In Fig. 6.10 the intensities of the quantum beat $\Delta E(8, 9)$ are compared for all three $\beta_L(v_{H^+}, \tau_{XX}, \tau_{XN})$ parameter $(L = 0, 2, 4)$. It can be seen that the three parameters oscillate in the same manner, i.e. in good approximation with the same phase and period. The agreement of the three β-parameters, as well as the fact that $\beta_L(v_{H^+}, \tau_{XX}, \tau_{XN})$ for $L \geq 6$ depicts only noise (not shown), is consistent with the fact that the observed dynamics are based on a 2 photon process.

6.3 Discussion

Firstly, it should be noted that in the following atomic units are used, i.e. $m = e = \hbar = 1$. Secondly, the following is based on the corresponding theory[2] given by solving the time-dependent Schrödinger equation (TDSE), which was performed by M. J. J. Vrakking and is published in [9].

The signals of the vibrational quantum beats are observed whenever the delay between the two ionizing XUV pulses is $\tau_{\text{XUV-XUV}} = 2n\pi/\Delta E(v, v')$, with n as an

[2]In the corresponding paper [9], the TDSE is solved in two dimensions, one dimension corresponds to the internuclear motion, and the other to the photoelectron motion. With the time-dependent surface flux (TSURFF) method [354, 355], the nuclear and photoelectron resolved H^+ fragment yield are obtained. In general, the calculation reproduced the experimental outcome, i.e. the oscillation of the intensity of the individual quantum beats as a function of $\tau_{\text{XUV-XUV}}$, with a minimum at $\tau_{\text{XUV-XUV}} = (2n + 1)\pi/\Delta E(v, v')$, and a maximum at $\tau_{\text{XUV-XUV}} = 2n\pi/\Delta E(v, v')$. A detailed description of the computational method can be found in [143].

integer, and the signals of the quantum beats are absent or only weakly observable whenever $\tau_{\text{XUV-XUV}} = (2n+1)\pi/\Delta E(v, v')$, with n as an integer. The observation of a quantum beat relies on the coherence properties between the two vibrational states. Consequently, if the quantum beats are only weakly observable, the degree of coherence between the two corresponding vibrational states is low.

According to sect. 2.1.4.3, the degree of vibrational coherence can be limited due to entanglement between the ion and photoelectron formed during the photoionization of H_2. So far the study of the quantum beats neglected the fact, that the system also includes a photoelectron. However, the correlation between the strength of the quantum beats, i.e. the degree of vibrational coherence, and the degree of ion+photoelectron entanglement can only be fully understood, if the properties of the photoelectron, which accompanies the formation of the different vibrational states are taken into account.

Let us consider the formation of two cationic vibrational levels $H_2^+(v)$ and $H_2^+(v')$. First of all, the accompanying photoelectron spectra are sensitive to the ionizing XUV spectrum, which exhibits a fringe pattern with a fringe spacing $\delta\omega_{\text{XUV}} = 2\pi/\tau_{\text{XUV-XUV}}$. Furthermore, due to energy conservation, the photoelectron spectra accompanying the formation of $H_2^+(v)$ are shifted by $\Delta E(v, v')$ to higher energies (if $v < v'$) compared to the photoelectron spectra accompanying $H_2^+(v')$.

In Fig. 6.11 the schematic photoelectron spectra, which accompany the formation of $H_2^+(v = 0)$ and $H_2^+(v' = 1)$ for two different $\tau_{\text{XUV-XUV}}$ are shown following the theoretical results from [9]. The photoelectron spectra are retrieved by simply assuming a gaussian distribution with a FWHM bandwidth of 5 eV, and a fringe modulation with a spacing of $\delta\omega_{\text{XUV}}$, thus following the XUV spectra, and depending on $\tau_{\text{XUV-XUV}}$. The photoelectron spectra accompanying the two different vibrational states $v = 0$ and $v = 1$ are shifted by $\Delta E(v = 0, v' = 1)$ towards each other.

In Fig. 6.11 (a) the pulse delay is $\tau_{\text{XUV-XUV}} = (2n + 1)\pi/\Delta E(v, v')$ with $n = 0$, which results in a fringe spacing of $\delta\omega_{\text{XUV}} = 2\Delta E(v = 0, v' = 1)$. Since the photoelectron spectra accompanying the formation of $H_2^+(v = 0)$, and $H_2^+(v' = 1)$ are shifted by $\Delta E(0, 1)$ relative to each other, the additional fringe modulation of the spectra due to the two pulse delay leads to a total shift of half-integer number $(2n+1)/2$ fringes (here with $n = 0$) between both spectra. Thus, a measurement of the photoelectron kinetic energy (or just the possibility of such a measurement) allows to distinguish between the formation of the cationic vibrational state $H_2^+(v)$ and $H_2^+(v')$.

Accordingly the wave function of the ion+photoelectron system is given by

$$|\Psi_{\text{total}}\rangle = c_{v,\varepsilon}\,|v\rangle \otimes |\varepsilon\rangle + c_{v',\varepsilon'}\,|v'\rangle \otimes |\varepsilon'\rangle\,, \tag{6.6}$$

where $c_{v,\varepsilon}$ is the coefficient matrix, $|v\rangle$ is the vibrational eigenstate with the vibrational quantum number v, and $|\varepsilon\rangle$ is the corresponding photoelectron eigenstate. In this case, the ion+photoelectron are entangled and the degree of coherence between the two vibrational states $H_2^+(v)$ and $H_2^+(v')$ is very low, limiting the observation of the quantum beat $\Delta E(v, v')$ in a pump-probe experiment.

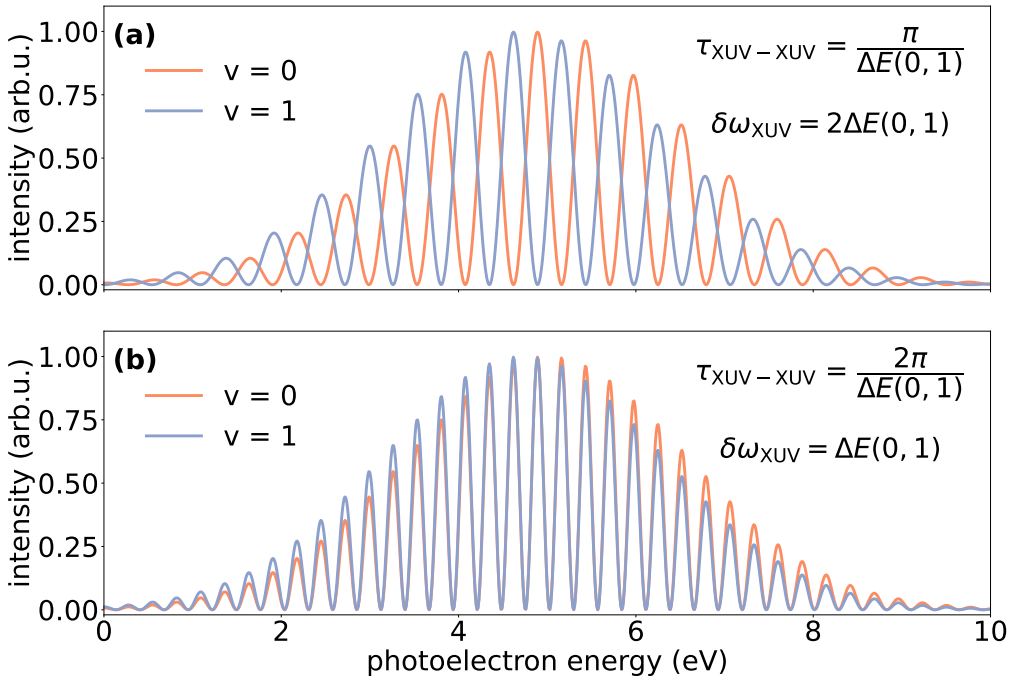

Figure 6.11: Schematic photoelectron spectra accompanying the formation of the cationic vibrational states $H_2^+(v=0)$ and $H_2^+(v'=1)$ for two different $\tau_{\text{XUV-XUV}}$ following the theoretical results derived in [9]. The here plotted spectra is a simplified model, i.e. a gaussian distribution with a FWHM bandwidth of 5 eV and a fringe spacing $\delta\omega_{\text{XUV}}$, which is inversely proportional to $\tau_{\text{XUV-XUV}}$. The spectra of $v = 0$ (orange) is shifted to higher energies by $\Delta E(0,1) = 0.27$ eV (calculated after Eq. 6.3 with the constants from [340]) compared to the spectra of $v = 1$ (blue). (a) The delay of the two XUV pulses is $\tau_{\text{XUV-XUV}} = (2n+1)\pi/\Delta E(v,v')$, with $n = 0$. The two spectra are shifted relative to each other in such a way, that a possible measurement of the photoelectron kinetic energy allows to determine whether $H_2^+(v=0)$ or $H_2^+(v'=1)$ is formed. Consequently, the ion+photoelectron are entangled limiting the degree of coherence between the two vibrational states v and v'. (b) The delay is $\tau_{\text{XUV-XUV}} = 2n\pi/\Delta E(v,v')$, with $n = 1$. The two spectra largely overlap, making it impossible to distinguish between the formation of $H_2^+(v=0)$ or $H_2^+(v'=1)$ with a possible measurement of the photoelectron. Accordingly, the two vibrational states are in a coherent superposition, and the degree of ion+photoelectron entanglement is low. The figure is inspired by Fig. 3 in [9].

Conversely, if $\tau_{\text{XUV-XUV}} = 2n\pi/\Delta E(v, v')$, as shown in Fig. 6.11 (b) for $n = 1$, the fringe spacing is $\delta\omega_{\text{XUV}} = \Delta E(v = 0, v' = 1)$, and the photoelectron spectrum accompanying $H_2^+(v = 0)$ is shifted by n fringes (here $n = 1$) compared to the photoelectron spectrum accompanying $H_2^+(v' = 1)$. The two photoelectron spectra largely overlap, and a possible measurement of the photoelectron would not allow to distinguish between the formation of $H_2^+(v = 0)$ and $H_2^+(v' = 1)$.

In this case the wave function can be written as

$$|\Psi_{\text{total}}\rangle \sim \left(c_v |v\rangle + c_{v'} |v'\rangle\right) \otimes |\chi_\varepsilon\rangle \,, \tag{6.7}$$

with $|\chi_\varepsilon\rangle = \sum_\varepsilon c_\varepsilon |\varepsilon\rangle$ as the photoelectron wave function. The two vibrational states $H_2^+(v)$ and $H_2^+(v')$ are in a coherent superposition, and consequently in an pump-probe experiment the ionizing pathways towards the final state involving the intermediate ionic states $|v\rangle$ and $|v'\rangle$ interfere constructively or destructively depending on the pump-probe delay leading to observable quantum beats $\Delta E(v, v')$ in the Fourier frequency domain.

It should be emphasized that the two XUV pulses are not used to resonantly tailor excited state population [332]. Generally, it is quite common to use a two-pulse sequence to control the excitation of bound states in atoms or molecules (as it is discussed for helium atoms in section 5.2). These experiments are based on Ramsey-type Fourier transform spectroscopy [356], and are used for example in coherent control experiment [357], multidimensional spectroscopy [310] or hyperspectral imaging [358, 359]. In the current experiment the vibrational states are not formed in a resonant bound-to-bound transition, but in an ionization process, and consequently the population of the vibration states do not depend on $\tau_{\text{XUV-XUV}}$ [9]. Except for the $\tau_{\text{XUV-XUV}}$ dependent fringe modulation, this is also true for the accompanying photoelectron spectrum. However, what changes with $\tau_{\text{XUV-XUV}}$ is the degree of entanglement between the photoelectron and the cation, and the degree of coherence between the different vibrational states, respectively.

6.3.1 Derivation of the reduced ionic density matrix

The dependence of the degree of coherence between different vibrational states on the time delay $\tau_{\text{XUV-XUV}}$, due to ion+photoelectron entanglement can be recognized directly in the reduced ionic density matrix of the system.
As described in detail in section 2.1.4.3, the off-diagonal elements of the reduced ionic density matrix are a quantification of the coherence between different vibration states, and the diagonal elements correspond to the population probability of the individual vibrational states.

The total wave function obtained in the current experiment can be expressed as a set of ion+photoelectron states

$$|\Psi_{\text{total}}\rangle = \sum_{v=0}^{N_v} \int \mathrm{d}\varepsilon c_{v,\varepsilon} |v\rangle \otimes |\varepsilon\rangle \,, \tag{6.8}$$

consisting of an ionic part, which is fully described by the vibrational quantum number v and the eigenstates $|v\rangle$, plus a photoelectronic part, which is fully

characterized by its kinetic energy ε and the corresponding eigenstate $|\varepsilon\rangle$. The coefficient matrix is $c_{v,\varepsilon}$.

The electric field of the first XUV pulse in the time domain is given by,

$$E_{1,\mathrm{XUV}}(t) = \mathrm{Re}\left\{\int E_{0,\mathrm{XUV}}(\omega_{\mathrm{XUV}})\exp(-i\omega_{\mathrm{XUV}}t)\mathrm{d}\omega_{\mathrm{XUV}}\right\}, \tag{6.9}$$

where ω_{XUV} is the XUV frequency, and $E_{0,\mathrm{XUV}}(\omega_{\mathrm{XUV}})$ is the spectral amplitude. The second pulse is just a replica of the first pulse delayed by $\tau_{\text{XUV-XUV}} = \tau_{\mathrm{XX}}$, i.e.

$$\begin{aligned} E_{2,\mathrm{XUV}}(t) &= E_{1,\mathrm{XUV}}(t-\tau_{\mathrm{XX}}) \\ &= \mathrm{Re}\left\{\int E_{0,\mathrm{XUV}}(\omega_{\mathrm{XUV}})\exp(-i\omega_{\mathrm{XUV}}(t-\tau_{\mathrm{XX}}))\mathrm{d}\omega_{\mathrm{XUV}}\right\}. \end{aligned} \tag{6.10}$$

The spectral amplitude of both interfering pulses is given by

$$\begin{aligned} E_{\mathrm{XUV}}(\omega_{\mathrm{XUV}}) &= E_{1,\mathrm{XUV}}(\omega_{\mathrm{XUV}}) + E_{2,\mathrm{XUV}}(\omega_{\mathrm{XUV}}) \\ &= E_{0,\mathrm{XUV}}(\omega_{\mathrm{XUV}})(1+\exp(i\omega_{\mathrm{XUV}}\tau_{\mathrm{XX}})) \\ &= 2E_{0,\mathrm{XUV}}(\omega_{\mathrm{XUV}})\exp(i\omega_{\mathrm{XUV}}\tau_{\mathrm{XX}}/2) \\ &\quad \times\cos(\omega_{\mathrm{XUV}}\tau_{\mathrm{XX}}/2). \end{aligned} \tag{6.11}$$

The term $\exp(i\omega_{\mathrm{XUV}}\tau_{\mathrm{XX}}/2)$ is linear in ω_{XUV}, and corresponds to a shift of the $t=0$ origin, i.e. instead of one pulse being at $t=0$ and the other at $t=\tau_{\mathrm{XX}}$, the pulses are now at $t=\pm\tau_{\mathrm{XX}}/2$. Accordingly, after shifting the origin of the time axis, the spectral amplitude of both interfering pulses can be expressed as

$$E_{\mathrm{XUV}}(\omega_{\mathrm{XUV}}) = 2E_{0,\mathrm{XUV}}(\omega_{\mathrm{XUV}})\cos(\omega_{\mathrm{XUV}}\tau_{\mathrm{XX}}/2). \tag{6.12}$$

Now it can be assumed, that the total ionic energy E_v plus photoelectron kinetic energy ε equals the energy of the absorbed XUV photon, i.e. $\omega_{\mathrm{XUV}} = \varepsilon + E_v$.

Thus, the total ion+photoelectron wave function is given by

$$|\Psi_{\mathrm{total}}\rangle = \sum_{v=0}^{N_v}\int \mathrm{d}\varepsilon\, c'_{v,\varepsilon}\,|v\rangle\otimes|\varepsilon\rangle\, E_{\mathrm{XUV}}(\varepsilon+E_v), \tag{6.13}$$

The corresponding reduced ionic density matrix ρ_{ion} is given according to Eq. 2.15 by

$$\rho_{\mathrm{ion}} = \sum_{v,v'=0}^{N_v}\int \mathrm{d}\varepsilon\, c'_{v,\varepsilon}c'^{*}_{v',\varepsilon}\,|v\rangle\langle v'|\, E_{\mathrm{XUV}}(\varepsilon+E_v)E^{*}_{\mathrm{XUV}}(\varepsilon+E_{v'}), \tag{6.14}$$

where the product $E_{\mathrm{XUV}}(\varepsilon+E_v)E^{*}_{\mathrm{XUV}}(\varepsilon+E_{v'}) = C$ can be written as a sum using a trigonometric identity, according to

$$\begin{aligned} C &= 4E_{0,\mathrm{XUV}}(\varepsilon+E_v)E^{*}_{0,\mathrm{XUV}}(\varepsilon+E_{v'}) \\ &\quad\times\Big\{\cos((\varepsilon+E_v)\tau_{\mathrm{XX}}/2)\cos((\varepsilon+E_{v'})\tau_{\mathrm{XX}}/2)\Big\} \\ &= 2E_{0,\mathrm{XUV}}(\varepsilon+E_v)E^{*}_{0,\mathrm{XUV}}(\varepsilon+E_{v'}) \\ &\quad\times\Big\{\cos(\Delta E_{v,v'}\tau_{\mathrm{XX}}/2)+\cos(((E_v+E_{v'})/2+\varepsilon)\tau_{\mathrm{XX}})\Big\}, \end{aligned} \tag{6.15}$$

with $\Delta E_{v,v'} = E_v - E_{v'}$.

Now the question is, when are the off-diagonal elements of the reduced ionic density matrix (i.e. $(\rho_{\text{ion}})_{vv'}$, where $v \neq v'$) zero?

The first term, i.e. $\cos(\Delta E_{v,v'}\tau_{\text{XX}}/2)$ in Eq. 6.15 is zero, whenever

$$\Delta E_{vv'}\tau_{\text{XX}} = (2n+1)\pi, \tag{6.16}$$

which agrees with the condition for entanglement derived with the experiment.

But what about the second term? The integral of the second term, i.e.

$$\int \mathrm{d}\varepsilon E_{0,\text{XUV}}(\varepsilon + E_v)E^*_{0,\text{XUV}}(\varepsilon + E_{v'})\cos(((E_v + E_{v'})/2 + \varepsilon)\tau_{\text{XX}}) = I_2, \tag{6.17}$$

can be written as

$$\begin{aligned} I_2 \;=\; & \Bigg[E_{0,\text{XUV}}(\varepsilon + E_v)E^*_{0,\text{XUV}}(\varepsilon + E_{v'}) \\ & \times \frac{1}{\tau_{\text{XX}}}\sin((E_v + E_{v'})/2 + \varepsilon)\tau_{\text{XX}})\Bigg]_{\varepsilon_{\min}}^{\varepsilon_{\max}} \\ & + \int \mathrm{d}\varepsilon \left(\frac{\mathrm{d}\left(E_{0,\text{XUV}}(\varepsilon + E_v)E^*_{0,\text{XUV}}(\varepsilon + E_{v'})\right)}{\mathrm{d}\varepsilon}\right. \\ & \left. \times \frac{1}{\tau_{\text{XX}}}\sin((E_v + E_{v'})/2 + \varepsilon)\tau_{\text{XX}})\right), \end{aligned} \tag{6.18}$$

using integration by parts.

For a sufficient large integration interval $[\varepsilon_{\min}, \varepsilon_{\max}]$, the spectral amplitude goes to zero at the edges of the interval, and the first term in Eq. 6.18 becomes zero. The integral in Eq. 6.18 contains a multiplication with $1/\tau_{\text{XX}}$, leading to a rather small amplitude of the sine function and spectral amplitude, since τ_{XX} is in the order of a few up to a hundred femtoseconds. Furthermore, the spectral amplitude can be defined as a gaussian, thus the derivative can be approximated as

$$\left|\frac{\mathrm{d}\left(E_{0,\text{XUV}}(\varepsilon + E_v)E^*_{0,\text{XUV}}(\varepsilon + E_{v'})\right)}{\mathrm{d}\varepsilon}\right| \lesssim \Delta t_{\text{XUV}} E_{0,\text{XUV}}(\varepsilon + E_v)E^*_{0,\text{XUV}}(\varepsilon + E_{v'}),$$

where Δt_{XUV} is the XUV pulse duration, which is on the order of a few hundred attoseconds. Thus, the characteristic frequency scale of the spectral amplitude is given by the pulse duration of the XUV pulse, whereas the frequency scale of the sine is given by τ_{XX}. Accordingly, the sine oscillates multiple times within the bandwidth of the spectral amplitude, and the value of the integral over the derivative and the sine function should be small.

In conclusion, Eq. 6.18 is sufficiently small, and can be neglected in Eq. 6.15. The values of the off-diagonal reduced density matrix elements are determined

by the first cosine term in Eq. 6.15, i.e. $\cos(\Delta E_{vv'}\tau_{\mathrm{XX}}/2)$, which oscillates in the same manner as the experimental observables. Accordingly, if $\cos(\Delta E_{vv'}\tau_{\mathrm{XX}}/2) = 0$, which is given whenever $\Delta E_{vv'}\tau_{\mathrm{XX}} = (2n+1)\pi$ (with n as an integer), the degree of coherence is zero, since the off-diagonal matrix elements are in good approximation zero, i.e. $(\rho_{\mathrm{ion}})_{vv'} \to 0$, where $v \neq v'$, and consequently the degree of entanglement is maximal. Contrary, if $\cos(\Delta E_{vv'}\tau_{\mathrm{XX}}/2) = 1$, which is fulfilled whenever $\Delta E_{vv'}\tau_{\mathrm{XX}} = 2n\pi$ (with n as an integer), the degree of coherence is maximal (i.e. $(\rho_{\mathrm{ion}})_{vv'} \to \max$, where $v \neq v'$), and the degree of entanglement is minimal, respectively.

6.3.2 Reduced density matrix from TDSE calculation

The aforementioned TDSE calculation [9] gives access to the 2D ion+photoelectron wave function, which allows to quantify the degree of entanglement between the ion and the photoelectron by calculating the purity or performing a Schmidt decomposition, as described in section 2.1.3 and 2.1.4.3. The here presented calculations were performed by M. J. J. Vrakking, and are summarized in [3]. The detailed derivation of the reduced ionic density matrix, and the calculation of the purity can be found in [9].

Reduced ionic density matrix The reduced ionic density matrix is shown in Fig. 6.12 (a) and (b) for $\tau_{\text{XUV-XUV}} = 7.2\,\mathrm{fs}$, and $\tau_{\text{XUV-XUV}} = 15.7\,\mathrm{fs}$, respectively. The diagonal matrix elements corresponding to the population probability of the vibrational states are independent of $\tau_{\text{XUV-XUV}}$, which agrees with the aforementioned statement that the two XUV pulses are not used to resonantly tailor the excited state population, but are rather used to control the degree entanglement between the ion and the photoelectron.
The population probability of the vibrational state $v = 0$ is the highest (red color of matrix element $\to 1$), which decreases with higher vibrational quantum number (blue color $\to 0$). The Franck-Condon principle [341] states, that if initially the H_2 molecule is in the vibrational ground state $v_g = 0$, after ionization the population probability is the highest for vibrational state $v = 0$ in H_2^+, and decreases with increasing v-number.

In Fig. 6.12 (a) the reduced density matrix for a delay of $\tau_{\text{XUV-XUV}} = 7.2\,\mathrm{fs}$ is shown. The first off-diagonal matrix elements representing the degree of coherence between nearest-neighbor vibrational states are zero, whereas the second off-diagonal matrix elements, which correspond to the degree of coherence between next-nearest-neighbor vibrational states are non-zero. Consequently, only vibrational states with odd- or even-vibrational quantum numbers, respectively, are in a coherent superposition.

In Fig. 6.12 (b) the reduced ionic density matrix for a delay of $\tau_{\text{XUV-XUV}} = 15.7\,\mathrm{fs}$ is shown. The diagonal as well as all off-diagonal matrix elements have a non-zero value, which concludes that all vibrational states are in a coherent superposition.

Decomposition of the reduced ionic density matrix Now the ionic density matrix can be diagonalized, which corresponds to a "Schmidt" decomposition

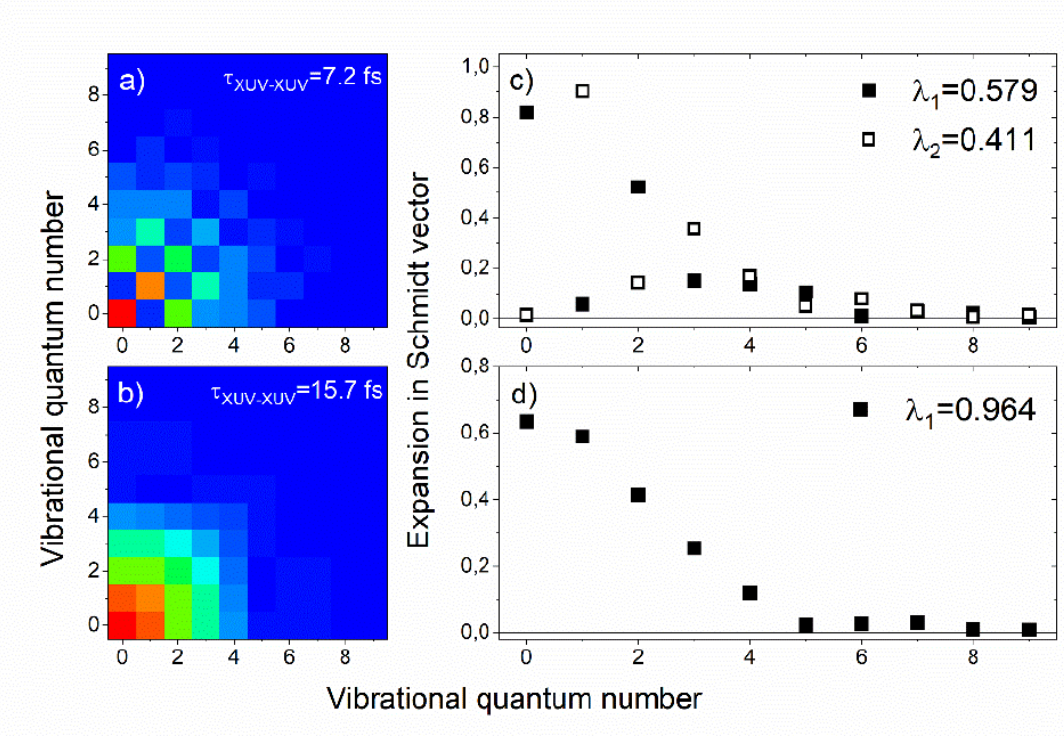

Figure 6.12: (a)-(b) Reduced ionic density matrix of the ion+photoelectron system as a quantification of the coherence properties between neighboring vibrational states in H_2^+ after ionization with two phase-locked XUV pulses with a delay $\tau_{\text{XUV-XUV}}$ of 7.2 fs and 15.7 fs. The diagonal matrix elements represent the population probability of the different vibrational states, which are independent of $\tau_{\text{XUV-XUV}}$. Whereas the off-diagonal elements indicate the degree of coherence between the different states (dark blue color → zero, i.e. no vibrational coherence). The values of the off-diagonal matrix elements are different for the two $\tau_{\text{XUV-XUV}}$, due to ion+photoelectron entanglement. (c)-(d) Schmidt decomposition of the reduced ionic density matrix presented in (a)-(b). (c) The total ion+photoelectron system is in a mixed state, with Schmidt rank 2, and the Schmidt vectors contain predominantly all the even-number vibrational states, and odd-number vibration states, respectively. (d) The ion+photoelectron system can be described as a pure state, with Schmidt rank 1, and the Schmidt vector contains all vibrational states. This figure is taken from [3]. The figure was made by M. J. J. Vrakking, and is reproduced with permission from Springer Nature.

of the reduced density matrix (typically a Schmidt decomposition refers to the decomposition of the total ion+photoelectron entangled system, cf. section 2.1.3), and gives

$$\rho_{\text{ion}} = \sum_{n=1}^{N} \lambda_n \left|\phi_n\right\rangle \left\langle\phi_n\right| , \tag{6.19}$$

where λ_n is the Schmidt coefficient, $|\phi_n\rangle$ is the Schmidt vector, and N corresponds to the Schmidt rank. In Fig. 6.12 (c) and (d) the Schmidt vector is shown as a function of the vibrational quantum number for $\tau_{\text{XUV-XUV}} = 7.2\,\text{fs}$ and $\tau_{\text{XUV-XUV}} = 15.6\,\text{fs}$, respectively.
In Fig. 6.12 (d) the Schmidt coefficient is $\lambda_1 = 0.964$, and thus the Schmidt rank is in a good approximated (within 4%) $N = 1$. The reduced ionic density matrix becomes

$$\rho_{\text{ion}} = \left|\phi_1\right\rangle \left\langle\phi_1\right| . \tag{6.20}$$

Accordingly the ion+photoelectron wave function is separable, and the Schmidt vector $|\phi_1\rangle$ contains all even- and odd-number vibrational states. The system can be described as a pure state.

Contrary, in Fig. 6.12 (c) the Schmidt rank is in good approximation 2, with the Schmidt coefficients $\lambda_1 = 0.579$ and $\lambda_2 = 0.411$. Consequently, the reduced ionic density matrix has to be written as

$$\rho_{\text{ion}} = \lambda_1 \left|\phi_1\right\rangle \left\langle\phi_1\right| + \lambda_2 \left|\phi_2\right\rangle \left\langle\phi_2\right| , \tag{6.21}$$

where the Schmidt vector $|\phi_1\rangle$ contains predominantly all even-number vibrational states, and the Schmidt vector $|\phi_2\rangle$ contains all the odd-number vibrational states. Accordingly, the even-v and odd-v states form a mixed quantum state. However, within the two subsystems the even-v vibrational states, and the odd-v states, respectively, are in a coherent superposition.

This agrees nicely with the former observation made in Fig. 6.12 (a), where the first off-diagonal elements of the reduced ionic density matrix are zero, whereas the second off-diagonal matrix elements are non-zero. Accordingly only vibrational states with the same parity are in a coherent superposition.

In conclusion, for certain $\tau_{\text{XUV-XUV}}$ all vibrational states are in a coherent superposition (Schmidt rank 1), and for other delays only the even-v, and odd-v vibrational states, respectively, are in a coherent superposition (Schmidt rank 2), due to ion+photoelectron entanglement, which is in agreement with the experimental observation.

6.3.3 Comparison of developed theory with experimental results

Finally, the experimental results can be analyzed in the light of the described theory.

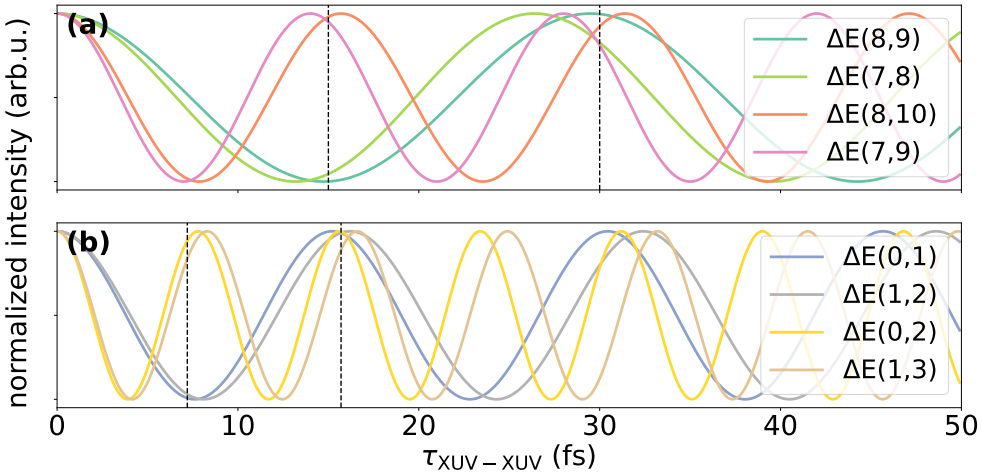

Figure 6.13: Theoretical prediction of the dynamics of the normalized intensities of different quantum beats $\Delta E(v, v')$ as a function of $\tau_{\text{XUV-XUV}}$ following the equation $\rho_{vv'} \sim \cos(\Delta E(v, v')\tau_{\text{XUV-XUV}}/2)$ for the off-diagonal elements of the reduced ionic density matrix as derived in section 6.3.1. The dashed black line in (a) are at $\tau_{\text{XUV-XUV}} = 15$ and 30 fs, and in (b) at $\tau_{\text{XUV-XUV}} = 7.2$ and 15.7 fs. It can be seen that the delays for which all vibrational states or only the even-v, and odd-v, respectively, are in a coherent superposition is quite different for high-, and low-number vibrational states. The energies of the quantum beats $\Delta E(v, v')$ are calculated after Eq. 6.3 with the constants from [340].

In Fig. 6.6, and 6.9 the main experimental results are presented, showing the intensities of the different quantum beats as a function of $\tau_{\text{XUV-XUV}}$ oscillating with a period of $T_{\text{exp}} = 2\pi/\Delta E(v, v')$ inversely proportional to the energy of the corresponding quantum beat.

The intensity of a quantum beat is a relative measure of the coherence properties of the two involved vibrational states. Accordingly, the intensities of the nearest-neighbor quantum beats represent the first off-diagonal, and the intensities of the next-nearest-neighbor quantum beats correspond to the second off-diagonal elements of the reduced ionic density matrix.

Thus, the experimental results can be compared to the theory presented in sect. 6.3.1. The derivation of the reduced ionic density matrix predicts an oscillation of the off-diagonal matrix elements according to Eq. 6.16, i.e. $\rho_{vv'} \sim \cos(\Delta E(v, v')\tau_{\text{XUV-XUV}}/2)$ with $v \neq v'$. In Fig. 6.13 different normalized off-diagonal matrix elements ($\rho_{vv'}$ with $v \neq v'$) as a function of $\tau_{\text{XUV-XUV}}$ are shown, which represent the arbitrary $\tau_{\text{XUV-XUV}}$-dependent intensities of different quantum beats $\Delta E(v, v')$. As predicted the intensities oscillate with a period of $T_{\text{theory}} = 2\pi/\Delta E(v, v')$, which agrees nicely with the experimental observation (i.e. $T_{\text{theory}} = T_{\text{exp}}$).

In addition the TDSE calculation presented in sect. 6.3.2 illustrates two significant different cases for two $\tau_{\text{XUV-XUV}}$. In the first case all vibrational states are in a coherent superposition, whereas in the second case only the odd-v, and even-v,

respectively, are in a coherent superposition. This can be seen in the experimental results in Fig. 6.7. For a delay of $\tau_{\text{XUV-XUV}} = 30\,\text{fs}$ the intensities of all four quantum beats are high, accordingly all vibrational states are in a coherent superposition. In contrast, for $\tau_{\text{XUV-XUV}} = 15\,\text{fs}$ the intensities of the nearest-neighbor quantum beats are minimal, whereas the intensities of the next-nearest-neighbor quantum beats are maximal. Accordingly, only vibrational states with same parity are in a coherent superposition.
The experimental delays for the two cases agree nicely with the delays found in the theoretical prediction as illustrated in Fig. 6.13 (a).

The first case occurs again for $\tau_{\text{XUV-XUV}} \sim 43\,\text{fs}$, and the second scenario repeats at $\tau_{\text{XUV-XUV}} \sim 58\,\text{fs}$. For longer delays the pattern becomes more difficult to describe. At a delay of for example $\tau_{\text{XUV-XUV}} = 90\,\text{fs}$ (cf. Fig. 6.7) the intensity of the quantum beat $\Delta E(7,8)$, and $\Delta E(7,9)$ is minimal, wheres the intensity of $\Delta E(8,9)$, and $\Delta E(8,10)$ is maximal. Here one could imagine the scenario that for example only vibrational levels with high enough v-number are in a coherent superposition.

It should be noted that the delays $\tau_{\text{XUV-XUV}}$ found in the TDSE calculation ($\tau_{\text{XUV-XUV}} = 7.2$, and $15.7\,\text{fs}$) are different to the experimental found delays ($\tau_{\text{XUV-XUV}} = 15$, and $30\,\text{fs}$), since in the TDSE calculation the population of the vibrational states above $v \geq 5$ is negligible, whereas in the experiment only the vibrational states $v = 7, 8, 9, 10$ are observed. All found delays are consistent with the prediction derived in sect. 6.3.1 for the respective vibrational levels (cf. Fig. 6.13).

6.4 Conclusion

In this chapter an experiment is presented, which shows that the degree of vibrational coherence in H_2^+ resulting from the ionization of H_2 by two phase-locked XUV pulses is controlled by the degree of ion+photoelectron entanglement created during the ionization process. A high degree of ion+photoelectron entanglement and a low degree of vibrational coherence, respectively, is observed whenever $\tau_{\text{XUV-XUV}} = (2n+1)\pi/\Delta E(v,v')$, with n as an integer. A low degree of ion+photoelectron entanglement, i.e. a high degree of vibrational coherence occurs whenever $\tau_{\text{XUV-XUV}} = 2n\pi/\Delta E(v,v')$, with n as an integer. Consequently by changing the time delay $\tau_{\text{XUV-XUV}}$ between the two ionizing pulses, the degree of ion+photoelectron entanglement, and conversely the degree of vibrational coherence is altered. The experimental results are interpreted by presenting the reduced ionic density matrix of the system, comparing the measurements to the reduced ionic density matrix retrieved by TDSE calculations [9], and the degree of entanglement is quantified by decomposing the latter. This study is a first demonstration of the limiting consequences of entanglement in attosecond pump-probe experiments, and is a first attempt to link ultrafast science with the basics, and fundamental theories of quantum information science.

CHAPTER 7

Ion+photoelectron entanglement vs electronic coherence

In this chapter, the crucial role of quantum-mechanical entanglement in attosecond science is further emphasized, by performing a second pump-probe experiment, which investigates coherence-based electron dynamics in the cation created during the dissociative photoionization of hydrogen molecules by a phase-locked pair of isolated attosecond pulses (IAPs) and a near-infrared (NIR) pulse. In particular, the role of entanglement between the ion and the departing photoelectron towards the observability of ultrafast electronic dynamics in the ion is studied. Furthermore, it is explored how the degree of electronic coherence in the ion and the degree of ion+photoelectron entanglement, respectively, depend on the delay between the two XUV pulses, as well as those pulses and the NIR probe pulse. In particular, in the current case, the electronic states of the ion are entangled with the orbital angular momentum and the kinetic energy of the photoelectron.

The experimental results presented here are accompanied by TDSE calculations performed by A. Rubio, A. Palacios, R. Bello and F. Martin. A manuscript about the experimental and theoretical results is in preparation.

7.1 Electron localization

Firstly, in this type of experiments an XUV pulse dissociatively ionizes neutral hydrogen molecules creating an entangled ion+photoelectron quantum system (cf. Fig. 7.1).

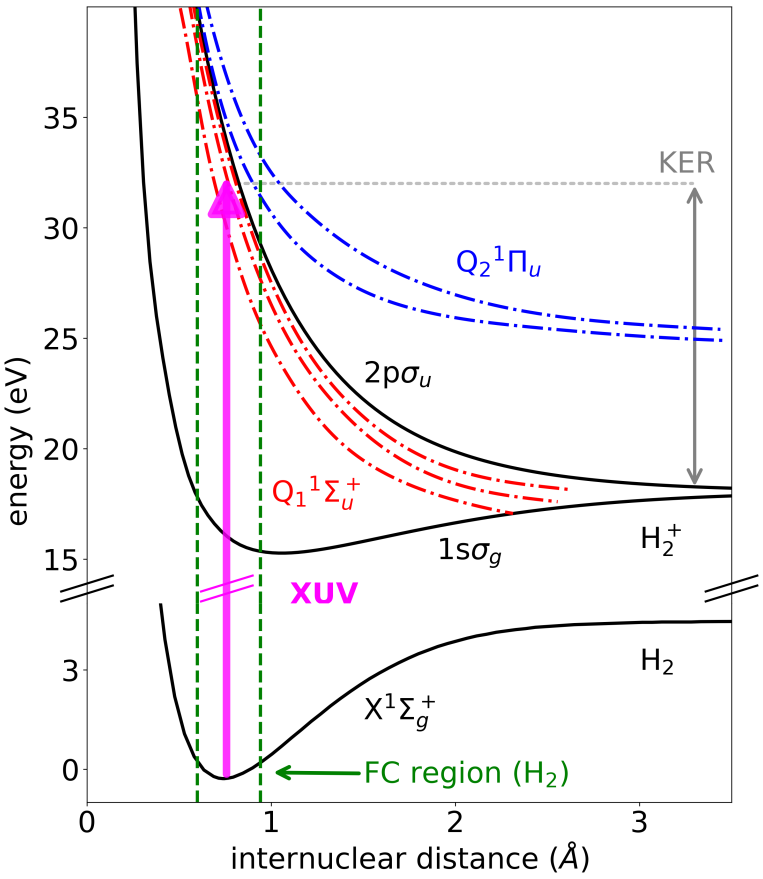

Figure 7.1: Illustration of the different states, which can be excited upon photoexcitation of a neutral hydrogen molecule with an XUV pulse (here: bandwidth $15 - 45\,\mathrm{eV}$) . Firstly, the doubly excited $Q_1{}^1\Sigma_u^+$ (red) and $Q_2{}^1\Pi_u$ (blue) states of H_2 can be excited. These states lead to autoionization of the molecule leaving H_2^+ in the $1s\sigma_g$ or $2p\sigma_u$ state, respectively. In addition the XUV pulse can directly ionize the molecule projecting the initial wave packet onto the $1s\sigma_g$ or $2p\sigma_u$ potential curve of H_2^+. The subsequent dissociation of the molecule leads to H + H^+-fragments with a kinetic energy distribution (KER) given by the difference between the initial energy on the excited potential curve and the dissociation potential of H_2^+ ($IP_{H_2^+} = 18.1\,\mathrm{eV}$ [352]), which is shown exemplary in grey. The data points for the $X^1\Sigma_g^1$, and $1s\sigma_g$ potential curve in H_2 and H_2^+, respectively, as well as the $2p\sigma_u$ potential curve are taken from [339]. The data for the $Q_1{}^1\Sigma_u^+$ and $Q_2{}^1\Pi_u$ states are extracted from [360]. The Franck-Condon (FC) region [341] (green dashed line) corresponds to the H_2 vibrational ground state $v_g = 0$.

As aforementioned, the ion+photoelectron wave function can be written in its most general form according to Eq. 2.20 for a certain ion kinetic energy release (KER) and photoelectron kinetic energy (EKE) as

$$|\Psi_{\mathrm{EKE+KER}}\rangle = \sum_{i=0,1} \sum_{l=0,1,\ldots} c_{il} \, |\phi_i\rangle \otimes |\chi_l\rangle \,, \tag{7.1}$$

where c_{il} is the coefficient matrix, $|\chi_l\rangle$ is the wave function of the photoelectron with the orbital angular momentum l, and $|\phi_i\rangle$ is the nuclear wave function moving along a specific electronic potential curve.

In the current case, the nuclear wave function dissociates on the electronic state $1s\sigma_g$ (first *gerade* electronic state in H_2^+) or $2p\sigma_u$ (first *ungerade* electronic state in H_2^+), respectively. Thus, the assignments of the ion electronic states are according to $|\phi_0\rangle \rightarrow 1s\sigma_g$, and $|\phi_1\rangle \rightarrow 2p\sigma_u$, and Eq. 7.1 has to be adjusted accordingly.

In particular, before ionization the neutral hydrogen molecule is in its ground state with an *even* parity. After ionization, and thus absorption of 1-XUV-photon, the parity of the ion+photoelectron system has to become *odd*, due to dipole selection rules (Laporte Rule [361]). Thus, the wave function after XUV ionization is given (for a specific EKE+KER) by

$$|\Psi_{\mathrm{EKE+KER,XUV}}\rangle = \sum_{l=1,3,\ldots} c_{0l} \, |\phi_{1s\sigma_g}\rangle \otimes |\chi_l\rangle + \sum_{l'=0,2,\ldots} c_{1l'} \, |\phi_{2p\sigma_u}\rangle \otimes |\chi_{l'}\rangle \,. \tag{7.2}$$

The formation of an ion with *even* parity, i.e. the *gerade* electronic state $1s\sigma_g$ is accompanied by a photoelectron with *odd* orbital angular momentum l. Respectively, the formation of an ion with *odd* parity, i.e. *ungerade* electronic state $2p\sigma_u$ is accompanied by a photoelectron with *even* angular momentum. If the weights c_{0l} and c_{1l} are comparable, the total system is maximally entangled, and thus strongly resembles a Bell's state [133].

Subsequently, a NIR probe pulse interacts with the entangled ion+photoelectron system during the dissociation process of the molecule. The NIR pulse can either change the parity of the ion, i.e. $c_{0l} \leftrightarrow c_{1l}$, or of the photoelectron, i.e. $c_{0l} \rightarrow c_{0l\pm1}$, or $c_{1l} \rightarrow c_{1l\pm1}$. In both cases, under the condition that $\{c_{0l} \neq 0, c_{1l} \neq 0\}$, a coherent superposition of the *gerade* and *ungerade* electronic state in the ion is created for a given EKE and KER, i.e.

$$|\Psi_{\mathrm{EKE+KER,XUV+NIR}}\rangle = \sum_{l=even/odd} \left(c_{0l} \, |\phi_{1s\sigma_g}\rangle + c_{1l} \, |\phi_{2p\sigma_u}\rangle \right) \otimes |\chi'_l\rangle \,. \tag{7.3}$$

The loss of a well defined parity of the ion+photoelectron system leads to electron localization, namely a favored localization of the bound electron in the ion at one of the two protons with the corresponding experimental observation of an asymmetry in the ejection of the ionic fragments in the laboratory-frame.

If the two ion electronic states are evenly populated, Eq. 7.3 can be adjusted accordingly, and the corresponding wave functions for the electron being on the

upper $|\Psi_{\mathrm{up}}\rangle$ or lower $|\Psi_{\mathrm{down}}\rangle$ proton becomes

$$\begin{aligned} |\Psi_{\mathrm{up}}\rangle &= 1/\sqrt{2}\left(\phi_{1\mathrm{s}\sigma_{\mathrm{g}}} + \phi_{2\mathrm{p}\sigma_{\mathrm{u}}}\right) \otimes \left[\sum_{l=even/odd} c_l \, |\chi_l'\rangle\right] \\ |\Psi_{\mathrm{down}}\rangle &= 1/\sqrt{2}\left(\phi_{1\mathrm{s}\sigma_{\mathrm{g}}} - \phi_{2\mathrm{p}\sigma_{\mathrm{u}}}\right) \otimes \left[\sum_{l=even/odd} c_l \, |\chi_l'\rangle\right] . \end{aligned} \tag{7.4}$$

This describes that the experimental observation of an up and down asymmetric emission of the ionic fragments is based on the fact that the two electronic states $1\mathrm{s}\sigma_{\mathrm{g}}$ and $2\mathrm{p}\sigma_{\mathrm{u}}$ of H_2^+ are brought into a coherent superposition.

Electron localization was and is still extensively studied in the laboratory- and molecular frame [113, 262, 362–368] starting with the pioneering experimental work by Kling et al. [160], followed by Singh et al. [369], and Sansone et al. [360]. Kling et al. [160] and Singh et al. [369] both investigated electron localization in D_2^+. Kling et al. [160] dissociatively ionized the molecule with an intense NIR pulse followed by Coulomb explosion or sequential excitation, whereas Singh et al. [369] used an attosecond pulse train (APT) including even and odd harmonics, and a many-cycle NIR probe pulse. Sansone et al. [360] investigated electron localization in H_2^+ using an IAP pump in combination with a NIR probe pulse. They observed an asymmetric emission of the dissociating ionic fragments as a function of the pump-probe delay (or in [160] the carrier-envelope phase) in the laboratory-frame, due to the formation of electronic coherence in the ion during the dissociation process, and the localization of the bound electron at one of the protons.

In the following experiment two phase-locked IAPs with variable delay $\tau_{\text{XUV-XUV}}$ serving as a pump pulse, and a many-cycle NIR probe pulse with variable pump-probe delay $\tau_{\text{XUV-NIR}}$ are used to dissociatively ionize H_2, and the asymmetry of the emission of the ionic fragments as a function of both delays is analyzed. The role of entanglement between the electronic states of the ion and the departing photoelectron (to be precise the orbital angular momentum and the kinetic energy of the photoelectron) is investigated towards the observability of ultrafast electronic dynamics in the ion by comparing the strength, i.e. the amplitude of the observed asymmetric ejection of the ionic fragments, as a function of $\tau_{\text{XUV-XUV}}$ and $\tau_{\text{XUV-NIR}}$. In particular, it is studied how the degree of electronic coherence in the ion and the degree of ion+photoelectron entanglement, respectively, depend on the delay $\tau_{\text{XUV-XUV}}$ between the two ionizing XUV pulses, as well as the pump-probe delay $\tau_{\text{XUV-NIR}}$.

This experiment is in a way similar to the experiment described in the previous chapter 6, since in both experiments the role of ion+photoelectron entanglement towards the observability of coherence-based dynamics in the ion is investigated. The main difference between both experiments is the coherent dynamics under investigation. In chapter 6, the vibrational coherence in H_2^+ is observed, whereas in this chapter the electronic coherence in H_2^+ is studied. The here presented experiments are in fact more challenging than before, since electronic dynamics in

H_2^+ are measured, which occur on a much faster timescale, i.e. on an attosecond timescale (chapter 6: nuclear motion, which occur on a femtosecond timescale). In this experiment, isolated attosecond pulses, a carrier-envelope phase (CEP) stability and attosecond phase-locking between all three pulses, i.e. not only between the two pump pulses, but also between the pump and probe pulse, were required.

7.2 Experimental results

In this section, first the experimental methods and the data processing are described. Then, the first experimental results are shown, where only a single XUV pulse ($\tau_{\text{XUV-XUV}} = 0\,\text{fs}$) and an NIR pulse is used to dissociatively ionize the hydrogen molecules (cf. sect. 7.2.2). Afterwards the main experimental results are presented, where two XUV pulses $\tau_{\text{XUV-XUV}} > 0\,\text{fs}$ and an NIR pulse are used to dissociatively ionize H_2, and the results are analyzed as a function of $\tau_{\text{XUV-NIR}}$, $\tau_{\text{XUV-XUV}}$ and the KER (cf. sect. 7.2.3). The dependence of electronic coherence on the ionizing pulse properties, i.e. $\tau_{\text{XUV-NIR}}$ and $\tau_{\text{XUV-XUV}}$ is shown, and is discussed in detail together with the role of ion+photoelectron entanglement in the second part of the discussion 7.3.

7.2.1 Experimental method

In the current experiment two phase-locked IAPs with a main bandwidth between $15 - 45\,\text{eV}$ are used (cf. Fig. 7.2). The NIR probe pulse passes a 40 nm bandpass interference filter centered at 800 nm to decrease its bandwidth and thus to increase its pulse duration to approximately 25 fs (FWHM). The NIR probe pulse, as well as the two NIR pulses used for HHG are CEP stabilized (cf. sect. 3.3). All pulses are phase-locked relative to each other. The achieved stability between the two XUV pulses is below 8 as, and between the XUV and NIR pulses is below 50 as.

After the neutral H_2 are ionized by the XUV+NIR pulses the H^+ fragments are measured with the VMI spectrometer as a function of the two XUV pulse delay $\tau_{\text{XUV-XUV}}$ ($\equiv \tau_{\text{XX}}$, pump) and XUV-NIR delay $\tau_{\text{XUV-NIR}}$ ($\equiv \tau_{\text{XN}}$, probe), where each image is recorded for 10 000 laser shots.

The delay $\tau_{\text{XUV-XUV}}$ between the two XUV pulses is scanned in a certain range in between 4 and 17 fs in 0.5 fs steps. The delay is measured with respect to XUV pulse B, which is fixed in time, and for a positive delay XUV pulse A comes prior to pulse B (cf. Fig. 7.3).
The pump-probe delay $\tau_{\text{XUV-NIR}}$ is scanned in a certain range in between 0 and 22 fs in 200 as steps with an uncertainty of $\tau_{\text{XUV-NIR}} \pm 1\,\text{fs}$, since it was rather difficult to define the exact time zero for such a long pulse. The pump-probe delay is measured with respect to XUV pulse B, and a positive $\tau_{\text{XUV-NIR}}$ corresponds to the NIR probe pulse coming after XUV pulse B (cf. Fig. 7.3).
The lower limit of $\tau_{\text{XUV-XUV}}$ is chosen to keep the optical interference of the two NIR pulses during the high harmonic generation process as small as possible (cf.

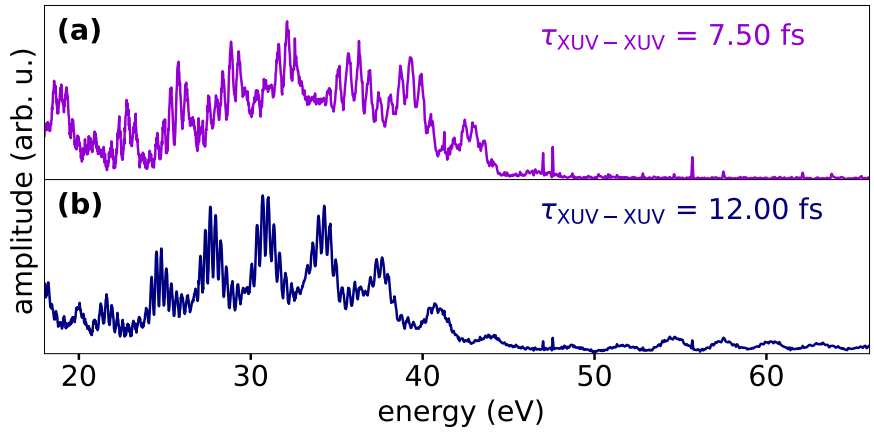

Figure 7.2: XUV spectra for two different $\tau_{\text{XUV-XUV}}$ recorded with the XUV spectrometer.

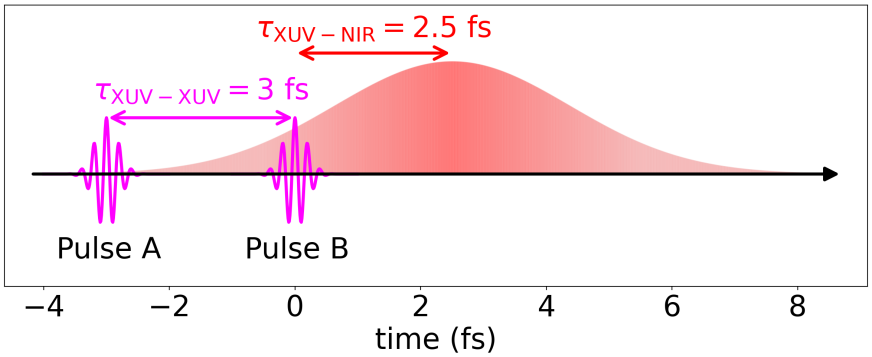

Figure 7.3: Depiction of the pulse sequence of the two XUV (pump) and the NIR (probe) pulse. For illustration purposes the NIR pulse has a pulse duration of only 5 fs (FWHM), instead of the actual 25 fs. All delays are measured with respect to XUV pulse B, which is fixed in time. For $\tau_{\text{XUV-XUV}} > 0$ fs XUV pulse A comes before pulse B, and for $\tau_{\text{XUV-NIR}} > 0$ fs the NIR pulse comes after XUV pulse B.

sect. 5.1.2; similar as in chapter 6), and the upper limit guarantees that for all chosen $\tau_{\text{XUV-NIR}}$ and $\tau_{\text{XUV-XUV}}$ the two XUV pulses are temporally overlapped with the NIR pulse.

In Fig. 7.2 (a) and (b) the XUV pulse spectra for two different $\tau_{\text{XUV-XUV}}$ are shown. The spectra are mostly continuous as expected for IAPs, and exhibit the typical fringe modulation with a fringe spacing inversely proportional to the XUV time delay $\delta\omega_{\text{XUV}} = 2\pi/\tau_{\text{XUV-XUV}}$. The two spectra have a cutoff at around 45 eV, although for certain delays, e.g. $\tau_{\text{XUV-XUV}} = 12$ fs there is a small tail, which stretches up to an energy of 65 eV. This tail is due to the interference of the two NIR pulses during the HHG process (cf. sect. 5.1.2). However, it is much smaller in magnitude than the main HHG spectrum, and thus can be ignored when analyzing the experimental results.

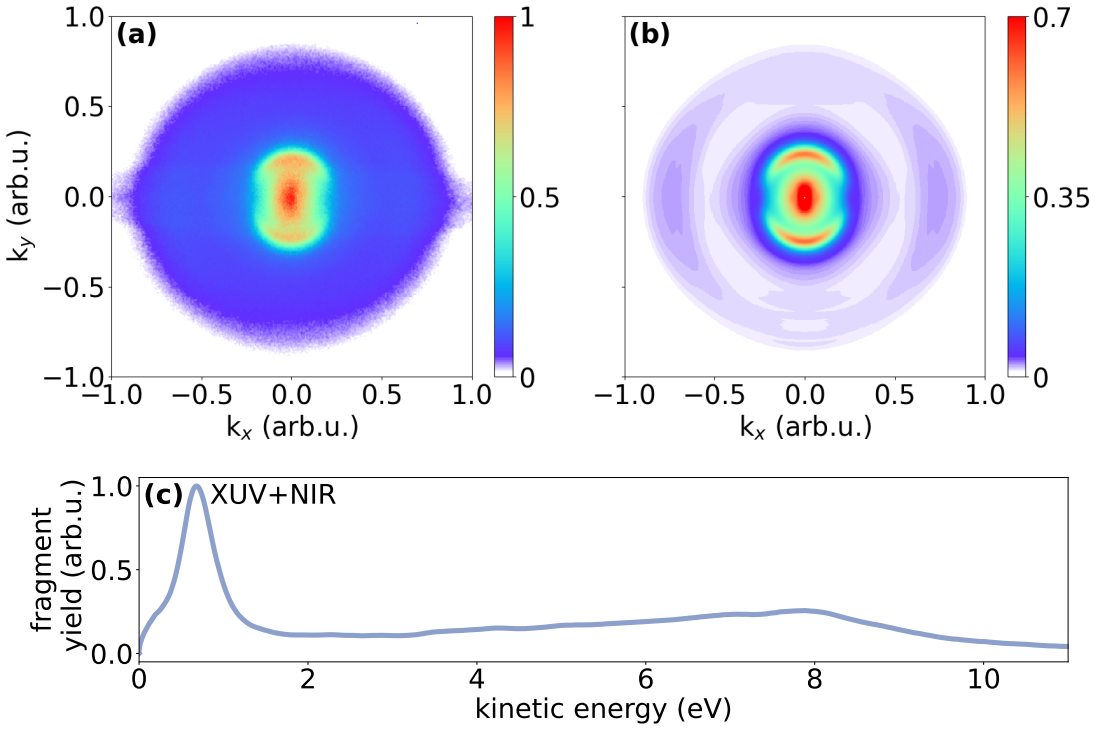

Figure 7.4: (a) Example of a measured VMI image of the H^+ fragment yield for a specific $\tau_{\text{XUV-XUV}} = 5.5\,\text{fs}$ and $\tau_{\text{XUV-NIR}} = 10.8\,\text{fs}$. The propagation direction of all pulses is along the x-direction, and the pulse polarization is along the y-direction. (b) Abel-inverted VMI image corresponding to a slice through the 3D momentum distribution. The vertical axis is given in pixel units of the CCD camera, which corresponds linearly to the H^+ momentum (arbitrary units). (c) Normalized fragment yield of the H^+ flying upwards (along positive k_y-axis) with respect to the laser propagation direction as a function of the KER, which corresponds to the probability distribution of the image shown in (b) at an angle of $\theta = 0$, i.e. $P\,(v_{H^+}, \theta = 0, \tau_{\text{XUV-XUV}} = 5.5\,\text{fs}, \tau_{\text{XUV-NIR}} = 10.8\,\text{fs})$. The angle θ is between the absolute H^+ velocity and the XUV+NIR polarization direction.

In Fig. 7.4 (a) an example of a measured VMI image is shown. Especially towards high momentum the H^+ yield becomes quite low. Thus, a Savitzky-Golay filter [370] is applied to the recorded images, with a window range of 21 pixels and a filter order of 2, which removes high frequency noise, smoothens the data, and compensates for the low signal.

Furthermore, the MCP detector has a lower efficiency at the lower half compared to the upper half of the detector due to an asymmetric wear, which leads to an τ-independent asymmetry of the strength of the signal between the lower and upper half of each VMI image. To compensate for this effect, the static asymmetry $\Delta(x, y)$ is calculated for each $\tau_{\text{XUV-XUV}}$ by averaging over the raw images for all

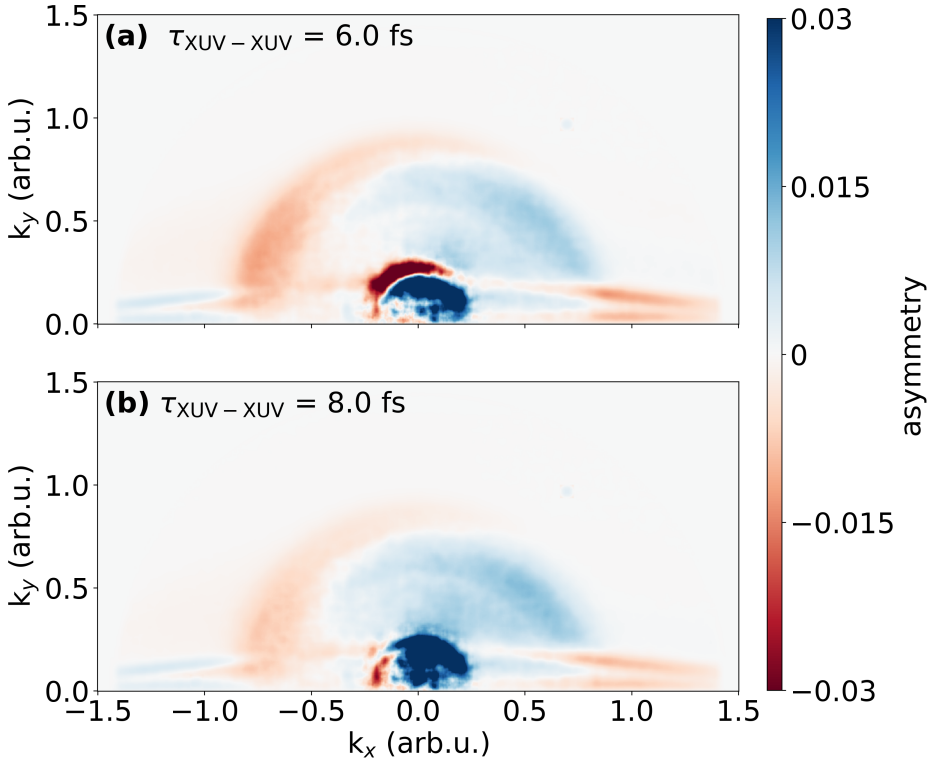

Figure 7.5: Static asymmetry $\Delta(x, y)$ for two different $\tau_{\text{XUV-XUV}}$, which is retrieved by averaging over the recorded VMI images for all $\tau_{\text{XUV-NIR}}$ for a given $\tau_{\text{XUV-XUV}}$, and subtracting the lower from the upper half of the image.

$\tau_{\text{XUV-NIR}}$, and subtracting the lower from the upper half of the averaged image, i.e. $\Delta(x, y) = S_{\text{avg}}(x, y) - S_{\text{avg}}(x, -y)$.

The static asymmetry $\Delta(x, y)$ exemplary for $\tau_{\text{XUV-XUV}} = 6\,\text{fs}$, and 8 fs is shown in Fig. 7.5. It can be seen that the structure of the static asymmetry is independent of the delay, and only the strength of $\Delta(x, y)$ varies slightly with $\tau_{\text{XUV-XUV}}$ depending on the HHG photon flux (higher HHG photon flux leads to a slightly more pronounced static asymmetry). Subsequently, the new images composed of the upper half $S_{\text{new}}(x, +y) = S_{\text{original}}(x, +y) - 1/2\Delta(x, y)$ and lower half $S_{\text{new}}(x, -y) = S_{\text{original}}(x, -y) + 1/2\Delta(x, y)$ are retrieved.

Finally the VMI images are inverse Abel transformed [14] using rBASEX [273, 274]. As in the previous chapters, the probability distribution of the XUV+NIR dissociative ionization is described by a series of Legendre polynomials [270]

$$P\left(v_{H^+}, \theta, \tau_{XX}, \tau_{XN}\right) = \beta_0\left(v_{H^+}, \tau_{XX}, \tau_{XN}\right) \times \left[1 + \sum_{n=1}^{4} \beta_n\left(v_{H^+}, \tau_{XX}, \tau_{XN}\right) P_n\left(\cos\theta\right)\right], \tag{7.5}$$

with $\tau_{\text{XUV-XUV}} = \tau_{XX}$, $\tau_{\text{XUV-NIR}} = \tau_{XN}$, and where θ is the angle between the absolute H^+ velocity v_{H^+} and the XUV and NIR polarization direction (cf. Fig. 7.4,

polarization is along the y-axis), and $P_n(\cos\theta)$ is the n-th order Legendre polynomial. Since the XUV+NIR dissociative ionization is a two-photon process, Legendre polynomials until the 4th order are included.
In Fig. 7.4 (b) the inverted VMI image is shown, which corresponds to the raw VMI image in Fig. 7.4 (a) after applying the Savitzky-Golay filter, and compensating for the static asymmetry $\Delta(x, y)$ of the detector before Abel inverting the image.

Photoexcitation of H_2 In Fig. 7.4 the H^+ signal consists of a contribution at the center of the image, which corresponds to a low H^+ momentum, and results from the direct dissociation from the $1s\sigma_g$ potential energy curve by absorption of 1-XUV-photon as already seen in the previous chapter.

In general, as described nicely for example in [360] and [371], the dissociative ionization of H_2 due to the absorption of 1-XUV-photon leads to H^+ fragments with different kinetic energies depending on the absorbed XUV photon energy (cf. Fig. 7.1). The fragments with the lowest KER (KER $< 2\,\text{eV}$) are due to direct ionization from the $1s\sigma_g$ potential by absorption of a photon with an energy of $18.1\,\text{eV} \leq \hbar\omega_{\text{XUV}} \leq 25\,\text{eV}$ [360,371], where the energy of 18.1 eV [352] corresponds to the dissociative ionization threshold of H_2^+.
For photon energies between $25\,\text{eV} < \hbar\omega_{\text{XUV}} < 36\,\text{eV}$, ion fragments are created with a KER between $0-20\,\text{eV}$ [360] (primarily between $4-14\,\text{eV}$ [372,373]). These fragments are due to the autoionization of the doubly-excited states $Q_1\,^1\Sigma_u^+$ in H_2 to the $1s\sigma_g$ state in H_2^+, which subsequently dissociates.
If the H_2 is in the vibrational ground state, the $2p\sigma_u$ state can be populated directly for photon energies of $\hbar\omega_{\text{XUV}} > 28\,\text{eV}$, and for $\hbar\omega_{\text{XUV}} \gtrsim 38\,\text{eV}$ the whole Franck-Condon region participates, thus ion fragments with high energy, i.e. KER $\sim 10 - 20\,\text{eV}$ are created [360, 371].

Subsequently, the interaction of the system with the NIR probe pulse can change the energy of the observed ion fragments, as for example bond softening can occur in the low KER region (KER $< 2\,\text{eV}$) as described in detail in sect. 6 (cf. Fig. 7.4 (a) and (b) upper and lower half circle around $k_y \sim \pm 0.25\,\text{arb. u.}$).
In Fig. 7.4 (c) the H^+ fragment yield as a function of the KER after XUV+NIR dissociative ionization of the H_2 molecules is shown.

Asymmetry parameter As mentioned earlier electron localization is the localization of the bound electron in the ion at one of the two protons, and a corresponding asymmetric ejection of the ionic fragments in the laboratory-frame. Thus, the observable of electron localization can be described by an asymmetry parameter

$$A(\text{KER}, \tau_{\text{XX}}, \tau_{\text{XN}}) = \frac{N_+(\text{KER}, \tau_{\text{XX}}, \tau_{\text{XN}}) - N_-(\text{KER}, \tau_{\text{XX}}, \tau_{\text{XN}})}{N_+(\text{KER}, \tau_{\text{XX}}, \tau_{\text{XN}}) + N_-(\text{KER}, \tau_{\text{XX}}, \tau_{\text{XN}})}, \tag{7.6}$$

which represents the normalized difference between the H^+ fragments flying up N_+ and downwards N_- with respect to the laser propagation direction (i.e. flying

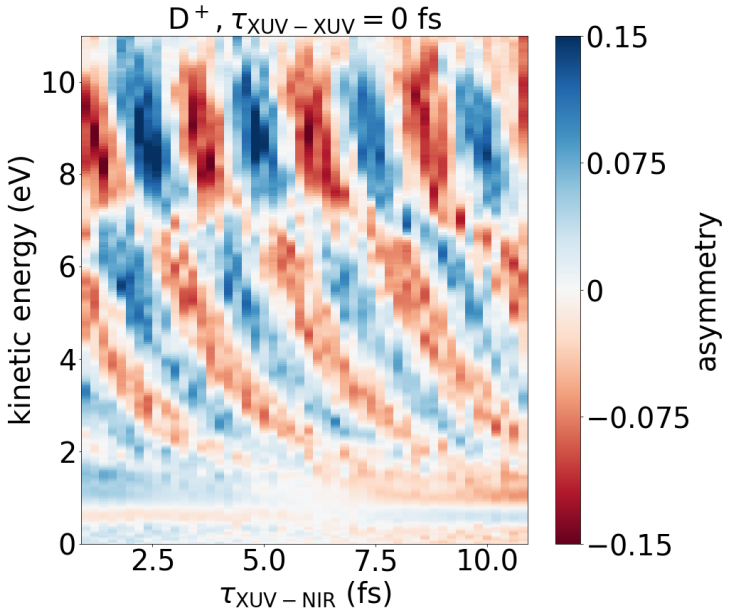

Figure 7.6: D^+ asymmetry parameter $A(\mathrm{KER}, \tau_{\text{XUV-XUV}} = 0, \tau_{\text{XUV-NIR}})$, i.e. normalized difference of the experimentally observed D^+ fragments flying up and downwards with respect to the laser propagation direction after the dissociative ionization of neutral D_2 by two phase-locked XUV pulses, and the interaction of the system with a NIR probe pulse as a function of the kinetic energy of the ion fragments (KER) and $\tau_{\text{XUV-NIR}}$ for $\tau_{\text{XUV-XUV}} = 0\,\mathrm{fs}$.

parallel along the laser polarization) as a function of the delays, and ion kinetic energy distribution (KER). The H^+ fragments flying up and downwards are given by the probability distribution, i.e. Eq. 7.5 at an angle of $\theta = 0°$ and $\theta = 180°$, respectively, (cf. Fig. 7.4 along positive and negative k_y-axis).

7.2.2 Asymmetry using a single XUV pulse

In the first step the asymmetry parameter is investigated using only a single IAP to ionize the molecules as a function of $\tau_{\text{XUV-NIR}}$. This is achieved by setting $\tau_{\text{XUV-XUV}} = 0\,\mathrm{fs}$. Accordingly, the results can be compared with the work of Sansone et al. [360].

It should be noted, that for this measurement only, the NIR probe pulse did not propagate through a bandpass filter, and thus the NIR pulse in this case is broadband with a pulse duration of approximately 5 fs. In addition, for this measurement, D_2 instead of H_2 is used, since the later experiments required larger amounts of gas, and only a small bottle of D_2 was available at that time. In general D_2 and H_2 lead qualitatively to the same experimental results [360, 363], only a π-shift of the $\tau_{\text{XUV-NIR}}$-dependent oscillation was observed between H^+ and D^+ in [262].

In Fig. 7.6 the D^+ asymmetry parameter $A(\mathrm{KER}, \tau_{\text{XUV-NIR}})$ as a function of the KER and $\tau_{\text{XUV-NIR}}$ is shown.
Firstly, it can be seen that the asymmetry parameter oscillates as a function of $\tau_{\text{XUV-NIR}}$, with a period given by the sub-cycle duration of the NIR probe pulse, i.e. $T_{\text{NIR}} = 2\pi/\omega_{\text{NIR}} \sim 2.7\,\text{fs}$, and a phase strongly depending on KER. During one NIR sub-cycle evolution the sign of the asymmetry alternates from a positive value (more D^+ fragments fly upwards in respect to the laser propagation direction) to zero (uniform distribution) to a negative value (more D^+ fragments fly downwards).
In addition, three different structural KER regions (high $\gtrsim 7\,\text{eV}$, middle, low $\lesssim 2\,\text{eV}$) are visible. Below KER $\lesssim 2\,\text{eV}$ no $\tau_{\text{XUV-NIR}}$-dependent asymmetry oscillation is visible, whereas at a KER of $\sim 7\,\text{eV}$, a π-phase shift of the asymmetry oscillation can be observed.
These results are similar to the observations done by Sansone et al. [360]. Accordingly, electron localization is successfully observed, and the conditions are given to further alter the experiment.

7.2.3 Asymmetry using an XUV pulse pair

The main goal of the current experiment is to investigate the oscillatory behavior of the asymmetry parameter as a function of $\tau_{\text{XUV-NIR}}$, when the time delay $\tau_{\text{XUV-XUV}}$ between the two ionizing XUV pulses is changed, and thus the XUV spectrum is tailored.
It should be noted that now the NIR probe pulse passes through a 40 nm bandpass filter increasing its pulse duration to approximately 25 fs centered at 800 nm. Furthermore H_2 instead of D_2 is used, which is as mentioned before mainly due to availability reasons of the gas. As aforementioned D_2 and H_2 lead qualitatively to the same experimental results.

In Fig. 7.7 the H^+ asymmetry parameter $A(\mathrm{KER}, \tau_{\text{XUV-XUV}}, \tau_{\text{XUV-NIR}})$ exemplary for four different $\tau_{\text{XUV-XUV}}$ as a function of the KER and $\tau_{\text{XUV-NIR}}$ are shown. In Fig. 7.7 (a) and (c) the H^+ asymmetry parameter is shown for $\tau_{\text{XUV-XUV}} = 6.0\,\text{fs}$, and $\tau_{\text{XUV-XUV}} = 9.5\,\text{fs}$, respectively, displaying the same behavior as already observed in Fig. 7.6 for D^+ and $\tau_{\text{XUV-XUV}} = 0\,\text{fs}$. The main difference is that now a $\tau_{\text{XUV-NIR}}$-dependent asymmetry below KER $\lesssim 2\,\text{eV}$ is visible, with a phase shift of the asymmetry oscillation as a function of $\tau_{\text{XUV-NIR}}$ at around 2 eV marking the transition from the low to the middle KER region. In addition, a second π-phase shift occurs at KER $\sim 7\,\text{eV}$ as seen before marking the middle from the high KER region.
In Fig. 7.7 (b) and (d) the asymmetry parameters for $\tau_{\text{XUV-XUV}} = 8\,\text{fs}$ and $\tau_{\text{XUV-XUV}} = 11.5\,\text{fs}$ are shown. The amplitude of the $\tau_{\text{XUV-NIR}}$-depending oscillation of the asymmetry parameter is clearly suppressed especially at the middle KER region.

To further compare the amplitude of the asymmetry oscillation as a function of $\tau_{\text{XUV-NIR}}$, the asymmetry parameter for all four $\tau_{\text{XUV-XUV}}$ is averaged exemplary between a KER of $4.2 - 5.1\,\text{eV}$, and the signal is fitted to a cosinusoidal fit as shown in Fig. 7.8. The asymmetry oscillates as a function of $\tau_{\text{XUV-NIR}}$ with a

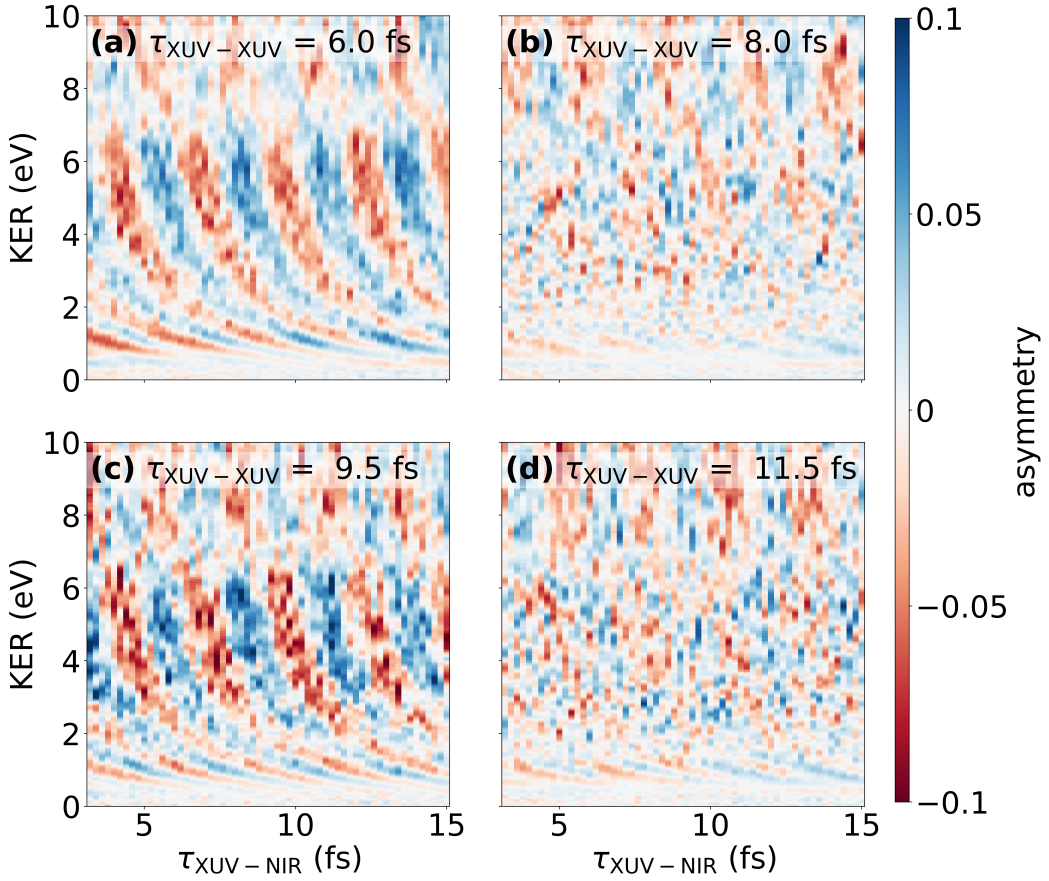

Figure 7.7: Asymmetry parameter $A(\mathrm{KER}, \tau_{\text{XUV-XUV}}, \tau_{\text{XUV-NIR}})$ as a function of the kinetic energy of the ion fragments (KER) and $\tau_{\text{XUV-NIR}}$ for different $\tau_{\text{XUV-XUV}}$ delays, i.e. (a) $\tau_{\text{XUV-XUV}} = 6.0\,\text{fs}$, (b) $\tau_{\text{XUV-XUV}} = 8.0\,\text{fs}$, (c) $\tau_{\text{XUV-XUV}} = 9.5\,\text{fs}$, (d) $\tau_{\text{XUV-XUV}} = 11.5\,\text{fs}$.

period of $T_{\text{NIR}} = 2\pi/\omega_{\text{NIR}} \sim 2.7\,\text{fs}$. The amplitude of the asymmetry A_{XN} is substantially smaller for $\tau_{\text{XUV-XUV}} = 8$ and $11.5\,\text{fs}$ than for $\tau_{\text{XUV-XUV}} = 6$ and $9.5\,\text{fs}$.

In the following the amplitude of the asymmetry is analyzed in different KER regions as a function of $\tau_{\text{XUV-XUV}}$. Therefore, similar pump-probe scans as shown in Fig. 7.7 were performed for $\tau_{\text{XUV-XUV}}$ between $4\,\text{fs}$ and $12.5\,\text{fs}$ in $0.5\,\text{fs}$ steps, and the amplitude of the oscillation of the asymmetry parameter as a function of $\tau_{\text{XUV-NIR}}$ is retrieved as described before for all $\tau_{\text{XUV-XUV}}$ in the three dominant KER regions separately.

In addition, to validate the consistency and reproducibility of the experimental observations multiple scans as in Fig. 7.7 were performed on different days (cf. Fig. 7.10). Each measurement campaign was carried out under slightly different experimental conditions, for example slightly different CEP stabilities (cf. table 7.1 in column 2) or $\tau_{\text{XUV-NIR}}$, and $\tau_{\text{XUV-XUV}}$ ranges. The results of all measurement campaigns are compared in table 7.1.

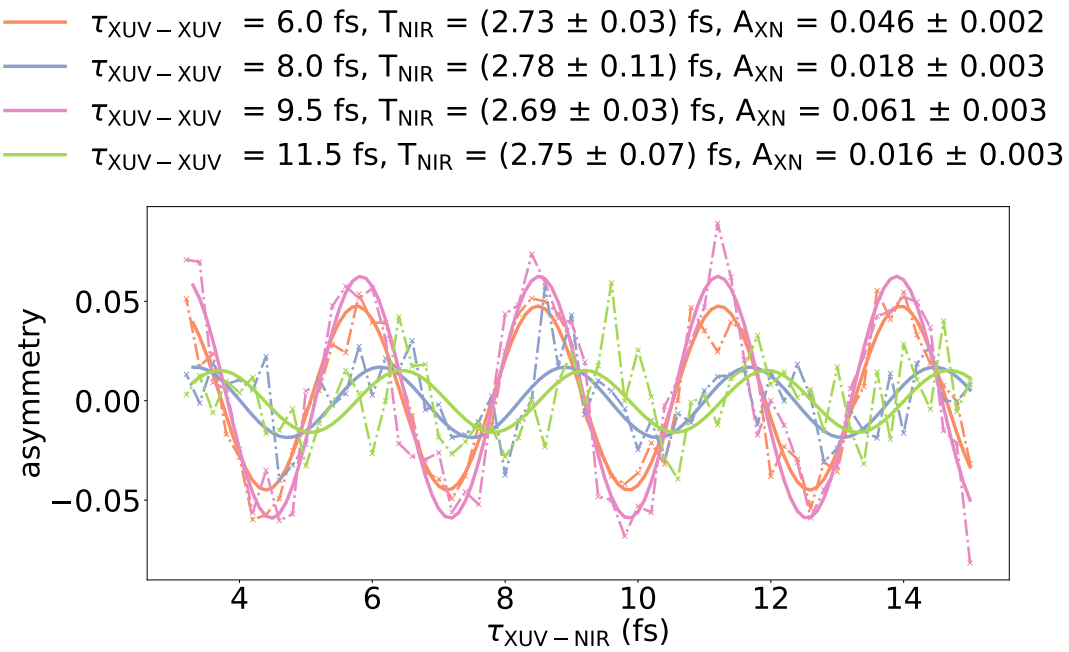

Figure 7.8: Asymmetry parameter as a function of $\tau_{\text{XUV-NIR}}$ for four different $\tau_{\text{XUV-XUV}}$ averaged between a KER of $4.2-5.1\,\text{eV}$, and fitted to a cosinusoidal function (solid line) $C_{\text{XN}} + A_{\text{XN}} \cos(2\pi(\tau_{\text{XUV-NIR}} - \tau_{\text{c,XN}})/T_{\text{NIR}})$ with the fit parameter $C_{\text{XN}}, A_{\text{c,XN}}, \tau_{\text{c,XN}}$ and T_{NIR}. The asymmetry oscillates as a function of $\tau_{\text{XUV-NIR}}$ with a period of T_{NIR}, and an amplitude A_{XN}. Both values are given at the top of the figure for the corresponding $\tau_{\text{XUV-XUV}}$.

Campaign	CEP (mrad)	Middle KER T_{asym} (fs)	High KER T_{asym} (fs)	Low KER T_{asym} (fs)	T_{HHG} (fs)
1.	580	3.23 ± 0.12	–	3.11 ± 0.20	3.11 ± 0.15
2.	600	3.10 ± 0.15	3.24 ± 0.10	3.13 ± 0.16	3.05 ± 0.07
3.	650	3.50 ± 0.19	3.71 ± 0.12	–	3.20 ± 0.07

Table 7.1: Comparison of three different measurement campaigns. In column 2 the CEP values of the different campaigns are presented. The periods of the $\tau_{\text{XUV-XUV}}$-dependent oscillation of the amplitude of the $\tau_{\text{XUV-NIR}}$-dependent asymmetry oscillation at a middle KER, i.e. $3.8-5.6\,\text{eV}$ are given in column 3 (cf. Fig. 7.7, 7.10 (b) and (d), in the first campaign no oscillation in this KER region is visible), at high KER, i.e. $6.1-7.7\,\text{eV}$ in column 4 (cf. Fig. 7.11), and at low KER, i.e. $\sim 1\,\text{eV}$ in column 5 (cf. Fig. 7.12, in the third campaign no oscillation is observed in this region). In column 6, T_{HHG} is the period of the HHG photon flux as a function of $\tau_{\text{XUV-XUV}}$, which is given by a sinusoidal curve fit of the averaged XUV intensities as a function of $\tau_{\text{XUV-XUV}}$ as shown in Fig. 7.15,and A.4, respectively.

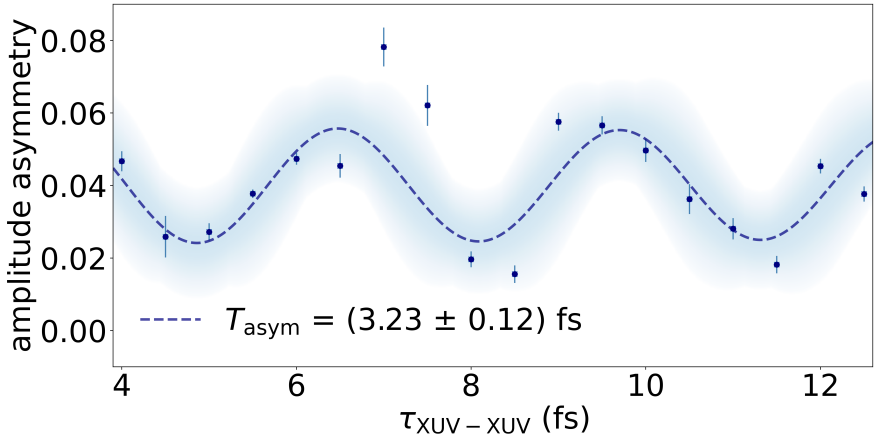

Figure 7.9: Middle KER region: Amplitude of the oscillation of the asymmetry parameter at middle KER as a function of $\tau_{\text{XUV-NIR}}$ plotted as a function of $\tau_{\text{XUV-XUV}}$. The amplitude of the asymmetry is retrieved by averaging the $\tau_{\text{XUV-NIR}}$-dependent asymmetry parameter in a KER region between $3.8 - 5.6\,\text{eV}$, and fitting the averaged signal to a cosinusoidal curve fit (cf. Fig. 7.8). The error bars of each data point (dots) correspond to the standard deviation of the cosinusoidal fit. The data points including the error bars are then fitted with a sinusoidal curve with a damped amplitude $(C_2 + A_2 \exp(-n_2 \tau_{\text{XUV-XUV}}) \sin(2\pi(\tau_{\text{XUV-XUV}} - \tau_{c2})/T_{\text{asym}})$ with the fit parameter $C_2, A_2, n_2, \tau_{c2}, T_{\text{asym}})$, illustrated as a dashed line. The amplitude of the asymmetry oscillates as a function of $\tau_{\text{XUV-XUV}}$ with a period of $T_{\text{asym}} = (3.23 \pm 0.12)\,\text{fs}$ retrieved by the fit. The shaded area represents the standard deviation of the fit.

Middle KER region Firstly, the asymmetry parameter at middle KER region is investigated in detail as a function of $\tau_{\text{XUV-XUV}}$. In the first campaign, for each $\tau_{\text{XUV-XUV}}$ the asymmetry parameter is averaged in a KER between 3.8 eV and 5.6 eV. This region is chosen, since here the asymmetry parameter as a function of $\tau_{\text{XUV-NIR}}$ depends in good approximation linearly on the KER, and the upper and lower limits are far enough from the π-phase shifts of the $\tau_{\text{XUV-NIR}}$-dependent asymmetry oscillation. As described before, the averaged signal is then fitted to a cosinusoidal curve, and the amplitude of the $\tau_{\text{XUV-NIR}}$-dependent asymmetry oscillation is retrieved.

In Fig. 7.9 the amplitude of the asymmetry is plotted as a function of $\tau_{\text{XUV-XUV}}$. The standard deviation of the amplitude retrieved by the cosinusoidal fit (cf. Fig. 7.8) is shown as error bars of the individual data points. The asymmetry amplitude oscillates as a function of $\tau_{\text{XUV-XUV}}$ with a period of $T_{\text{asym}} = (3.23 \pm 0.12)\,\text{fs}$, which is found by a sinusoidal curve fit of the data points. The sinusoidal function includes a damped amplitude, since the amplitude of the asymmetry decrease with increasing $\tau_{\text{XUV-XUV}}$. The shaded area represents the standard deviation of the sinusoidal curve fit.

In Fig. 7.10 the experimental results of two further campaigns are shown. In Fig. 7.10 (a) and (c) the H^+ asymmetry parameter $A(\text{KER}, \tau_{\text{XUV-XUV}}, \tau_{\text{XUV-NIR}})$

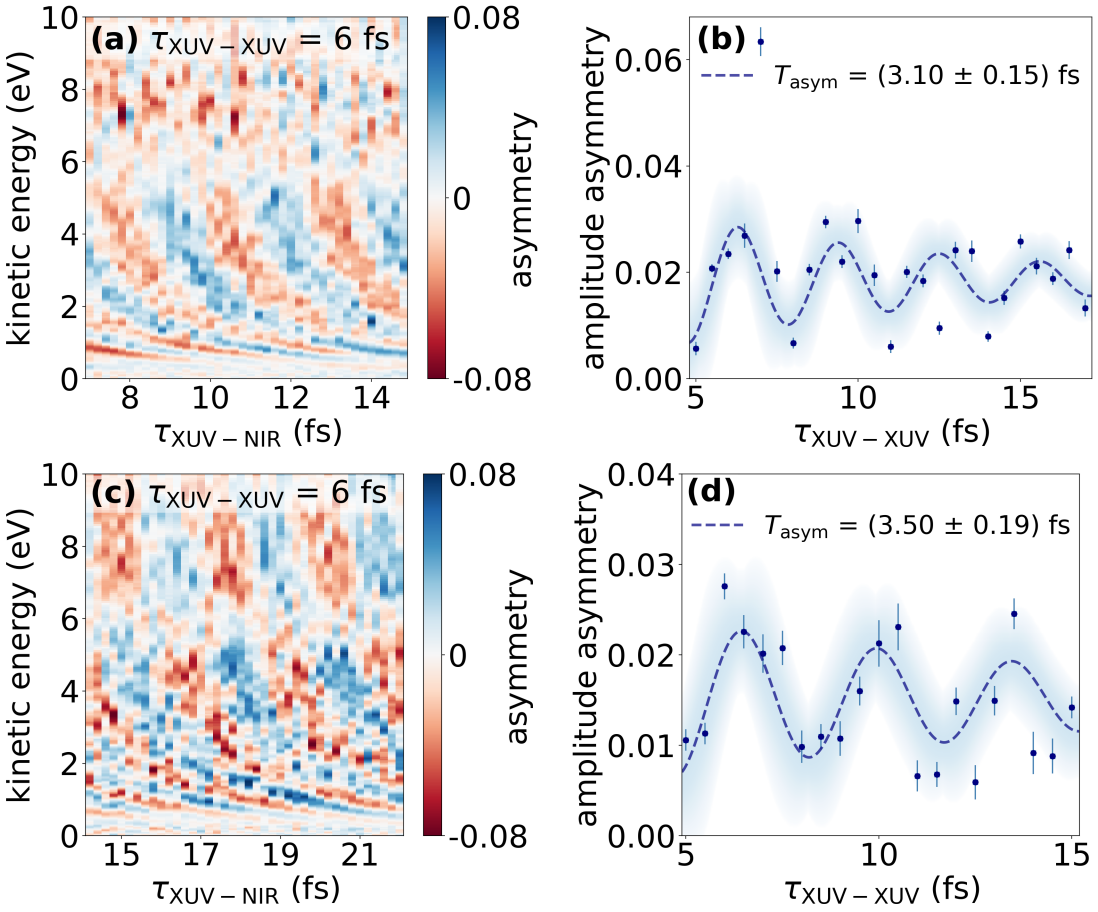

Figure 7.10: Results of a second (a)-(b), and third (c)-(d) measurement campaign investigating electron localization as a function of $\tau_{\text{XUV-XUV}}$. (a)&(c) H^+ asymmetry parameter $A(\text{KER}, \tau_{\text{XUV-XUV}}, \tau_{\text{XUV-NIR}})$ at $\tau_{\text{XUV-XUV}} = 6\,\text{fs}$ as a function of $\tau_{\text{XUV-NIR}}$, which shows the oscillation of the asymmetry parameter as a function of $\tau_{\text{XUV-NIR}}$ depicting three different structural KER regions. (b)&(d) Amplitude of the $\tau_{\text{XUV-NIR}}$-dependent oscillation of the asymmetry parameter at middle KER region as a function of $\tau_{\text{XUV-XUV}}$. The amplitude of the asymmetry is retrieved by averaging the asymmetry parameter between 3.8 eV and 5.6 eV, and fitting the signal to a cosinusoidal curve. The amplitude of the asymmetry oscillates as a function of $\tau_{\text{XUV-XUV}}$ with a period of (b) $T_{\text{asym}} = (3.10 \pm 0.15)\,\text{fs}$, and (d) $T_{\text{asym}} = (3.50 \pm 0.19)\,\text{fs}$, which are retrieved by a weighted sinusoidal curve fit with a damped amplitude (dashed line) of the data points (symbols) as before. The shaded area corresponds to the standard deviation of the sinusoidal fit.

as a function of $\tau_{\text{XUV-NIR}}$ exemplary for $\tau_{\text{XUV-XUV}} = 6\,\text{fs}$ is shown, depicting the three different $\tau_{\text{XUV-NIR}}$-dependent KER regions. However here the upper π-phase shift occurs at a lower KER of $\sim 6\,\text{eV}$.

It should be noted that slight energy difference between measurement campaigns can be explained by small calibration inaccuracies. Unfortunately, the current measurements do not allow to calibrate the y-axis directly. Thus an independent measurement of photoelectrons by XUV+NIR ionization of helium atoms was used to calibrate the energy axis of the VMI spectrometer, since the helium Rydberg states are very well known (cf. sect. 5.2). The retrieved energy axis can then be adapted to the current measurement by taking the voltages applied to the VMI spectrometer (repeller and extractor electrodes) of the different experiments into account. The voltages are important, since the maximal energy of the particles observed on the detector scales linearly with the applied voltages. Unfortunately, this indirect calibration is just an approximation method, which leaves some uncertainty within the energy axis (approx. $\pm 1\,\text{eV}$). A detailed description of the energy calibration can be found in the appendix A.2.

In Fig. 7.10 (b) and (d) the amplitude of the asymmetry parameter at the middle KER region is plotted as a function of $\tau_{\text{XUV-XUV}}$ similar to the results shown in Fig. 7.9. It can be seen that the amplitude oscillates with a period of $T_{\text{asym}} = (3.10 \pm 0.15)\,\text{fs}$, and $T_{\text{asym}} = (3.50 \pm 0.19)\,\text{fs}$, respectively. The periods of the amplitude asymmetry oscillations of all three measurements agree within their error bars as can be seen in table 7.1 in column 3. In Fig. 7.10 (b) the data point at $\tau_{\text{XUV-XUV}} = 12.5\,\text{fs}$ deviates from the overall behavior of the rest. One measurement campaign takes several hours, and an outlier can thus be explained by a short-term instability of the system, e.g. a drop of the CEP stability, the loss of IAPs, or a loss of the phase-locking between all three pulses. Nevertheless a clear oscillation of the amplitude of the asymmetry as a function of $\tau_{\text{XUV-XUV}}$ can be seen.

High KER region Secondly, the $\tau_{\text{XUV-XUV}}$-dependence of the asymmetry parameter is investigated at high KER. Therefore, in the second, and third campaign the asymmetry as a function of $\tau_{\text{XUV-NIR}}$ is averaged between $6.1 - 7.7\,\text{eV}$, and the signal is fitted to a cosinusoidal function. The upper value is chosen to avoid the highest energy region, where the measured H^+ fragment yield becomes too low for a $\tau_{\text{XUV-XUV}}$ with low photon flux, and the lower value is just above the π-phase shift of the $\tau_{\text{XUV-NIR}}$-dependent asymmetry oscillation.
As before the standard deviations of the cosinusoidal fits are given as error bars of the corresponding data points.

The retrieved amplitude of the $\tau_{\text{XUV-NIR}}$-dependent oscillation of the asymmetry is plotted as a function of $\tau_{\text{XUV-XUV}}$ in Fig. 7.11 for the (a) second, and (b) third measurement campaign, respectively. It should be noted that in the first campaign (cf. Fig. 7.7) there is no clear oscillation of the amplitude of the asymmetry as a function of $\tau_{\text{XUV-XUV}}$ observable in this KER region (first campaign: $7.7 - 9\,\text{eV}$, since π-phase shift is at a higher energy). The amplitude of the asymmetry stays rather constant with a mean value of 0.03 ± 0.01.

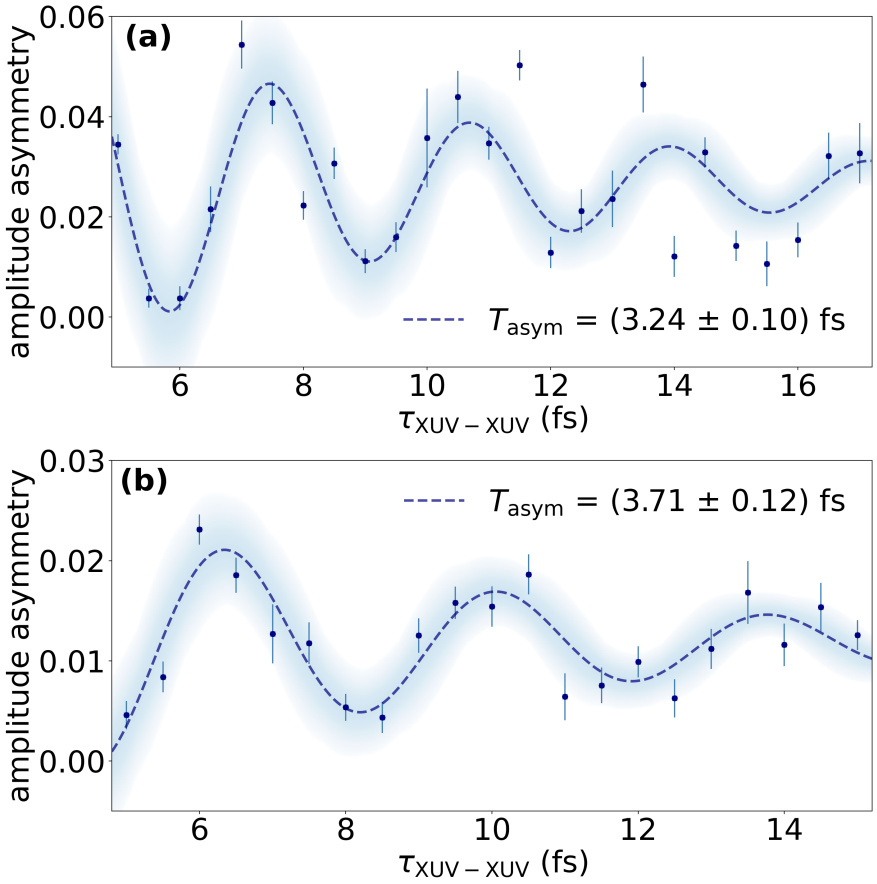

Figure 7.11: High KER region: Amplitude of the $\tau_{\text{XUV-NIR}}$-dependent oscillation of the asymmetry parameter at a high KER as a function of $\tau_{\text{XUV-XUV}}$ for two different measurement campaigns ((a) second, (b) third campaign). Similar to before the amplitude is retrieved by averaging the asymmetry parameter as a function of $\tau_{\text{XUV-NIR}}$ between $6.1 - 7.7\,\text{eV}$, and subsequently fitting the averaged signal to a cosinusoidal function. The standard deviation of each curve fit is given as error bar of the corresponding data point. The amplitude of the asymmetry oscillates as a function of $\tau_{\text{XUV-XUV}}$ with a period of (a) $T_{\text{asym}} = (3.24 \pm 0.10)\,\text{fs}$, and (b) $T_{\text{asym}} = (3.71 \pm 0.12)\,\text{fs}$, which is retrieved by a weighted sinusoidal curve fit with a damped amplitude as before. The shaded area is the standard deviation of the sinusoidal fit.

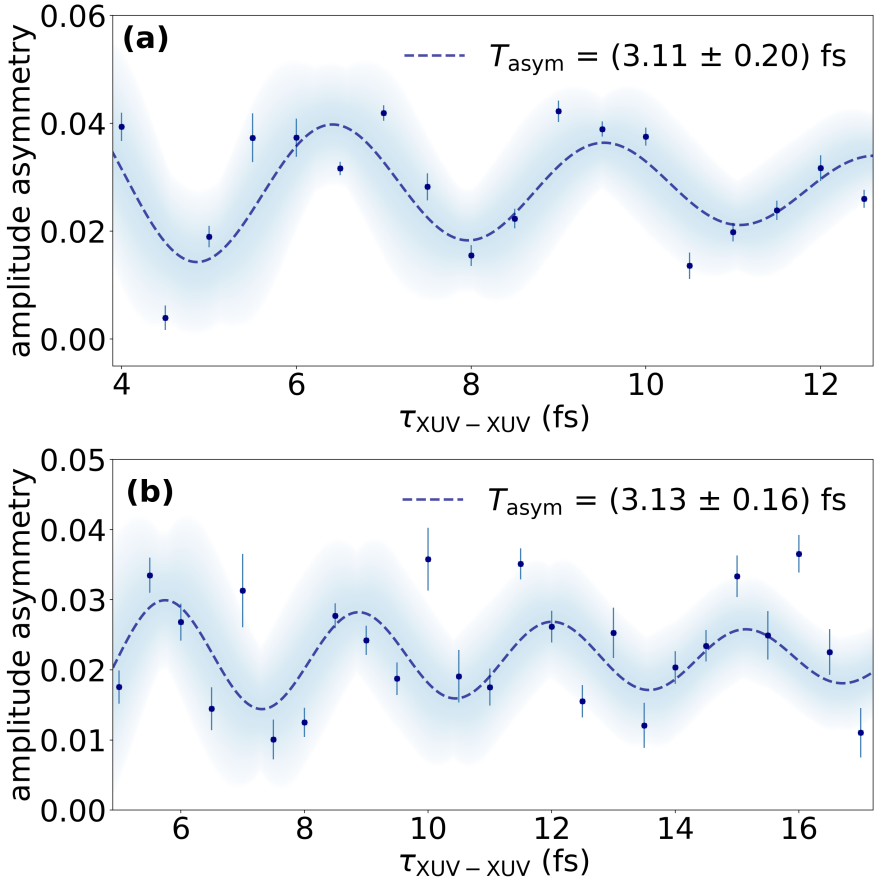

Figure 7.12: Low KER region: Amplitude of the oscillation of the asymmetry parameter as a function of $\tau_{\text{XUV-NIR}}$ plotted as a function of $\tau_{\text{XUV-XUV}}$ for the (a) first, and (b) second measurement campaign by averaging the asymmetry parameter around 1 eV. The amplitude is given as points for each $\tau_{\text{XUV-XUV}}$, which is retrieved by a cosinusoidal curve fit of the averaged signal. The error bars of the data points are the standard deviations of the cosinusoidal curve fits. The amplitude of the asymmetry oscillates as a function of $\tau_{\text{XUV-XUV}}$ with a period of (a) $T_{\text{asym}} = (3.11 \pm 0.20)$ fs, and (b) $T_{\text{asym}} = (3.13 \pm 0.16)$ fs, which is retrieved by a weighted sinusoidal curve fit with a damped amplitude as before. The shaded area is the standard deviation of the sinusoidal fit.

In Fig. 7.11 (a) the data point at $\tau_{\text{XUV-XUV}} = 14$ fs deviates from the rest. Nevertheless, it can be seen that the amplitude of the asymmetry oscillates as a function of $\tau_{\text{XUV-XUV}}$ with a period of (a) $T_{\text{asym}} = (3.24 \pm 0.10)$ fs, and (b) $T_{\text{asym}} = (3.71 \pm 0.12)$ fs.

The periods are compared to the times retrieved for the middle KER region in table 7.1 column 3, and 4. In both campaigns the period at high KER is around 20 as longer than the period at middle KER, however they still agree within their error bars.

Low KER region Finally, the amplitude of the $\tau_{\text{XUV-NIR}}$-dependent asymmetry parameter oscillation is extracted at a low KER, i.e. around 1 eV. Once again the averaged signal is fitted to a cosinusoidal curve and the retrieved amplitude is plotted as a function of $\tau_{\text{XUV-XUV}}$, which is shown in Fig. 7.12 (a) for the first (cf. Fig. 7.7), and in Fig. 7.12 (b) for the second measurement campaign (cf. Fig. 7.10 (a)).
The asymmetry amplitude oscillates as a function of $\tau_{\text{XUV-XUV}}$ with a period of (a) $T_{\text{asym}} = (3.11 \pm 0.20)$, and (b) $T_{\text{asym}} = (3.13 \pm 0.16)$ fs, which is retrieved by a sinusoidal curve fit of the data points as before.

In the second measurement campaign, already a few outliers can be observed, and for the third measurement campaign no clear oscillation of the amplitude of the asymmetry as a function of $\tau_{\text{XUV-XUV}}$ is visible in this KER region. In the latter the asymmetry amplitude stays constant over all $\tau_{\text{XUV-XUV}}$ with a mean value of 0.01 ± 0.003.

7.3 Discussion

In the following section the different experimental observations as a function of $\tau_{\text{XUV-NIR}}$, $\tau_{\text{XUV-XUV}}$ and KER are discussed. In the first part, the results and effects that have already been studied in the literature [160, 360, 362, 363, 369] are explained. In the second part, the newly found results are discussed, in particular regarding the degree of electronic coherence and the degree of ion+photoelectron entanglement, respectively, as a function of $\tau_{\text{XUV-XUV}}$ as well as $\tau_{\text{XUV-NIR}}$.

7.3.1 Dependence of the asymmetry parameter on the pump-probe delay $\tau_{\text{XUV-NIR}}$

The dependence of the asymmetry parameter on $\tau_{\text{XUV-NIR}}$ is typical for electron localization [360, 369]. The asymmetry parameter is determined by the phase relation between the XUV pulse and the sub-cycle evolution of the NIR pulse, which can be explained as follows (i.e. following the explanation given by Sansone et al. [360], and the dissertation of F. Kelkensberg [366]):

At the start of the dissociation process, the splitting $\omega_0(R)$ between the *gerade* and *ungerade* electronic state is large compared to the NIR-laser-induced dipole coupling between them, i.e. $\omega_0(R) \gg \mu(R)E_{\text{NIR}}(t)$, where $\mu(R)$ is the electronic dipole moment, and $E_{\text{NIR}}(t)$ is the electric field of the NIR pulse. In this case the transition probability between the two electronic states is small, the nuclear wave packet is in an adiabatic state, and is defined.
When $\omega_0(R) \approx \mu(R)E_{\text{NIR}}(t)$, the wave packet passes through a mixed adiabatic/diabatic region slowly merging into a coherent superposition of the two electronic states.
Close to the end of the dissociation process, i.e. $\omega_0(R) \ll \mu(R)E_{\text{NIR}}(t)$, the wave packet is in a diabatic state, and jumps between the *gerade* and *ungerade* electronic state. At this point the localization acquired before is fixed, and the

electron can no longer switch between the upper and lower proton, which defines electron localization.

Thus, the observed asymmetry parameter depends on the internuclear distance, where the nuclear wave packet is created upon XUV ionization and the phase relative to the NIR probe pulse. As a result, the asymmetry parameter oscillates as a function of $\tau_{\text{XUV-NIR}}$ with a phase depending on KER.
Accordingly, stabilizing the CEP is crucial in order to observe electron localization.

7.3.2 Different mechanisms leading to electron localization

In general, upon XUV dissociative ionization and interaction of the NIR pulse with the system different mechanisms exist, which all result in electron localization. Each mechanism describes the interference of two pathways in the final state involving the two ionic intermediate states, i.e. *gerade* and *ungerade* electronic state in H_2^+ (cf. sect. 2.2.3). The pathways lead to ion fragments with the same KER, and photoelectrons with the same EKE and orbital angular momentum (l = *even* or *odd*), thus making them indistinguishable. Hence a coherent superposition of the *gerade* and *ungerade* electronic state is created according to Eq. 7.3.
Different mechanisms, i.e. interfering pathways, which lead to electronic coherence and the observation of electron localization have been studied extensively in the literature, and can be found for example in [160, 360, 362, 363, 369].
In the following five different mechanisms are listed, and illustrated in Fig. 7.13, which are based on the ones found in the aforementioned TDSE calculation performed by Rubio et al. In each mechanism pathway 1 and 2 interfere in the final state, leading to electronic coherence. One of the pathways includes an interaction with solely the XUV pulse, whereas the other one involves an interaction with the XUV+NIR pulse sequence.

- Mechanism I:
  - **1. pathway:** H_2 ground state $\xrightarrow{\text{XUV}}$ $1s\sigma_g + e^-$ with $l = 1, 3, ...$
  - **2. pathway:** H_2 ground state $\xrightarrow{\text{XUV}}$ $1s\sigma_g + e^-$ with $l = 1, 3, ...$ $\xrightarrow{\text{NIR}}$ $2p\sigma_u + e^-$ with $l = 1, 3, ...$
- Mechanism II:
  - **1. pathway:** H_2 ground state $\xrightarrow{\text{XUV}}$ $2p\sigma_u + e^-$ with $l = 0, 2, ...$
  - **2. pathway:** H_2 ground state $\xrightarrow{\text{XUV}}$ $2p\sigma_u + e^-$ with $l = 0, 2, ...$ $\xrightarrow{\text{NIR}}$ $1s\sigma_g + e^-$ with $l = 0, 2, ...$
- Mechanism III:
  - **1. pathway:** H_2 ground state $\xrightarrow{\text{XUV}}$ $2p\sigma_u + e^-$ with $l = 0, 2, ...$

  - **2. pathway:** H_2 ground state $\xrightarrow{\text{XUV}}$ $Q_1{}^1\Sigma_u^+$ (H_2) $\xrightarrow{\text{decay}}$ $1s\sigma_g$ + e^- with $l = 1, 3, ...$ $\xrightarrow{\text{NIR}}$ $1s\sigma_g$ + e^- with $l = 0, 2, ...$

  or:

  - **1. pathway:** H_2 ground state $\xrightarrow{\text{XUV}}$ $2p\sigma_u$ + e^- with $l = 0, 2, ...$ $\xrightarrow{\text{NIR}}$ $2p\sigma_u$ + e^- with $l = 1, 3, ...$
  - **2. pathway:** H_2 ground state $\xrightarrow{\text{XUV}}$ $Q_1{}^1\Sigma_u^+$ (H_2) $\xrightarrow{\text{decay}}$ $1s\sigma_g$ + e^- with $l = 1, 3, ...$

- Mechanism IV:
  - **1. pathway:** H_2 ground state $\xrightarrow{\text{XUV}}$ $Q_1{}^1\Sigma_u^+$ (H_2) $\xrightarrow{\text{decay}}$ $1s\sigma_g$ + e^- with $l = 1, 3, ...$
  - **2. pathway:** H_2 ground state $\xrightarrow{\text{XUV}}$ $1s\sigma_g$ + e^- with $l = 1, 3, ...$ $\xrightarrow{\text{NIR}}$ $2p\sigma_u$ + e^- with $l = 1, 3, ...$

- Mechanism V:
  - **1. pathway:** H_2 ground state $\xrightarrow{\text{XUV}}$ $Q_1{}^1\Sigma_u^+$ (H_2) $\xrightarrow{\text{decay}}$ $1s\sigma_g$ + e^- with $l = 1, 3, ...$
  - **2. pathway:** H_2 ground state $\xrightarrow{\text{XUV}}$ $Q_1{}^1\Sigma_u^+$ (H_2) $\xrightarrow{\text{decay}}$ $\xrightarrow{\text{NIR}}$ $2p\sigma_u$ + e^- with $l = 1, 3, ...$

The first two mechanisms sketch the interaction of the NIR pulse with the ion. In Fig. 7.13 (a) mechanism I is shown, displaying a wave packet dissociating in the $1s\sigma_g$ state by direct XUV ionization, which interferes with a wave packet in the $2p\sigma_u$ state created due to the absorption of 1-NIR-photon during the dissociation process (NIR: $c_{0l} \rightarrow c_{1l}, l = odd$).

The second mechanism II (cf. Fig. 7.13 (b)) describes the interference of a wave packet created by direct 1-XUV-photon ionization of H_2 dissociating in the $2p\sigma_u$ state with a wave packet in the $1s\sigma_g$ state by stimulated emission of 1-NIR-photon during the dissociating process (NIR: $c_{1l} \rightarrow c_{0l}, l = even$). [360]

On the other hand, mechanism III describes the interaction of the NIR pulse with the photoelectron (cf. Fig. 7.13 (c)). Here a wave packet in the $2p\sigma_u$ state of H_2^+ launched by direct XUV ionization of H_2 interferes with a wave packet in the $1s\sigma_g$ state created through autoionization of the $Q_1{}^1\Sigma_u^+$ states. The wave packet in the $1s\sigma_g$ state is accompanied by a photoelectron with *odd*-number orbital angular momentum ($l = odd$), whereas the wave packet in the $2p\sigma_u$ state is accompanied by a photoelectron with $l = even$. The NIR pulse can either interact with the photoelectron from the first or second pathway, thus changing the photoelectrons parity from *even* to *odd* or vice versa (NIR: $c_{0l} \rightarrow c_{0l\pm1}$, or $c_{1l} \rightarrow c_{1l\pm1}$). [360]

The next mechanisms also include the autoionizing states, however here the NIR interacts again with the ion. The fourth mechanism IV describes a wave packet in the $1s\sigma_g$ state due to the autoionization of the $Q_1{}^1\Sigma_u^+$ states upon 1-XUV-photon

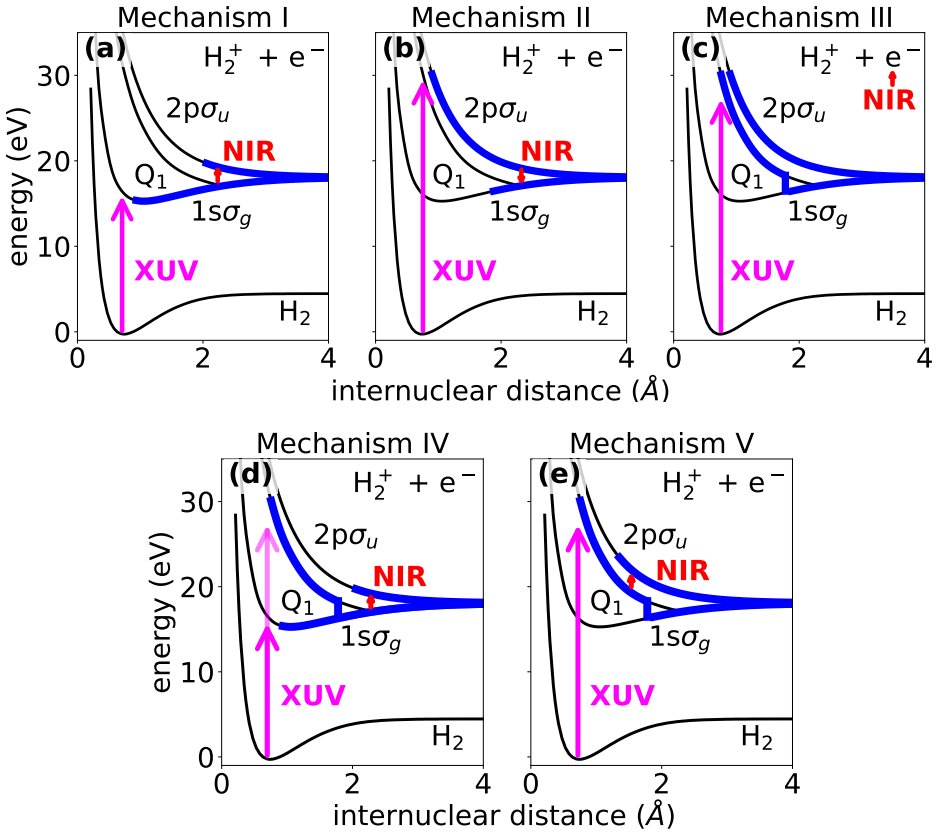

Figure 7.13: Schematic representation of different mechanisms [160, 360, 362, 363, 369] in H_2^+ leading to electron localization. (a) Mechanism I shows the interference of a wave packet created by direct XUV ionization, which dissociates in the $1s\sigma_g$ state, and a wave packet in the $2p\sigma_u$ state by absorption of 1-NIR-photon during the dissociation. (b) Mechanism IIdisplays the interference of a wave packet in the $1s\sigma_g$ state caused by stimulated emission of 1-NIR-photon during the dissociation on the $2p\sigma_u$ state, and a wave packet in the $2p\sigma_u$ state upon direct XUV ionization. (c) Mechanism III describes the interference of a wave packet stemming from direct XUV ionization of H_2 dissociating in the $2p\sigma_u$ state of H_2^+ with a wave packet in the $1s\sigma_g$ state originating from autoionization of the $Q_1{}^1\Sigma_u^+$ states. The NIR pulse then interacts with the photoelectron changing its parity from *even* to *odd* or vice versa. (d) Mechanism IV shows a wave packet in the $2p\sigma_u$ state originating from 1-NIR-photon absorption during the dissociation of the $1s\sigma_g$ state upon 1-XUV-photon ionization of the molecule, which interferes with a wave packet in the $1s\sigma_g$ state due to the autoionization of the $Q_1{}^1\Sigma_u^+$ states. (e) Mechanism V firstly includes a wave packet in the $Q_1{}^1\Sigma_u^+$ states due to the absorption of 1-XUV-photon. Subsequently, during the autoionization of the molecule the absorption of 1-NIR-photon can lead to the projection of the wave packet from the $Q_1{}^1\Sigma_u^+$ states to the $2p\sigma_u$ state. The interference of the latter with a wave packet due to the autoionization of the molecule into the $1s\sigma_g$ state is described by mechanism V.

ionization of H_2, which interferes with a wave packet in the $2p\sigma_u$ state due to 1-NIR-photon absorption during the dissociation of the $1s\sigma_g$ state launched by 1-XUV-photon ionization of the neutral molecule (NIR: $c_{0l} \rightarrow c_{1l}, l = odd$).

The last mechanism V describes a wave packet in the $1s\sigma_g$ state resulting from autoionization of the $Q_1{}^1\Sigma_u^+$ states by 1-XUV-photon absorption (photoelectron with $l = odd$), which interferes with a wave packet in the $2p\sigma_u$ state. The latter comes from the 1-XUV-photon autoionization of the $Q_1{}^1\Sigma_u^+$ states and the subsequent absorption of 1-NIR-photon before the state has decayed. In particular, the pathways $H_2 \rightarrow$ pre-decay $Q_1{}^1\Sigma_u^+ \rightarrow 2p\sigma_u$ is accompanied by a photoelectron with $l = odd$.

In general each mechanism describes the launch of a wavepacket in different electronic states. As described in detail in the paragraph about the photoexcitation of H_2, the ionic fragments with the highest KER are due to direct dissociation of the $2p\sigma_u$ state, whereas the fragments with the lowest KER are from direct dissociation of the $1s\sigma_g$ state. Accordingly, the five mechanisms result in ion fragments with different KERs. The ion fragments with the lowest KER should occur predominantly due to mechanism I and IV, where the maximal fragment energy for mechanism IV should be higher than for mechanism I. The ion fragments with the highest KER should emerge due to mechanism II, III, and V, where the minimal fragment energy out of those three should occur from mechanism V.

As aforementioned the phase of the asymmetry oscillation depends on the internuclear distance, where the wave packet is created and the phase relative to the NIR probe pulse [360]. In addition, autoionizing states have a defined lifetime (e.g. lifetime of $Q_1{}^1\Sigma_u^+$ is $\sim 2\,\mathrm{fs}$ [374]) leading to a delayed ionization of the molecule. Thus, each mechanism should be responsible for an asymmetry parameter oscillating as a function of $\tau_{\text{XUV-NIR}}$ with a specific KER dependent phase. Accordingly, a phase shift of the $\tau_{\text{XUV-NIR}}$-dependent asymmetry oscillation could possibly mark the transition between different KER regions (low, middle, high), where the asymmetry parameters due to different mechanisms overlap (e.g. low KER: mech. I and IV; middle KER: mech. IV and V; high KER: mech. II,III and V).

It should be noted that an involvement of the autoionizing $Q_2^1\Pi_u$ states can not be ruled out as mentioned in [360]. For a better signal-to-noise ratio the evaluation of the asymmetry parameter includes H^+ fragments within a $\sim 22.5\,^\circ$ cone around the laser polarization axis, due to the fact that the inversion to retrieve the full 3D probability distribution is done with a highest Legendre polynomials order of 4. As discussed in sect. 3.5.1, the zero order corresponds to an angle-integrated signal, and with increasing order, the angle, which is integrated over decreases (e.g. 2nd order $\widehat{=} 45\,^\circ$).
As a consequence, not only contributions of molecules aligned along the laser polarization axis are taken into account, but also ion fragments resulting from perpendicular transition excitation [360]. Above an XUV photon energy of 31 eV, molecules aligned orthogonal to the laser polarization axis exhibit a preferential perpendicular transition excitation to the $Q_2{}^1\Pi_u$ states [360], due to the nature of the π orbital [375], and which decay through the $1s\sigma_g$ and $2p\sigma_u$ channel leading

to ion fragments with a KER between $\sim 2-10\,\mathrm{eV}$ and $\sim 10-16\,\mathrm{eV}$ [376], respectively. The possible involvement of the $Q_2{}^1\Pi_u$ states can thus cause an increase of the signal measured in these KER regions [360], as well as a possible phase shift.

Furthermore, all mechanisms which involve autoionizing states rely on the overlap between the pump and probe pulses [360]. This explains the decrease of the amplitude of the $\tau_{\text{XUV-NIR}}$-dependent asymmetry as a function of $\tau_{\text{XUV-XUV}}$, since for long delays at least one of the XUV pulses only overlaps with the tail of the NIR pulse, and which thus leads to a decrease of the observed asymmetry parameter.

7.3.3 Dependence of the asymmetry parameter on the XUV-XUV delay

In the following sections the new discoveries and main experimental results of this chapter are discussed in detail, i.e. the oscillation of the amplitude of the $\tau_{\text{XUV-NIR}}$-dependent asymmetry parameter as a function of $\tau_{\text{XUV-XUV}}$, and the role of ion+photoelectron entanglement.

In general, if the amplitude of the asymmetry is maximal, electron localization emerges in most of the ions, however if the amplitude is minimal the formation of electron localization is suppressed. Thus the question arises, what can control the formation of electronic coherence, and thus the observation of electron localization?

According to Eq. 7.2, there exist two different ionization pathways, i.e. the hydrogen molecule can either absorb 1-XUV-photon ($E_{\text{XUV},1} = \hbar\omega_{\text{XUV},1}$) creating an ion in the *gerade* electronic state, or absorb 1-XUV-photon ($E_{\text{XUV},2} = \hbar\omega_{\text{XUV},2}$) and excite the *ungerade* electronic state in the ion accompanied by the corresponding photoelectron. Subsequently, the ion+photoelectron system interacts with the NIR pulse, which leads to the absorption or emission of 1-NIR-photon ($\pm\hbar\omega_{\text{NIR}}$). To create a coherent superposition of the *gerade* and *ungerade* electronic state, the total energy (KER+EKE) must be identical for the two pathways making it impossible to distinguish between them in the final state (cf. Eq. 7.3).

As described in detail in the previous section, for each aforementioned mechanism, which leads to electron localization, there exists one pathway, which involves the absorption of 1-XUV and 1-NIR-photon, and one pathway, which includes only the interaction with the XUV pulses. Accordingly, to end up in the same final state, the energy difference of the two XUV photons of the first and second pathway has to be $\Delta E_{\text{XUV}} = \hbar\omega_{\text{XUV},1} - \hbar\omega_{\text{XUV},2} = \hbar\omega_{\text{NIR}}$.

As mentioned before, the spectrum of the two interfering XUV pulses exhibits a fringe pattern with a spacing of $\delta\omega_{\text{XUV}} = 2\pi/\tau_{\text{XUV-XUV}}$. Consequently, if the two XUV pulses are separated in time by $\tau_{\text{XUV-XUV}} = 2n\pi/\omega_{\text{NIR}}$, where n is an integer, the two necessary XUV photons ($E_{\text{XUV},1} + E_{\text{XUV},2}$) can be found in the spectrum, as shown in Fig. 7.14. The two pathways are indistinguishable, and a coherent superposition of the electronic states is formed, and electron localization is observed.

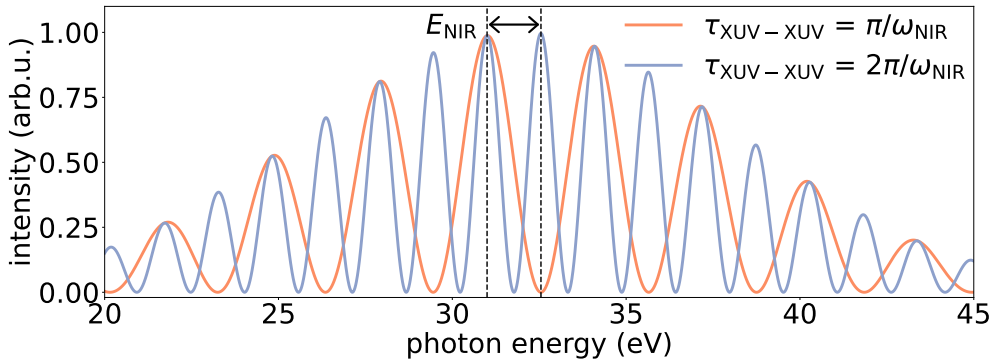

Figure 7.14: Exemplary calculated spectra of two interfering gaussian pulses with different time delays $\tau_{\mathrm{XUV\text{-}XUV}}$, which represent the XUV spectra in the current experiment of two specific cases. For a time delay of $\tau_{\mathrm{XUV\text{-}XUV}} = \pi/\omega_{\mathrm{NIR}}$ (orange line), the spectrum exhibits a fringe modulation with a spacing of twice the NIR photon energy, i.e. $2E_{\mathrm{NIR}} = 2\hbar\omega_{\mathrm{NIR}}$ (here: $\omega_{\mathrm{NIR}} = 1.55\,\mathrm{eV}$). For a time delay of $\tau_{\mathrm{XUV\text{-}XUV}} = 2\pi/\omega_{\mathrm{NIR}}$ (blue line), the fringe spacing is exactly $E_{\mathrm{NIR}} = \hbar\omega_{\mathrm{NIR}}$.

However, if the two XUV pulses are separated by $\tau_{\mathrm{XUV\text{-}XUV}} = (2n+1)\pi/\omega_{\mathrm{NIR}}$, with n as an integer, one of the necessary XUV photons is missing, and thus no electronic coherence is formed, since the two pathways become distinguishable in energy.
As a result, the amplitude of the asymmetry should oscillate with a period of $T_{\mathrm{asym}} = 2\pi/\omega_{\mathrm{NIR}}$ as a function of $\tau_{\mathrm{XUV\text{-}XUV}}$.

Period of amplitude asymmetry oscillation Since the NIR probe pulse is centered at 800 nm, one would expect that the amplitude of the asymmetry oscillates with a period of $T_{\mathrm{asym,theory}} = 2\pi/\omega_{\mathrm{NIR}} \sim 2.7\,\mathrm{fs}$ in all KER regions. However, according to column $3-5$ in table 7.1 the period is longer, i.e. $T_{\mathrm{asym}} > 3\,\mathrm{fs}$. A period of 3 fs corresponds to a wavelength of 900 nm. The NIR probe pulse has a bandwidth of 40 nm, accordingly this wavelength is not included in the NIR spectrum.

This poses the question, what other effect can lead to an increase of the period of the $\tau_{\mathrm{XUV\text{-}XUV}}$-dependent amplitude asymmetry oscillation?

In every campaign for each delay point $\tau_{\mathrm{XUV\text{-}XUV}}$, and $\tau_{\mathrm{XUV\text{-}NIR}}$ not only the H^+ fragment yield, but also the spectra of the two ionizing XUV pulses are recorded. The interference signal of the two XUV pulses (cf. sect. 5.1.2) as a function of $\tau_{\mathrm{XUV\text{-}XUV}}$ is shown in Fig. 7.15 for the first measurement campaign (cf. Fig. 7.7, the signal for the two other campaigns can be found in appendix A.3 Fig. A.4). The two ionizing XUV pulses are not generated independently, due to the interference of the NIR pulses during the HHG (cf. sect. 5.1.2). This leads to an oscillation of the harmonic yield as a function of $\tau_{\mathrm{XUV\text{-}XUV}}$ with a period of $T_{\mathrm{HHG}} = 2\pi/\omega_{\mathrm{NIR}}$.

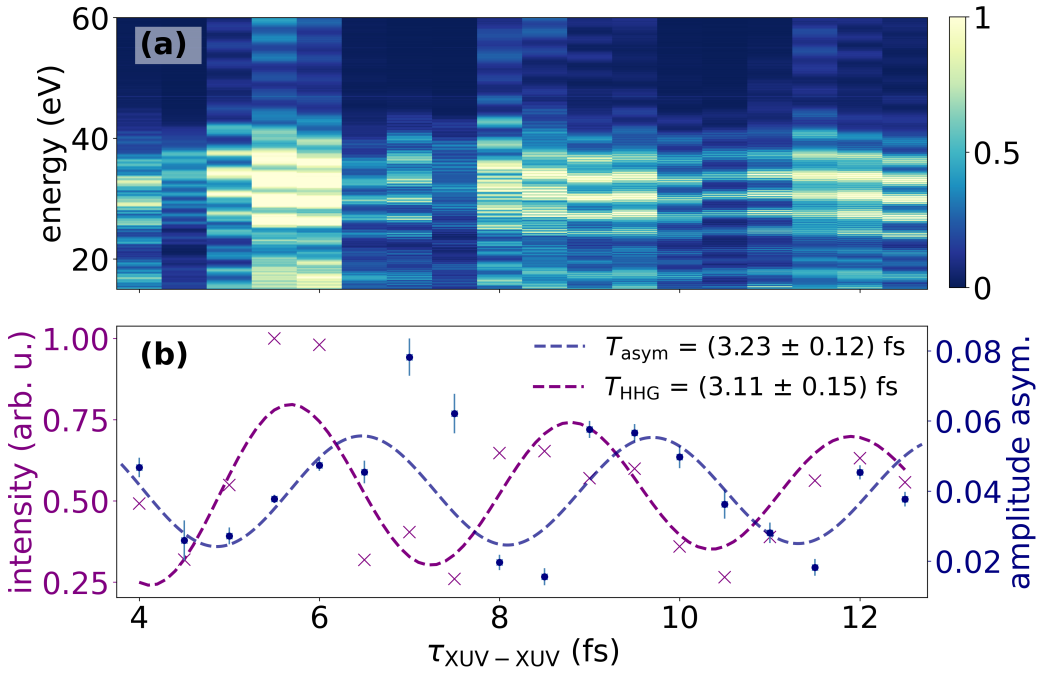

Figure 7.15: (a) Recorded spectra of the two phase-locked isolated attosecond pulses used to dissociatively ionize hydrogen molecules in the first measurment campaign as a function of $\tau_{\text{XUV-XUV}}$ and the energy spectrum. (b) Normalized energy-integrated $(25-40\,\text{eV})$ intensity of the autocorrelation signal shown in (a) as a function of $\tau_{\text{XUV-XUV}}$ (blue curve). The harmonic yield oscillates with a period of $T_{\text{HHG}} = (3.11 \pm 0.15)\,\text{fs}$, due to the interference of the two driving NIR pulses during the HHG process. The period is retrieved by fitting the data points (purple crosses) to a cosinusoidal function with a damped amplitude (dashed purple line) $C_3 + A_3 \exp(-n_3 \tau_{\text{XUV-XUV}}) \sin(2\pi(\tau_{\text{XUV-XUV}} - \tau_{c3})/T_{\text{HHG}}))$ with the fit parameter $C_3, A_3, n_3, \tau_{c3}, T_{\text{HHG}}$. In addition the amplitude of the asymmetry at middle KER (axis on the right side of figure (b)) as a function of $\tau_{\text{XUV-XUV}}$ is shown with the corresponding sinusoidal fit (dark blue dashed line) of the data points (dark blue dots) as in Fig. 7.7. The amplitude of the asymmetry oscillates with a comparable period as the oscillation of the XUV photon flux.

As can be seen in Fig. 7.15 (b) the normalized energy-integrated XUV intensity oscillates with a period of $T_{\text{HHG}} = (3.11 \pm 0.15)\,\text{fs}$, which is found by a cosinusoidal curve fit of the data points. The period T_{HHG} is longer than expected for NIR driving pulses centered at 770 nm, however as explained in detail in sect. 5.1.2 a period of $T_{\text{HHG}} \gtrsim 3\,\text{fs}$ is not unusual for a delay range of $\tau_{\text{XUV-XUV}} \sim 4 - 17\,\text{fs}$, and can be explained by a small chirp in the tail of the NIR driving pulses.
In addition in Fig. 7.15 (b) the amplitude of the asymmetry at middle KER is shown at the right vertical axis oscillating with a period of $T_{\text{asym}} = (3.23 \pm 0.12)\,\text{fs}$, which is comparable to the period of the oscillation of the HHG flux T_{HHG}.
The periods retrieved in all measurement campaigns are shown in table 7.1 column $3-5$ and are compared with column 6. In each campaign T_{asym} is in the same

order of magnitude as T_{HHG}, with $T_{\mathrm{asym}} \geq T_{\mathrm{HHG}}$. In the first two campaigns the periods agree within their error bars. In the third campaign the period T_{asym} is slightly longer than T_{HHG} including the error bars.

Firstly, the $\tau_{\mathrm{XUV\text{-}XUV}}$-dependent harmonic yield superimposes with the signal of the asymmetry parameter. At $\tau_{\mathrm{XUV\text{-}XUV}}$, where the harmonic yield is low, the H^+ fragment yield is decreased correspondingly leading to an asymmetry parameter with a higher signal-to-noise ratio compared to a $\tau_{\mathrm{XUV\text{-}XUV}}$ where the yield is high. As described before, the asymmetry parameter as a function of $\tau_{\mathrm{XUV\text{-}NIR}}$ is fitted to a cosinusoidal curve fit to extract the amplitude of the asymmetry as shown in Fig. 7.8. Accordingly, the noisier the signal, the bigger is the error bar of the fit parameter A_{XN}. Thus, the harmonic yield first of all attributes to the strength of the error bars of the data points of the amplitude of the asymmetry as shown in e.g. Fig. 7.9.

Secondly, the amplitude and phase of the states prepared in H_2^+ upon XUV absorption depend on the spectra of the two interfering XUV pulses, which is modulated with T_{HHG}. Accordingly, the states, which are brought into interference by the NIR pulse have been determined by the XUV amplitude and phase, and thus are influenced by T_{HHG}.

Accordingly, it could be possible that the time scale introduced during HHG competes against the aforementioned simple model, which predicts an amplitude asymmetry oscillation with $T_{\mathrm{asym,theory}}$, and an interplay of these two timescales could then lead to an increase of the measured T_{asym}, since $T_{\mathrm{HHG}} > T_{\mathrm{asym,theory}}$. To fully understand this relation and the underlying mechanism additional theory would be required.

7.3.4 Role of entanglement

According to Eq. 7.2 the XUV pulses firstly create an entangled ion+photoelectron system and the NIR pulse can subsequently create a coherent superposition of electronic states according to Eq. 7.3. The $\tau_{\mathrm{XUV\text{-}XUV}}$ dependence of the asymmetry parameter reflects the ability of the NIR pulse to do so. However, now the question arises if ion+photoelectron entanglement actually plays a role in the aforementioned mechanisms?

Mechanism I, II, IV, V In the case of mechanism I, IV, and V, upon absorption of 1-XUV-photon, Eq. 7.2 becomes

$$|\Psi_{\mathrm{I,IV,V,\ EKE+KER,XUV}}\rangle = \sum_{l=1,3,\ldots} c_{0l}\,|\phi_{1\mathrm{s}\sigma_\mathrm{g}}\rangle \otimes |\chi_l\rangle\,. \tag{7.7}$$

It should be noted that mechanism IV and V are in a sense quite similar to mechanism I, with the main difference that the $1s\sigma_g$ state is not excited directly, but rather through the autoionization of the $Q_1\,{}^1\Sigma_u^+$ states.

In terms of mechanism II, Eq. 7.2 is given by

$$|\Psi_{\mathrm{II,EKE+KER,XUV}}\rangle = \sum_{l=0,2,\ldots} c_{1l}\,|\phi_{2\mathrm{p}\sigma_\mathrm{u}}\rangle \otimes |\chi_l\rangle\,. \tag{7.8}$$

In all the above, the interaction of the system with the NIR pulse occurs with the ionic part projecting the $1s\sigma_g$ (or $Q_1\,^1\Sigma_u^+$, mech. V) onto the $2p\sigma_u$ state, or vice versa, i.e. $c_{0l} \leftrightarrow c_{1l}$, which creates electron localization according to Eq. 7.3, where $\{c_{0l} \neq 0, c_{1l} \neq 0\}$ exists.

The parity of the photoelectron is well defined upon XUV ionization, the total wave function is a pure state, and accordingly entanglement plays no role here. The dependence of the formation of electron localization on $\tau_{\text{XUV-XUV}}$ in this case merely describes the condition to find the necessary XUV photons in the spectrum.

Mechanism III This however changes for mechanism III. Here Eq. 7.2 can not be simplified, creating a maximally entangled system upon ionization of the molecule with the XUV pulse pair. After the interaction with the NIR pulse, and the photoelectron orbital angular momentum is changed from *odd* to *even*, or vice versa.

In the first case, the wave function becomes for a certain KER+EKE

$$\begin{aligned} |\Psi_{\text{III,EKE+KER,XUV+NIR}}\rangle \;=\; & \sum_{l=l'=0,2,\ldots} \Big(c_{0l'}\,|\phi_{1s\sigma_g}\rangle + c_{1l}\,|\phi_{2p\sigma_u}\rangle\Big) \otimes |\chi'_l\rangle \\ & + \sum_{l''=1,3,\ldots} c_{0l''}\,|\phi_{1s\sigma_g}\rangle\Big) \otimes |\chi_{l''}\rangle\,, \end{aligned} \tag{7.9}$$

with $l' = l_{odd} \pm 1$ describing the transitions $c_{0l} \rightarrow c_{0l\pm1}$.

In the second case, the wave function is

$$\begin{aligned} |\Psi_{\text{III,EKE+KER,XUV+NIR}}\rangle \;=\; & \sum_{l=0,2,\ldots} c_{1l}\,|\phi_{2p\sigma_u}\rangle \otimes |\chi_l\rangle \\ & + \sum_{l''=l'''=1,3,\ldots} \Big(c_{0l''}\,|\phi_{1s\sigma_g}\rangle + c_{1l'''}\,|\phi_{2p\sigma_u}\rangle\Big) \otimes |\chi'_{l''}\rangle\,, \end{aligned} \tag{7.10}$$

with $l''' = l_{even} \pm 1$, which describes the transitions $c_{1l} \rightarrow c_{1l\pm1}$.

In both cases, the *gerade* and *ungerade* electronic states are in a coherent superposition leading to the observation of electron localization.

The degree of entanglement in Eq. 7.9 and 7.10 is lower than in Eq. 7.2, due to the superposition of the electronic states, and can become even zero for $c_{0l''} = 0$ in Eq. 7.9, and for $c_{1l} = 0$ in Eq. 7.10. Thus, in mechanism III ion+photoelectron entanglement indeed plays a role, and the dependence on $\tau_{\text{XUV-XUV}}$ reflects the ability of the NIR pulse to convert the initially entangled system into electronic coherence.

Furthermore, the degree of entanglement depends on the pump-probe delay, i.e. $\tau_{\text{XUV-NIR}}$. As described earlier, the asymmetry parameter oscillates as a function of $\tau_{\text{XUV-NIR}}$, as seen in e.g. Fig. 7.7 (a). If the asymmetry parameter has a maximal or minimal value, the remaining electron is highly localized at the upper or lower proton, respectively. Accordingly, at those delays the degree of electronic

coherence is high, whereas the degree of ion+photoelectron entanglement is low. If however, the asymmetry parameter is zero, the measured H^+ fragments are uniformly distributed, since the electron is not localized. For those delays the degree of coherence is low, and the degree of ion+photoelectron entanglement is high. Accordingly, the degree of ion+photoelectron entanglement oscillates as a function of $\tau_{\text{XUV-NIR}}$ with half the period of the oscillation of the asymmetry parameter, i.e. $T_{\text{NIR}}/2$.

A more detailed investigation of the role of entanglement in the current experiment is done with the results retrieved from the TDSE calculation by Rubio et al., which can be found in the future publication.

7.4 Conclusion

In this chapter, an experiment is presented, where an entangled ion+photoelectron system is created upon dissociative ionization of neutral H_2 by two phase-locked IAPs. Subsequently, a NIR pulse projects the system into a coherent superposition of the first *gerade* and *ungerade* electronic state of H_2^+, creating electron localization. The ability of the NIR pulse to convert the initially entangled system into electronic coherence is determined by the time delay between the two ionizing XUV pulses. Electron localization is observed for $\tau_{\text{XUV-XUV}} = 2n\pi/\omega_{\text{NIR}}$, whereas it is absent for $\tau_{\text{XUV-XUV}} = (2n+1)\pi/\omega_{\text{NIR}}$, with n as an integer. The degree of electronic coherence and the degree of ion+photoelectron entanglement, respectively, is controlled by tailoring the pulse excitation, i.e. the XUV pulse delay $\tau_{\text{XUV-XUV}}$, as well as the pump-probe delay $\tau_{\text{XUV-NIR}}$. This experiment is a second example, which demonstrates the important role of ion+photoelectron entanglement in attosecond science, and shows its limiting role towards the observability of coherence-based dynamics.

chapter 8

Summary and Outlook

The main goal of this thesis is to emphasize the important role of quantum-mechanical entanglement in attosecond science. Here two pump-probe experiments are presented, which investigate the role of ion+photoelectron entanglement during the ionization of hydrogen molecules, and how entanglement between the two subsystems can limit the coherence between different intermediate states in the ion.

In the first experiment, the degree of vibrational coherence in H_2^+ is controlled by changing the time delay between the two ionizing phase-locked XUV pulses, due to ion+photoelectron entanglement generated in the ionization process. A high degree of ion+photoelectron entanglement is observed, whenever $\tau_{\text{XUV-XUV}} = (2n+1)\pi/\Delta E_{v,v'}$, whereas a high degree of vibrational coherence occurs whenever $\tau_{\text{XUV-XUV}} = 2n\pi/\Delta E_{v,v'}$ (with n as an integer, and $\Delta E_{v,v'}$ is the energy difference between the two vibrational states v and v').

In the second experiment, the properties of electronic coherence in H_2^+ are investigated resulting from the dissociative ionization of H_2 by two phase-locked isolated attosecond pulses (IAPs) and the subsequent interaction of the system with a NIR pulse. In the laboratory-frame, a favored localization of the bound electron in the ion at one of the two protons is observed, whenever the initially entangled ion+photoelectron system resulting upon XUV ionization is converted into a coherent superposition of the first *gerade* and *ungerade* electronic state in H_2^+ by the NIR probe pulse. By changing the time delay between the two XUV pulses, the ability of the NIR pulse to create electron localization is controlled. For a time delay of $\tau_{\text{XUV-XUV}} = 2n\pi/\omega_{\text{NIR}}$, the NIR pulse is able to create electronic coherence, and electron localization is observed, whereas for $\tau_{\text{XUV-XUV}} = (2n+1)\pi/\omega_{\text{NIR}}$ the coherence is absent, and the ion+photoelectron system remains entangled (with n as an integer).

On the one hand, both experiments can be understood as an important model case of how ion+photoelectron entanglement can prevent the observation of coherent dynamics in ions, and photoelectrons in attosecond experiments.
On the other hand, these experiments also show the possibility to control entanglement and coherence by tailoring the ionizing pulse properties, and thus the opportunities given by combining attosecond science with quantum optics and quantum information theory.

The advance of quantum-mechanical entanglement in attosecond science has led to a variety of work investigating entanglement between different atomic, and molecular subsystems in the last years [2, 9, 111–113, 115, 118, 119, 121, 122, 143], where the characterization and the control of entanglement is of big interest.
In particular, there is a lot of interest in the role of entangled states during strong-field ionization and their impact on high harmonic generation [377–382]. An overview of the latter research field can be found in [102, 383]. Using light to engineer quantum states with non-classical properties is the essence of quantum optics, which is at the core of quantum technologies [124–126]. Quantum light exhibits strong quantum correlations, as well as it provides reduced noise, which is a big advantage compared to classical light. Furthermore, non-classical and entangled states of light are more robust with respect to decoherence compared to entangled states of other particles, as the interaction of photons with the environment can be more easily controlled and limited. Non-classical and entangled light therefore plays a crucial role in quantum information science, communication, teleportation, among others, however so far the application is limited by a low photon number. Combining quantum information science with attosecond science could solve this problem, thus creating massive, and robust entangled states with a high photon number, which would allow the controlled use of decoherence [102].

In conclusion, there are many opportunities to investigate and exploit entanglement in attosecond science. In particular, the exploitation of the active control of entanglement by tailoring the pulse excitation is only just beginning, and can be applied to study many more systems as well as different entangled subsystems. In addition, the use of two phase-locked APTs (attosecond pulse trains), and especially two phase-locked IAPs with variable delay offers a wide range of possibilities for applications in other research areas, as for example in attosecond multidimensional spectroscopy [238, 240, 251–253, 255, 256, 320–322] or multidimensional attosecond transient absorption spectroscopy [384].

Since Galileo the knowledge about light has increased tremendously,
but as Einstein already said:
"Je mehr ich weiß, um so mehr weiß ich, dass ich nicht(s) weiß."
("The more I know, the more I know that I don't know.")

APPENDIX A

Appendix

A.1 Derivation of the general uncertainty principle

The uncertainty principle was generalized by Howard P. Robertson [385] in 1929. The following derivation is based on the one given in [132].

First, two hermitian operators $\hat{A}$ and $\hat{B}$, with the expectation values of

$$\begin{aligned} \langle \hat{A} \rangle &= \frac{\langle \psi | \hat{A} | \psi \rangle}{\langle \psi | \psi \rangle} \\ \langle \hat{B} \rangle &= \frac{\langle \psi | \hat{B} | \psi \rangle}{\langle \psi | \psi \rangle} \end{aligned} \tag{A.1}$$

are considered. Further, $\Delta\hat{A} \equiv \hat{A} - \langle \hat{A} \rangle$, and $\Delta\hat{B} \equiv \hat{B} - \langle \hat{B} \rangle$ are defined.

Then, the expectation values $\langle (\Delta\hat{A})^2 \rangle$, and $\langle (\Delta\hat{B})^2 \rangle$ can be calculated, which are found to be equal to the variance σ, according to

$$\begin{aligned} \langle (\Delta\hat{A})^2 \rangle &= \langle \hat{A}^2 \rangle - \langle \hat{A} \rangle^2 = \sigma_{\mathrm{A}}^2 \\ \langle (\Delta\hat{B})^2 \rangle &= \langle \hat{B}^2 \rangle - \langle \hat{B} \rangle^2 = \sigma_{\mathrm{B}}^2. \end{aligned} \tag{A.2}$$

In addition, the states $|f\rangle$ and $|g\rangle$ are defined to be

$$\begin{aligned} |f\rangle &\equiv \Delta\hat{A} \, |\psi\rangle \\ |g\rangle &\equiv \Delta\hat{B} \, |\psi\rangle \, . \end{aligned} \tag{A.3}$$

Subsequently, the Schwarz inequality [386] can be applied to the two states, according to

$$\langle f|f\rangle \langle g|g\rangle \geq |\langle f|g\rangle|^2. \tag{A.4}$$

This can be rewritten as

$$\langle\psi|(\Delta\hat{A})^2|\psi\rangle \langle\psi|(\Delta\hat{B})^2|\psi\rangle \geq \left(\frac{1}{2i}\left(\langle f|g\rangle - \langle g|f\rangle\right)\right)^2, \tag{A.5}$$

exploiting the fact that $\langle f|g\rangle$ is a complex number z, where the following applies: $|z|^2 = \Re(z)^2 + \Im(z)^2 \geq \Im(z)^2 = \left(\frac{z-z*}{2i}\right)^2$.
Using that $\langle f|g\rangle = \langle\hat{A}\hat{B}\rangle - \langle\hat{A}\rangle\langle\hat{B}\rangle$, and $\langle g|f\rangle = \langle\hat{B}\hat{A}\rangle - \langle\hat{A}\rangle\langle\hat{B}\rangle$ the term in the brackets on the r.h.s. in Eq. A.5 becomes

$$\langle f|g\rangle - \langle g|f\rangle = \langle\hat{A}\hat{B}\rangle - \langle\hat{B}\hat{A}\rangle = \left\langle\psi\middle|\left[\hat{A},\hat{B}\right]\middle|\psi\right\rangle. \tag{A.6}$$

Finally, the equation becomes

$$\sigma_{\mathrm{A}}^2\sigma_{\mathrm{B}}^2 \geq \left(\frac{1}{2i}\left\langle\psi\middle|\left[\hat{A},\hat{B}\right]\middle|\psi\right\rangle\right)^2, \tag{A.7}$$

which is the general uncertainty principle.

Now one can replace $\hat{A} = \hat{x}$ with the position, and $\hat{B} = \hat{p_{\mathrm{x}}} = -i\hbar\partial/\partial x$ with the momentum operator, where the relation $[\hat{x},\hat{p_{\mathrm{x}}}]\,\psi(x) = (\hat{x}\hat{p_{\mathrm{x}}} - \hat{p_{\mathrm{x}}}\hat{x})\,\psi(x) = (-i\hbar x\partial/\partial x + i\hbar\,(1 + x\partial/\partial x))\,\psi(x) = i\hbar\psi(x)$ applies.

This leads to the well known expression of the position and momentum uncertainty principle

$$\sigma_{\mathrm{x}}\sigma_{\mathrm{p}} \geq \hbar/2. \tag{A.8}$$

A.2 Calibration of the KER axis

In chapter 7 the energy axis is calibrated with the help of the experimental results presented in chapter 5.2.
In the experiment described in chapter 5.2 the Rydberg states in helium atoms are excited by a two XUV pulse sequence with variable delay $\tau_{\text{XUV-XUV}}$, and are subsequently ionized by a NIR pulse. The photoelectrons are then measured as a function of $\tau_{\text{XUV-XUV}}$, which allows to retrieve the prior excited and very well known helium Rydberg states.

In Fig.A.1 the main experimental results of chapter 5.2 are presented, showing in the left figure the oscillation of the population of the Rydberg states as a function of $\tau_{\text{XUV-XUV}}$, and in the right figure the strong peaks in the frequency domain,

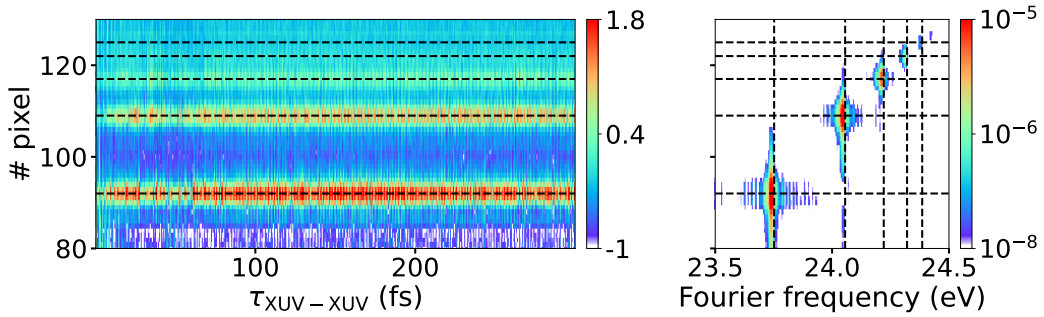

Figure A.1: See chapter 5.2: Measurement of photoelectrons, due to the excitation of helium atoms by two phase locked XUV pulses, and subsequent ionization by a NIR probe pulse (cf. Fig. 5.11). In the right figure $\beta_2(p_{e^-}, \tau_{\text{XUV-XUV}})$ is shown as a function of $\tau_{\text{XUV-XUV}}$. The y-axis is given in pixel numbers of the CCD camera, which recorded the VMI images. The pixel number corresponds linearly to the momentum of the photoelectrons. In the right figure the signal of $\beta_2(p_{e^-}, \tau_{\text{XUV-XUV}})$ is Fourier transformed along $\tau_{\text{XUV-XUV}}$, leading to pronounced peaks in the frequency domain, which correspond to the energies of different helium Rydberg states (1s4p−1s8p)

which correspond to the Rydberg states 1s4p up to 1s8p. The y-axis is given in pixel units of the CCD camera, which is used to measure the individual VMI images, and which corresponds linearly to the momentum of the photoelectrons.

Accordingly, the photoelectrons from the different Rydberg states have a measured energy of

$$S_{1snp} = E_{1snp} + E_{\text{NIR}} - \text{IP}, \tag{A.9}$$

where E_{1snp} is the energy of the Rydberg state 1snp [328] (with $n = 4 - 8$), $E_{\text{NIR}} = 1.55\,\text{eV}$ is the energy of the NIR probe laser, and IP $\sim 24.6\,\text{eV}$ [328] is the ionization potential of helium.
Thus, the y-axis can be calibrated by assigning the pixel, where the signal of the photoelectrons is measured to the different Rydberg energies. Since the pixel number is linear in momentum, the energy and the pixel number are correlated by a second order polynomial fit as shown in Fig. A.2.

The here found calibration can now be applied to the experiment of chapter 7, where H^+ ions are measured as a function of $\tau_{\text{XUV-XUV}}$ and $\tau_{\text{XUV-NIR}}$.
First of all, the voltages applied to the VMI spectrometer (repeller and extractor electrodes) have to be taken into account. This is important, since the energy of the measured particle scales linearly with the applied voltages. By increasing the voltages, the maximal energy, which can be observed on the detector increases. This in turn means that the energy axis is compressed, and the resolution of the images decreases.

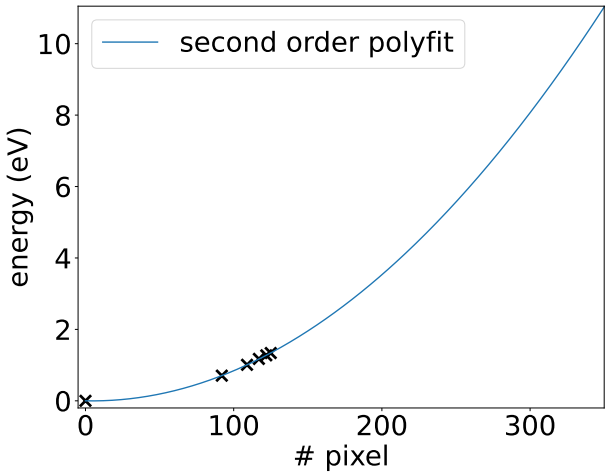

Figure A.2: Energy-pixel calibration curve determined by a second order polynomial fit (solid line) of the data points of the helium Rydberg energies as a function of the pixel number.

Whereas if the voltages are decreased, the maximal observed energy of the particles decreases, and the energy axis expands leading to a better resolution of the images.
Thus, it becomes obvious that if a measured signal has a broad bandwidth, it is important to apply high voltages. Whereas if a detailed resolution of small features is required, one should apply small voltages.

In chapter 5.2 the repeller and extractor voltages had a value of $\mathrm{Rep_{He}} = 2694\,\mathrm{V}$, and $\mathrm{Ext_{He}} = 2244\,\mathrm{V}$, respectively. Whereas in chapter 7 the voltages were $\mathrm{Rep_{H_2}} = 1554\,\mathrm{V}$, and $\mathrm{Ext_{H_2}} = 1387\,\mathrm{V}$, respectively. This leads to an averaged ratio between the two repeller, and extractor voltages of $\mathrm{Ratio_{He/H_2}} = \frac{1}{2}(\mathrm{Rep_{He}}/\mathrm{Rep_{H_2}} + \mathrm{Ext_{He}}/\mathrm{Ext_{H_2}}) \sim 1.68$.

Now, the energy axis for the experiment in chapter 7 can be calculated, according to

$$\mathrm{KER_{H_2}} = 2 \cdot \mathrm{polyfit_{He}}(N_{\mathrm{pixel,H_2}})/\mathrm{Ratio_{He/H_2}}. \tag{A.10}$$

First of all the y-axis measured in the H_2 experiments given in pixel numbers is applied to the polynomial fit retrieved with the data of chapter 5.2. In addition the energies have to be divided by the ratio of the applied VMI voltages to compensate for the different energy regions of the two measurements. At last, the energy has to be taken times two, since the kinetic energy release (KER) is two times the kinetic energy of the measured H^+ ions.
For comparison in Fig. A.3 the main experimental results of chapter 7 are shown as a function of the pixel number, and as a function of the calibrated y-axis, i.e. the kinetic energy release (KER).

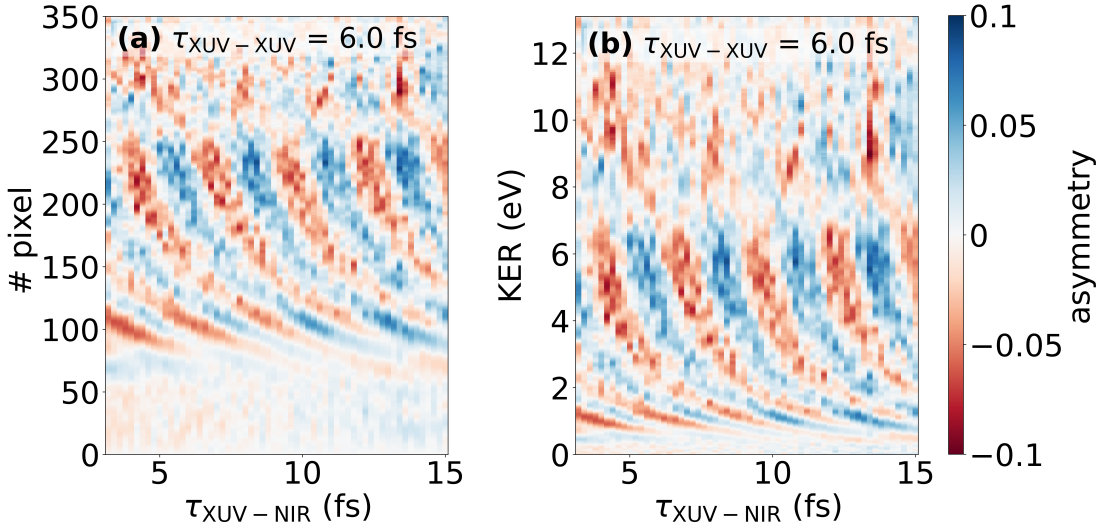

Figure A.3: See chapter 7: Measurement of the asymmetry parameter, i.e. the difference between the H^+ fragments flying up and downwards in respect to the laser propagation direction after dissociative ionization of H_2 atoms with two phase-locked XUV pulses and an NIR pulse (cf. Fig. 7.7 (a)). The asymmetry parameter is shown as function of $\tau_{\text{XUV-NIR}}$ for $\tau_{\text{XUV-XUV}} = 6\,\text{fs}$. The y-axis is given in pixel units of the CCD camera in (a), whereas in (b) the y-axis is calibrated and now corresponds to the kinetic energy release (KER) of the system.

A.3 Interference signal of the two XUV pulses as a function of the delay

The figure is on the next page.

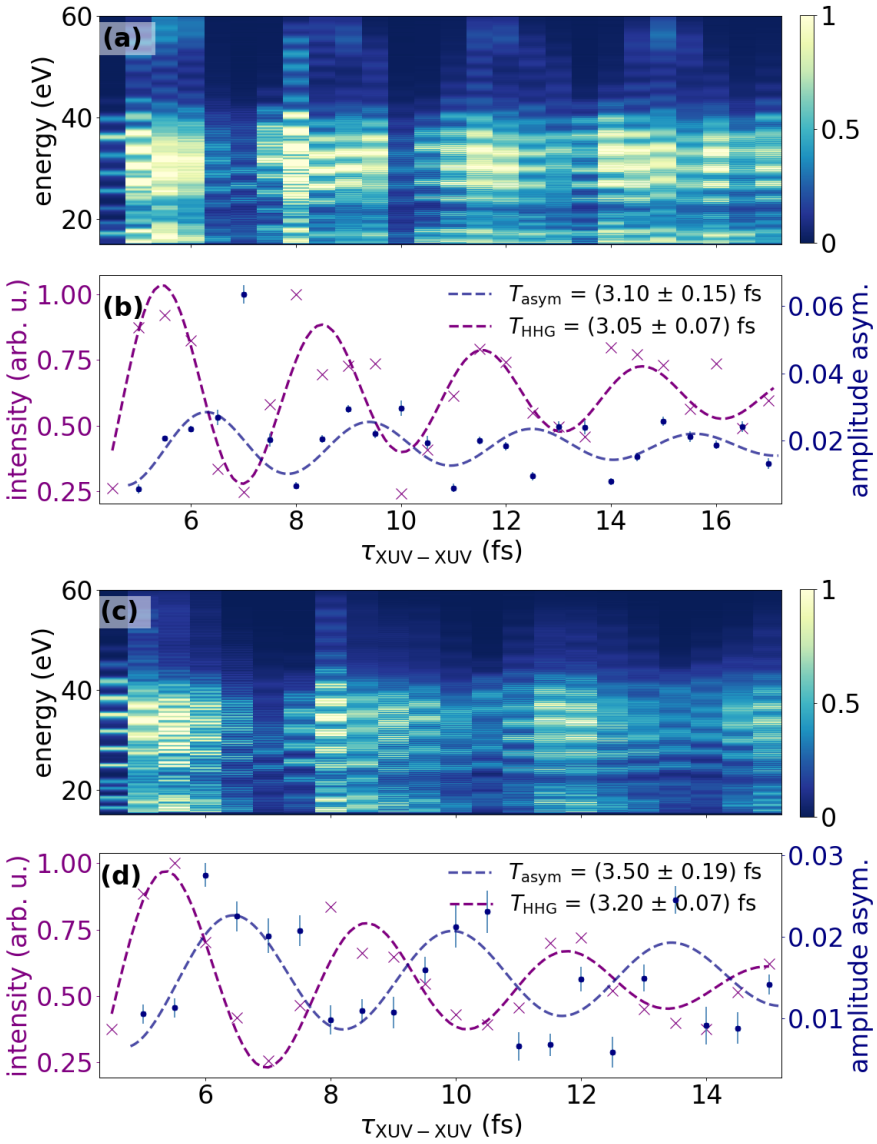

Figure A.4: (a)-(b) Second, and (c)-(d) third measurement campaign of electron localization in hydrogen molecules: (a)&(c) XUV spectrum of the two phase-locked isolated attosecond pulses (IAPs) for the dissociative ionization of neutral hydrogen molecules as a function of $\tau_{\text{XUV-XUV}}$. (b)&(d) Normalized energy-integrated (25 − 40 eV) XUV intensity oscillation as a function of $\tau_{\text{XUV-XUV}}$ with a period of (b) $T_{\text{HHG}} = (3.05 \pm 0.07)$ fs, and (d) $T_{\text{HHG}} = (3.20 \pm 0.07)$ fs, which is retrieved by a cosinusoidal fit with a damped amplitude (dashed purple line) of the data points (crosses). For comparison the corresponding amplitude of the oscillation of the asymmetry parameter at a middle KER (dots) as a function of $\tau_{\text{XUV-NIR}}$ is given as a function of $\tau_{\text{XUV-XUV}}$. The sinusoidal curve fit of the data points is shown as a dashed dark blue line. The amplitude of the asymmetry oscillates with a period of (b) $T_{\text{asym}} = (3.10 \pm 0.15)$ fs, and (d) $T_{\text{asym}} = (3.50 \pm 0.19)$ fs, which is comparable to the period of oscillation of the XUV photon flux.

Acknowledgment

I would like to begin by expressing my greatest appreciation to my family and friends, especially my husband, who have been an incredible support system throughout this journey. Their tireless encouragement made all the difference, giving me the best support anyone could wish for!

I owe my warmest thank you to Tobias Kampfrath for taking on the role of my primary supervisor and for his invaluable assistance in the final months of my PhD. I am also grateful to Guiseppe Sansone for co-refereeing my thesis, contributing to its success.

During the most challenging times of my PhD, Mikhail Ivanov and Emilio Pisanty provided crucial support that enabled me to keep going. Without their help, I truly would not have been able to finish my thesis.

I also want to highlight the significant support I received from remarkable female scientists like Nirit Dudovich, Alicia Palacios, Maria Richter, Laura Rammelt, and Olga Smirnova, who showed me that women in science have to stick together.

In addition, I want to express my thanks to Tobias Witting for his supervision, and guidance in the lab, and to Oleg Kornilov for both scientific insights and personal support throughout the years. Their mentorship has been priceless for my professional development.

A special acknowledgment goes to Ahmet Akin Uenal, whose expertise kept the laser running smoothly – without him, I wouldn't have been able to finish my PhD on time. I also want to give my appreciation to Roman Peslin for his technical support and non-scientific advice throughout my time at MBI, which has really improved my experience.

I want to thank Laura Maikowski for making my start at MBI a lot of fun. I'm also grateful to Lorenz Drescher for teaching me the essential skills needed to operate the attosecond beamline, as well as for the great times we shared at various conferences.

Furthermore, I would like to thank C. P. Schulz for patiently answering my questions about hydrogen molecules, and Arnaud Rouzée for consistently arriving in the lab just when we needed to enhance our VMI images..

I also want to express my sincere appreciation to the current and former PhD students – Ulrich, Mikhail, Zoey, Miguel, Nicola, Thomas, Alex, Nikolai, and Peter – whose company made my time at the MBI far more enjoyable.

Lastly, I'd like to highlight a few individuals from the Atto community, who supported me in various ways and with whom I've created wonderful memories: Jasper Peschel, Omer Kneller, Noa Yaffe, Chen Mor, Adrian Rubio, and Ignacio Casasús.

Thank you all for your parts in making this an unforgettable journey!

Bibliography

[1] L.-M. Koll, L. Maikowski, L. Drescher, M. J. J. Vrakking, and T. Witting, "Phase-locking of time-delayed attosecond XUV pulse pairs," *Optics Express*, vol. 30, no. 5, pp. 7082–7095, 2022. https://doi.org/10.1364/OE.452018.

[2] L.-M. Koll, L. Maikowski, L. Drescher, T. Witting, and M. J. J. Vrakking, "Experimental control of quantum-mechanical entanglement in an attosecond pump-probe experiment," *Physical Review Letters*, vol. 128, no. 4, p. 043201, 2022. https://doi.org/10.1103/PhysRevLett.128.043201.

[3] L.-M. Koll, T. Witting, and M. J. J. Vrakking, "Control of photoelectron-ion entanglement in attosecond laser-induced photoionization of H_2," in *Proceedings of the 8th International Conference on Attosecond Science and Technology (ATTO 8)* (L. Argenti, M. Chini, and L. Fang, eds.), vol. 300, (Cham), pp. 155–165, Springer International Publishing, 2024. https://doi.org/10.1007/978-3-031-47938-0_15.

[4] M. Nisoli, S. De Silvestri, and O. Svelto, "Generation of high energy 10 fs pulses by a new pulse compression technique," *Applied Physics Letters*, vol. 68, no. 20, pp. 2793–2795, 1996. https://doi.org/10.1063/1.116609.

[5] F. Krausz and M. Ivanov, "Attosecond physics," *Reviews of modern physics*, vol. 81, no. 1, p. 163, 2009. https://link.aps.org/doi/10.1103/RevModPhys.81.163.

[6] A. T. Eppink and D. H. Parker, "Velocity map imaging of ions and electrons using electrostatic lenses: Application in photoelectron and photofragment ion imaging of molecular oxygen," *Review of Scientific Instruments*, vol. 68, no. 9, pp. 3477–3484, 1997. https://doi.org/10.1063/1.1148310.

[7] T. Kita, T. Harada, N. Nakano, and H. Kuroda, "Mechanically ruled aberration-corrected concave gratings for a flat-field grazing-incidence spectrograph," *Applied optics*, vol. 22, no. 4, pp. 512–513, 1983. https://doi.org/10.1364/AO.22.000512.

[8] L. Maikowski, "Fourier transform spectroscopy with XUV pulses," Master's thesis, Freie Universität Berlin, 2021.

[9] M. J. J. Vrakking, "Control of attosecond entanglement and coherence," *Physical Review Letters*, vol. 126, no. 11, p. 113203, 2021. https://link.aps.org/doi/10.1103/PhysRevLett.126.113203.

[10] H. R. Telle, G. Steinmeyer, A. E. Dunlop, J. Stenger, D. H. Sutter, and U. Keller, "Carrier-envelope offset phase control: A novel concept for absolute optical frequency measurement and ultrashort pulse generation," *Applied Physics B*, vol. 69, pp. 327–332, 1999. https://doi.org/10.1007/s003400050813.

[11] M. Kakehata, H. Takada, Y. Kobayashi, K. Torizuka, Y. Fujihira, T. Homma, and H. Takahashi, "Single-shot measurement of carrier-envelope phase changes by spectral interferometry," *Optics letters*, vol. 26, no. 18, pp. 1436–1438, 2001. https://doi.org/10.1364/OL.26.001436.

[12] A. Baltuska, M. Uiberacker, E. Goulielmakis, R. Kienberger, V. S. Yakovlev, T. Udem, T. W. Hansch, and F. Krausz, "Phase-controlled amplification of few-cycle laser pulses," *IEEE Journal of Selected Topics in Quantum Electronics*, vol. 9, no. 4, pp. 972–989, 2003. https://doi.org/10.1109/JSTQE.2003.819107.

[13] C. Iaconis and I. A. Walmsley, "Spectral phase interferometry for direct electric-field reconstruction of ultrashort optical pulses," *Optics letters*, vol. 23, no. 10, pp. 792–794, 1998. https://doi.org/10.1364/OL.23.000792.

[14] B. J. Whitaker, *Imaging in molecular dynamics: technology and applications*. Cambridge university press, 2003. https://doi.org/10.1017/CBO9780511535437.

[15] I. Newton, *Opticks, or, a treatise of the reflections, refractions, inflections & colours of light*. Courier Corporation, 1952. https://books.google.de/books?id=sv_CDwAAQBAJ.

[16] C. Huygens, *Traité de la lumiére/ Treatise on Light: In which are Explained the Causes of that which Occurs in Reflexion, & in Refraction. And Particularly in the Strange Refraction of Iceland Crystal*. Chez Pierre vander Aa, marchand libraire, A Leide, 1690. https://doi.org/10.5479/sil.294285.39088000545160, Translation provided by Silvanus P. Thomson.

[17] T. Young, "II. The Bakerian Lecture. On the theory of light and colours," *Philosophical transactions of the Royal Society of London*, no. 92, pp. 12–48, 1802. https://doi.org/10.1098/rstl.1802.0004.

[18] M. Faraday, *Experimental Researches In Electricity-Volume 1*, vol. 1. Read Books Ltd, 2016. https://books.google.de/books?id=gDZRDAAAQBAJ.

[19] J. C. Maxwell, *A treatise on electricity and magnetism*, vol. 1. Clarendon press, 1873. https://books.google.de/books?id=92QSAAAAIAAJ.

[20] M. Planck, *Über das Gesetz der Energieverteilung im Normalspektrum/ On the Energy Distribution Law in the Normal Spectrum Radiation*. Springer, 1978. https://doi.org/10.1007/978-3-663-13885-3_16.

[21] A. Einstein, "Über einen die Erzeugung und Verwandlung des Lichtes betreffenden heuristischen Gesichtspunkt/On a heuristic viewpoint concerning the emission and transformation of light," *Annalen der Physik*, vol. 322, no. 6, pp. 132–148, 1905. https://doi.org/10.1002/andp.19053220607.

[22] L. de Broglie, *Recherches sur la théorie des quanta*. PhD thesis, Migration-université en cours d'affectation, 1924. https://theses.hal.science/tel-00006807,Translation provided by Hirokazu Nishimura.

[23] M. Born and P. Jordan, "Zur Quantenmechanik/ On quantum mechanics," *Zeitschrift für Physik*, vol. 34, no. 1, pp. 858–888, 1925. https://doi.org/10.1007/BF01328531.

[24] W. Heisenberg, "Über quantentheoretische Umdeutung kinematischer und mechanischer Beziehungen/On the quantum-theoretical reinterpretation of kinematical and mechanical relationships," *Zeitschrift für Physik*, vol. 33, pp. 879–893, 1925. https://doi.org/10.1007/BF01328377.

[25] M. Born, W. Heisenberg, and P. Jordan, "Zur Quantenmechanik. II./On quantum mechanics II.," *Zeitschrift für Physik*, vol. 35, no. 8-9, pp. 557–615, 1926. https://doi.org/10.1007/BF01379806.

[26] E. Schrödinger, "An undulatory theory of the mechanics of atoms and molecules," *Physical review*, vol. 28, no. 6, p. 1049, 1926. https://link.aps.org/doi/10.1103/PhysRev.28.1049.

[27] O. Donati, G. Missiroli, and G. Pozzi, "An experiment on electron interference," *American Journal of Physics*, vol. 41, no. 5, pp. 639–644, 1973. https://doi.org/10.1119/1.1987321.

[28] R. Bach, D. Pope, S.-H. Liou, and H. Batelaan, "Controlled double-slit electron diffraction," *New Journal of Physics*, vol. 15, no. 3, p. 033018, 2013. https://doi.org/10.1088/1367-2630/15/3/033018.

[29] O. Nairz, M. Arndt, and A. Zeilinger, "Quantum interference experiments with large molecules," *American Journal of Physics*, vol. 71, no. 4, pp. 319–325, 2003. https://doi.org/10.1119/1.1531580.

[30] W. Heisenberg, "Über den anschaulichen Inhalt der quantentheoretischen Kinematik und Mechanik/ The actual content of quantum theoretical kinematics and mechanics," *Zeitschrift für Physik*, vol. 43, no. 3-4, pp. 172–198, 1927. https://doi.org/10.1007/BF01397280.

[31] J. Mehra and H. Rechenberg, *"The" Conceptual Completion and the Extensions of Quantum Mechanics 1932-1941; Epilogue: Aspects of the Further Development of Quantum Theory 1942-1999: 6, The completion of quantum mechanics 1926-1941 Pt. 2.* Springer Science & Business Media, 2001. https://books.google.de/books?id=9l61Dy9FBfYC.

[32] N. Bohr, "Über die Serienspektra der Elemente/ On the series spectra of elements," *Zeitschrift für Physik*, vol. 2, no. 5, pp. 423–469, 1920. https://doi.org/10.1007/BF01329978.

[33] N. Bohr, "The quantum postulate and the recent development of atomic theory," *Nature*, vol. 121, pp. 580–590, 1928. https://doi.org/10.1038/121580a0.

[34] J. A. Wheeler and W. H. Zurek, *Quantum theory and measurement*, vol. 40. Princeton University Press, 2014. https://www.jstor.org/stable/j.ctt7ztxn5.

[35] E. Schrödinger, "Die gegenwärtige Situation in der Quantenmechanik/ The present situation in quantum mechanics," *Naturwissenschaften*, vol. 23, no. 48, pp. 807–812, 1935. https://doi.org/10.1007/BF01491987.

[36] W. H. Zurek, "Pointer basis of quantum apparatus: Into what mixture does the wave packet collapse?," *Physical review D*, vol. 24, no. 6, p. 1516, 1981. https://link.aps.org/doi/10.1103/PhysRevD.24.1516.

[37] W. H. Zurek, "Environment-induced superselection rules," *Physical review D*, vol. 26, no. 8, p. 1862, 1982. https://link.aps.org/doi/10.1103/PhysRevD.26.1862.

[38] W. H. Zurek, "Decoherence, einselection, and the quantum origins of the classical," *Reviews of modern physics*, vol. 75, no. 3, p. 715, 2003. https://link.aps.org/doi/10.1103/RevModPhys.75.715.

[39] K. Camilleri, "A history of entanglement: Decoherence and the interpretation problem," *Studies in History and Philosophy of Science Part B: Studies in History and Philosophy of Modern Physics*, vol. 40, no. 4, pp. 290–302, 2009. https://doi.org/10.1016/j.shpsb.2009.09.003.

[40] W. H. Zurek, "Decoherence and the transition from quantum to classical – revisited," *arXiv*, 2003. https://arxiv.org/pdf/quant-ph/0306072.

[41] M. Brune, E. Hagley, J. Dreyer, X. Maitre, A. Maali, C. Wunderlich, J.-M. Raimond, and S. Haroche, "Observing the progressive decoherence of the "meter" in a quantum measurement," *Physical review letters*, vol. 77, no. 24,

p. 4887, 1996. https://link.aps.org/doi/10.1103/PhysRevLett.77.4887.

[42] P. E. Black, D. R. Kuhn, and C. J. Williams, "Quantum computing and communication," in *Advances in Computers*, vol. 56, pp. 189–244, Elsevier, 2002. https://doi.org/10.1016/S0065-2458(02)80007-9.

[43] A. Einstein, B. Podolsky, and N. Rosen, "Can quantum-mechanical description of physical reality be considered complete?," *Physical review*, vol. 47, no. 10, p. 777, 1935. https://link.aps.org/doi/10.1103/PhysRev.47.777.

[44] A. Einstein and N. Rosen, "The particle problem in the general theory of relativity," *Physical Review*, vol. 48, no. 1, p. 73, 1935. https://link.aps.org/doi/10.1103/PhysRev.48.73.

[45] N. Brunner, D. Cavalcanti, S. Pironio, V. Scarani, and S. Wehner, "Bell nonlocality," *Reviews of modern physics*, vol. 86, no. 2, p. 419, 2014. https://link.aps.org/doi/10.1103/RevModPhys.86.419.

[46] D. Bohm and Y. Aharonov, "Discussion of experimental proof for the paradox of Einstein, Rosen, and Podolsky," *Physical Review*, vol. 108, no. 4, p. 1070, 1957. https://link.aps.org/doi/10.1103/PhysRev.108.1070.

[47] J. S. Bell, "On the Einstein Podolsky Rosen paradox," *Physics Physique Fizika*, vol. 1, pp. 195–200, Nov 1964. https://link.aps.org/doi/10.1103/PhysicsPhysiqueFizika.1.195.

[48] J. F. Clauser, M. A. Horne, A. Shimony, and R. A. Holt, "Proposed experiment to test local hidden-variable theories," *Physical review letters*, vol. 23, no. 15, p. 880, 1969. https://link.aps.org/doi/10.1103/PhysRevLett.23.880.

[49] S. J. Freedman and J. F. Clauser, "Experimental test of local hidden-variable theories," *Physical Review Letters*, vol. 28, no. 14, p. 938, 1972. https://link.aps.org/doi/10.1103/PhysRevLett.28.938.

[50] A. Aspect, P. Grangier, and G. Roger, "Experimental tests of realistic local theories via Bell's theorem," *Physical review letters*, vol. 47, no. 7, p. 460, 1981. https://link.aps.org/doi/10.1103/PhysRevLett.47.460.

[51] A. Aspect, J. Dalibard, and G. Roger, "Experimental test of Bell's inequalities using time-varying analyzers," *Physical review letters*, vol. 49, no. 25, p. 1804, 1982. https://link.aps.org/doi/10.1103/PhysRevLett.49.1804.

[52] A. Aspect, P. Grangier, and G. Roger, "Experimental realization of Einstein-Podolsky-Rosen-Bohm Gedankenexperiment: A new violation of Bell's inequalities," *Physical review letters*, vol. 49, no. 2, p. 91, 1982. https://link.aps.org/doi/10.1103/PhysRevLett.49.91.

[53] G. Weihs, T. Jennewein, C. Simon, H. Weinfurter, and A. Zeilinger, "Violation of Bell's inequality under strict Einstein locality conditions," *Phys. Rev. Lett.*, vol. 81, pp. 5039–5043, Dec 1998. https://link.aps.org/doi/10.1103/PhysRevLett.81.5039.

[54] B. Hensen, H. Bernien, A. E. Dréau, A. Reiserer, N. Kalb, M. S. Blok, J. Ruitenberg, R. F. Vermeulen, R. N. Schouten, C. Abellán, *et al.*, "Loophole-free bell inequality violation using electron spins separated by 1.3 kilometres," *Nature*, vol. 526, no. 7575, pp. 682–686, 2015. https://doi.org/10.1038/nature15759.

[55] M. Giustina, M. A. M. Versteegh, S. Wengerowsky, J. Handsteiner, A. Hochrainer, K. Phelan, F. Steinlechner, J. Kofler, J.-A. Larsson, C. Abellán, W. Amaya, V. Pruneri, M. W. Mitchell, J. Beyer, T. Gerrits, A. E. Lita, L. K. Shalm, S. W. Nam, T. Scheidl, R. Ursin, B. Wittmann, and A. Zeilinger, "Significant-loophole-free test of bell's theorem with entangled photons," *Phys. Rev. Lett.*, vol. 115, p. 250401, Dec 2015. https://link.aps.org/doi/10.1103/PhysRevLett.115.250401.

[56] L. K. Shalm, E. Meyer-Scott, B. G. Christensen, P. Bierhorst, M. A. Wayne, M. J. Stevens, T. Gerrits, S. Glancy, D. R. Hamel, M. S. Allman, K. J. Coakley, S. D. Dyer, C. Hodge, A. E. Lita, V. B. Verma, C. Lambrocco, E. Tortorici, A. L. Migdall, Y. Zhang, D. R. Kumor, W. H. Farr, F. Marsili, M. D. Shaw, J. A. Stern, C. Abellán, W. Amaya, V. Pruneri, T. Jennewein, M. W. Mitchell, P. G. Kwiat, J. C. Bienfang, R. P. Mirin, E. Knill, and S. W. Nam, "Strong loophole-free test of local realism," *Phys. Rev. Lett.*, vol. 115, p. 250402, Dec 2015. https://link.aps.org/doi/10.1103/PhysRevLett.115.250402.

[57] D. Salart, A. Baas, C. Branciard, N. Gisin, and H. Zbinden, "Testing the speed of 'spooky action at a distance'," *Nature*, vol. 454, no. 7206, pp. 861–864, 2008. https://doi.org/10.1038/nature07121.

[58] S. Gröblacher, T. Paterek, R. Kaltenbaek, Č. Brukner, M. Żukowski, M. Aspelmeyer, and A. Zeilinger, "An experimental test of non-local realism," *Nature*, vol. 446, no. 7138, pp. 871–875, 2007. https://doi.org/10.1038/nature05677.

[59] W. Tittel, J. Brendel, H. Zbinden, and N. Gisin, "Violation of Bell inequalities by photons more than 10 km apart," *Physical review letters*, vol. 81, no. 17, p. 3563, 1998. https://link.aps.org/doi/10.1103/PhysRevLett.81.3563.

[60] P. W. Shor, "Polynomial-time algorithms for prime factorization and discrete logarithms on a quantum computer," *SIAM review*, vol. 41, no. 2, pp. 303–332, 1999. https://doi.org/10.1137/S0036144598347011.

[61] R. Jozsa and N. Linden, "On the role of entanglement in quantum-computational speed-up," *Proceedings of the Royal Society of London. Se-*

ries A: Mathematical, Physical and Engineering Sciences, vol. 459, no. 2036, pp. 2011–2032, 2003. https://doi.org/10.1098/rspa.2002.1097.

[62] G. Jaeger, *Quantum entanglement*. Springer, 2007. https://link.springer.com/chapter/10.1007/978-0-387-36944-0_6.

[63] A. Gatti, E. Brambilla, and L. Lugiato, "Entangled imaging and wave-particle duality: from the microscopic to the macroscopic realm," *Physical review letters*, vol. 90, no. 13, p. 133603, 2003. https://link.aps.org/doi/10.1103/PhysRevLett.90.133603.

[64] M. Genovese, "Real applications of quantum imaging," *Journal of Optics*, vol. 18, no. 7, p. 073002, 2016. https://doi.org/10.1088/2040-8978/18/7/073002.

[65] A. K. Ekert, "Quantum cryptography based on Bell's theorem," *Physical review letters*, vol. 67, no. 6, p. 661, 1991. https://link.aps.org/doi/10.1103/PhysRevLett.67.661.

[66] S. Pirandola, U. L. Andersen, L. Banchi, M. Berta, D. Bunandar, R. Colbeck, D. Englund, T. Gehring, C. Lupo, C. Ottaviani, *et al.*, "Advances in quantum cryptography," *Advances in optics and photonics*, vol. 12, no. 4, pp. 1012–1236, 2020. https://doi.org/10.1364/AOP.361502.

[67] C. H. Bennett, G. Brassard, C. Crépeau, R. Jozsa, A. Peres, and W. K. Wootters, "Teleporting an unknown quantum state via dual classical and Einstein-Podolsky-Rosen channels," *Physical review letters*, vol. 70, no. 13, p. 1895, 1993. https://link.aps.org/doi/10.1103/PhysRevLett.70.1895.

[68] D. Bouwmeester, J.-W. Pan, K. Mattle, M. Eibl, H. Weinfurter, and A. Zeilinger, "Experimental quantum teleportation," *Nature*, vol. 390, no. 6660, pp. 575–579, 1997. https://doi.org/10.1038/37539.

[69] S. Pirandola, J. Eisert, C. Weedbrook, A. Furusawa, and S. L. Braunstein, "Advances in quantum teleportation," *Nature photonics*, vol. 9, no. 10, pp. 641–652, 2015. https://doi.org/10.1038/nphoton.2015.154.

[70] D. O. Hall and K. Rao, *Photosynthesis*. Cambridge University Press, 1999. https://books.google.de/books?id=6F7yuf1Sj30C.

[71] T. Cornsweet, *Visual perception*. Academic press, 2012. https://books.google.de/books?id=ubaGAAAAQBAJ.

[72] R. Stupp, W. P. Mason, M. J. Van Den Bent, M. Weller, B. Fisher, M. J. Taphoorn, K. Belanger, A. A. Brandes, C. Marosi, U. Bogdahn, *et al.*, "Radiotherapy plus concomitant and adjuvant temozolomide for glioblastoma," *New England journal of medicine*, vol. 352, no. 10, pp. 987–996, 2005. https://doi.org/10.1056/NEJMoa043330.

[73] D. Schaue and W. H. McBride, "Opportunities and challenges of radiotherapy for treating cancer," *Nature reviews Clinical oncology*, vol. 12, no. 9, pp. 527–540, 2015. https://doi.org/10.1038/nrclinonc.2015.120.

[74] A. H. Zewail, "Femtochemistry: Atomic-scale dynamics of the chemical bond," *The Journal of Physical Chemistry A*, vol. 104, no. 24, pp. 5660–5694, 2000. https://doi.org/10.1021/jp001460h.

[75] T. H. Maiman *et al.*, "Stimulated optical radiation in ruby," *Nature*, vol. 187, pp. 493–494, 1960. https://doi.org/10.1038/187493a0.

[76] A. Javan, W. R. Bennett Jr, and D. R. Herriott, "Population inversion and continuous optical maser oscillation in a gas discharge containing a He-Ne mixture," *Physical Review Letters*, vol. 6, no. 3, p. 106, 1961. https://link.aps.org/doi/10.1103/PhysRevLett.6.106.

[77] R. N. Hall, G. E. Fenner, J. Kingsley, T. Soltys, and R. Carlson, "Coherent light emission from GaAs junctions," *Physical Review Letters*, vol. 9, no. 9, p. 366, 1962. https://link.aps.org/doi/10.1103/PhysRevLett.9.366.

[78] V. Letokhov, *Laser photoionization spectroscopy*. Elsevier Science, 2012. https://books.google.de/books?id=y6DL5V9e7sUC.

[79] D. W. Pratt, "High resolution spectroscopy in the gas phase: Even large molecules have well-defined shapes," *Annual review of physical chemistry*, vol. 49, no. 1, pp. 481–530, 1998. https://doi.org/10.1146/annurev.physchem.49.1.481.

[80] R. Thompson, "High resolution laser spectroscopy of atomic systems," *Reports on Progress in Physics*, vol. 48, no. 4, p. 531, 1985. https://doi.org/10.1088/0034-4885/48/4/003.

[81] F. J. McClung and R. W. Hellwarth, "Giant optical pulsations from ruby," *Applied Optics*, vol. 1, no. 101, pp. 103–105, 1962. https://doi.org/10.1364/AO.1.S1.000103.

[82] L. Hargrove, R. L. Fork, and M. Pollack, "Locking of He–Ne laser modes induced by synchronous intracavity modulation," *Applied Physics Letters*, vol. 5, no. 1, pp. 4–5, 1964. https://doi.org/10.1063/1.1754025.

[83] A. J. DeMaria, W. H. Glenn, M. J. Brienza, and M. E. Mack, "Picosecond laser pulses," *Proceedings of the IEEE*, vol. 57, no. 1, pp. 2–25, 1969. https://doi.org/10.1109/PROC.1969.6864.

[84] A. DeMaria, D. Stetser, and H. Heynau, "Self mode-locking of lasers with saturable absorbers," *Applied Physics Letters*, vol. 8, no. 7, pp. 174–176, 1966. https://doi.org/10.1063/1.1754541.

[85] P. W. Smith, M. Duguay, and E. Ippen, "Mode-locking of lasers," *Progress in Quantum Electronics*, vol. 3, pp. 107–229, 1974. https://doi.org/10.1016/0079-6727(74)90002-0.

[86] C. Shank and E. Ippen, "Subpicosecond kilowatt pulses from a mode-locked cw dye laser," *Applied Physics Letters*, vol. 24, no. 8, pp. 373–375, 1974. https://doi.org/10.1063/1.1655222.

[87] L. Zhu, V. Kleiman, X. Li, S. P. Lu, K. Trentelman, and R. J. Gordon, "Coherent laser control of the product distribution obtained in the photoexcitation of HI," *Science*, vol. 270, no. 5233, pp. 77–80, 1995. https://doi.org/10.1126/science.270.5233.77.

[88] L. Zhu, K. Suto, J. A. Fiss, R. Wada, T. Seideman, and R. J. Gordon, "Effect of resonances on the coherent control of the photoionization and photodissociation of HI and DI," *Physical review letters*, vol. 79, no. 21, p. 4108, 1997. https://link.aps.org/doi/10.1103/PhysRevLett.79.4108.

[89] R. J. Gordon and S. A. Rice, "Active control of the dynamics of atoms and molecules," *Annual review of physical chemistry*, vol. 48, no. 1, pp. 601–641, 1997. https://doi.org/10.1146/annurev.physchem.48.1.601.

[90] J. Posthumus, "The dynamics of small molecules in intense laser fields," *Reports on Progress in Physics*, vol. 67, no. 5, p. 623, 2004. https://doi.org/10.1088/0034-4885/67/5/R01.

[91] D. J. Tannor and S. A. Rice, "Coherent pulse sequence control of product formation in chemical reactions," *Advances in Chemical Physics: Evolution of Size Effects in Chemical Dynamics Part 1*, vol. 70, pp. 441–523, 1988. https://doi.org/10.1002/9780470141199.

[92] P. Brumer and M. Shapiro, "Coherence chemistry: controlling chemical reactions [with lasers]," *Accounts of Chemical Research*, vol. 22, no. 12, pp. 407–413, 1989. https://doi.org/10.1021/ar00168a001.

[93] R. Fork, B. Greene, and C. V. Shank, "Generation of optical pulses shorter than 0.1 psec by colliding pulse mode locking," *Applied Physics Letters*, vol. 38, no. 9, pp. 671–672, 1981. https://doi.org/10.1063/1.92500.

[94] L. F. Mollenauer and R. H. Stolen, "The soliton laser," *Optics letters*, vol. 9, no. 1, pp. 13–15, 1984. https://doi.org/10.1364/OL.9.000013.

[95] D. E. Spence, P. N. Kean, and W. Sibbett, "60-fsec pulse generation from a self-mode-locked Ti: sapphire laser," *Optics letters*, vol. 16, no. 1, pp. 42–44, 1991. https://doi.org/10.1364/OL.16.000042.

[96] W. Sibbett, A. Lagatsky, and C. Brown, "The development and application of femtosecond laser systems," *Optics Express*, vol. 20, no. 7, pp. 6989–7001, 2012. https://doi.org/10.1364/OE.20.006989.

[97] A. McPherson, G. Gibson, H. Jara, U. Johann, T. S. Luk, I. McIntyre, K. Boyer, and C. K. Rhodes, "Studies of multiphoton production of vacuum-ultraviolet radiation in the rare gases," *JOSA B*, vol. 4, no. 4, pp. 595–601, 1987. https://doi.org/10.1364/JOSAB.4.000595.

[98] M. Ferray, A. L'Huillier, X. Li, L. Lompre, G. Mainfray, and C. Manus, "Multiple-harmonic conversion of 1064 nm radiation in rare gases," *Journal of Physics B: Atomic, Molecular and Optical Physics*, vol. 21, no. 3, p. L31, 1988. https://doi.org/10.1088/0953-4075/21/3/001.

[99] M. Drescher, M. Hentschel, R. Kienberger, M. Uiberacker, V. Yakovlev, A. Scrinzi, T. Westerwalbesloh, U. Kleineberg, U. Heinzmann, and F. Krausz, "Time-resolved atomic inner-shell spectroscopy," *Nature*, vol. 419, no. 6909, pp. 803–807, 2002. https://doi.org/10.1038/nature01143.

[100] M. Nisoli, P. Decleva, F. Calegari, A. Palacios, and F. Martín, "Attosecond electron dynamics in molecules," *Chemical reviews*, vol. 117, no. 16, pp. 10760–10825, 2017. https://doi.org/10.1021/acs.chemrev.6b00453.

[101] M. F. Kling and M. J. J. Vrakking, "Attosecond electron dynamics," *Annu. Rev. Phys. Chem.*, vol. 59, pp. 463–492, 2008. https://doi.org/10.1146/annurev.physchem.59.032607.093532.

[102] U. Bhattacharya, T. Lamprou, A. S. Maxwell, A. Ordonez, E. Pisanty, J. Rivera-Dean, P. Stammer, M. F. Ciappina, M. Lewenstein, and P. Tzallas, "Strong laser physics, non-classical light states and quantum information science," *Reports on Progress in Physics*, 2023. https://doi.org/10.1088/1361-6633/acea31.

[103] M. C. Tichy, F. Mintert, and A. Buchleitner, "Essential entanglement for atomic and molecular physics," *Journal of Physics B: Atomic, Molecular and Optical Physics*, vol. 44, no. 19, p. 192001, 2011. https://doi.org/10.1088/0953-4075/44/19/192001.

[104] J. Breidbach and L. Cederbaum, "Migration of holes: Formalism, mechanisms, and illustrative applications," *The Journal of chemical physics*, vol. 118, no. 9, pp. 3983–3996, 2003. https://doi.org/10.1063/1.1540618.

[105] F. Remacle and R. D. Levine, "An electronic time scale in chemistry," *Proceedings of the National Academy of Sciences*, vol. 103, no. 18, pp. 6793–6798, 2006. https://doi.org/10.1073/pnas.0601855103.

[106] F. Calegari, D. Ayuso, A. Trabattoni, L. Belshaw, S. De Camillis, S. Anumula, F. Frassetto, L. Poletto, A. Palacios, P. Decleva, *et al.*, "Ultrafast electron dynamics in phenylalanine initiated by attosecond pulses," *Science*, vol. 346, no. 6207, pp. 336–339, 2014. https://doi.org/10.1126/science.1254061.

[107] P. M. Kraus, B. Mignolet, D. Baykusheva, A. Rupenyan, L. Hornỳ, E. F. Penka, G. Grassi, O. I. Tolstikhin, J. Schneider, F. Jensen, *et al.*, "Measurement and laser control of attosecond charge migration in ionized

iodoacetylene," *Science*, vol. 350, no. 6262, pp. 790–795, 2015. https://doi.org/10.1126/science.aab2160.

[108] S. Pabst, L. Greenman, P. J. Ho, D. A. Mazziotti, and R. Santra, "Decoherence in attosecond photoionization," *Physical Review Letters*, vol. 106, no. 5, p. 053003, 2011. https://link.aps.org/doi/10.1103/PhysRevLett.106.053003.

[109] O. Smirnova, "Attosecond prints of electrons," *Nature*, vol. 466, no. 7307, pp. 701–702, 2010. https://doi.org/10.1038/466700a.

[110] E. Goulielmakis, Z.-H. Loh, A. Wirth, R. Santra, N. Rohringer, V. S. Yakovlev, S. Zherebtsov, T. Pfeifer, A. M. Azzeer, M. F. Kling, *et al.*, "Real-time observation of valence electron motion," *Nature*, vol. 466, no. 7307, pp. 739–743, 2010. https://doi.org/10.1038/nature09212.

[111] M. Ruberti, "Onset of ionic coherence and ultrafast charge dynamics in attosecond molecular ionisation," *Physical Chemistry Chemical Physics*, vol. 21, no. 32, pp. 17584–17604, 2019. https://doi.org/10.1039/C9CP03074C.

[112] T. Nishi, E. Lötstedt, and K. Yamanouchi, "Entanglement and coherence in photoionization of H_2 by an ultrashort XUV laser pulse," *Physical Review A*, vol. 100, no. 1, p. 013421, 2019. https://link.aps.org/doi/10.1103/PhysRevA.100.013421.

[113] F. Shobeiry, P. Fross, H. Srinivas, T. Pfeifer, R. Moshammer, and A. Harth, "Sub-femtosecond optical control of entangled states," *arXiv preprint arXiv:2110.06668*, 2021. https://doi.org/10.48550/arXiv.2110.06668.

[114] P.-L. He, K. Z. Hatsagortsyan, and C. H. Keitel, "Double-slit interference in the ion dynamics of dissociative photoionization," *Physical Review Letters*, vol. 131, no. 1, p. 013201, 2023. https://link.aps.org/doi/10.1103/PhysRevLett.131.013201.

[115] H. Laurell, D. Finkelstein-Shapiro, C. Dittel, C. Guo, R. Demjaha, M. Ammitzböll, R. Weissenbilder, L. Neoričić, S. Luo, M. Gisselbrecht, *et al.*, "Continuous-variable quantum state tomography of photoelectrons," *Physical Review Research*, vol. 4, no. 3, p. 033220, 2022. https://link.aps.org/doi/10.1103/PhysRevResearch.4.033220.

[116] H. Laurell, S. Luo, R. Weissenbilder, M. Ammitzböll, S. Ahmed, H. Söderberg, C. L. M. Petersson, V. Poulain, C. Guo, C. Dittel, *et al.*, "Measuring the quantum state of photoelectrons," *arXiv preprint arXiv:2309.13945*, 2023. https://doi.org/10.48550/arXiv.2309.13945.

[117] L. Morrigan, S. P. Neville, M. Gregory, A. E. Boguslavskiy, R. Forbes, I. Wilkinson, R. Lausten, A. Stolow, M. S. Schuurman, P. Hockett, *et al.*, "Ultrafast molecular frame quantum tomography," *Physical Review Letters*,

vol. 131, no. 19, p. 193001, 2023. https://link.aps.org/doi/10.1103/PhysRevLett.131.193001.

[118] D. Busto, H. Laurell, D. Finkelstein-Shapiro, C. Alexandridi, M. Isinger, S. Nandi, R. J. Squibb, M. Turconi, S. Zhong, C. L. Arnold, *et al.*, "Probing electronic decoherence with high-resolution attosecond photoelectron interferometry," *The European Physical Journal D*, vol. 76, no. 7, p. 112, 2022. https://doi.org/10.1140/epjd/s10053-022-00438-y.

[119] M. Blavier, R. D. Levine, and F. Remacle, "Time evolution of entanglement of electrons and nuclei and partial traces in ultrafast photochemistry," *Physical Chemistry Chemical Physics*, vol. 24, no. 29, pp. 17516–17525, 2022. https://doi.org/10.1039/D2CP01440H.

[120] M. Blavier, N. Gelfand, R. Levine, and F. Remacle, "Entanglement of electrons and nuclei: A most compact representation of the molecular wave function," *Chemical Physics Letters*, vol. 804, p. 139885, 2022. https://doi.org/10.1016/j.cplett.2022.139885.

[121] A. S. Maxwell, L. B. Madsen, and M. Lewenstein, "Entanglement of orbital angular momentum in non-sequential double ionization," *Nature Communications*, vol. 13, no. 1, p. 4706, 2022. https://doi.org/10.1038/s41467-022-32128-z.

[122] S. Eckart, D. Trabert, J. Rist, A. Geyer, L. P. H. Schmidt, K. Fehre, and M. Kunitski, "Ultrafast preparation and detection of entangled atoms," *Science Advances*, vol. 9, no. 36, p. eabq8227, 2023. https://doi.org/10.1126/sciadv.abq8227.

[123] M. Ruberti, V. Averbukh, and F. Mintert, "Bell test of quantum entanglement in attosecond photoionization," *arXiv preprint arXiv:2312.05036*, 2023. https://doi.org/10.48550/arXiv.2312.05036.

[124] A. Acín, I. Bloch, H. Buhrman, T. Calarco, C. Eichler, J. Eisert, D. Esteve, N. Gisin, S. J. Glaser, F. Jelezko, *et al.*, "The quantum technologies roadmap: a european community view," *New Journal of Physics*, vol. 20, no. 8, p. 080201, 2018. https://doi.org/10.1088/1367-2630/aad1ea.

[125] I. Walmsley, "Quantum optics: Science and technology in a new light," *Science*, vol. 348, no. 6234, pp. 525–530, 2015. https://doi.org/10.1126/science.aab0097.

[126] I. H. Deutsch, "Harnessing the power of the second quantum revolution," *PRX Quantum*, vol. 1, no. 2, p. 020101, 2020. https://link.aps.org/doi/10.1103/PRXQuantum.1.020101.

[127] F. Mintert, A. R. Carvalho, M. Kuś, and A. Buchleitner, "Measures and dynamics of entangled states," *Physics Reports*, vol. 415, no. 4, pp. 207–259, 2005. https://doi.org/10.1016/j.physrep.2005.04.006.

[128] M. B. Plenio and S. Virmani, "An introduction to entanglement measures.," *Quantum Inf. Comput.*, vol. 7, no. 1, pp. 1–51, 2007. https://doi.org/10.26421/QIC7.1-2-1.

[129] R. Horodecki, P. Horodecki, M. Horodecki, and K. Horodecki, "Quantum entanglement," *Reviews of modern physics*, vol. 81, no. 2, p. 865, 2009. https://link.aps.org/doi/10.1103/RevModPhys.81.865.

[130] A. Buchleitner, C. Viviescas, and M. Tiersch, *Entanglement and decoherence: foundations and modern trends*, vol. 768. Springer Science & Business Media, 2008. https://doi.org/10.1007/978-3-540-88169-8.

[131] T. N. C. for Physics, "For experiments with entangled photons, establishing the violation of Bell inequalities and pioneering quantum information science," 2022. https://www.nobelprize.org/uploads/2023/10/advanced-physicsprize2022-4.pdf.

[132] D. J. Griffiths and D. F. Schroeter, *Introduction to quantum mechanics*. Cambridge ; New York, NY: Cambridge University Press, third edition ed., 2018. https://books.google.de/books?id=LWRnDwAAQBAJ.

[133] M. A. Nielsen and I. L. Chuang, *Quantum computation and quantum information*. Cambridge university press, 2010. https://books.google.de/books?id=-s4DEy7o-a0C.

[134] A. Einstein, "Bestimmt Schrödinger's Wellenmechanik die Bewegung eines Systems vollständig oder nur im Sinne der Statistik?/ Does Schrödinger's wave mechanics determine the motion of a system completely or only in the statistical sense?," *Prussian Academy of Sciences*, vol. 5, pp. 2–100, 1927. can be found in: The collected papers of Albert Einstein, volume 15: The Berlin Years: Writings and Correspondence, June 1925-May 1927 Page 810.

[135] J. S. Bell, "On the Einstein Podolsky Rosen paradox," *Physics Physique Fizika*, vol. 1, no. 3, p. 195, 1964. https://link.aps.org/doi/10.1103/PhysicsPhysiqueFizika.1.195.

[136] G. H. Golub and C. Reinsch, "Singular value decomposition and least squares solutions," in *Handbook for Automatic Computation: Volume II: Linear Algebra*, pp. 134–151, Springer, 1971. https://doi.org/10.1007/978-3-642-86940-2_10.

[137] M. Vatasescu, "Entanglement between electronic and vibrational degrees of freedom in a laser-driven molecular system," *Physical Review A*, vol. 88, no. 6, p. 063415, 2013. https://link.aps.org/doi/10.1103/PhysRevA.88.063415.

[138] J. Von Neumann, *Mathematische Grundlagen der Quantenmechanik Mathematical foundations of quantum mechanics*, vol. 2. Springer-Verlag, 1996. https://doi.org/10.1007/978-3-642-61409-5.

[139] D. Petz, "Entropy, von Neumann and the von Neumann entropy: Dedicated to the memory of Alfred Wehrl," in *John von Neumann and the foundations of quantum physics*, pp. 83–96, Springer, 2001. https://doi.org/10.48550/arXiv.math-ph/0102013.

[140] C. E. Shannon, "A mathematical theory of communication," *The Bell system technical journal*, vol. 27, no. 3, pp. 379–423, 1948. https://doi.org/10.1002/j.1538-7305.1948.tb01338.x.

[141] C. H. Bennett, H. J. Bernstein, S. Popescu, and B. Schumacher, "Concentrating partial entanglement by local operations," *Physical Review A*, vol. 53, no. 4, p. 2046, 1996. https://link.aps.org/doi/10.1103/PhysRevA.53.2046.

[142] M. Vatasescu, "Measures of electronic-vibrational entanglement and quantum coherence in a molecular system," *Physical Review A*, vol. 92, no. 4, p. 042323, 2015. https://link.aps.org/doi/10.1103/PhysRevA.92.042323.

[143] M. J. J. Vrakking, "Ion-photoelectron entanglement in photoionization with chirped laser pulses," *Journal of Physics B: Atomic, Molecular and Optical Physics*, vol. 55, no. 13, p. 134001, 2022. https://doi.org/10.1088/1361-6455/ac6e17.

[144] Y. Nabekawa and K. Midorikawa, "Analysis of attosecond entanglement and coherence using feasible formulae," *Physical Review Research*, vol. 5, no. 3, p. 033083, 2023. https://link.aps.org/doi/10.1103/PhysRevResearch.5.033083.

[145] M. B. Plenio and S. Virmani, "An introduction to entanglement measures," 2006. https://doi.org/10.48550/arXiv.quant-ph/0504163.

[146] W. K. Wootters, "Entanglement of formation of an arbitrary state of two qubits," *Phys. Rev. Lett.*, vol. 80, pp. 2245–2248, Mar 1998. https://link.aps.org/doi/10.1103/PhysRevLett.80.2245.

[147] C. H. Bennett, G. Brassard, S. Popescu, B. Schumacher, J. A. Smolin, and W. K. Wootters, "Purification of noisy entanglement and faithful teleportation via noisy channels," *Phys. Rev. Lett.*, vol. 76, pp. 722–725, Jan 1996. https://link.aps.org/doi/10.1103/PhysRevLett.76.722.

[148] M. B. Plenio, "Logarithmic negativity: a full entanglement monotone that is not convex," *Physical review letters*, vol. 95, no. 9, p. 090503, 2005. https://link.aps.org/doi/10.1103/PhysRevLett.95.090503.

[149] M. Horodecki, P. Horodecki, and R. Horodecki, "Separability of mixed states: necessary and sufficient conditions," *Physics Letters A*, vol. 223, no. 1, pp. 1–8, 1996. https://www.sciencedirect.com/science/article/pii/S0375960196007062.

[150] B. M. Terhal, "Detecting quantum entanglement," *Theoretical Computer Science*, vol. 287, no. 1, pp. 313–335, 2002. https://doi.org/10.1016/S0304-3975(02)00139-1.

[151] M. Schultze, M. Fieß, N. Karpowicz, J. Gagnon, M. Korbman, M. Hofstetter, S. Neppl, A. L. Cavalieri, Y. Komninos, T. Mercouris, *et al.*, "Delay in photoemission," *science*, vol. 328, no. 5986, pp. 1658–1662, 2010. https://doi.org/10.1126/science.118940.

[152] M. Isinger, R. Squibb, D. Busto, S. Zhong, A. Harth, D. Kroon, S. Nandi, C. Arnold, M. Miranda, J. M. Dahlström, *et al.*, "Photoionization in the time and frequency domain," *Science*, vol. 358, no. 6365, pp. 893–896, 2017. https://doi.org/10.1126/science.aao7043.

[153] P. Eckle, A. Pfeiffer, C. Cirelli, A. Staudte, R. Dorner, H. Muller, M. Buttiker, and U. Keller, "Attosecond ionization and tunneling delay time measurements in helium," *science*, vol. 322, no. 5907, pp. 1525–1529, 2008. https://doi.org/10.1126/science.1163439.

[154] I. Christov, R. Bartels, H. Kapteyn, and M. Murnane, "Attosecond time-scale intra-atomic phase matching of high harmonic generation," *Physical Review Letters*, vol. 86, no. 24, p. 5458, 2001. https://link.aps.org/doi/10.1103/PhysRevLett.86.5458.

[155] C. Ott, A. Kaldun, P. Raith, K. Meyer, M. Laux, J. Evers, C. H. Keitel, C. H. Greene, and T. Pfeifer, "Lorentz meets Fano in spectral line shapes: a universal phase and its laser control," *Science*, vol. 340, no. 6133, pp. 716–720, 2013. https://doi.org/10.1126/science.1234407.

[156] L. B. Drescher, *Transient Dipole-Interactions on Sub-Cycle Timescales*. PhD thesis, Freie Universität Berlin (Germany), 2020. http://dx.doi.org/10.17169/refubium-27484.

[157] D. Shafir, H. Soifer, B. D. Bruner, M. Dagan, Y. Mairesse, S. Patchkovskii, M. Y. Ivanov, O. Smirnova, and N. Dudovich, "Resolving the time when an electron exits a tunnelling barrier," *Nature*, vol. 485, no. 7398, pp. 343–346, 2012. https://doi.org/10.1038/nature11025.

[158] S. Pabst, "Atomic and molecular dynamics triggered by ultrashort light pulses on the atto-to picosecond time scale," *The European Physical Journal Special Topics*, vol. 221, no. 1, pp. 1–71, 2013. https://doi.org/10.1140/epjst/e2013-01819-x.

[159] A. D. Bandrauk, S. Chelkowski, and H. S. Nguyen, "Attosecond localization of electrons in molecules," *International journal of quantum chemistry*, vol. 100, no. 6, pp. 834–844, 2004. https://doi.org/10.1002/qua.20252.

[160] M. Kling, C. Siedschlag, A. J. Verhoef, J. Khan, M. Schultze, T. Uphues, Y. Ni, M. Uiberacker, M. Drescher, F. Krausz, *et al.*, "Control of electron

localization in molecular dissociation," *Science*, vol. 312, no. 5771, pp. 246–248, 2006. https://doi.org/10.1126/science.1126259.

[161] M. Spanner, O. Smirnova, P. B. Corkum, and M. Y. Ivanov, "Reading diffraction images in strong field ionization of diatomic molecules," *Journal of Physics B: Atomic, Molecular and Optical Physics*, vol. 37, no. 12, p. L243, 2004. https://doi.org/10.1088/0953-4075/37/12/L02.

[162] M. Osolodkov, *Attosecond XUV-IR Pump-probe Measurements of Small Molecules Using 3D Momentum Spectroscopy*. PhD thesis, Freie Universität Berlin (Germany), 2022. http://dx.doi.org/10.17169/refubium-37001.

[163] I. Jordan, M. Huppert, D. Rattenbacher, M. Peper, D. Jelovina, C. Perry, A. Von Conta, A. Schild, and H. J. Wörner, "Attosecond spectroscopy of liquid water," *Science*, vol. 369, no. 6506, pp. 974–979, 2020. https://doi.org/10.1126/science.abb0979.

[164] A. L. Cavalieri, N. Müller, T. Uphues, V. S. Yakovlev, A. Baltuška, B. Horvath, B. Schmidt, L. Blümel, R. Holzwarth, S. Hendel, *et al.*, "Attosecond spectroscopy in condensed matter," *Nature*, vol. 449, no. 7165, pp. 1029–1032, 2007. https://doi.org/10.1038/nature06229.

[165] X. Gong, S. Heck, D. Jelovina, C. Perry, K. Zinchenko, R. Lucchese, and H. J. Wörner, "Attosecond spectroscopy of size-resolved water clusters," *Nature*, vol. 609, no. 7927, pp. 507–511, 2022. https://doi.org/10.1038/s41586-022-05039-8.

[166] J. Lu, E. F. Cunningham, Y. S. You, D. A. Reis, and S. Ghimire, "Interferometry of dipole phase in high harmonics from solids," *Nature Photonics*, vol. 13, no. 2, pp. 96–100, 2019. https://doi.org/10.1038/s41566-018-0326-x.

[167] A. L'Huillier and P. Balcou, "High-order harmonic generation in rare gases with a 1-ps 1053-nm laser," *Physical Review Letters*, vol. 70, no. 6, p. 774, 1993. https://link.aps.org/doi/10.1103/PhysRevLett.70.774.

[168] T. Gaumnitz, A. Jain, Y. Pertot, M. Huppert, I. Jordan, F. Ardana-Lamas, and H. J. Wörner, "Streaking of 43-attosecond soft-x-ray pulses generated by a passively cep-stable mid-infrared driver," *Optics express*, vol. 25, no. 22, pp. 27506–27518, 2017. https://doi.org/10.1364/OE.25.027506.

[169] M. Gavrila, *Atoms in intense laser fields*. San Diego, CA (United States); Academic Press Inc., 1992. http://inis.iaea.org/search/search.aspx?orig_q=RN:24013259.

[170] T. Brabec and F. Krausz, "Intense few-cycle laser fields: Frontiers of nonlinear optics," *Reviews of Modern Physics*, vol. 72, no. 2, p. 545, 2000. https://link.aps.org/doi/10.1103/RevModPhys.72.545.

[171] R. Weissenbilder, S. Carlström, L. Rego, C. Guo, C. Heyl, P. Smorenburg, E. Constant, C. Arnold, and A. L'huillier, "How to optimize high-order harmonic generation in gases," *Nature Reviews Physics*, vol. 4, no. 11, pp. 713–722, 2022. https://doi.org/10.1038/s42254-022-00522-7.

[172] S. Ghimire, A. D. DiChiara, E. Sistrunk, P. Agostini, L. F. DiMauro, and D. A. Reis, "Observation of high-order harmonic generation in a bulk crystal," *Nature physics*, vol. 7, no. 2, pp. 138–141, 2011. https://doi.org/10.1038/nphys1847.

[173] O. Schubert, M. Hohenleutner, F. Langer, B. Urbanek, C. Lange, U. Huttner, D. Golde, T. Meier, M. Kira, S. W. Koch, *et al.*, "Sub-cycle control of terahertz high-harmonic generation by dynamical Bloch oscillations," *Nature photonics*, vol. 8, no. 2, pp. 119–123, 2014. https://doi.org/10.1038/nphoton.2013.349.

[174] T. T. Luu, M. Garg, S. Y. Kruchinin, A. Moulet, M. T. Hassan, and E. Goulielmakis, "Extreme ultraviolet high-harmonic spectroscopy of solids," *Nature*, vol. 521, no. 7553, pp. 498–502, 2015. https://doi.org/10.1038/nature14456.

[175] M. Hohenleutner, F. Langer, O. Schubert, M. Knorr, U. Huttner, S. W. Koch, M. Kira, and R. Huber, "Real-time observation of interfering crystal electrons in high-harmonic generation," *Nature*, vol. 523, no. 7562, pp. 572–575, 2015. https://doi.org/10.1038/nature14652.

[176] S. Ghimire and D. A. Reis, "High-harmonic generation from solids," *Nature physics*, vol. 15, no. 1, pp. 10–16, 2019. https://doi.org/10.1038/s41567-018-0315-5.

[177] J.-C. Diels and W. Rudolph, *Ultrashort laser pulse phenomena*. Elsevier, 2006. https://doi.org/10.1016/B978-0-12-215493-5.X5000-9.

[178] W. Kaiser and D. H. Auston, *Ultrashort laser pulses: generation and applications*. Springer, 1993. https://doi.org/10.1007/BFb0070977.

[179] Z. Chang, *Fundamentals of attosecond optics*. CRC press, 2016. https://books.google.de/books?id=J5HLBQAAQBAJ.

[180] J. . J. Macklin, J. Kmetec, and C. Gordon III, "High-order harmonic generation using intense femtosecond pulses," *Physical review letters*, vol. 70, no. 6, p. 766, 1993. https://link.aps.org/doi/10.1103/PhysRevLett.70.766.

[181] T. Hänsch, "A proposed sub-femtosecond pulse synthesizer using separate phase-locked laser oscillators," *Optics Communications*, vol. 80, no. 1, pp. 71–75, 1990. https://doi.org/10.1016/0030-4018(90)90509-R.

[182] G. Farkas and C. Tóth, "Proposal for attosecond light pulse generation using laser induced multiple-harmonic conversion processes in rare gases,"

Physics Letters A, vol. 168, no. 5-6, pp. 447–450, 1992. https://doi.org/10.1016/0375-9601(92)90534-S.

[183] S. Harris, J. J. Macklin, and T. Hänsch, "Atomic scale temporal structure inherent to high-order harmonic generation," *Optics communications*, vol. 100, no. 5-6, pp. 487–490, 1993. https://doi.org/10.1016/0030-4018(93)90250-9.

[184] A. L'Huillier, K. J. Schafer, and K. C. Kulander, "Theoretical aspects of intense field harmonic generation," *Journal of Physics B: Atomic, Molecular and Optical Physics*, vol. 24, no. 15, p. 3315, 1991. https://doi.org/10.1088/0953-4075/24/15/004.

[185] J. L. Krause, K. J. Schafer, and K. C. Kulander, "High-order harmonic generation from atoms and ions in the high intensity regime," *Physical Review Letters*, vol. 68, no. 24, p. 3535, 1992. https://link.aps.org/doi/10.1103/PhysRevLett.68.3535.

[186] P. B. Corkum, "Plasma perspective on strong field multiphoton ionization," *Physical review letters*, vol. 71, no. 13, p. 1994, 1993. https://link.aps.org/doi/10.1103/PhysRevLett.71.1994.

[187] J. Tate, T. Auguste, H. Muller, P. Salières, P. Agostini, and L. DiMauro, "Scaling of wave-packet dynamics in an intense midinfrared field," *Physical review letters*, vol. 98, no. 1, p. 013901, 2007. https://link.aps.org/doi/10.1103/PhysRevLett.98.013901.

[188] A. D. Shiner, C. Trallero-Herrero, N. Kajumba, H.-C. Bandulet, D. Comtois, F. Légaré, M. Giguère, J.-C. Kieffer, P. B. Corkum, and D. Villeneuve, "Wavelength scaling of high harmonic generation efficiency," *Physical Review Letters*, vol. 103, no. 7, p. 073902, 2009. https://link.aps.org/doi/10.1103/PhysRevLett.103.073902.

[189] A. L. Lytle, *Phase matching and coherence of high-order harmonic generation in hollow waveguides*. PhD thesis, University of Colorado at Boulder, 2008. https://jila.colorado.edu/sites/default/files/2019-05/lytle_thesis.pdf.

[190] K. Kulander, K. Schafer, and J. Krause, "Dynamics of short-pulse excitation, ionization and harmonic conversion," *Super-intense laser-atom physics*, pp. 95–110, 1993. https://doi.org/10.1007/978-1-4615-7963-2_10.

[191] M. Lewenstein, P. Balcou, M. Y. Ivanov, A. L'huillier, and P. B. Corkum, "Theory of high-harmonic generation by low-frequency laser fields," *Physical Review A*, vol. 49, no. 3, p. 2117, 1994. https://link.aps.org/doi/10.1103/PhysRevA.49.2117.

[192] A. Zheltikov, "Keldysh parameter, photoionization adiabaticity, and the tunneling time," *Physical Review A*, vol. 94, no. 4, p. 043412, 2016. https://link.aps.org/doi/10.1103/PhysRevA.94.043412.

[193] M. Hentschel, R. Kienberger, C. Spielmann, G. A. Reider, N. Milosevic, T. Brabec, P. Corkum, U. Heinzmann, M. Drescher, and F. Krausz, "Attosecond metrology," *Nature*, vol. 414, no. 6863, pp. 509–513, 2001. https://doi.org/10.1038/35107000.

[194] M. J. J. Vrakking, D. Villeneuve, and A. Stolow, "Observation of fractional revivals of a molecular wave packet," *Physical Review A*, vol. 54, no. 1, p. R37, 1996. https://link.aps.org/doi/10.1103/PhysRevA.54.R37.

[195] H. Niikura, F. Légaré, R. Hasbani, M. Y. Ivanov, D. Villeneuve, and P. Corkum, "Probing molecular dynamics with attosecond resolution using correlated wave packet pairs," *Nature*, vol. 421, no. 6925, pp. 826–829, 2003. https://doi.org/10.1038/nature01430.

[196] F. Kelkensberg, C. Lefebvre, W. Siu, O. Ghafur, T. Nguyen-Dang, O. Atabek, A. Keller, V. Serov, P. Johnsson, M. Swoboda, *et al.*, "Molecular dissociative ionization and wave-packet dynamics studied using two-color XUV and IR pump-probe spectroscopy," *Physical review letters*, vol. 103, no. 12, p. 123005, 2009. https://link.aps.org/doi/10.1103/PhysRevLett.103.123005.

[197] T. Okino, Y. Furukawa, Y. Nabekawa, S. Miyabe, A. Amani Eilanlou, E. J. Takahashi, K. Yamanouchi, and K. Midorikawa, "Direct observation of an attosecond electron wave packet in a nitrogen molecule," *Science advances*, vol. 1, no. 8, p. e1500356, 2015. https://doi.org/10.1126/sciadv.1500356.

[198] Y. Cheng, M. Chini, X. Wang, A. González-Castrillo, A. Palacios, L. Argenti, F. Martín, and Z. Chang, "Reconstruction of an excited-state molecular wave packet with attosecond transient absorption spectroscopy," *Physical Review A*, vol. 94, no. 2, p. 023403, 2016. https://link.aps.org/doi/10.1103/PhysRevA.94.023403.

[199] T. Remetter, P. Johnsson, J. Mauritsson, K. Varjú, Y. Ni, F. Lépine, E. Gustafsson, M. Kling, J. Khan, R. López-Martens, *et al.*, "Attosecond electron wave packet interferometry," *Nature Physics*, vol. 2, no. 5, pp. 323–326, 2006. https://doi.org/10.1038/nphys290.

[200] K. Klünder, J. Dahlström, M. Gisselbrecht, T. Fordell, M. Swoboda, D. Guenot, P. Johnsson, J. Caillat, J. Mauritsson, A. Maquet, *et al.*, "Probing single-photon ionization on the attosecond time scale," *Physical Review Letters*, vol. 106, no. 14, p. 143002, 2011. https://link.aps.org/doi/10.1103/PhysRevLett.106.143002.

[201] M. Shapiro and P. Brumer, "Coherent control of molecular dynamics," *Reports on Progress in Physics*, vol. 66, no. 6, p. 859, 2003. https://doi.org/10.1088/0034-4885/66/6/201.

[202] J. Manz and L. Wöste, "Femtosecond chemistry," *VCH Verlagsgesellschaft mbH*, 1995. https://doi.org/10.1002/9783527619436.

[203] M. Ivanov, "Lecture III & IV– 2023. Microscopic nonlinear response of a quantum system, Part I & II," October 2023. Max Born Institute and Humboldt University.

[204] L. Drescher, O. Kornilov, T. Witting, G. Reitsma, N. Monserud, A. Rouzée, J. Mikosch, M. J. J. Vrakking, and B. Schütte, "Extreme-ultraviolet refractive optics," *Nature*, vol. 564, no. 7734, pp. 91–94, 2018. https://doi.org/10.1038/s41586-018-0737-3.

[205] L. Drescher, G. Reitsma, T. Witting, S. Patchkovskii, J. Mikosch, and M. J. J. Vrakking, "State-resolved probing of attosecond timescale molecular dipoles," *The Journal of Physical Chemistry Letters*, vol. 10, no. 2, pp. 265–269, 2018. https://doi.org/10.1021/acs.jpclett.8b02878.

[206] L. Drescher, O. Kornilov, T. Witting, V. Shokeen, M. J. J. Vrakking, and B. Schütte, "Extreme-ultraviolet spectral compression by four-wave mixing," *Nature Photonics*, vol. 15, no. 4, pp. 263–266, 2021. https://doi.org/10.1038/s41566-020-00758-8.

[207] L. Drescher, T. Witting, O. Kornilov, and M. J. J. Vrakking, "Phase dependence of resonant and antiresonant two-photon excitations," *Physical Review A*, vol. 105, no. 1, p. L011101, 2022. https://link.aps.org/doi/10.1103/PhysRevA.105.L011101.

[208] J. Reichert, R. Holzwarth, T. Udem, and T. W. Hänsch, "Measuring the frequency of light with mode-locked lasers," *Optics communications*, vol. 172, no. 1-6, pp. 59–68, 1999. https://doi.org/10.1016/S0030-4018(99)00491-5.

[209] S. Koke, C. Grebing, H. Frei, A. Anderson, A. Assion, and G. Steinmeyer, "Direct frequency comb synthesis with arbitrary offset and shot-noise-limited phase noise," *Nature Photonics*, vol. 4, no. 7, pp. 462–465, 2010. https://doi.org/10.1038/nphoton.2010.91.

[210] F. Verluise, V. Laude, Z. Cheng, C. Spielmann, and P. Tournois, "Amplitude and phase control of ultrashort pulses by use of an acousto-optic programmable dispersive filter: pulse compression and shaping," *Optics letters*, vol. 25, no. 8, pp. 575–577, 2000. https://doi.org/10.1364/OL.25.000575.

[211] T. Oksenhendler, D. Kaplan, P. Tournois, G. Greetham, and F. Estable, "Intracavity acousto-optic programmable gain control for ultra-wide-band

regenerative amplifiers," *Applied Physics B*, vol. 83, pp. 491–494, 2006. https://doi.org/10.1007/s00340-006-2231-0.

[212] R. Paschotta, J. Aus der Au, G. Spühler, S. Erhard, A. Giesen, and U. Keller, "Passive mode locking of thin-disk lasers: effects of spatial hole burning," *Applied Physics B*, vol. 72, pp. 267–278, 2001. https://doi.org/10.1007/s003400100486.

[213] A. Suda, M. Hatayama, K. Nagasaka, and K. Midorikawa, "Generation of sub-10-fs, 5-mJ-optical pulses using a hollow fiber with a pressure gradient," *Applied Physics Letters*, vol. 86, no. 11, p. 111116, 2005. https://doi.org/10.1063/1.1883706.

[214] R. H. Stolen and C. Lin, "Self-phase-modulation in silica optical fibers," *Physical Review A*, vol. 17, no. 4, p. 1448, 1978. https://link.aps.org/doi/10.1103/PhysRevA.17.1448.

[215] V. Pervak, I. Ahmad, M. Trubetskov, A. Tikhonravov, and F. Krausz, "Double-angle multilayer mirrors with smooth dispersion characteristics," *Optics express*, vol. 17, no. 10, pp. 7943–7951, 2009. https://doi.org/10.1364/OE.17.007943.

[216] F. Silva, M. Miranda, B. Alonso, J. Rauschenberger, V. Pervak, and H. Crespo, "Simultaneous compression, characterization and phase stabilization of GW-level 1.4 cycle VIS-NIR femtosecond pulses using a single dispersion-scan setup," *Optics express*, vol. 22, no. 9, pp. 10181–10191, 2014. https://doi.org/10.1364/OE.22.010181.

[217] H. Timmers, Y. Kobayashi, K. F. Chang, M. Reduzzi, D. M. Neumark, and S. R. Leone, "Generating high-contrast, near single-cycle waveforms with third-order dispersion compensation," *Optics letters*, vol. 42, no. 4, pp. 811–814, 2017. https://doi.org/10.1364/OL.42.000811.

[218] T. Witting, F. Frank, C. A. Arrell, W. A. Okell, J. P. Marangos, and J. W. Tisch, "Characterization of high-intensity sub-4-fs laser pulses using spatially encoded spectral shearing interferometry," *Optics letters*, vol. 36, no. 9, pp. 1680–1682, 2011. https://doi.org/10.1364/OL.36.001680.

[219] P. Salières, L. Le Déroff, T. Auguste, P. Monot, P. d'Oliveira, D. Campo, J.-F. Hergott, H. Merdji, and B. Carré, "Frequency-domain interferometry in the XUV with high-order harmonics," *Physical Review Letters*, vol. 83, no. 26, p. 5483, 1999. https://link.aps.org/doi/10.1103/PhysRevLett.83.5483.

[220] R. Lopez-Martens, K. Varjú, P. Johnsson, J. Mauritsson, Y. Mairesse, P. Salieres, M. B. Gaarde, K. J. Schafer, A. Persson, S. Svanberg, *et al.*, "Amplitude and phase control of attosecond light pulses," *Physical Review Letters*, vol. 94, no. 3, p. 033001, 2005. https://link.aps.org/doi/10.1103/PhysRevLett.94.033001.

[221] O. Ghafur, W. Siu, P. Johnsson, M. F. Kling, M. Drescher, and M. J. J. Vrakking, "A velocity map imaging detector with an integrated gas injection system," *Review of Scientific Instruments*, vol. 80, no. 3, p. 033110, 2009. https://doi.org/10.1063/1.3085799.

[222] B. E. Schmidt, A. D. Shiner, P. Lassonde, J.-C. Kieffer, P. B. Corkum, D. M. Villeneuve, and F. Légaré, "CEP stable 1.6 cycle laser pulses at 1.8 μm," *Optics express*, vol. 19, no. 7, pp. 6858–6864, 2011. https://doi.org/10.1364/OE.19.006858.

[223] V. Cardin, N. Thiré, S. Beaulieu, V. Wanie, F. Légaré, and B. E. Schmidt, "0.42 TW 2-cycle pulses at 1.8 μm via hollow-core fiber compression," *Applied Physics Letters*, vol. 107, no. 18, 2015. https://doi.org/10.1063/1.4934861.

[224] G. Fan, T. Balčiūnas, T. Kanai, T. Flöry, G. Andriukaitis, B. E. Schmidt, F. Légaré, and A. Baltuška, "Hollow-core-waveguide compression of multi-millijoule CEP-stable 3.2 μm pulses," *Optica*, vol. 3, no. 12, pp. 1308–1311, 2016. https://doi.org/10.1364/OPTICA.3.001308.

[225] D. Fabris, *Ultrafast light sources and methods for attosecond pump-probe experiments*. PhD thesis, Imperial College London, 2015. https://doi.org/10.25560/25283.

[226] W. Okell, *Ultrafast measurements in condensed matter*. PhD thesis, Imperial College London, 2014. https://doi.org/10.25560/24755.

[227] I. H. Malitson, "Interspecimen comparison of the refractive index of fused silica," *Josa*, vol. 55, no. 10, pp. 1205–1209, 1965. https://doi.org/10.1364/JOSA.55.001205.

[228] C. Tan, "Determination of refractive index of silica glass for infrared wavelengths by IR spectroscopy," *Journal of Non-Crystalline Solids*, vol. 223, no. 1-2, pp. 158–163, 1998. https://doi.org/10.1016/S0022-3093(97)00438-9.

[229] D. J. Jones, S. A. Diddams, J. K. Ranka, A. Stentz, R. S. Windeler, J. L. Hall, and S. T. Cundiff, "Carrier-envelope phase control of femtosecond mode-locked lasers and direct optical frequency synthesis," *Science*, vol. 288, no. 5466, pp. 635–639, 2000. https://doi.org/10.1126/science.288.5466.635.

[230] P. A. Franken, A. E. Hill, C. W. Peters, and G. Weinreich, "Generation of optical harmonics," *Phys. Rev. Lett.*, vol. 7, pp. 118–119, Aug 1961. https://link.aps.org/doi/10.1103/PhysRevLett.7.118.

[231] H. Liu, J. Yao, and A. Puri, "Second and third harmonic generation in BBO by femtosecond Ti: sapphire laser pulses," *Optics communications*, vol. 109, no. 1-2, pp. 139–144, 1994. https://doi.org/10.1016/0030-4018(94)90751-X.

[232] M. Hobden, "Phase-matched second-harmonic generation in biaxial crystals," *Journal of Applied Physics*, vol. 38, no. 11, pp. 4365–4372, 1967. https://doi.org/10.1063/1.1709130.

[233] M. Takeda, H. Ina, and S. Kobayashi, "Fourier-transform method of fringe-pattern analysis for computer-based topography and interferometry," *JosA*, vol. 72, no. 1, pp. 156–160, 1982. https://doi.org/10.1364/JOSA.72.000156.

[234] S. Cundiff, T. Fortier, J. Ye, and J. Hall, "Carrier-envelope phase stabilization of femtosecond modelocked lasers and direct optical frequency synthesis," in *Technical Digest. Summaries of papers presented at the Conference on Lasers and Electro-Optics. Postconference Technical Digest (IEEE Cat. No. 01CH37170)*, p. 130, IEEE, 2001. http://doi.org/10.1109/CLEO.2001.947591.

[235] A. Apolonski, A. Poppe, G. Tempea, C. Spielmann, T. Udem, R. Holzwarth, T. W. Hänsch, and F. Krausz, "Controlling the phase evolution of few-cycle light pulses," *Physical Review Letters*, vol. 85, no. 4, p. 740, 2000. https://link.aps.org/doi/10.1103/PhysRevLett.85.740.

[236] A. Poppe, R. Holzwarth, A. Apolonski, G. Tempea, C. Spielmann, T. W. Hänsch, and F. Krausz, "Few-cycle optical waveform synthesis," *Applied Physics B*, vol. 72, pp. 373–376, 2001. https://doi.org/10.1007/s003400000526.

[237] E. Goulielmakis, G. Nersisyan, N. Papadogiannis, D. Charalambidis, G. Tsakiris, and K. Witte, "A dispersionless Michelson interferometer for the characterization of attosecond pulses," *Applied Physics B*, vol. 74, pp. 197–206, 2002. https://doi.org/10.1007/s003400200794.

[238] Y. Nabekawa, Y. Furukawa, T. Okino, A. Amani Eilanlou, E. J. Takahashi, K. Yamanouchi, and K. Midorikawa, "Sub-10-fs control of dissociation pathways in the hydrogen molecular ion with a few-pulse attosecond pulse train," *Nature communications*, vol. 7, no. 1, p. 12835, 2016. https://doi.org/10.1038/ncomms12835.

[239] P. Tzallas, D. Charalambidis, N. Papadogiannis, K. Witte, and G. D. Tsakiris, "Direct observation of attosecond light bunching," *Nature*, vol. 426, no. 6964, pp. 267–271, 2003. https://doi.org/10.1038/nature02091.

[240] T. Okino, Y. Furukawa, T. Shimizu, Y. Nabekawa, K. Yamanouchi, and K. Midorikawa, "Nonlinear Fourier transformation spectroscopy of small molecules with intense attosecond pulse train," *Journal of Physics B: Atomic, Molecular and Optical Physics*, vol. 47, no. 12, p. 124007, 2014. https://doi.org/10.1088/0953-4075/47/12/124007.

[241] Y. Nabekawa, T. Shimizu, Y. Furukawa, E. J. Takahashi, and K. Midorikawa, "Interferometry of attosecond pulse trains in the extreme ultraviolet wavelength region," *Physical review letters*, vol. 102, no. 21, p. 213904, 2009. https://link.aps.org/doi/10.1103/PhysRevLett.102.213904.

[242] D. Fabris, T. Witting, W. Okell, D. Walke, P. Matia-Hernando, J. Henkel, T. Barillot, M. Lein, J. Marangos, and J. Tisch, "Synchronized pulses generated at 20 ev and 90 ev for attosecond pump–probe experiments," *Nature Photonics*, vol. 9, no. 6, pp. 383–387, 2015. https://doi.org/10.1038/nphoton.2015.77.

[243] T. Barillot, P. Matia-Hernando, D. Greening, D. Walke, T. Witting, L. Frasinski, J. Marangos, and J. Tisch, "Towards XUV pump-probe experiments in the femtosecond to sub-femtosecond regime: New measurement of the helium two-photon ionization cross-section," *Chemical Physics Letters*, vol. 683, pp. 38–42, 2017. https://doi.org/10.1016/j.cplett.2017.05.026.

[244] P. Tzallas, E. Skantzakis, L. Nikolopoulos, G. D. Tsakiris, and D. Charalambidis, "Extreme-ultraviolet pump–probe studies of one-femtosecond-scale electron dynamics," *Nature Physics*, vol. 7, no. 10, pp. 781–784, 2011. https://doi.org/10.1038/nphys2033.

[245] O. Faucher, P. Tzallas, E. Benis, J. Kruse, A. Peralta Conde, C. Kalpouzos, and D. Charalambidis, "Four-dimensional investigation of the 2nd order volume autocorrelation technique," *Applied Physics B*, vol. 97, pp. 505–510, 2009. https://doi.org/10.1007/s00340-009-3559-z.

[246] Y. Meng, C. Zhang, C. Marceau, A. Y. Naumov, P. Corkum, and D. Villeneuve, "Octave-spanning hyperspectral coherent diffractive imaging in the extreme ultraviolet range," *Optics Express*, vol. 23, no. 22, pp. 28960–28969, 2015. https://doi.org/10.1364/OE.23.028960.

[247] G. Jansen, D. Rudolf, L. Freisem, K. Eikema, and S. Witte, "Spatially resolved fourier transform spectroscopy in the extreme ultraviolet," *Optica*, vol. 3, no. 10, pp. 1122–1125, 2016. https://doi.org/10.1364/OPTICA.3.001122.

[248] J. Tross, G. Kolliopoulos, and C. A. Trallero-Herrero, "Self referencing attosecond interferometer with zeptosecond precision," *Optics Express*, vol. 27, no. 16, pp. 22960–22969, 2019. https://doi.org/10.1364/OE.27.022960.

[249] J. Köhler, M. Wollenhaupt, T. Bayer, C. Sarpe, and T. Baumert, "Zeptosecond precision pulse shaping," *Optics Express*, vol. 19, no. 12, pp. 11638–11653, 2011. https://doi.org/10.1364/OE.19.011638.

[250] A. Monmayrant, S. Weber, and B. Chatel, "A newcomer's guide to ultrashort pulse shaping and characterization," *Journal of Physics B: Atomic,*

Molecular and Optical Physics, vol. 43, no. 10, p. 103001, 2010. https://doi.org/10.1088/0953-4075/43/10/103001.

[251] M. Bellini, C. Lyngå, A. Tozzi, M. Gaarde, T. Hänsch, A. L'Huillier, and C.-G. Wahlström, "Temporal coherence of ultrashort high-order harmonic pulses," *Physical Review Letters*, vol. 81, no. 2, p. 297, 1998. https://link.aps.org/doi/10.1103/PhysRevLett.81.297.

[252] D. Descamps, C. Lyngå, J. Norin, A. L'Huillier, C.-G. Wahlström, J.-F. Hergott, H. Merdji, P. Salières, M. Bellini, and T. Hänsch, "Extreme ultraviolet interferometry measurements with high-order harmonics," *Optics letters*, vol. 25, no. 2, pp. 135–137, 2000. https://doi.org/10.1364/OL.25.000135.

[253] M. Kovačev, S. Fomichev, E. Priori, Y. Mairesse, H. Merdji, P. Monchicourt, P. Breger, J. Norin, A. Persson, A. L'Huillier, *et al.*, "Extreme ultraviolet Fourier-transform spectroscopy with high order harmonics," *Physical review letters*, vol. 95, no. 22, p. 223903, 2005. https://link.aps.org/doi/10.1103/PhysRevLett.95.223903.

[254] R. Eramo, S. Cavalieri, C. Corsi, I. Liontos, and M. Bellini, "Method for high-resolution frequency measurements in the extreme ultraviolet regime: Random-sampling Ramsey spectroscopy," *Physical review letters*, vol. 106, no. 21, p. 213003, 2011. https://link.aps.org/doi/10.1103/PhysRevLett.106.213003.

[255] A. Wituschek, O. Kornilov, T. Witting, L. Maikowski, F. Stienkemeier, M. J. J. Vrakking, and L. Bruder, "Phase cycling of extreme ultraviolet pulse sequences generated in rare gases," *New Journal of Physics*, vol. 22, no. 9, p. 092001, 2020. https://dx.doi.org/10.1088/1367-2630/abb43a.

[256] A. Wituschek, L. Bruder, E. Allaria, U. Bangert, M. Binz, R. Borghes, C. Callegari, G. Cerullo, P. Cinquegrana, L. Giannessi, *et al.*, "Tracking attosecond electronic coherences using phase-manipulated extreme ultraviolet pulses," *Nature communications*, vol. 11, no. 1, p. 883, 2020. https://doi.org/10.1038/s41467-020-14721-2.

[257] D. R. Austin, T. Witting, C. A. Arrell, F. Frank, A. S. Wyatt, J. P. Marangos, J. W. Tisch, and I. A. Walmsley, "Lateral shearing interferometry of high-harmonic wavefronts," *Optics letters*, vol. 36, no. 10, pp. 1746–1748, 2011. https://doi.org/10.1364/OL.36.001746.

[258] O. Smirnova, Y. Mairesse, S. Patchkovskii, N. Dudovich, D. Villeneuve, P. Corkum, and M. Y. Ivanov, "High harmonic interferometry of multi-electron dynamics in molecules," *Nature*, vol. 460, no. 7258, pp. 972–977, 2009. https://doi.org/10.1038/nature08253.

[259] S. Beaulieu, E. Bloch, L. Barreau, A. Comby, D. Descamps, R. Géneaux, F. Légaré, S. Petit, and Y. Mairesse, "Phase-resolved two-dimensional spectroscopy of electronic wave packets by laser-induced XUV free induction decay," *Physical Review A*, vol. 95, no. 4, p. 041401, 2017. https://link.aps.org/doi/10.1103/PhysRevA.95.041401.

[260] D. Azoury, Kneller, S. Rozen, B. D. Bruner, A. Clergerie, Y. Mairesse, B. Fabre, B. Pons, N. Dudovich, and M. Krüger, "Electronic wavefunctions probed by all-optical attosecond interferometry," *Nature Photonics*, vol. 13, no. 1, pp. 54–59, 2019. https://doi.org/10.1038/s41566-018-0303-4.

[261] A. González-Castrillo, F. Martín, and A. Palacios, "Quantum state holography to reconstruct the molecular wave packet using an attosecond XUV–XUV pump-probe technique," *Scientific reports*, vol. 10, no. 1, p. 12981, 2020. https://doi.org/10.1038/s41598-020-69733-1.

[262] W. K. Siu, *Probing molecular dynamics using novel light sources*. PhD thesis, FOM Institute AMOLF, 2011. https://hdl.handle.net/2066/90925.

[263] J. L. Wiza *et al.*, "Microchannel plate detectors," *Nucl. Instrum. Methods*, vol. 162, no. 1-3, pp. 587–601, 1979. https://doi.org/10.1016/0029-554X(79)90734-1.

[264] V. Fock, "Näherungsmethode zur Lösung des quantenmechanischen Mehrkörperproblems/ Approximation method for solving the quantum mechanical many-body problem," *Zeitschrift für Physik*, vol. 61, pp. 126–148, 1930. https://doi.org/10.1007/BF01340294.

[265] D. R. Hartree, "The wave mechanics of an atom with a non-Coulomb central field. Part i. Theory and methods," in *Mathematical Proceedings of the Cambridge Philosophical Society*, vol. 24, pp. 89–110, Cambridge university press, 1928. https://doi.org/10.1017/S0305004100011919.

[266] H. Bruus and K. Flensberg, *Many-body quantum theory in condensed matter physics: an introduction*. OUP Oxford, 2004. https://books.google.de/books?id=zeaMBAAAQBAJ.

[267] J. C. Tully, R. S. Berry, and B. J. Dalton, "Angular distribution of molecular photoelectrons," *Physical Review*, vol. 176, no. 1, p. 95, 1968. https://link.aps.org/doi/10.1103/PhysRev.176.95.

[268] J. Cooper and R. N. Zare, "Angular distribution of photoelectrons," *The Journal of Chemical Physics*, vol. 48, no. 2, pp. 942–943, 1968. https://doi.org/10.1063/1.1668742.

[269] S. T. Manson and A. F. Starace, "Photoelectron angular distributions: energy dependence for s subshells," *Reviews of Modern Physics*, vol. 54, no. 2, p. 389, 1982. https://link.aps.org/doi/10.1103/RevModPhys.54.389.

[270] K. L. Reid, "Photoelectron angular distributions," *Annual review of physical chemistry*, vol. 54, no. 1, pp. 397–424, 2003. https://doi.org/10.1146/annurev.physchem.54.011002.103814.

[271] J. W. Cooper and S. T. Manson, "Photo-ionization in the soft x-ray range: angular distributions of photoelectrons and interpretation in terms of subshell structure," *Physical Review*, vol. 177, no. 1, p. 157, 1969. https://link.aps.org/doi/10.1103/PhysRev.177.157.

[272] G. A. Garcia, L. Nahon, and I. Powis, "Two-dimensional charged particle image inversion using a polar basis function expansion," *Review of Scientific Instruments*, vol. 75, no. 11, pp. 4989–4996, 2004. https://doi.org/10.1063/1.1807578.

[273] M. Ryazanov, *Development and implementation of methods for sliced velocity map imaging. Studies of overtone-induced dissociation and isomerization dynamics of hydroxymethyl radical (CH_2OH and CD_2OH)*. PhD thesis, University of Southern California, 2012. https://doi.org/10.25549/usctheses-c3-112619.

[274] D. D. Hickstein, S. T. Gibson, R. Yurchak, D. D. Das, and M. Ryazanov, "A direct comparison of high-speed methods for the numerical abel transform," *Review of Scientific Instruments*, vol. 90, no. 6, p. 065115, 2019. https://doi.org/10.1063/1.5092635.

[275] I. P. Christov, M. M. Murnane, and H. C. Kapteyn, "High-harmonic generation of attosecond pulses in the "single-cycle" regime," *Physical Review Letters*, vol. 78, no. 7, p. 1251, 1997. https://link.aps.org/doi/10.1103/PhysRevLett.78.1251.

[276] R. Kienberger, E. Goulielmakis, M. Uiberacker, A. Baltuska, V. Yakovlev, F. Bammer, A. Scrinzi, T. Westerwalbesloh, U. Kleineberg, U. Heinzmann, *et al.*, "Atomic transient recorder," *Nature*, vol. 427, no. 6977, pp. 817–821, 2004. https://doi.org/10.1038/nature02277.

[277] A. Baltuška, T. Udem, M. Uiberacker, M. Hentschel, E. Goulielmakis, C. Gohle, R. Holzwarth, V. S. Yakovlev, A. Scrinzi, T. W. Hänsch, *et al.*, "Attosecond control of electronic processes by intense light fields," *Nature*, vol. 421, no. 6923, pp. 611–615, 2003. https://doi.org/10.1038/nature01414.

[278] P. Corkum, N. Burnett, and M. Y. Ivanov, "Subfemtosecond pulses," *Optics letters*, vol. 19, no. 22, pp. 1870–1872, 1994. https://doi.org/10.1364/OL.19.001870.

[279] C. Altucci, C. Delfin, L. Roos, M. B. Gaarde, A. L'Huillier, I. Mercer, T. Starczewski, and C.-G. Wahlström, "Frequency-resolved time-gated high-order harmonics," *Physical Review A*, vol. 58, no. 5, p. 3934, 1998. https://link.aps.org/doi/10.1103/PhysRevA.58.3934.

[280] O. Tcherbakoff, E. Mével, D. Descamps, J. Plumridge, and E. Constant, "Time-gated high-order harmonic generation," *Physical Review A*, vol. 68, no. 4, p. 043804, 2003. https://link.aps.org/doi/10.1103/PhysRevA.68.043804.

[281] I. Sola, E. Mével, L. Elouga, E. Constant, V. Strelkov, L. Poletto, P. Villoresi, E. Benedetti, J.-P. Caumes, S. Stagira, *et al.*, "Controlling attosecond electron dynamics by phase-stabilized polarization gating," *Nature physics*, vol. 2, no. 5, pp. 319–322, 2006. https://doi.org/10.1038/nphys281.

[282] G. Sansone, E. Benedetti, F. Calegari, C. Vozzi, L. Avaldi, R. Flammini, L. Poletto, P. Villoresi, C. Altucci, R. Velotta, *et al.*, "Isolated single-cycle attosecond pulses," *Science*, vol. 314, no. 5798, pp. 443–446, 2006. https://doi.org/10.1126/science.1132838.

[283] H. Mashiko, S. Gilbertson, C. Li, S. D. Khan, M. M. Shakya, E. Moon, and Z. Chang, "Double optical gating of high-order harmonic generation with carrier-envelope phase stabilized lasers," *Phys. Rev. Lett.*, vol. 100, p. 103906, Mar 2008. https://link.aps.org/doi/10.1103/PhysRevLett.100.103906.

[284] X. Feng, S. Gilbertson, H. Mashiko, H. Wang, S. D. Khan, M. Chini, Y. Wu, K. Zhao, and Z. Chang, "Generation of isolated attosecond pulses with 20 to 28 femtosecond lasers," *Physical review letters*, vol. 103, no. 18, p. 183901, 2009. https://doi.org/10.1103/PhysRevLett.103.183901.

[285] K. T. Kim, C. Zhang, T. Ruchon, J.-F. Hergott, T. Auguste, D. Villeneuve, P. Corkum, and F. Quéré, "Photonic streaking of attosecond pulse trains," *Nature Photonics*, vol. 7, no. 8, pp. 651–656, 2013. https://doi.org/10.1038/nphoton.2013.170.

[286] T. Pfeifer, A. Jullien, M. J. Abel, P. M. Nagel, L. Gallmann, D. M. Neumark, and S. R. Leone, "Generating coherent broadband continuum soft-x-ray radiation by attosecond ionization gating," *Optics Express*, vol. 15, no. 25, pp. 17120–17128, 2007. https://doi.org/10.1364/OE.15.017120.

[287] M. J. Abel, T. Pfeifer, P. M. Nagel, W. Boutu, M. J. Bell, C. P. Steiner, D. M. Neumark, and S. R. Leone, "Isolated attosecond pulses from ionization gating of high-harmonic emission," *Chemical Physics*, vol. 366, no. 1-3, pp. 9–14, 2009. https://doi.org/10.1016/j.chemphys.2009.09.016.

[288] A. Bouhal, P. Salières, P. Breger, P. Agostini, G. Hamoniaux, A. Mysyrowicz, A. Antonetti, R. Constantinescu, and H. Muller, "Temporal dependence of high-order harmonics in the presence of strong ionization," *Physical Review A*, vol. 58, no. 1, p. 389, 1998. https://doi.org/10.1103/PhysRevA.58.389.

[289] W. Cao, P. Lu, P. Lan, X. Wang, and G. Yang, "Single-attosecond pulse generation with an intense multicycle driving pulse," *Physical Review A*,

vol. 74, no. 6, p. 063821, 2006. https://doi.org/10.1103/PhysRevA.74.063821.

[290] T. Sekikawa, A. Kosuge, T. Kanai, and S. Watanabe, "Nonlinear optics in the extreme ultraviolet," *Nature*, vol. 432, no. 7017, pp. 605–608, 2004. https://doi.org/10.1038/nature03108.

[291] A. Jullien, T. Pfeifer, M. J. Abel, P. Nagel, M. Bell, D. M. Neumark, and S. R. Leone, "Ionization phase-match gating for wavelength-tunable isolated attosecond pulse generation," *Applied Physics B*, vol. 93, pp. 433–442, 2008. https://doi.org/10.1007/s00340-008-3187-z.

[292] E. J. Takahashi, P. Lan, O. D. Mücke, Y. Nabekawa, and K. Midorikawa, "Attosecond nonlinear optics using gigawatt-scale isolated attosecond pulses," *Nature communications*, vol. 4, no. 1, p. 2691, 2013. https://doi.org/10.1038/ncomms3691.

[293] E. Neyra, F. Videla, J. A. Pérez-Hernández, M. F. Ciappina, L. Roso, and G. A. Torchia, "High-order harmonic generation driven by chirped laser pulses induced by linear and non linear phenomena," *The European Physical Journal D*, vol. 70, pp. 1–6, 2016. https://doi.org/10.1140/epjd/e2016-70320-5.

[294] Z. Chang, A. Rundquist, H. Wang, I. Christov, H. Kapteyn, and M. Murnane, "Temporal phase control of soft-x-ray harmonic emission," *Physical Review A*, vol. 58, no. 1, p. R30, 1998. https://doi.org/10.1103/PhysRevA.58.R30.

[295] D. G. Lee, J.-H. Kim, K.-H. Hong, and C. H. Nam, "Coherent control of high-order harmonics with chirped femtosecond laser pulses," *Physical Review Letters*, vol. 87, no. 24, p. 243902, 2001. https://doi.org/10.1103/PhysRevLett.87.243902.

[296] J. Zhou, J. Peatross, M. Murnane, H. Kapteyn, and I. Christov, "Enhanced high-harmonic generation using 25 fs laser pulses," *Physical Review Letters*, vol. 76, no. 5, p. 752, 1996. https://link.aps.org/doi/10.1103/PhysRevLett.76.752.

[297] M. Lewenstein, P. Salieres, and A. L'huillier, "Phase of the atomic polarization in high-order harmonic generation," *Physical Review A*, vol. 52, no. 6, p. 4747, 1995. https://link.aps.org/doi/10.1103/PhysRevA.52.4747.

[298] L. E. Chipperfield, J. S. Robinson, P. L. Knight, J. P. Marangos, and J. W. Tisch, "The generation and utilisation of half-cycle cut-offs in high harmonic spectra," *Laser & Photonics Reviews*, vol. 4, no. 6, pp. 697–719, 2010. https://doi.org/10.1002/lpor.200900028.

[299] C. Haworth, L. Chipperfield, J. Robinson, P. Knight, J. Marangos, and J. Tisch, "Half-cycle cutoffs in harmonic spectra and robust carrier-envelope

phase retrieval," *Nature Physics*, vol. 3, no. 1, pp. 52–57, 2007. https://doi.org/10.1038/nphys463.

[300] E. P. Hunter and S. G. Lias, "Evaluated gas phase basicities and proton affinities of molecules: an update," *Journal of Physical and Chemical Reference Data*, vol. 27, no. 3, pp. 413–656, 1998. https://doi.org/10.1063/1.556018.

[301] P.-M. Paul, E. S. Toma, P. Breger, G. Mullot, F. Augé, P. Balcou, H. G. Muller, and P. Agostini, "Observation of a train of attosecond pulses from high harmonic generation," *Science*, vol. 292, no. 5522, pp. 1689–1692, 2001. https://doi.org/10.1126/science.1059413.

[302] H. . G. Muller, "Reconstruction of attosecond harmonic beating by interference of two-photon transitions," *Applied Physics B*, vol. 74, pp. s17–s21, 2002. https://doi.org/10.1007/s00340-002-0894-8.

[303] Y. Mairesse, A. De Bohan, L. Frasinski, H. Merdji, L. Dinu, P. Monchicourt, P. Breger, M. Kovacev, R. Taïeb, B. Carré, *et al.*, "Attosecond synchronization of high-harmonic soft x-rays," *Science*, vol. 302, no. 5650, pp. 1540–1543, 2003. https://doi.org/10.1126/science.1090277.

[304] J. Itatani, F. Quéré, G. L. Yudin, M. Y. Ivanov, F. Krausz, and P. B. Corkum, "Attosecond streak camera," *Physical review letters*, vol. 88, no. 17, p. 173903, 2002. https://link.aps.org/doi/10.1103/PhysRevLett.88.173903.

[305] M. Drescher, M. Hentschel, R. Kienberger, G. Tempea, C. Spielmann, G. A. Reider, P. B. Corkum, and F. Krausz, "X-ray pulses approaching the attosecond frontier," *Science*, vol. 291, no. 5510, pp. 1923–1927, 2001. https://doi.org/10.1126/science.1058561.

[306] M. Kitzler, N. Milosevic, A. Scrinzi, F. Krausz, and T. Brabec, "Quantum theory of attosecond XUV pulse measurement by laser dressed photoionization," *Physical review letters*, vol. 88, no. 17, p. 173904, 2002. https://link.aps.org/doi/10.1103/PhysRevLett.88.173904.

[307] J. Gagnon, *Attosecond Electron Spectroscopy*. PhD thesis, LMU Munich, 2011. https://doi.org/10.5282/edoc.12537.

[308] F. Quéré, Y. Mairesse, and J. Itatani, "Temporal characterization of attosecond XUV fields," *Journal of Modern Optics*, vol. 52, no. 2-3, pp. 339–360, 2005. https://doi.org/10.1080/09500340412331307942.

[309] P. Hamm, M. Lim, and R. M. Hochstrasser, "Structure of the amide I band of peptides measured by femtosecond nonlinear-infrared spectroscopy," *The Journal of Physical Chemistry B*, vol. 102, no. 31, pp. 6123–6138, 1998. https://doi.org/10.1021/jp9813286.

[310] M. Asplund, M. T. Zanni, and R. M. Hochstrasser, "Two-dimensional infrared spectroscopy of peptides by phase-controlled femtosecond vibrational photon echoes," *Proceedings of the National Academy of Sciences*, vol. 97, no. 15, pp. 8219–8224, 2000. https://doi.org/10.1073/pnas.140227997.

[311] S. Mukamel, "Multidimensional femtosecond correlation spectroscopies of electronic and vibrational excitations," *Annual review of physical chemistry*, vol. 51, no. 1, pp. 691–729, 2000. https://doi.org/10.1146/annurev.physchem.51.1.691.

[312] K. Okumura, D. M. Jonas, and Y. Tanimura, "Two-dimensional spectroscopy and harmonically coupled anharmonic oscillators," *Chemical Physics*, vol. 266, no. 2-3, pp. 237–250, 2001. https://doi.org/10.1016/S0301-0104(01)00252-X.

[313] P. Tian, D. Keusters, Y. Suzaki, and W. S. Warren, "Femtosecond phase-coherent two-dimensional spectroscopy," *Science*, vol. 300, no. 5625, pp. 1553–1555, 2003. https://doi.org/10.1126/science.1083433.

[314] D. M. Jonas, "Two-dimensional femtosecond spectroscopy," *Annual review of physical chemistry*, vol. 54, no. 1, pp. 425–463, 2003. https://doi.org/10.1146/annurev.physchem.54.011002.103907.

[315] T. Brixner, J. Stenger, H. M. Vaswani, M. Cho, R. E. Blankenship, and G. R. Fleming, "Two-dimensional spectroscopy of electronic couplings in photosynthesis," *Nature*, vol. 434, no. 7033, pp. 625–628, 2005. https://doi.org/10.1038/nature03429.

[316] W. Kuehn, K. Reimann, M. Woerner, and T. Elsaesser, "Phase-resolved two-dimensional spectroscopy based on collinear n-wave mixing in the ultrafast time domain," *The Journal of chemical physics*, vol. 130, no. 16, p. 164503, 2009. https://doi.org/10.1063/1.3120766.

[317] J. Bredenbeck, A. Ghosh, H.-K. Nienhuys, and M. Bonn, "Interface-specific ultrafast two-dimensional vibrational spectroscopy," *Accounts of chemical research*, vol. 42, no. 9, pp. 1332–1342, 2009. https://doi.org/10.1021/ar900016c.

[318] P. Hamm and M. Zanni, *Concepts and methods of 2D infrared spectroscopy*. Cambridge University Press, 2011. https://doi.org/10.1017/CBO9780511675935.

[319] H. J. Marroux, A. P. Fidler, D. M. Neumark, and S. R. Leone, "Multidimensional spectroscopy with attosecond extreme ultraviolet and shaped near-infrared pulses," *Science advances*, vol. 4, no. 9, p. eaau3783, 2018. https://doi.org/10.1126/sciadv.aau3783.

[320] T. Kaneyasu, Y. Hikosaka, M. Fujimoto, H. Iwayama, and M. Katoh, "Electron wave packet interference in atomic inner-shell excitation," *Phys. Rev.*

Lett., vol. 126, p. 113202, Mar 2021. https://link.aps.org/doi/10.1103/PhysRevLett.126.113202.

[321] D. Z. Kandula, C. Gohle, T. J. Pinkert, W. Ubachs, and K. S. E. Eikema, "Extreme ultraviolet frequency comb metrology," *Phys. Rev. Lett.*, vol. 105, p. 063001, Aug 2010. https://link.aps.org/doi/10.1103/PhysRevLett.105.063001.

[322] X. Li, G. Yuan, X. Tang, Y. Fu, K. Wang, B. Wang, and C. Jin, "Modification of laser-induced state in atomic attosecond transient absorption by the XUV pulse pair," *Communications in Theoretical Physics*, vol. 75, no. 1, p. 015503, 2022. https://doi.org/10.1088/1572-9494/ac9be9.

[323] O. Kneller, D. Azoury, Y. Federman, M. Krueger, A. J. Uzan, G. Orenstein, B. D. Bruner, O. Smirnova, S. Patchkovskii, M. Ivanov, *et al.*, "A look under the tunnelling barrier via attosecond-gated interferometry," *Nature photonics*, vol. 16, no. 4, pp. 304–310, 2022. https://doi.org/10.1038/s41566-022-00955-7.

[324] W. Demtröder, *Laserspektroskopie: Grundlagen und Techniken/ Laser Spectroscopy: Spectroscopy with Lasers*. Springer-Verlag, 2007. https://books.google.de/books?id=AhckBAAAQBAJ.

[325] R. J. I. Marks, *Introduction to Shannon sampling and interpolation theory*. Springer Science & Business Media, 2012. https://books.google.de/books?id=JZvhBwAAQBAJ.

[326] N. Papadogiannis, E. Hertz, C. Kalpouzos, and D. Charalambidis, "Laser-intensity effects in high-order autocorrelation calculations," *Physical Review A*, vol. 66, no. 2, p. 025803, 2002. https://link.aps.org/doi/10.1103/PhysRevA.66.025803.

[327] D. Gabor, "Theory of communication. Part 1: The analysis of information," *Journal of the Institution of Electrical Engineers-part III: radio and communication engineering*, vol. 93, no. 26, pp. 429–441, 1946. https://doi.org/10.1049/ji-3-2.1946.0074.

[328] A. Kramida, Yu. Ralchenko, J. Reader, and and NIST ASD Team. NIST Atomic Spectra Database (ver. 5.11), [Online]. Available: https://physics.nist.gov/asd [2024, January 16]. National Institute of Standards and Technology, Gaithersburg, MD., 2023.

[329] D. C. Morton, Q. Wu, and G. W. Drake, "Energy levels for the stable isotopes of atomic helium (^{4}He I and ^{3}He I)," *Canadian Journal of Physics*, vol. 84, no. 2, pp. 83–105, 2006. https://doi.org/10.1139/p06-009.

[330] I. S. Averbukh and N. Perelman, "Fractional revivals: Universality in the long-term evolution of quantum wave packets beyond the correspondence principle dynamics," *Physics Letters A*, vol. 139, no. 9, pp. 449–453, 1989. https://doi.org/10.1016/0375-9601(89)90943-2.

[331] I. S. Averbukh and N. F. Perel'man, "The dynamics of wave packets of highly-excited states of atoms and molecules," *Soviet Physics Uspekhi*, vol. 34, p. 572, july 1991. https://dx.doi.org/10.1070/PU1991v034n07ABEH002447.

[332] N. F. Scherer, R. J. Carlson, A. Matro, M. Du, A. J. Ruggiero, V. Romero-Rochin, J. A. Cina, G. R. Fleming, and S. A. Rice, "Fluorescence-detected wave packet interferometry: Time resolved molecular spectroscopy with sequences of femtosecond phase-locked pulses," *The Journal of chemical physics*, vol. 95, no. 3, pp. 1487–1511, 1991. https://doi.org/10.1063/1.461064.

[333] S. Vetchinkin, A. Vetchinkin, V. Eryomin, and I. Umanskii, "Gaussian wavepacket dynamics in an anharmonic system," *Chemical physics letters*, vol. 215, no. 1-3, pp. 11–16, 1993. https://doi.org/10.1016/0009-2614(93)89255-G.

[334] S. Vetchinkin and V. Eryomin, "The structure of wavepacket fractional revivals in a morse-like anharmonic system," *Chemical physics letters*, vol. 222, no. 4, pp. 394–398, 1994. https://doi.org/10.1016/0009-2614(94)87080-2.

[335] A. Rudenko, T. Ergler, B. Feuerstein, K. Zrost, C. Schröter, R. Moshammer, and J. Ullrich, "Real-time observation of vibrational revival in the fastest molecular system," *Chemical physics*, vol. 329, no. 1-3, pp. 193–202, 2006. https://doi.org/10.1016/j.chemphys.2006.06.038.

[336] R. W. Robinett, "Quantum wave packet revivals," *Physics reports*, vol. 392, no. 1-2, pp. 1–119, 2004. https://doi.org/10.1016/j.physrep.2003.11.002.

[337] T. Ergler, A. Rudenko, B. Feuerstein, K. Zrost, C. D. Schröter, R. Moshammer, and J. Ullrich, "Spatiotemporal imaging of ultrafast molecular motion: Collapse and revival of the D_2^+ nuclear wave packet," *Phys. Rev. Lett.*, vol. 97, p. 193001, Nov 2006. https://link.aps.org/doi/10.1103/PhysRevLett.97.193001.

[338] T. Lohmüller, V. Engel, J. Beswick, and C. Meier, "Fractional revivals in the rovibrational motion of I_2," *The Journal of chemical physics*, vol. 120, no. 22, pp. 10442–10449, 2004. https://doi.org/10.1063/1.1711809.

[339] T. Sharp, "Potential-energy curves for molecular hydrogen and its ions," *Atomic Data and Nuclear Data Tables*, vol. 2, pp. 119–169, 1970. https://doi.org/10.1016/S0092-640X(70)80007-9.

[340] K. P. Huber and G. H. Herzberg, *Constants of Diatomic Molecules.* NIST Chemistry WebBook, NIST Standard Reference Database Number 69, Eds. P.J. Linstrom and W.G. Mallard, National Institute of Standards and Technology, Gaithersburg MD, 20899, Decem-

ber 2023. https://webbook.nist.gov/cgi/cbook.cgi?ID=C12184906&Units=SI&Mask=1000#Diatomic.

[341] J. Franck and E. Dymond, "Elementary processes of photochemical reactions," *Transactions of the Faraday Society*, vol. 21, no. February, pp. 536–542, 1926. https://doi.org/10.1039/TF9262100536.

[342] P. M. Morse, "Diatomic molecules according to the wave mechanics. II. Vibrational levels," *Physical review*, vol. 34, no. 1, p. 57, 1929. https://link.aps.org/doi/10.1103/PhysRev.34.57.

[343] A. D. Bandrauk and M. L. Sink, "Photodissociation in intense laser fields: Predissociation analogy," *The Journal of Chemical Physics*, vol. 74, no. 2, pp. 1110–1117, 1981. https://doi.org/10.1063/1.441217.

[344] A. Giusti-Suzor, F. H. Mies, L. F. DiMauro, E. Charron, and B. Yang, "Dynamics of H_2^+ in intense laser fields," *Journal of Physics B: Atomic, Molecular and Optical Physics*, vol. 28, p. 309, feb 1995. https://dx.doi.org/10.1088/0953-4075/28/3/006.

[345] K. Sändig, H. Figger, and T. W. Hänsch, "Dissociation dynamics of H_2^+ in intense laser fields: Investigation of photofragments from single vibrational levels," *Phys. Rev. Lett.*, vol. 85, pp. 4876–4879, Dec 2000. https://link.aps.org/doi/10.1103/PhysRevLett.85.4876.

[346] A. Giusti-Suzor, X. He, O. Atabek, and F. H. Mies, "Above-threshold dissociation of H_2^+ in intense laser fields," *Phys. Rev. Lett.*, vol. 64, pp. 515–518, Jan 1990. https://link.aps.org/doi/10.1103/PhysRevLett.64.515.

[347] P. H. Bucksbaum, A. Zavriyev, H. G. Muller, and D. W. Schumacher, "Softening of the H_2^+ molecular bond in intense laser fields," *Phys. Rev. Lett.*, vol. 64, pp. 1883–1886, Apr 1990. https://link.aps.org/doi/10.1103/PhysRevLett.64.1883.

[348] G. Jolicard and O. Atabek, "Above-threshold-dissociation dynamics of H_2^+ with short intense laser pulses," *Phys. Rev. A*, vol. 46, pp. 5845–5855, Nov 1992. https://link.aps.org/doi/10.1103/PhysRevA.46.5845.

[349] J.-M. Yuan and T. F. George, "Semiclassical study of reactive scattering in a laser field: F+H_2+h/ω (1.06 μm) system," *The Journal of Chemical Physics*, vol. 70, no. 2, pp. 990–994, 1979. https://doi.org/10.1063/1.437489.

[350] A. M. F. Lau and C. K. Rhodes, "Field-induced avoided crossing and new transition channels in atomic and molecular gases irradiated by lasers," *Phys. Rev. A*, vol. 16, pp. 2392–2412, Dec 1977. https://link.aps.org/doi/10.1103/PhysRevA.16.2392.

[351] T. T. Nguyen-Dang and A. D. Bandrauk, "Higher order adiabatic separation of strongly coupled systems. I. Two-body systems and dressed hydrogen atom," *The Journal of chemical physics*, vol. 85, no. 12, pp. 7224–7231, 1986. https://doi.org/10.1063/1.451359.

[352] F. Martín, "Ionization and dissociation using B-splines: photoionization of the hydrogen molecule," *Journal of Physics B: Atomic, Molecular and Optical Physics*, vol. 32, no. 16, p. R197, 1999. https://doi.org/10.1088/0953-4075/32/16/201.

[353] K.-P. Huber, *Molecular spectra and molecular structure: IV. Constants of diatomic molecules*. Springer Science & Business Media, 2013. https://doi.org/10.1007/978-1-4757-0961-2.

[354] A. Scrinzi, "t-SURFF: fully differential two-electron photo-emission spectra," *New Journal of Physics*, vol. 14, no. 8, p. 085008, 2012. https://doi.org/10.1088/1367-2630/14/8/085008.

[355] L. Yue and L. B. Madsen, "Dissociation and dissociative ionization of H_2^+ using the time-dependent surface flux method," *Physical Review A*, vol. 88, no. 6, p. 063420, 2013. https://link.aps.org/doi/10.1103/PhysRevA.88.063420.

[356] J. Morgenweg, I. Barmes, and K. S. Eikema, "Ramsey-comb spectroscopy with intense ultrashort laser pulses," *Nature Physics*, vol. 10, no. 1, pp. 30–33, 2014. https://doi.org/10.1038/nphys2807.

[357] H. Katsuki, H. Chiba, C. Meier, B. Girard, and K. Ohmori, "Actively tailored spatiotemporal images of quantum interference on the picometer and femtosecond scales," *Physical review letters*, vol. 102, no. 10, p. 103602, 2009. https://link.aps.org/doi/10.1103/PhysRevLett.102.103602.

[358] S. Witte, V. T. Tenner, D. W. Noom, and K. S. Eikema, "Lensless diffractive imaging with ultra-broadband table-top sources: from infrared to extreme-ultraviolet wavelengths," *Light: Science & Applications*, vol. 3, no. 3, pp. e163–e163, 2014. https://doi.org/10.1038/lsa.2014.44.

[359] A. Perri, B. N. De Faria, D. T. Ferreira, D. Comelli, G. Valentini, F. Preda, D. Polli, A. De Paula, G. Cerullo, and C. Manzoni, "Hyperspectral imaging with a TWINS birefringent interferometer," *Optics express*, vol. 27, no. 11, pp. 15956–15967, 2019. https://doi.org/10.1364/OE.27.015956.

[360] G. Sansone, F. Kelkensberg, J. Pérez-Torres, F. Morales, M. F. Kling, W. Siu, O. Ghafur, P. Johnsson, M. Swoboda, E. Benedetti, *et al.*, "Electron localization following attosecond molecular photoionization," *Nature*, vol. 465, no. 7299, pp. 763–766, 2010. https://doi.org/10.1038/nature09084.

[361] O. Laporte and W. F. Meggers, "Some rules of spectral structure," *Josa*, vol. 11, no. 5, pp. 459–463, 1925. https://doi.org/10.1364/JOSA.11.000459.

[362] F. Martín, J. Fernández, T. Havermeier, L. Foucar, T. Weber, K. Kreidi, M. Schoffler, L. Schmidt, T. Jahnke, O. Jagutzki, *et al.*, "Single photon-induced symmetry breaking of H_2 dissociation," *Science*, vol. 315, no. 5812, pp. 629–633, 2007. https://doi.org/10.1126/science.1136598.

[363] D. Ray, F. He, S. De, W. Cao, H. Mashiko, P. Ranitovic, K. Singh, I. Znakovskaya, U. Thumm, G. Paulus, *et al.*, "Ion-energy dependence of asymmetric dissociation of D_2 by a two-color laser field," *Physical review letters*, vol. 103, no. 22, p. 223201, 2009. https://link.aps.org/doi/10.1103/PhysRevLett.103.223201.

[364] M. Kremer, B. Fischer, B. Feuerstein, V. L. de Jesus, V. Sharma, C. Hofrichter, A. Rudenko, U. Thumm, C. D. Schröter, R. Moshammer, *et al.*, "Electron localization in molecular fragmentation of H_2 by carrier-envelope phase stabilized laser pulses," *Physical review letters*, vol. 103, no. 21, p. 213003, 2009. https://link.aps.org/doi/10.1103/PhysRevLett.103.213003.

[365] F. He, C. Ruiz, and A. Becker, "Coherent control of electron wave packets in dissociating H_2^+," *Journal of Physics B: Atomic, Molecular and Optical Physics*, vol. 41, no. 8, p. 081003, 2008. https://doi.org/10.1088/0953-4075/41/8/081003.

[366] F. Kelkensberg, *Capturing atomic and electronic motion with high harmonic generation light pulses*. PhD thesis, FOM Institute AMOLF, 2011. https://hdl.handle.net/2066/90924.

[367] F. Morales, J. F. Pérez-Torres, J. L. Sanz-Vicario, and F. Martín, "Probing H_2 quantum autoionization dynamics with XUV atto and femtosecond laser pulses," *Chemical Physics*, vol. 366, no. 1-3, pp. 58–63, 2009. https://doi.org/10.1016/j.chemphys.2009.09.008.

[368] G. Sansone, F. Kelkensberg, F. Morales, J. Perez-Torres, F. Martín, and M. J. Vrakking, "Attosecond time-resolved electron dynamics in the hydrogen molecule," *IEEE Journal of Selected Topics in Quantum Electronics*, vol. 18, no. 1, pp. 520–530, 2011. https://doi.org/10.1109/JSTQE.2011.2155624.

[369] K. Singh, F. He, P. Ranitovic, W. Cao, S. De, D. Ray, S. Chen, U. Thumm, A. Becker, M. Murnane, *et al.*, "Control of electron localization in deuterium molecular ions using an attosecond pulse train and a many-cycle infrared pulse," *Physical Review Letters*, vol. 104, no. 2, p. 023001, 2010. https://link.aps.org/doi/10.1103/PhysRevLett.104.023001.

[370] A. Savitzky and M. J. Golay, "Smoothing and differentiation of data by simplified least squares procedures.," *Analytical chemistry*, vol. 36, no. 8, pp. 1627–1639, 1964. https://doi.org/10.1021/ac60214a047.

[371] A. González-Castrillo, A. Palacios, F. Catoire, H. Bachau, and F. Martín, "Reproducibility of observables and coherent control in molecular photoionization: from continuous wave to ultrashort pulsed radiation," *The Journal of Physical Chemistry A*, vol. 116, no. 11, pp. 2704–2712, 2012. https://doi.org/10.1021/jp2078049.

[372] I. Sánchez and F. Martín, "Origin of unidentified structures in resonant dissociative photoionization of H_2," *Physical review letters*, vol. 79, no. 9, p. 1654, 1997. https://link.aps.org/doi/10.1103/PhysRevLett.79.1654.

[373] I. Sánchez and F. Martín, "Resonant dissociative photoionization of h_2 and d_2," *Physical Review A*, vol. 57, no. 2, p. 1006, 1998. https://link.aps.org/doi/10.1103/PhysRevA.57.1006.

[374] J. F. Pérez-Torres, F. Morales, J. L. Sanz-Vicario, and F. Martín, "Asymmetric electron angular distributions in resonant dissociative photoionization of H_2 with ultrashort XUV pulses," *Physical Review A*, vol. 80, no. 1, p. 011402, 2009. https://link.aps.org/doi/10.1103/PhysRevA.80.011402.

[375] P. W. Atkins, J. De Paula, and J. Keeler, *Atkins' physical chemistry*. Oxford university press, 2023. https://books.google.de/books?id=4gamEAAAQBAJ.

[376] K. Ito, R. I. Hall, and M. Ukai, "Dissociative photoionization of H_2 and D_2 in the energy region of 25–45 ev," *The Journal of chemical physics*, vol. 104, no. 21, pp. 8449–8457, 1996. https://doi.org/10.1063/1.471594.

[377] M. Lewenstein, M. F. Ciappina, E. Pisanty, J. Rivera-Dean, P. Stammer, T. Lamprou, and P. Tzallas, "Generation of optical Schrödinger cat states in intense laser–matter interactions," *Nature Physics*, vol. 17, no. 10, pp. 1104–1108, 2021. https://doi.org/10.1038/s41567-021-01317-w.

[378] P. Stammer, J. Rivera-Dean, T. Lamprou, E. Pisanty, M. F. Ciappina, P. Tzallas, and M. Lewenstein, "High photon number entangled states and coherent state superposition from the extreme ultraviolet to the far infrared," *Physical Review Letters*, vol. 128, no. 12, p. 123603, 2022. https://link.aps.org/doi/10.1103/PhysRevLett.128.123603.

[379] P. Stammer, "Theory of entanglement and measurement in high-order harmonic generation," *Physical Review A*, vol. 106, no. 5, p. L050402, 2022. https://link.aps.org/doi/10.1103/PhysRevA.106.L050402.

[380] P. Stammer, J. Rivera-Dean, A. Maxwell, T. Lamprou, A. Ordóñez, M. F. Ciappina, P. Tzallas, and M. Lewenstein, "Quantum electrodynamics of intense laser-matter interactions: A tool for quantum state engineering," *PRX Quantum*, vol. 4, no. 1, p. 010201, 2023. https://link.aps.org/doi/10.1103/PRXQuantum.4.010201.

[381] J. Rivera-Dean, P. Stammer, A. S. Maxwell, T. Lamprou, P. Tzallas, M. Lewenstein, and M. F. Ciappina, "Light-matter entanglement after above-threshold ionization processes in atoms," *Physical Review A*, vol. 106, no. 6, p. 063705, 2022. https://link.aps.org/doi/10.1103/PhysRevA.106.063705.

[382] J. Rivera-Dean, P. Stammer, A. S. Maxwell, T. Lamprou, A. F. Ordóñez, E. Pisanty, P. Tzallas, M. Lewenstein, and M. F. Ciappina, "Quantum optical analysis of high-harmonic generation in solids within a wannier-bloch picture," *arXiv preprint arXiv:2211.00033*, 2022. https://doi.org/10.48550/arXiv.2211.00033.

[383] M. Lewenstein, N. Baldelli, U. Bhattacharya, J. Biegert, M. F. Ciappina, T. Grass, P. T. Grochowski, A. S. Johnson, T. Lamprou, A. S. Maxwell, A. Ordóñez, E. Pisanty, J. Rivera-Dean, P. Stammer, and P. Tzallas, "Attosecond physics and quantum information science," in *Proceedings of the 8th International Conference on Attosecond Science and Technology* (L. Argenti, M. Chini, and L. Fang, eds.), (Cham), pp. 27–44, Springer International Publishing, 2024. https://doi.org/10.1007/978-3-031-47938-0_4.

[384] O. Kneller, C. Mor, N. Yaffe, M. Krüger, D. Azoury, Y. Federman, D. Rajak, B. Bruner, M. Ivanov, O. Smirnova, *et al.*, "Attosecond transient interferometry," 2023. https://doi.org/10.21203/rs.3.rs-2615689/v1.

[385] H. P. Robertson, "The uncertainty principle," *Phys. Rev.*, vol. 34, pp. 163–164, Jul 1929. https://link.aps.org/doi/10.1103/PhysRev.34.163.

[386] J. M. Steele, *The Cauchy-Schwarz master class: an introduction to the art of mathematical inequalities*. Cambridge University Press, 2004. https://books.google.de/books?id=7GDyRMrlgDsC.

Selbstständigkeitserklärung

Name: Koll

Vorname: Lisa-Marie

Ich erkläre gegenüber der Freien Universität Berlin, dass ich die vorliegende Dissertation selbstständig und ohne Benutzung anderer als der angegebenen Quellen und Hilfsmittel angefertigt habe. Die vorliegende Arbeit ist frei von Plagiaten. Alle Ausführungen, die wörtlich oder inhaltlich aus anderen Schriften entnommen sind, habe ich als solche kenntlich gemacht. Diese Dissertation wurde in gleicher oder ähnlicher Form noch in keinem früheren Promotionsverfahren eingereicht. Mit einer Prüfung meiner Arbeit durch ein Plagiatsprüfungsprogramm erkläre ich mich einverstanden.

Datum: 11.10.2024

Unterschrift: